



**Three-Dimensional Numerical and Physical
Modelling of Soft Soil Improvement Using Concrete
Injected Columns**

A thesis in fulfilment of the requirement
for the award of the degree

Doctor of Philosophy

from

University of Technology Sydney

by

Hamed Mahdavi, BSc Eng, MSc Eng

School of Civil and Environmental Engineering,
Faculty of Engineering and Information Technology

July 2018

CERTIFICATE OF ORIGINAL AUTHORSHIP

I certify that the work in this thesis has not previously been submitted for a degree nor has it been submitted as part of requirements for a degree except as fully acknowledged within the text.

I also certify that the thesis has been written by me. Any help that I have received in my research work and the preparation of the thesis itself has been acknowledged. In addition, I certify that all information sources and literature used are indicated in the thesis.

Signature of Candidate:

Production Note:
Signature removed prior to publication.

Hamed Mahdavi

July 2018

To My Family

ABSTRACT

Concrete injected columns (CICs) are a popular method for improving soft soil properties to support road and bridge approach embankments due to quick construction, absence of spoil, and limited post-construction settlement. While the limited settlement of CICs makes them attractive for cases where there are stringent settlement criteria, low-cost methods of improving soils are used where there are no such limitations. The lack of comprehensive experimental studies on CICs in the available literature showed the necessity of further laboratory modelling. Moreover, the equivalent comparison between frictional and socketed CICs has not been thoroughly studied.

In this study, a well-instrumented physical modelling of soft clay improved with CICs was performed. A granular layer was used to model the load transfer platform (LTP), and a geotextile layer was utilised to model the geosynthetic reinforcement (GR) layer. The load was applied and controlled in stages using a large loading frame on top of the granular layer. Pore pressure dissipation, stresses transferred to the soft soil and CICs, and the strains in the geotextile were monitored with time. A three-dimensional numerical model was also developed using finite difference software FLAC^{3D}, and the results were validated against the experimental data. The numerical model considered coupled flow-deformation allowing prediction of the excess pore water pressure (EPWP) dissipation with time, while the permeability of the soft soil varied with time. Modified Cam-Clay (MCC) soft soil model was used as the constitutive model for the soft clay deposit, while elastic-perfectly plastic Mohr-Coulomb failure criterion was used to simulate the LTP layer. Hoek-Brown constitutive model was used to model the unreinforced concrete used for CIC construction. A good agreement was perceived between the numerical results and the

measurements from the experiment. Referring to both measurements and predictions, despite the low permeability of the soft clay, a rather quick dissipation in the EPWP occurred due to the load transfer mechanism between the soft soil and CICs. The stress concentration ratio decreased at the beginning of the loading stages and then later increased with time, and was higher for higher applied loads.

This thesis also sets out to investigate the options available for the transition zone from CICs to other ground improvement methods away from the abutment. Two possible alternatives were numerically simulated using FLAC^{3D} software considering the dissipation of pore water pressure and variation of soil permeability with time. A geosynthetic layer was introduced into the load transfer platform (LTP) located above the CICs, and interface elements were incorporated to simulate CIC-soil interaction. The first option for the transition zone was widely spaced CICs socketed into stiff material and the second was using shorter, closely spaced, frictional CICs. A comparison was then made between the predicted ground settlement, the force mobilised in the geosynthetic, the excess pore water pressure, and stresses in the CICs for the two scenarios. The total length of the CICs and thus the total volume of the concrete used for their construction were kept the same for both alternatives. Indeed, the embankment on frictional CICs experienced less settlement, the forces mobilised in the geosynthetic were reduced, and the bending moments and shear forces generated in the columns were less than the corresponding values for the case of socketed CICs. This study showed that for a given volume of concrete, shorter, frictional CICs perform better than longer CICs socketed into stiff strata.

Furthermore, a comparison was made between drained and coupled flow-deformation numerical analyses. This study revealed that while performing drained analysis by simply assigning drained parameters to the material was less computationally demanding, it led to inaccuracies in the predictions. The perceived discrepancies were attributed to the difference in the stress-path of drained and coupled analyses.

The results from this study can be beneficial for the practicing engineers for designing structures on CIC-improved grounds, particularly for predicting the time-dependent performance of the system.

ACKNOWLEDGMENT

I would like to sincerely acknowledge the support of the people who made the completion of this thesis possible. I would like to express my gratitude to my principal supervisor, A/Prof. Behzad Fatahi, for his patience and boundless support during my candidacy. He was always available to discuss the project during this time. I would also like to thank my co-supervisor A/Prof. Hadi Khabbaz for his encouragement, optimistic approach, and constructive guidance throughout this time.

I gratefully acknowledge and appreciate the financial support and technical advice received from Roads and Maritime Services (RMS), SMEC Australia, Fulton Hogan, and Menard-Oceania to complete my PhD studies.

I specially thank Dr. Aslan Sadeghi Hokmabadi, and Dr. Babak Azari for generously sharing their experiences and insight, and helping me on this journey. I also extend my gratitude to the UTS laboratory technical staff Dr. Lam Nguyen, Peter Brown, and Antonio Reyno, and also PhD students Balaka Ghosh and Harry Nguyen for their valuable help.

The completion of this work would have not been possible without the encouragement and support of my family. Their unconditional support and unfailing confidence in me made this moment achievable. Special thanks to my sister who has been a friend and inspiration to me, and my beautiful partner for her patience and support.

LIST OF PUBLICATIONS

1. Mahdavi, H., Fatahi, B., Khabbaz, H., 2018. “Physical and Numerical Modelling of Ground Improvement Using Concrete Injected Columns and Geosynthetics Reinforced Load Transfer Platform.” Submitted to *Geotextiles and Geomembranes*
2. Mahdavi, H., Fatahi, B., Khabbaz, H., 2018. “A Comparison of Frictional and Socketed Concrete Injected Columns in a Transition Zone.” Submitted to *Geosynthetics International*
3. Mahdavi, H., Fatahi, B., Khabbaz, H., Vincent, P. and Kelly, R., 2016. “Comparison of Coupled Flow-deformation and Drained Analyses for Road Embankments on CMC-Improved Ground.” *Procedia engineering, 143*, pp.462-469.
4. Mahdavi, H., Fatahi, B., Khabbaz, H., Krzeminski, M., Santos, R. and Marix-Evans, M., 2016. “Three-Dimensional Simulation of a Load Transfer Mechanism for Frictional and End-Bearing CMC-Supported Embankments on Soft Soil.” In *Geo-China 2016*, pp. 60-67

TABLE OF CONTENTS

CONTENTS

1	INTRODUCTION.....	1
1.1	Background.....	1
1.2	Concrete Injected Columns for Ground Improvement.....	2
1.3	Load Sharing between Soil and CICs	3
1.4	Objectives of the Present Study	4
1.5	Organisation of Dissertation	6
2	LITERATURE REVIEW.....	7
2.1	General.....	7
2.2	CIC Ground Improvement Method.....	7
2.2.1	<i>Construction Process</i>	10
2.2.2	<i>Advantages of CICs in Comparison to Other Ground Improvement Techniques</i>	15
2.2.3	<i>Design</i>	16
2.3	Experimental Background on Column Supported Embankments.....	31
2.3.1	<i>Tests Investigating the Stress Concentration Ratio</i>	31
2.3.2	<i>Tests Investigating the Failure Modes of the Columns</i>	34
2.3.3	<i>Tests Investigating the Influence of Different Parameters on the Overall Performance</i>	41
2.4	Raft Foundations	47
2.5	Physical Modelling of Axially Loaded Piles	48
2.6	Numerical Background on Column Supported Embankments	52
2.7	Material Models for Plain Concrete Simulation	67
2.8	Summary	67

3 PHYSICAL AND NUMERICAL MODELLING OF GROUND IMPROVEMENT USING CONCRETE INJECTED COLUMNS 70

3.1 General..... 70

3.2 Physical Modelling 72

3.2.1 *Dimensional Analysis and Materials* 72

3.2.2 *Test set-up* 80

3.3 Three-Dimensional Numerical Simulation 88

3.3.1 *Clay Deposit Properties*..... 91

3.3.2 *CIC Simulation*..... 93

3.3.3 *Interface Elements*..... 95

3.3.4 *Geotextile Layer*..... 96

3.4 Results and Discussion..... 97

3.4.1 *Stress Concentration Ratio (SCR)*..... 97

3.4.2 *Settlement*..... 106

3.4.3 *Pore Pressure*..... 109

3.4.4 *Tension in the Geotextile Layer* 112

3.5 Summary 115

4 A COMPARISON BETWEEN FRICTIONAL AND SOCKETED CONCRETE INJECTED COLUMNS FOR DESIGNING GROUND IMPROVEMENT IN A TRANSITION ZONE 117

4.1 General..... 117

4.2 Numerical Modelling 119

4.2.1 *Model Geometry and Overview* 119

4.2.2 *Soft Soil Properties* 123

4.2.3 *CIC Simulation*..... 127

4.2.4 *Geosynthetic Layer* 130

4.2.5 *Embankment Properties and Construction Sequence* 131

4.3 Results and Discussion..... 131

4.3.1	<i>Settlement Predictions</i>	131
4.3.2	<i>Excess Pore Water Pressure Predictions</i>	136
4.3.3	<i>Tension in the Geosynthetic Layer</i>	138
4.3.4	<i>Axial Stresses in the CICs</i>	141
4.3.5	<i>Predicted Lateral Displacement</i>	145
4.3.6	<i>Predicted Bending Moments and Shear Forces in CICs</i>	149
4.4	Verification Exercise Against Analytical Solution.....	155
4.5	Summary.....	157
5	COMPARISON OF COUPLED FLOW-DEFORMATION AND DRAINED ANALYSES FOR ROAD EMBANKMENTS ON CIC-IMPROVED GROUND	159
5.1	General.....	159
5.2	Numerical Modelling.....	159
5.3	Results and Discussion.....	163
5.3.1	<i>Settlement</i>	163
5.3.2	<i>Tension in the Geosynthetic Layer</i>	164
5.3.3	<i>Lateral Displacement</i>	165
5.3.4	<i>Summary</i>	167
6	CONCLUSIONS AND RECOMMENDATIONS	169
6.1	Summary.....	169
6.2	Key Conclusions.....	170
6.3	Recommendations for Future Research.....	173
	REFERENCES	175
	APPENDIX A	191
	APPENDIX B	197

LIST OF FIGURES

Figure 1.1 CIC installation, Heathcote project, NSW, Australia.....	3
Figure 1.2 Load transfer mechanism in CIC-improved ground.....	4
Figure 2.1 Different types of inclusions (Modified after Yee et al. 2012).....	10
Figure 2.2 CIC Installation augers (Courtesy of Menard 2018).	13
Figure 2.3 CIC installation steps (Courtesy of Menard 2016).	14
Figure 2.4 Load sharing mechanism in CIC (Modified after ASIRI 2012).....	17
Figure 2.5 Stress distribution in soil-CIC mass, σ_{soil} = stress transferred to the soil, u_{soil} = vertical deformation of the soil, σ_{CIC} = stress transferred to the CIC, u_{CIC} = vertical deformation of the CIC (Modified after Simon & Schlosser 2006)	17
Figure 2.6 Distribution of vertical effective stress around an inclusion awn (Modified after ASIRI 2012).....	19
Figure 2.7 Group of rigid inclusions (Modified after ASIRI 2012).....	21
Figure 2.8 Negative skin friction for inclusions in a group (Modified after Combarieu 1985)	22
Figure 2.9 Fictitious inclusion method for LTP design (Modified after Combarieu 1988)	26
Figure 2.10 Failure mode in the load transfer platform (Modified after ASIRI 2012)	28
Figure 2.11 Inverted pyramid load transfer mechanism in the LTP according to Carlsson (1987).....	28
Figure 2.12 (a) Shaft friction on a CIC and (b) the position of neutral planes in a CIC system (Modified after ASIRI 2012)	29
Figure 2.13 <i>Egg carton (or mushroom) effect on rigid inclusions (ASIRI 2012)</i>	30
Figure 2.14 Failure modes for single columns (Modified after Broms 2004).....	37
Figure 2.15 Photographs of deformed sand columns exhumed at the end of footing penetration (arrows indicate original level of column bases):(a) $L/ro=2$, $A_s=24\%$, $rc=$ $5:5$ mm, (b) $L/ro= 2$, $A_s=30\%$, $rc=8:75$ mm, (c) $L/ro=3:4$, $A_s=24\%$, $rc=8:75$ mm and (d) $L/ro=3:2$, $A_s=24\%$, $rc=5:5$ mm (Wood et al. 2000).....	39

Figure 2.16 Sketches of deformation modes: (a) bulging and shear failure plane mode, (b) Short column versus long column, and (c) slender column (Modified after Wood et al. 2000).....	40
Figure 2.17 Foundation systems (Modified after Mandolini et al. 2013)	47
Figure 2.18 Idealization of H-section pile (Modified after Fleming et al. 2008).....	49
Figure 2.19 Pile under axial loading (Modified after Wood 2004).....	51
Figure 3.1 The set-up of CIC-improved ground	73
Figure 3.2 CIC arrangement in the consolidation cell showing hexagonal unit cell tributary area	75
Figure 3.3 Schematic diagram of the physical model and instrument locations (in mm) (a) cross-section view and (b) plan view (Note: cylindrical coordinates in brackets; first number shows the radial distance (mm), second number is the azimuth or angular coordinate, and the third number is the distance from the bottom of the cell (mm)).....	82
Figure 3.4 (a) Three-dimensional view of the CICs with the clay excavated after the test completion and (b) Plan view of the position of EPCs on the CICs and soft soil	84
Figure 3.5 Schematic diagram of the large consolidometer set-up	85
Figure 3.6 (a) Locations and orientations of strain gauges on the geotextile layer (Note: SGX: strain gauge in X direction; SGY: strain gauge in Y direction) and (b) Geotextile harnessed using two timber washers and epoxy glue.....	87
Figure 3.7 Model geometry and zoning (a) elevation view, (b) 3D view and (c) cross section view.....	90
Figure 3.8 Boundary conditions in (a) the numerical simulation and (b) the experiment.....	91
Figure 3.9 Permeability variation versus void ratio	93
Figure 3.10 Stress on (a) CIC1 measured by EPC1 and (b) CIC2 measured by EPC2 versus time	99
Figure 3.11 Stress on soil measured by EPC5 versus time	100
Figure 3.12 Stress concentration ratio (SCR) versus time based on stresses measured by EPC2 and EPC5	101
Figure 3.13 Stress on the side wall measured by EPC3	102

Figure 3.14 Stress at the bottom of the cell measured by EPC4.....	103
Figure 3.15 Stress variation with depth in CIC1 and the soft soil midway between CIC1 and CIC6 at the end of the test under 80 kPa surcharge.....	104
Figure 3.16 Variations of stress concentration ratio (SCR) with depth at the end of the test under 80 kPa surcharge.....	104
Figure 3.17 Contours of vertical stress on the soil surface at the end of the test.....	105
Figure 3.18 Settlement of the soil surface measured by the LVDT on the loading platen.....	106
Figure 3.19 Deformed shape of the system at the end of the test under 80 kPa surcharge.....	107
Figure 3.20 Settlement profile at the CIC-head level along Section A-A at the end of the test under 80 kPa surcharge.....	108
Figure 3.21 Differential settlement at the CIC-head level along Section A-A at the end of the test under 80 kPa surcharge.....	108
Figure 3.22 Variations of EPWP with time measured by PWPT1 between the two CICs.....	109
Figure 3.23 Variations of EPWP with time measured by PWPT2 between the two CIC.....	110
Figure 3.24 Variations of EPWP with time for PWPT3 on the side wall.....	111
Figure 3.25 Variations of EPWP with time for PWPT4 at the bottom of the cell...	111
Figure 3.26 Tension in the geotextile layer in Y-direction.....	112
Figure 3.27 Tension in the geotextile layer in X-direction.....	113
Figure 3.28 Profile of the tension in the geotextile along Section A-A at the end of the test under 80kPa surcharge.....	114
Figure 3.29 Contours of tensile stress in the geotextile at the end of the test under 80kPa surcharge.....	114
Figure 4.1 Longitudinal cross section of a typical transition zone design of a CIC project (a) Frictional CICs (b) Socketed CICs.....	119
Figure 4.2 Model geometry for socketed CICs: (a) elevation view (b) cross section A-A.....	120

Figure 4.3 Model geometry for frictional CICs: (a) elevation view (b) cross section A'-A'	121
Figure 4.4 FLAC ^{3D} model for socketed CICs	122
Figure 4.5 Variation of permeability versus void ratio in the soft soil	125
Figure 4.6 Variations of (a) vertical effective stress; (b) overconsolidation ratio; (c) shear strength of the soil with depth	126
Figure 4.7 Construction sequence of the embankment	131
Figure 4.8 Settlement profile at the end of consolidation at the embankment base along Sections A-A and A'- A'	132
Figure 4.9 Settlement profile at the end of consolidation on the embankment surface	133
Figure 4.10 Deformed shape of the embankment at the end of consolidation for (a) socketed CICs (Magnification Factor: 10) , and (b) frictional CICs (Magnification Factor: 10)	134
Figure 4.11 Additional stress in soil at the end of consolidation along Sections B-B and B'- B'	134
Figure 4.12 Differential settlement profile at the end of consolidation at the embankment base along Sections A-A and A'- A'	135
Figure 4.13 Illustration of method to determine Change in Grade (CIG) (modified after His 2016)	136
Figure 4.14 Pore pressure dissipation versus time at points C and C'	137
Figure 4.15 Excess pore water pressure profile with depth along Sections B-B and B'-B' one week after completion of embankment construction	138
<i>Figure 4.16 Tension in the geosynthetic layer at the end of consolidation along Sections A-A and A'-A'</i>	<i>139</i>
Figure 4.17 Contour of tensile forces in the geosynthetic layer at the end of consolidation for (a) socketed CICs (b) frictional CICs	140
Figure 4.18 Change in the maximum tension in the geosynthetic layer vs. time at the edge of the socketed CIC1 and frictional CIC1	141
Figure 4.19 Axial stress at the end of consolidation in socketed CIC1 and frictional CIC1 versus depth	142

Figure 4.20 Settlement of the soil at the end of consolidation along Sections B-B and B'-B'	143
Figure 4.21 Axial stress at the end of consolidation in (a) socketed CICs (b) frictional CICs	144
Figure 4.22 Lateral displacement at the end of consolidation in soil with depth along section X-X and X'- X'	145
Figure 4.23 Lateral displacement at the end of consolidation of the (a) socketed CICs (b) frictional CICs with depth	147
Figure 4.24 Lateral displacement contours at the end of consolidation for (a) socketed CICs and (b) frictional CICs	148
Figure 4.25 Bending moment at the end of consolidation in (a) socketed CICs (b) frictional CICs versus depth.....	151
Figure 4.26 Yielded zones in tension at the end of consolidation on the (a) socketed CICs and (b) frictional CICs	152
Figure 4.27 Shear forces at the end of consolidation in (a) socketed CICs and (b) frictional CICs.....	154
Figure 5.1 Model geometry for end-bearing CIC (a) cross-section view and (b) plan view	161
Figure 5.2 Model mesh with CIC-soil interfaces	162
Figure 5.3 Settlement at the base of the embankment	163
Figure 5.4 Differential settlement at the base of the embankment	164
Figure 5.5 Tension in the geosynthetic layer	165
Figure 5.6 Lateral displacement at the geosynthetic level	166
Figure 5.7 Lateral displacement contours for drained analysis (S_{max} : 23mm).....	166
Figure 5.8 Lateral displacement contours for coupled flow-deformation analysis (S_{max} : 38mm).....	167
Figure A.1 Slurry placed in layers in the consolidation cell	192
Figure A.2 A strain gauge attached on the epoxy base in the direction of the geotextile fibres.....	192
Figure A.3 Initial simplified tensile tests on a single strain gauge using weights ...	193

Figure A.4 Initial simplified tests on the effect of boundary condition on the geotextile layer	193
Figure A.5 Butyl rubber (SB) tape applied on the strain gauge to water-proof and protect the gauges.....	194
Figure A.6 Earth pressure cell (EPC) positioned and fixed on the CIC using plaster of Paris.....	194
Figure A.7 Top view of the test after half the soft soil was excavated	195
Figure A.8 CICs at the end of the test after the soft soil was excavated.....	195
Figure A.9 Vane shear test to determine the shear strength of the soft soil.....	196

LIST OF TABLES

Table 2.1 Experimental studies on columnar ground improvement methods.....	45
Table 2.2 The degree of influence of different parameters in percentages(after Yapage & Liyanapathirana 2014)	54
Table 2.3 Numerical background on columnar ground improvement methods.....	64
Table 3.1 Concrete mix design for CIC construction for one cubic meter	76
Table 3.2 Composition of the soil mix used in this study	80
Table 3.3 Properties of the soil mix used in this study	80
Table 3.4 Properties adopted in the numerical simulation.....	92
Table 3.5 Proprieties adopted for CIC simulation	95
Table 3.6 Adopted geotextile properties in the numerical simulation*	96
Table 4.1 Material models and properties.....	124
Table 4.2 CIC material model and properties adopted in this study	129
Table 4.3 Geosynthetic properties adopted in this study	130
Table 4.4 Comparison of numerical predictions in this study and existing analytical solutions for the socketed CICs	157
Table 5.1 Material properties adopted in this study.....	162

LIST OF SYMBOLS

a	Pile cap width
A_r	Area replacement ratio
c'	Effective cohesion
C_k	Slope of the logk-e graph
c_u	Undrained shear strength of the soft soil
D	Inclusion diameter
d_{LTP}	Average size of the LTP granular material
e	Void ratio
E	Elastic modulus
e_0	Reference void ratio/Initial void ratio
E_c	Elastic modulus of the CIC material
E_{LTP}	Elastic modulus of the LTP material
E_s	Elastic modulus of the soft soil
f_c'	Characteristic compressive (cylinder) strength of concrete
f_{cmi}	Mean value of the in situ compressive strength of concrete
f_{ct}	Characteristic uniaxial tensile strength of concrete
F_N	Resultant of negative friction
G	Shear modulus
H	LTP height
h_a	Height of the upper plane of equal settlement
h_c	Height of negative friction action taking place in the soft layer (critical height)
H_m or H_M	Platform height
h_r, h_a	Height of negative friction application on the fictitious column positioned on top of the inclusion head
I	Area moment of inertia
J	Geosynthetic stiffness
K	Bulk modulus
k	Permeability
K_0	Coefficient of lateral earth pressure at rest
$K_{0(NC)}$	Lateral earth pressure coefficient at rest for normally consolidated soils
$K_{0(OC)}$	Lateral earth pressure coefficient at rest for over-consolidated soils
K_a	Coefficient of active earth pressure
k_i	Reference permeability
k_n	Interface normal stiffness

K_p	Coefficient of passive earth pressure
k_s	Interface shear stiffness
L	CIC length
m	Exponent capturing the increase in strength due to preconsolidation
M	Critical state stress ratio
n	Porosity
N	Scaling factor
n_s	Stress concentration ratio
p_0	Uniform pressure applied on the geosynthetic
p'_c	Preconsolidation pressure
Q_p	Vertical net force of loads applied at the head of an inclusion
q_s^+	Stress applied on the soft soil (without an inclusion)
Q_{Ult}	Ultimate bearing capacity of the CIC-supported ground
R_c	Interface interaction coefficient for soil-CIC
R_G	Interface interaction coefficient for geotextile-LTP
R_{int}	Coefficient for interface strength reduction
r_p	Inclusion radius
s	Hoek-Brown constant
S	CIC spacing
S_u	Shear strength of soil
t	Geosynthetic thickness
T	Tension in the geosynthetic
T_{ult}	Tensile strength of the geosynthetic
u	Pore water pressure
V	Initial specific volume
W_p	Weight of the load platform supported by an inclusion head in a unit cell

Greek Symbols

α_L	Scaling factor for length
α_T	Scaling factor for geosynthetic tensile strength
α_σ	Scaling factor for stress
γ	Unit weight
γ_c	Unit weight of the CIC material
γ_{dry}	Dry unit weight
γ_{LTP}	Unit weight of the LTP soil
γ_r	Unit weight of the embankment
γ_s	Unit weight of the soft soil
ε	Strain

κ	Slope of elastic swelling line
λ	Slope of normal consolidation line
ρ	Density of the concrete
σ'	Effective stress
σ_1	Major principal effective stress
σ_3	Minor principal effective stress
σ_c	Stress on the inclusion
σ_{cs}	Uniaxial strength of the concrete
σ_M	Extreme stress due to bending
σ_N	Axial stress in CIC
σ_s	Stress on soil
σ_v	Total vertical stress
σ_v'	Effective vertical stress
σ_v^*	Average effective vertical stress within a horizontal cross-section
ν	Poisson's ratio
ϕ	Friction angle
ϕ'	Effective friction angle
ϕ'_{LTP}	Angle of internal friction for LTP material
ψ	Dilation angle

LIST OF ABBREVIATIONS AND ACRONYMS

<i>2D</i>	Two-dimensional
<i>3D</i>	Three-dimensional
<i>CIC</i>	Concrete Injected Columns
<i>DL</i>	Data logger
<i>DT</i>	Data taker
<i>EPC</i>	Earth pressure cells
<i>EPWP</i>	Excess pore water pressure
<i>GRCS</i>	Geosynthetic-reinforced column-supported
<i>KBS</i>	Kaolin-Bentonite-Sand
<i>LC</i>	Load cell
<i>LTP</i>	load transfer platform
<i>LVDT</i>	Linear variable differential transformer
<i>MCC</i>	Modified Cam-clay
<i>MT</i>	mobile tray
<i>PWPT</i>	Pore water pressure transducer
<i>SCR</i>	Stress Concentration Ratio
<i>SG</i>	Strain Gauge
<i>SRR</i>	Stress reduction ratio

CHAPTER 1

1 INTRODUCTION

1.1 Background

In order to fix and modernise the nation's road infrastructure, lower transport costs, tackle the rising cost of urban congestion and cut travel times, there is an urgent need to reduce both road construction costs by having the most economic design and future maintenance costs by reducing damage or cracks to infrastructure. Whether immediately or a long time after construction, damage and cracks in structures are challenging issues for organisations that design and construct foundations on improved soft clay. Generally, a maximum post-construction settlement less than a certain value (e.g. 100-200mm) over the structure's life-time is allowed, and the differential settlement is limited to a certain change in grade (e.g. 0.5% and 0.3% for flexible and rigid pavements, respectively). Thus, precise predictions of the mechanical properties of concrete injected column (CIC) improved ground including stress-strain relationship, strength and compressibility parameters, is vital for an engineering design. Although many geotechnical organisations, consider various methods to reduce settlement of structures, some expected post-construction and differential settlements are still observed. This clearly indicates that uncertainties in the existing methods are excessive and unacceptable. This problem may not be significant if observed deformations are within the design criteria or expectation. However, significant variability and uncertainties regarding lateral deformations and differential settlement can cause serious problems. Under-predicting lateral deformations can result in unsatisfactory performance of the project, and conservative design to account for uncertainties can result in an uneconomic design. Within the applied range of stresses in which CICs behave elastically, the columns carry a large portion of the total

applied stresses, which can be calculated from the available theories. However, as the applied vertical stress is combined with the lateral stresses due to horizontal movement of soil between columns particularly close to embankment batters, the load transfer mechanism changes and the surrounding soil will start to squeeze; and therefore, settle further.

Bridge approach embankments constructed on soft ground are prone to long term settlements which could potentially lead to unacceptable differential settlements at bridge abutments. CICs are one of the popular ways to minimize such differential settlements. Unlike piles, the load is shared between the soft soil and the CICs; however, rigid inclusions may also share the load with the surrounding soil by using shorter length for piles or extending a limited length in the stiff layer (Wong and Muttuvel, 2012). Nevertheless, the load transfer mechanism is very different for the rigid piles where the load is transferred through a rigid reinforced concrete slab. Fioravante (2012) showed through centrifuge physical model tests that the existence of a granular layer beneath a raft changes the pile shaft behaviour significantly due to the generation of negative skin friction compared to the case where the pile is in direct contact with the raft. With no pile cap and/or RC slab and using shorter length of inclusions, CICs have proven to be a more cost effective option compared with piled foundations (Yee et al. 2012).

1.2 Concrete Injected Columns for Ground Improvement

Concrete injected columns are constructed of highly workable plain concrete or grout with no reinforcement. The CIC is created by the penetration of a special auger with flights in two opposite directions, which transfer the spoil to a displacement body to displace the soft soil laterally producing no spoil on the ground surface. As the auger reaches the desired depth based on the real-time monitoring data recorded by the installation rig, the concrete is pumped, while the auger is extracted. The displacement method could be beneficial by providing a certain degree of compaction to the surrounding soil and increasing the shaft resistance by increasing the lateral stresses on the inclusion shaft. However, it could damage the previously installed CICs by

creating problems such as squeezing of the adjacent unset CICs which could lead to necking (loss of CIC cross-section area), and by causing cracks in the set CICs, separating the cracked segments of the CICs, lifting the CICs from the base, and therefore, leading to the loss of the tip resistance. The use of different installation sequences, such as hit-1 miss-1 approach could mitigate the adverse effects of installation on adjacent columns. The displacement method, use of plain concrete, load sharing with the surrounding soft soil, and the acceptability of possible development of cracks in the inclusion (King et al. 2018; Wong & Muttevel 2012a) is what differentiates CICs from other ground improvement methods such as piled-embankments. Figure 1.1 shows the installation of a CIC in progress.



Figure 1.1 CIC installation, Heathcote project, NSW, Australia

1.3 Load Sharing between Soil and CICs

The stress transfer to the CICs is usually facilitated using a load transfer platform (LTP) constructed of a well-compacted granular layer and one or more layers of geosynthetic. However, the aim of CICs as a ground improvement method is to improve the soft soil mass, and is different to piles where the goal is to bypass the soft soil and transfer all the loads to the stiff strata. As Figure 1.2 illustrates, when the load

is applied on the CIC-improved ground, the difference in the stiffness of the CICs and the soft soil leads to differential settlement in the LTP granular material. The soil mass between the two CICs tends to move downwards; however, this movement is countered by the shear resistance of the stationary soil mass above the CICs which is known as the arching effect. The differential settlement also triggers the trampoline effect in the geosynthetic layer which further contributes to the transfer of the loads onto the CICs. In the upper section of the CICs, as the soft soil settles more than the CICs, negative skin friction is generated and the stress in the CICs continues to increase moving downwards. There exists a point where the settlement of the CIC and the soft soil is equal. This plane is referred to as the neutral plane where the skin friction is turned from negative to positive. On the other hand, in the deeper layers, as the soil settlement is negligible compared to the CIC deformation, the positive skin friction on the CIC shaft leads to the reduction of the stress in the CIC.

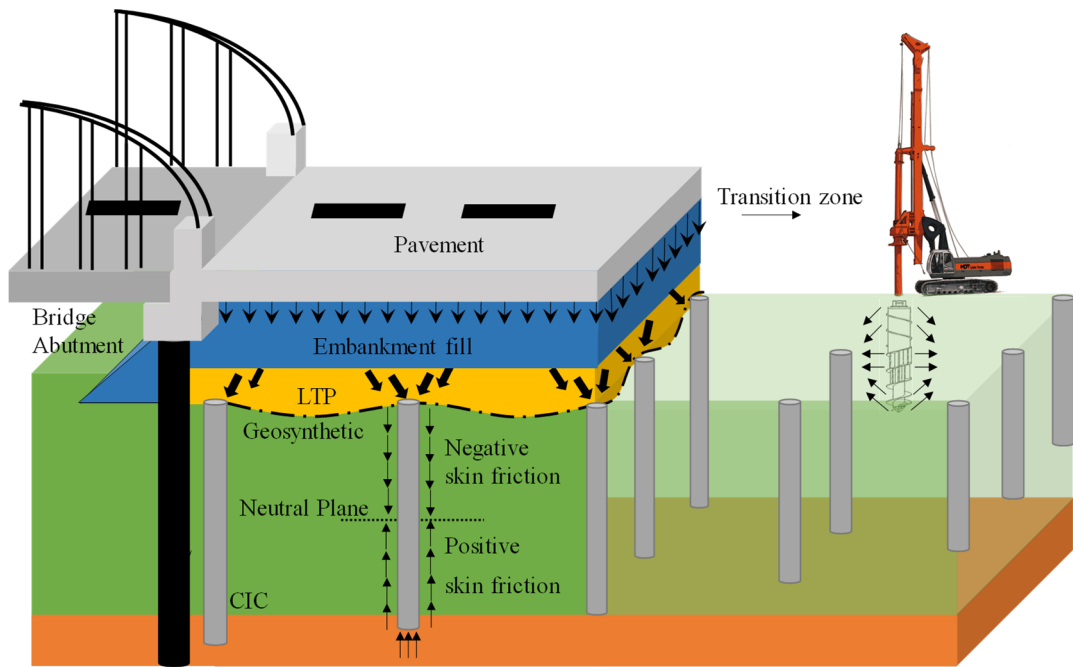


Figure 1.2 Load transfer mechanism in CIC-improved ground

1.4 Objectives of the Present Study

One of the primary goals of this project is to study how the overall performance of the CIC-supported embankment is influenced if the columns are not

extended down to the stiff layer, and compare the load transfer mechanism for the two cases of frictional and socketed CICs. The effect of the geosynthetic layer was also investigated and compared for frictional and socketed CICs. One of the most important parameters in the design of the column supported embankments is the stress concentration ratio (SCR), which is defined as the ratio of the load transferred to the column to the load sustained by the surrounding soil. The SCR for CIC-improved ground was evaluated using numerical modelling, and then was validated against the laboratory results in this research to help engineers optimise the design.

The specific aims of this research are as follows:

- Understanding the stress transfer mechanism in CIC-supported embankments. The stress transfer mechanism in the CIC system is very different to piled rafts since there is no rigid slab connecting the CICs and there is a load sharing between the soil and the columns. This study aims to give a better understanding of this mechanism.
- Comparing the stress transfer mechanisms for frictional and socketed CICs to understand how the bearing condition of the CIC tip influences the performance of the improved ground, and how the uncertainties in the bedrock/stiff layer level influence the settlement and stability of embankments on the CIC-improved ground. The optimised arrangement for CICs, especially in the transition zone is investigated. The efficiency of using “longer columns with larger spacing” is compared to “shorter columns with closer spacing” for the transition zone design.
- Evaluating the SCR for CIC-improved ground through laboratory scale physical modelling. The SCR variations with time through physical modelling and numerical simulations are investigated. Despite CICs’ popularity and widespread use, there is no rigorous experimental work performed to understand its behaviour. In this study, physical modelling of a CIC-improved ground is conducted in a consolidation cell, and a proper set of instrumentation is used to monitor different variables such as pore water pressure, stress distribution in the system, and deformation of the ground during consolidation to understand the basic patterns of its response.

1.5 Organisation of Dissertation

In Chapter 1, an introduction is provided to the scope and the goals of this research work. In Chapter 2, a literature review of the relevant past studies has been provided. A summary of CICs for ground improvement, and the construction and design processes are discussed.

In Chapter 3, a comparison is made between two numerical modelling approaches of coupled flow-deformation analysis and drained analysis on a CIC-improved ground. The two simulation approaches are evaluated based on the results for total and differential vertical settlements, lateral displacements, and the mobilised tensile stresses in the geosynthetic reinforcement layer.

In Chapter 4, a numerical simulation is undertaken to compare the behaviour of two alternatives for the transition zone of the CIC-improved ground. In the first option, the widely spaced CICs are socketed into the stiff strata while in the second option, the closely spaced CICs are frictional and shorter in length. This chapter provides the details of the developed code in FLAC^{3D}, and the constitutive models adopted to simulate the material behaviour. Performance of the two options are compared in terms of total and differential settlements, tensile force mobilised in the geosynthetic layer, lateral displacements, and the stresses in the CICs.

In Chapter 5, the details of a well instrumented physical model of CIC-improved ground is provided. The variations of different parameters such as pore water pressure, stresses in the CICs, and the tension in the geotextile layer are investigated. In addition, this chapter explains the details of a laboratory-scale numerical model using FLAC^{3D}. The verification of the numerical results is also conducted in this chapter.

In Chapter 6, the conclusions of this research work is presented, and recommendations for future research are provided.

CHAPTER 2

2 LITERATURE REVIEW

2.1 General

This chapter provides a summary of the literature on experimental and numerical works performed on columnar ground improvement methods. In the first section of the chapter, a brief introduction on Concrete Injected Columns (CICs) construction method and design is presented. This section explains the merits and shortcomings of CIC method compared to other ground improvement techniques. Other issues discussed in this section are the construction stages, installation gear, and load transfer mechanism. The next part is a summary of the experimental works on CIC, deep cement mixing (DCM), and stone columns. In this section, the set-up of the experiments, scaling, instrumentation, load application method, and a brief description of the experiments are presented. When possible, a schematic diagram of the test set-up is shown. Furthermore, the objectives and the outcomes of the experiments are mentioned. In the next section, the relevant numerical works on piled embankments are presented and discussed. In the following section, a discussion is provided on raft foundations illustrating the similarities and differences between this system and CICs.

2.2 CIC Ground Improvement Method

Bridge approach embankments constructed on soft ground are prone to long term settlements which could potentially lead to unacceptable differential settlements at bridge abutments. Foundation treatments are therefore required to control and minimize such differential settlements in order to satisfy the functionality of the road. In recent years, the use of concrete injected columns (CICs) to accelerate the construction program has gained popularity in support of rail and road bridge approach

embankments on soft soils. Proprietary names such as Controlled Modulus Columns (CMC), Controlled Stiffness Columns (CSC), or general terms such as drilled displacement columns (DDCs) or soil-displacement concrete piles are used to refer to this method in the literature. In this thesis, they will be referred to as concrete injected columns or CICs; a term used in Australia. CICs are rigid or semi-rigid inclusions, depending on their design, constructed using grout, concrete or a combination of cementitious materials including waste products such as fly ash and slag. CICs are constructed as unreinforced concrete columns; however, close to the slope batters a centrally positioned single reinforcement bar might be used. The role of this reinforcement bar is only to keep the cracked CIC in place and prevent the sliding due to the lateral loads, and not to provide structural resistance to bending. Unlike pile supported structures, there is a sharing of load between the CICs and the surrounding soil. Rigid columns made of concrete or grout may also share load with the surrounding soil by socketing them only a limited amount into the underlying stiff soils, or by installing them partially penetrating in the soft soil layer. CICs are typically constructed in diameters ranging from 300mm to 500mm installed at a spacing ranging from 1.3m to 2.5m (Wong & Muttuvel 2012c). Availability of modern equipment with a high torque capacity and static down thrust has made it possible to install CICs using a special displacement auger to displace the soil laterally which renders this technique virtually spoil free. CICs can be constructed up to 30m using standard piling equipment (Larisch et al. 2014).

A granular layer consisting of one or more than one layer of geosynthetic is commonly placed on top of the CICs to facilitate the load transfer from the embankment to columns. Such a platform is known as the load transfer platform (LTP). This load transfer platform is made of well compacted granular material, and has a thickness of 0.4m to 0.8m depending on the type of structure and the soil conditions.

A load transfer platform may or may not be required depending on the embankment height and spacing of the CICs. As previously mentioned, since the soft soil shares the applied load with the CICs, LTP is not necessarily required to transfer

the entire embankment loads to the columns. Instead, the need for LTP should be assessed based on the differential settlement tolerance on the embankment surface. In most cases, for high embankments on CIC-improved ground, the differential settlements could be dissipated in the compacted fill. Sharing the embankment load between the soft soil and the CICs is possible without the use of high strength geosynthetic-reinforced LTP to transfer the entire embankment load to the CICs. The embankment settlement will be greater, but this approach will also result in a more economical solution (Wong & Muttuvel 2012a; 2012c).

Displacement piles are designed based on the piling concept; that is, to transfer a surface loading to a competent layer of high bearing capacity at depth, and therefore, bridging less competent material and mitigating settlements. CIC, in contrast to displacement piles, seek to enhance the engineering properties of the less competent soils by improving the global moduli of those soils through which they are installed, and control and contain the settlement characteristics of the otherwise incompetent soil strata within acceptable limits. CICs are particularly suited to support large uniform loads, such as under road embankments, storage tanks and warehouses.

For CICs close to the batters of the embankment, or at transition zones between the CIC-improved ground and non-treated zone, the columns will be subjected to bending and shear due to non-uniform loading (Wong & Muttuvel 2012c).

CICs are used where ground conditions are very poor for flexible or semi-flexible inclusions such as stone columns or vertical drains to be used, and rigid inclusions such as reinforced concrete piles are too costly. Usually, CICs are used in the structurally sensitive zones close to the abutment where there is a stringent settlement criterion. However, since the maximum allowable settlement increases while moving away from the bridge abutment, other cheaper forms of ground improvement (GI) techniques such as preloading or stone columns can be used. CIC method was specifically developed to fill in the gap between conventional ground improvement methods such as vertical drains or stone columns (non-rigid inclusion) and that of reinforced concrete (RC) piles (rigid inclusion). The semi-rigid CIC

inclusions are not prone to column bulging as non-rigid stone columns in very soft soil. Semi-rigid inclusions of CIC perform better than non-rigid inclusions in very poor ground and less costly than rigid inclusions of RC piles. For rigid RC piles, imposed load is transferred by the pile cap or RC slab through the rigid pile shaft to load bearing layer deep below ground as in most cases. For the composite soil-CIC mass, the load is uniformly distributed by the upper layer of compacted sand. Without the pile cap and/or RC slab and shorter length of inclusions, CIC has proven to be the cheaper option compared with piled foundations (Yee et al. 2012). Figure 2.2 compares the non-rigid, semi-rigid, and rigid inclusions for the purpose of soil improvement schematically.

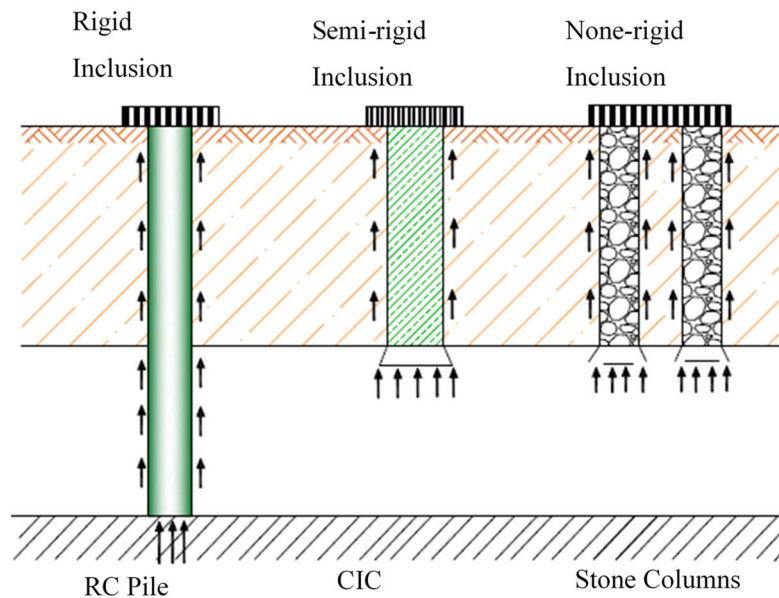


Figure 2.1 Different types of inclusions (Modified after Yee et al. 2012)

2.2.1 Construction Process

CICs are installed using a hollow stem equipped with a displacement auger coupled with a high torque coming from a high capacity pull-down CIC installation rig, which displaces the soil laterally with virtually no spoil and vibration (Plomteux & Porbaha 2004). The displacement auger (Figure 2.2) consists of three components:

The bottom section of the auger will move the spoil upward during penetration. The middle part of the auger is the displacement body and displaces the soil laterally and prevents it from coming upwards and provides a degree of compaction. The upper part of the auger with flight in the opposite direction to the lower part of the auger, moves any spoil in case of the collapse of the hole down to the displacement section. Hence, it improves the efficiency and the overall quality and continuity of the CIC inclusion.

The CIC rig has a high torque and strong downward thrust. The auger penetrates the ground while rotating with no grout is injected. The drilling continues to the required depth based on the real-time data from the monitoring system on the installation rig (NeSmith & NeSmith 2006b). When the desired depth for the CIC is reached, grout injection starts with sufficient pressure to prevent the hole from caving in. The auger is then extracted while rotation continues and the CIC construction is complete. Figure 2.3 shows the installation steps for CIC.

Data acquisition system on the installation rig provides the possibility of gathering various information such as torque, crowd, rotation, and penetration rate which allows for the monitoring of the installation process (NeSmith & NeSmith 2006a). The collected and processed data alongside the geotechnical site characterisation provides real-time information on soil profile and can also be an indicator of pile capacity (NeSmith & NeSmith 2006b). The automated data monitoring system is also part of the quality control and quality assurance (Brettmann & NeSmith 2005).

The CIC construction process is vibration and spoil free which renders this method particularly suitable for contaminated grounds. The special installation method also helps increase the lateral stresses on the columns which in turn increases the skin friction leading to a possible increase in the CIC capacity; however, this increase is usually ignored in design. The displacement method also provides a certain level of densification for the surrounding soil.

Ni et al. (2010) investigated the soil movement due to the penetration of a rotary displacement auger in transparent soil using PIV. Their study revealed that the soil movement around the displacement pile depended on the rotation speed of the auger. When rotated at a sufficient speed, the soil around the auger moved upward and then was forced to displace past the displacement body of the auger. However, at the lower rotation speed, the soil around the auger moved downward and outward. They compared their small-scale experiment results for lateral displacements with prototype field data reported by Skinner et al. (2003) and observed a similar trends.

The displacement method of installation, however, can have a negative effect on saturated fine grained soils where little or no improvement is gained through displacement, and remoulding could have adverse effects on the shear strength of the surrounding soil (Brown 2005). This installation method also creates numerous problems for the existing CICs. As the soil is displaced laterally by the auger, it starts to move vertically as it is restrained in all other directions. This vertical movement of the soil or heave induced by the CIC installation could have adverse effects on the existing CICs and cause defects in the pre-installed CICs. Such adverse effects include squeezing, necking, cracking, CIC shaft lifting from its base, loss of capacity for the end-bearing CIC due to loss of base contact, tensile stress generation on the CICs, and separation of the cracked sections of the CICs.

Larisch et al. (2014) used axisymmetric finite element analyses in ABAQUS to numerically simulate the CIC installation in clay. They conducted undrained analyses using hypo-plastic constitutive model to simulate the clay. They, however, did not simulate the shape of the auger, the auger rotation, and different installation parameters such as torque and pull-down. They presented the displacement field, pore-water pressure, and stress field around the installed CIC. They intended to use their simulation results as predictions for the field tests they planned to run in the future.

Larisch & Scheuermann (2015) reported heaves of up to 500mm and lateral shift up to 150mm in CIC installation projects in clay. Larisch & Scheuermann (2015) investigated the effect of auger shape and the penetration rate of the installation rig on

the heave volume created on the surface. They installed three full-scale CICs, 4m in depth and 450mm in diameter in stiff clay, and compared their results to predictions from shallow strain path method (SSPM) (Sagaseta 1987); a theoretical method for predicting the heave on the ground used for driven piles in clay. Their investigation revealed that the auger shape did not have any effect on the induced heave. However, they observed that the ground heave increased when the minimum penetration rate calculated based on findings of Viggiani (1993) was not reached due to the inadequate rig capacity. Viggiani (1993) proposed a formula based on the auger dimensions, and indicated that if the penetration rate and the rate of rotation of the auger satisfies the proposed formula, the volume of the removed soil is equal to the displaced soil, and the surrounding soil is not decompressed. Based on CPT tests, Larisch & Scheuermann (2015) attributed the increase in ground heave to the disturbance of the clay in deep layers caused by inadequate penetration rate.



Figure 2.2 CIC Installation augers (Courtesy of Menard 2018).

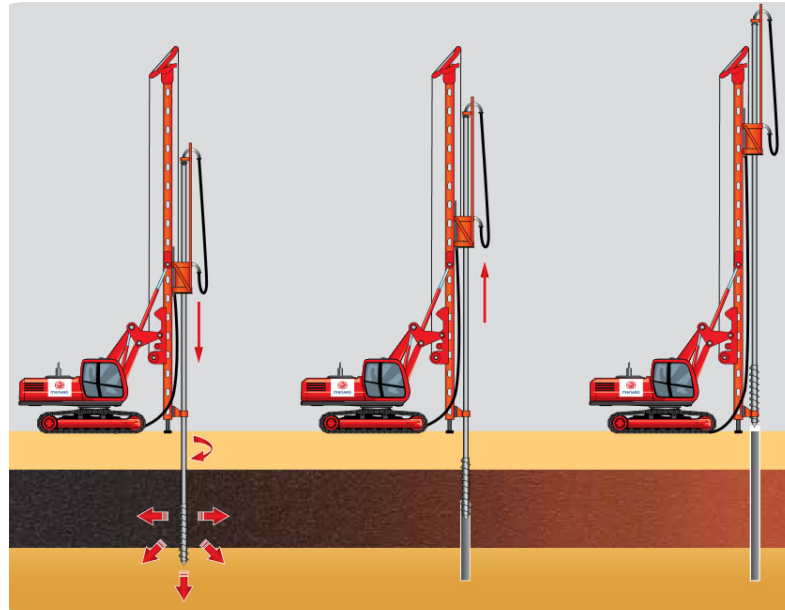


Figure 2.3 CIC installation steps (Courtesy of Menard 2016).

Larisch et al. (2015) conducted full-scale tests on two 4m long CICs in stiff to hard clay installed at two different rates of penetration. Through CPT tests, they reported up to 43% increase in the in situ stress conditions in stiff clay where adequate penetration rate was maintained which resulted in significant increase in the pile capacities. They concluded that the slow penetration rate remoulds and shears the surrounding soil, and reduces the in situ stresses by disturbing the soil, and hence, the pile capacity is reduced.

Suleiman et al. (2016) used an instrumented full-scale experiment to study the short term CIC installation effects. They monitored the pore water pressure, lateral stress and displacement in soil during installation and the load test at 1D, 2D, 3D, and 4D away from the CIC shaft (D is the diameter of the CIC). They found out there was an increase in the horizontal stress and lateral displacement of the soil during the CIC installation. The horizontal stresses and pore water pressure increased while the mandrel was advanced into the ground and reached a maximum when the mandrel passed the sensors. Then the horizontal stresses and the pore water pressure experienced a decrease followed by another increase when the mandrel passed the

sensor while being retrieved. They also concluded that the installation effects extended to 2 to 3 times the diameter of the CIC.

Different installation patterns have been implemented to mitigate the adverse installation effects. Plomteux & Porbaha (2004) reported installing CICs in two passes which increased the spacing from dense spacing of 1m to 1.4m in order to reduce the installation effect.

King et al. (2018) also adopted a hit-1 miss-1 approach used by Plomteux & Porbaha (2004) where CICs were spaced 2m from each other. In this method, the CICs adjacent to the installed CIC are missed, and are constructed later in a different pass. However, they suggested a hit-1 miss-2 installation sequence where CICs were spaced closer, say 1.5m from each other in order to prevent the loss of cross sectional area due to installation effects.

2.2.2 Advantages of CICs in Comparison to Other Ground Improvement Techniques

The following advantages make the CIC method a popular and competitive ground improvement technique:

- Shared loading between the soil and the inclusion makes CICs a competitive and economical solution
- Minimal or no spoil makes CICs suitable for contaminated grounds, brownfields, or old landfills
- Significantly shorter construction time compared to other ground improvement solutions such as preloading
- The displacement method provides a certain degree of compaction to the surrounding soil, and a higher lateral stress on the shaft which leads to the increased capacity of the CIC

However, the following drawbacks should be considered when CIC is chosen as a ground improvement technique:

- The displacement technique may cause defects in the existing newly constructed CICs
- The installation technique may disturb and reduce the shear strength of fine grained soils

2.2.3 Design

2.2.3.1 Differences between CICs and piled-embankments

It should be noted that there is a distinction between piled embankments and CIC-supported embankments. CICs, as a ground improvement technique, are designed as geotechnical elements with a higher level of redundancy (King et al. 2018) to improve the overall performance of the soft soil as a mass, whereas piles are considered as structural elements and are designed to take all the embankment loads and transfer the loads to a competent layer; and as such, are subject to rigorous tests and design criteria. CICs are semi-rigid inclusions constructed using unreinforced concrete where cracks could potentially develop as long as the deformations are within the limits (Wong & Muttuvel 2012a). Kitazume & Maruyama (2007) using centrifuge modelling on deep mixing method (DMM) columns, concluded that the columns provided support for the embankment even after cracking. They also concluded that all the columns did not fail simultaneously, but they failed one by one.

The CIC method, as a ground improvement technique, also considers the contribution of the soft soil in sustaining part of the applied load, where in piled embankments all the loads are sustained by the piles, and are designed accordingly.

2.2.3.2 Negative Skin Friction

For structures on CICs, the governing factor is usually deformation (settlement), however, the design of CICs considers both serviceability and stability. The global stability of the embankments on CICs should also be checked especially during construction. The deformation analysis is based on the load sharing between the CICs and the soft soil. The load transfer is facilitated by a layer of compacted granular layer on top of the CICs acting as load distribution layer, and not transferring

100% of the load to the CICs. Figure 2.4 and Figure 2.5 demonstrate the stress transfer mechanism in the CIC system.

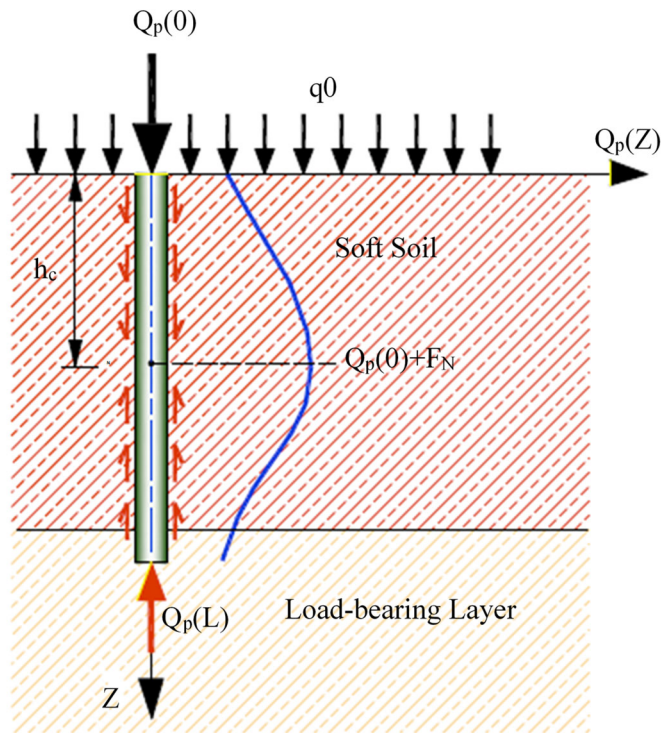


Figure 2.4 Load sharing mechanism in CIC (Modified after ASIRI 2012)

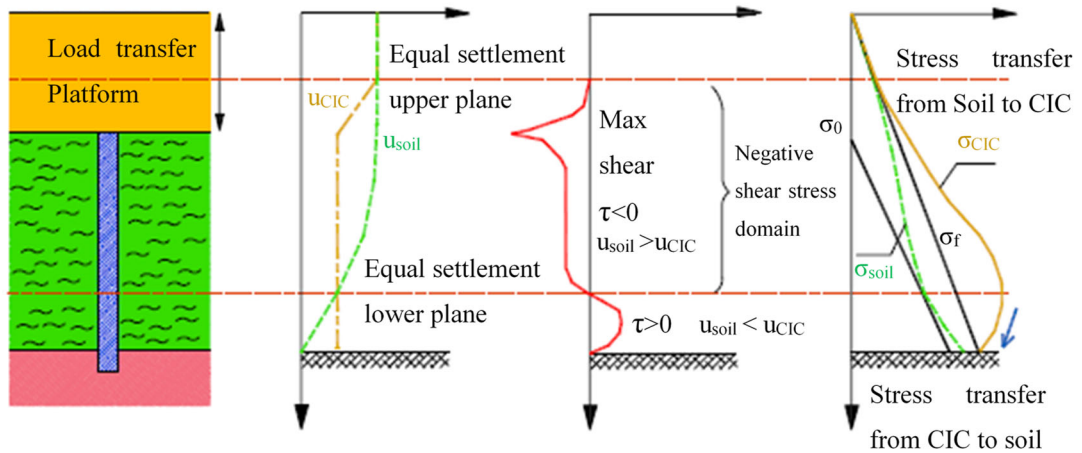


Figure 2.5 Stress distribution in soil-CIC mass, σ_{soil} = stress transferred to the soil, u_{soil} = vertical deformation of the soil, σ_{CIC} = stress transferred to the CIC, u_{CIC} = vertical deformation of the CIC (Modified after Simon & Schlosser 2006)

The stress transferred to the soil (σ_{soil}) leads to vertical deformation (settlement) of the soil (u_{soil}) through consolidation. Since the CICs and the surrounding soil have different stiffnesses (stiffness ratio between CICs and the soil is between 1:1,000 to 1:10,000), there is a difference in the settlement of the CICs and the soil, which in turn leads to stress transfer from the surrounding soil to the CICs or vice versa. In shallower depths where $u_{\text{soil}} > u_{\text{CIC}}$, the stress is transferred from the soil to the CICs and negative skin friction is developed. At greater depth where $u_{\text{CIC}} > u_{\text{soil}}$, stress is transferred from the CICs back to the soil which induces positive skin friction and base resistance. The depth at which the soil and inclusion displacements are equal is referred to as the neutral plane.

Figure 2.5 shows the location of the neutral plane where deformation of CIC and soil is the same. At this location, the CIC column carries the maximum stress. The equilibrium is achieved where the tip resistance, friction resistance and soil resistance is equal to the total load.

For a single inclusion, considering h_c as the critical height along which the negative skin friction is generated, the negative friction acting on the shaft of the inclusion can be calculated using Eq. (2.1) as follows:

$$F_N = 2\pi r_p \int_0^{h_c} K \tan\delta \sigma'_v(z, r_p) dz \quad (2.1)$$

where K is the coefficient of lateral earth pressure, $\tan\delta$ is the coefficient of soil-inclusion friction, $\sigma'_v(z, r_p)$ is the effective vertical stress along the inclusion shaft. $\sigma'_v(z, r_p)$ is equal to σ'_v assuming that the stress state around the inclusion is not disturbed. However, the stress state around the inclusion is disturbed due to the downdrag effect. The negative skin friction on the inclusion shaft leads to the unloading of the surrounding soil, and reduces the effective vertical stress. The effective vertical stress at a distance r from the inclusion axis, $\sigma'_v(z, r)$ varies as shown in Figure 2.6.

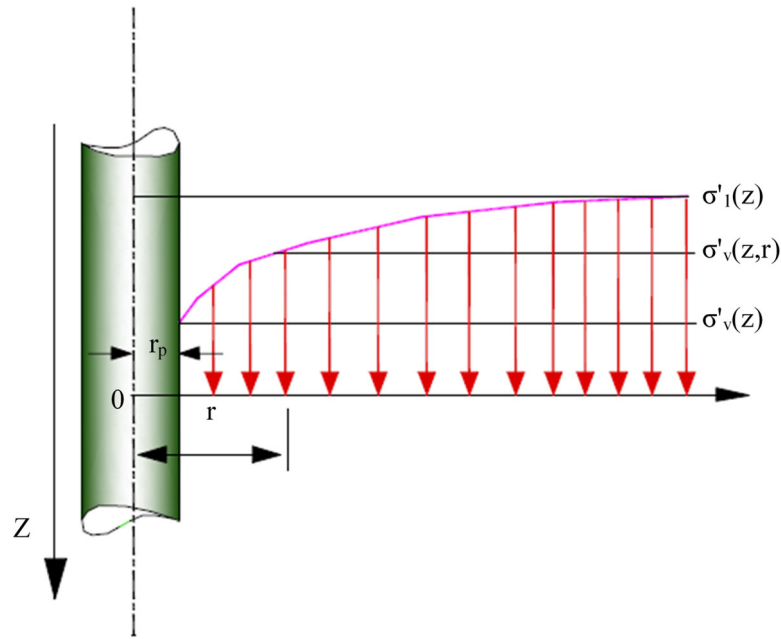


Figure 2.6 Distribution of vertical effective stress around an inclusion awn
(Modified after ASIRI 2012)

Combarieu (1974) proposed a method to modify the stress state around an inclusion due to the downdrag effect. Combarieu (1974) defined the variation of effective vertical stress with depth for $r > r_p$ as:

$$\sigma'(z, r) = \sigma'_v(z) + (\sigma'_1(z) - \sigma'_v(z)) \left(1 - e^{-\lambda \frac{r-r_p}{r_p}} \right) \quad (2.2)$$

where $\sigma'_1(z)$ is the effective vertical stress for the undisturbed condition, $\sigma'_v(z) = \sigma'(z, r_p)$ is the effective vertical stress in the soil along the inclusion, and $\sigma'(z, r)$ is the effective vertical stress at distance r from the inclusion axis. The coefficient λ could be determined using experimental Eqs. (2.3) - (2.5):

$$\lambda = \frac{1}{0.5 + 0.25K \tan \delta} \quad \text{if} \quad K \tan \delta \leq 0.15 \quad (2.3)$$

$$\lambda = 0.385 - K \tan \delta \quad \text{if} \quad 0.15 \leq K \tan \delta \leq 0.385 \quad (2.4)$$

$$\lambda = 0 \quad \text{if} \quad K \tan \delta \geq 0.385 \quad (2.5)$$

where $\lambda = 0$ presents the case where there is no reduction in the vertical stress due to the presence of the inclusion.

Combarieu (1985) based on the equilibrium of the vertical forces derived the following:

$$\frac{d\sigma'_v(z)}{dz} + \mu(\lambda)\sigma'_v(z) = \frac{d\sigma'_1(z)}{dz} \quad (2.6)$$

$$\mu(\lambda) = \frac{\lambda^2}{1 + \lambda} \frac{K \tan \delta}{r_p} \quad (2.7)$$

Solving Eq. (2.6) yields the effective vertical stress $\sigma'_v(z)$ expressed over $d\sigma'_v(z)/dz$ intervals as shown in Eq. (2.8):

$$\sigma'_v(z) = \frac{1}{\mu(\lambda)} \frac{d\sigma'_v(z)}{dz} + e^{-\mu(\lambda)z} \left(\sigma'_v(0) - \frac{1}{\mu(\lambda)} \frac{d\sigma'_v(z)}{dz} \right) \quad (2.8)$$

Considering a homogenous saturated soft soil layer with the ground water level at the soft soil surface under a uniform surcharge q_0 , the $d\sigma'_v(z)/dz$ is constant and equal to the submerged unit weight of the soft soil, γ' . Substituting $d\sigma'_v(z)/dz = \gamma'$ in Eq. (2.8), the effective vertical stress on the soil-pile interface could be written as:

$$\sigma'_v(z) = \frac{\gamma'}{\mu(\lambda)} + e^{-\mu(\lambda)z} \left(q_0 - \frac{\gamma'}{\mu(\lambda)} \right) \quad (2.9)$$

Substituting a skin friction of zero in the critical depth of h_c in Eq. (2.8), we will have:

$$e^{-\mu(\lambda)h_c} = \frac{\mu(\lambda)h_c - 1}{\mu(\lambda) \frac{q_0}{\gamma'} - 1} \quad (2.10)$$

Considering a value of h_c less than the depth of the soft soil, F_N from Eq. (2.1) could be written as:

$$F_N = \frac{2\pi r_p K \tan \delta}{\mu(\lambda)} q_0 \quad (2.11)$$

which shows the negative skin friction is proportional to the applied surcharge, q_0 . However, when the critical depth, h_c is greater than the soft soil depth, the negative skin friction will be applied on the entire depth of the soft soil, and F_N could be estimated using Eq. (2.12):

$$F_N = \frac{2\pi r_p K \tan \delta}{\mu(\lambda)} (\gamma' h_c + q_0 - \sigma'_v(h_c)) \quad (2.12)$$

where $\sigma'_v(h_c)$ could be determined based on Eq. (2.9):

$$\sigma'_v(h_c) = \frac{\gamma'}{\mu(\lambda)} + e^{-\mu(\lambda)h_c} \left(q_0 - \frac{\gamma'}{\mu(\lambda)} \right) \quad (2.13)$$

with the F_N reaching its maximum at the end of consolidation.

Considering a group of unlimited number of inclusions shown in Figure 2.7, the radius of the influence area of a single inclusion is a cylindrical mesh with a radius R , calculated using Eq. (2.14):

$$R = \sqrt{\frac{ab}{\pi}} \quad (2.14)$$

where a and b are the spacing of the inclusions in the two directions.

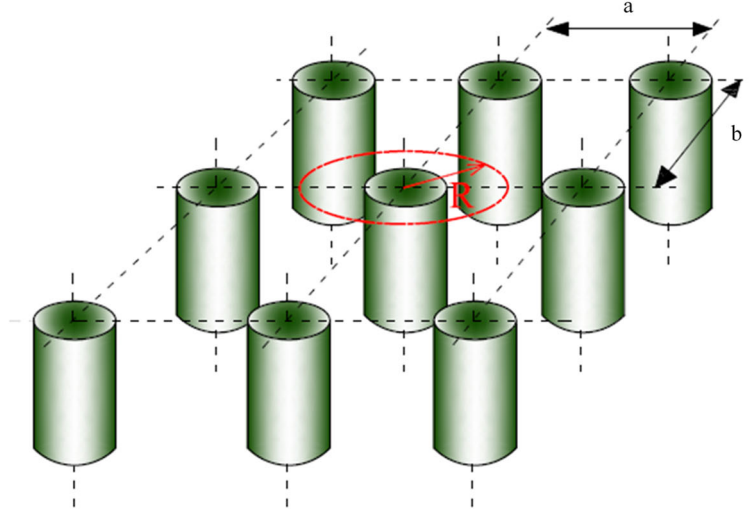


Figure 2.7 Group of rigid inclusions (Modified after ASIRI 2012)

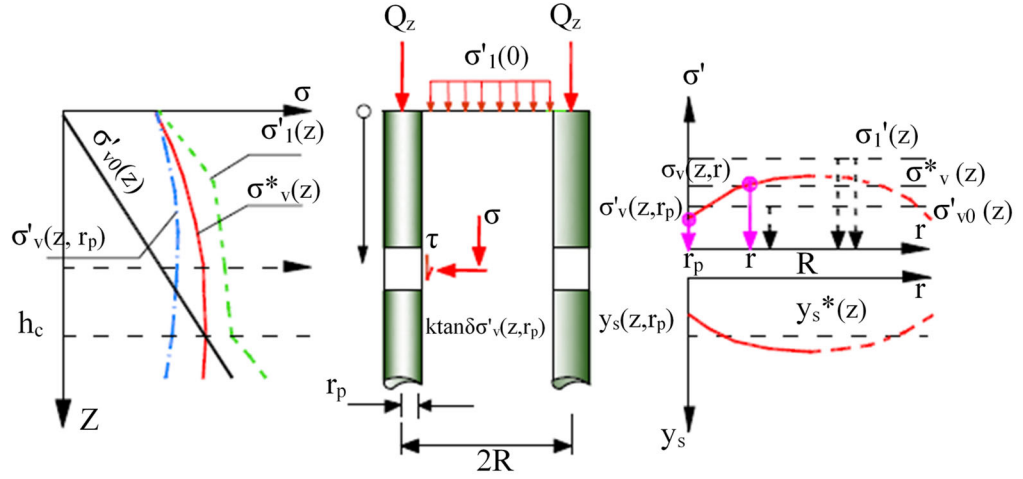


Figure 2.8 Negative skin friction for inclusions in a group (Modified after Combarieu 1985)

The equilibrium of the vertical forces results in a similar equation to Eq. (2.6) (Combarieu 1985):

$$\frac{d\sigma'_v(z, r_p)}{dz} + \mu(\lambda, R)\sigma'_v(z, r_p) = \frac{d\sigma'_1(z)}{dz} \quad (2.15)$$

$$\mu(\lambda, R) = \frac{\lambda^2}{1 + \lambda(1 + \frac{\lambda}{r_p})e^{-\lambda\frac{R-r_p}{r_p}}} \frac{K \tan \delta}{r_p} \text{ if } \lambda \neq 0 \quad (2.16)$$

$$\mu(0, R) = \frac{2}{(\frac{R}{r_p} - 1)} \frac{K \tan \delta}{r_p} \text{ if } \lambda = 0 \quad (2.17)$$

Solving Eq. (2.15) yield the average vertical stress between the inclusions as presented in Eq. (2.9):

$$\sigma_v^*(z) = \sigma'_1(z) - (\sigma'_1(z) - \sigma'_v(z, r_p)) \frac{2K \tan \delta r_p}{(R^2 - r_p^2)\mu(\lambda, \frac{R}{r_p})} \quad (2.18)$$

It is often assumed that the negative skin friction only acts when the $\sigma'_v(z, r_p)$ is greater than the initial stress, and the critical height, h_c is then calculated.

NeSmith (2002) recommended an empirical method for the design of CICs (referred to as augured, pressure-injected displacement piles, APID) in granular

materials based on 28 load tests. NeSmith (2002) argued that prior to the installation of the CICs, the K_0 changes to K_p whereas the design methods for augured piles are based on K_a in the soil surrounding the pile which will lead to over-conservative designs. NeSmith (2002) presented empirical equations for estimation of shaft and toe resistance for CICs based on the CPT and SPT results. This method is recommended in the Geotechnical Engineering Circular No. 8 (Brown et al. 2007) to calculate the axial capacity of CICs.

Moshfeghi & Eslami (2018) based on a database of 65 CIC (referred to as drilled-displacement piles) load tests and the CPT profiles performed reliability assessment on 6 CPT-based methods for determining the capacity of CICs. They categorised their analyses into four parts of soil type, pile construction type, shaft type, and the toe geometric shape. They concluded that the majority of the methods under-predicted the capacity of the CICs.

Basu et al. (2010) reviewed the design methods for CICs (drilled-displacement piles). They compared the results from three different empirical design methods for CICs constructed with five types of auger shapes, and compared the results with pile load tests from literature. They concluded that the design methods did not provide an accurate estimate of the column capacity. They attributed the discrepancies to the degree of soil disturbance caused by each type of auger. They also concluded the shaft capacities would be a source of the discrepancy as different methods would create different shapes and capacities for the shafts.

Park et al. (2012) and Park et al. (2011) proposed a design method for CIC (drilled displacement piles) in sandy soils using a t-z model where the pile-soil interface resistance along the shaft and the tip was simulated using a series of non-linear springs. Based on static pile-load tests from two construction sites, they back-calculated the interface and tip parameters of the spring model to match the load-settlement curves. They evaluated their proposed model by comparing the predicted and measured load-settlement and load-transfer curves.

Basu et al. (2014) investigated the stress change in a soil disk around a pile shaft due to CIC (referred to as drilled-displacement piles) installation using finite element modelling. They used a two-surface plasticity constitutive model to simulate the behaviour of the sand. They assumed the soil disk being far enough from the ground surface and the pile base experienced negligible vertical strain, and therefore, the analysis was independent of the soil thickness rendering the model one dimensional. Based on their numerical study, they proposed equations to estimate the ratio of coefficient of lateral earth pressure to the at-rest lateral earth pressure coefficient (K/K_0) to predict the limit shaft resistance for a CIC.

2.2.3.3 LTP Design

Several design guidelines such as BS 8006 (2010), the German guideline of EBGEO (2010), or the Dutch design guideline CUR 226 (Van Eekelen & Brugman 2016) have been published for the design of basal reinforced piled embankments. The analytical methods include two calculation steps. The first step evaluates the arching behaviour of the fill and divides the total vertical load into two parts; part A or arching A, and part B+C, or the residual part. Part A is the part of the vertical load transferred directly onto the piles, part B of the residual part B+C is transferred to the GR and part C is transferred to the subsoil. Several methods have been proposed to calculate part A or arching A. van Eekelen et al. (2013) divided these methods into four categories of i) frictional models (McKelvey 1994; Russell & Pierpoint 1997; Naughton 2007; Britton & Naughton 2008; McGuire et al. 2012) which are based on Terzaghi (1943) ii) the rigid arch models adopted in Scandinavian studies (Carlsson 1987; Rogbeck et al. 1998; Svanø et al. 2000; Van Eekelen et al. 2003) iii) models considering mechanical elements (Deb 2010; Filz et al. 2012; Zhang et al. 2012; Deb & Mohapatra 2013), and iv) limit equilibrium methods (Hewlett & Randolph 1988; Zaeske 2001). The limit equilibrium model by Hewlett & Randolph (1988) was adopted by the French ASIRI (2012), and also suggested in BS 8006 (2010) as an alternative to the empirical approach based on Jones et al. (1990), and the model by Zaeske (2001) was adopted in the German standard of EBGEO (2010) and the Dutch standard of CUR226 (2010). However, Lawson (2012) concluded that there is little consistency between

different design methods. Ariyaratne & Liyanapathirana (2015) also compared seven current analytical methods with two-dimensional and three-dimensional numerical results of an instrumented embankment. They also highlighted the inconsistencies of the different design methods.

The design methods (Hewlett & Randolph 1988; BS 8006 2010; Guido 1987; Terzaghi 1943; Carlsson 1987) which do not consider the sub-soil effect are not suitable for the CIC design. Stewart & Filz (2005) also emphasised the great significance of the compressibility of the soil and the importance of considering it as a factor in the design.

ASIRI (2012) recommends two methods for LTP design. In the first method called “the fictitious inclusion method”, the inclusion is assumed to extend into the load transfer platform, considering the negative skin friction developed in this length.

In the second method, the load transfer is assumed to occur by means of diffusion above the inclusion. A brief summary of these methods are presented here.

Fictitious inclusion method

ASIRI (2012) presented the method developed by Combarieu (1988) for a special case where the embankment is constructed of cohesionless materials, and suggested a $K \tan \varphi_r = 1$, where φ_r is the friction angle for the embankment material, yielding the downdrag coefficient of $\lambda = 0$. However, the original Combarieu (1988) method showed an increase in the stress reduction ratio ($SRR = \frac{q_s^+}{\gamma_r h_r}$) with the increase in the embankment height. This behaviour, however, is in contradiction with the experimental and theoretical findings where there is a threshold value for SRR. ASIRI (2012) presented an improvement to the method by determining the position of the upper plane of equal settlement. The modified relation for determining the stress between the inclusions considering the upper plane of equal settlement, q_s^+ could be determined using Eq. (2.19):

$$q_s^+ = q(h_a) = \frac{\gamma_r}{\mu_r} (1 + e^{-\mu_r h_a}) + \gamma_r (h_r - h_a) e^{-\mu_r h_a} \quad (2.19)$$

$$\mu_r = \frac{2r_p K \tan \phi_r}{R^2 - r_p^2} \quad (2.20)$$

where h_r is equal to H_R , the embankment height, h_a is the height of the upper plane of equal settlement from the inclusion heads, r_p is the radius of the inclusion, q_0 is a uniform load on a flexible structure, and R is the equivalent mesh radius with the inclusion spacing of $2R$.

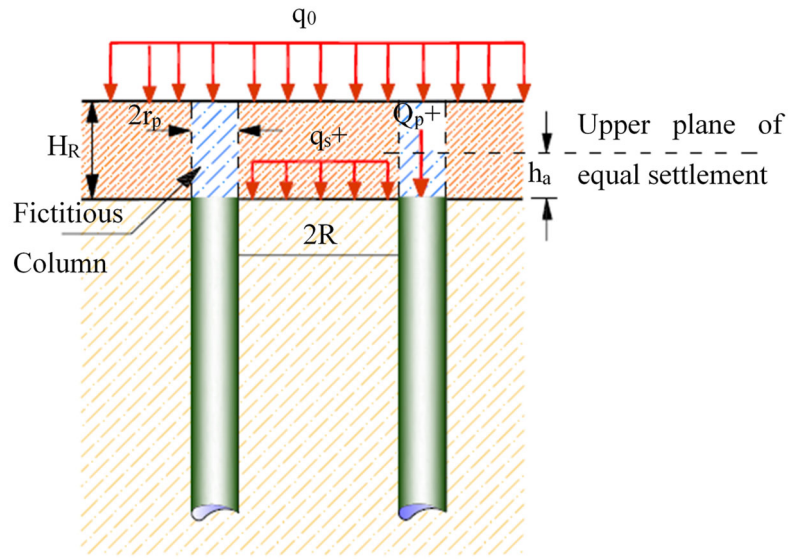


Figure 2.9 Fictitious inclusion method for LTP design (Modified after Combarieu 1988)

To determine h_a Eqs. (2.21) and (2.22) could be used:

$$\frac{h_a}{r_p} = 10 - 0.4 \left(6 - \frac{R}{r_p} \right)^2 \quad \text{if } \frac{R}{r_p} < 6 \quad (2.21)$$

$$\frac{h_a}{r_p} = 10 \quad \text{if } \frac{R}{r_p} > 6 \quad (2.22)$$

where h_a is the height of the upper plane of equal settlement from the inclusion heads and is equal to H_R when h_a is greater than H_R , R is the equivalent circular mesh, and r_p is the inclusion radius.

The coefficient of $K \tan \delta$ is also estimated using empirical relation presented in Eq. (2.23):

$$K \tan \delta = 1.1 - e^{\frac{E}{E_0}} \quad (2.23)$$

where E is the modulus of the layer of thickness h_a , and $E_0=50$ MPa.

The force applied on the inclusion head can be estimated as $F_N + \pi r_p^2 \gamma_r h_r$ where F_N is the negative skin friction over the height of h_r , and $\pi r_p^2 \gamma_r h_r$ is the weight of the fictitious inclusion.

Diffusion cone method

The load transfer mechanism in the diffusion cone method is assumed to take place through shear along the inverted pyramids on the inclusion heads making angle θ with the vertical direction. As shown in Figure 2.10 and Figure 2.11, the weight of the inverted pyramid and the surcharge on this area are assumed to be transferred to the inclusion, whereas the weight of the soil block between the pyramids and the surcharge on it is assumed to be sustained by the soft soil. Eqs. (2.24) and (2.25) are derived based on a circular cross-section for the inclusion with a diameter a :

$$Q_p = q\pi \left(\frac{a}{2} + h_m \tan \theta \right)^2 \text{ for } h_m \leq h^* = \frac{s-a}{2 \tan \theta} \quad (2.24)$$

$$W_p = \frac{\gamma \pi h_m}{3} \left(\left(\frac{a}{2} \right)^2 + \left(\frac{a}{2} + h_m \tan \theta \right)^2 + a \left(\frac{a}{2} + h_m \tan \theta \right) / 2 \right) \quad (2.25)$$

where Q_p is the share of the surcharge, W_p is the weight of the inverted pyramid, h_m is the height of the embankment, s is the inclusion spacing, and angle θ is usually taken as the peak friction angle for the embankment material. However, for large deformations, a smaller angle of friction should be used.

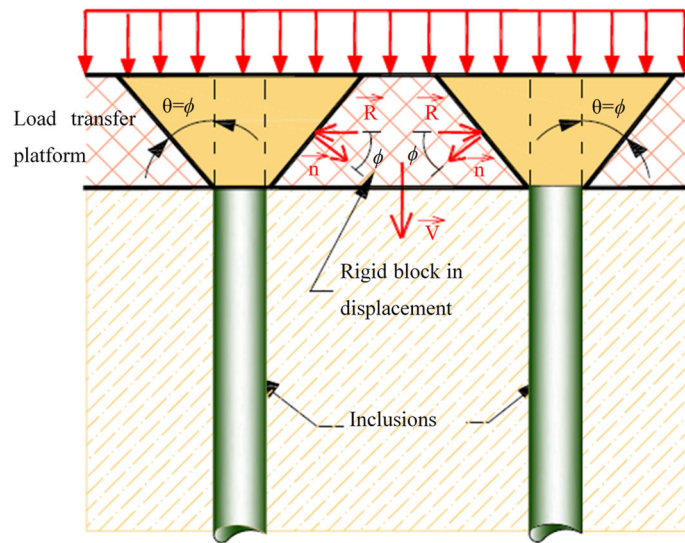


Figure 2.10 Failure mode in the load transfer platform (Modified after ASIRI 2012)

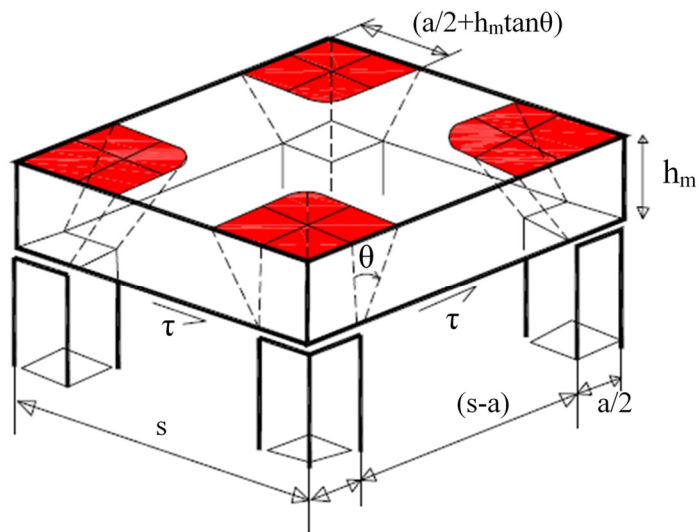


Figure 2.11 Inverted pyramid load transfer mechanism in the LTP according to Carlsson (1987)

The diffusion cone method is similar to the method of the Nordic Handbook (2005), with the difference that the angle θ is assumed to be 15° in the Nordic Handbook (2005) based on the study by Carlsson (1987). However, Chevalier et al. (2010) based

on coupled discrete elements and finite elements analyses, concluded that this angle is closer to the peak friction angle.

Considering the load transfer platform and the soil below the inclusion, two more neutral planes are defined as shown in Figure 2.12. The bottom neutral plane is the depth where the settlements in the soil become uniform again. The top neutral plane is where the settlements in the embankment are uniform, and the height of the embankment less than this value will lead to the “mushroom effect” or “egg carton” deformation on the surface as shown in Figure 2.13.

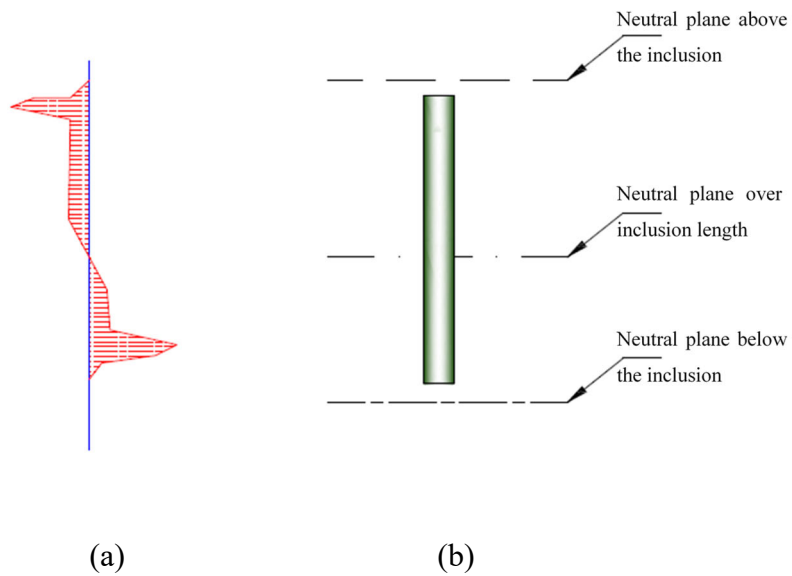


Figure 2.12 (a) Shaft friction on a CIC and (b) the position of neutral planes in a CIC system (Modified after ASIRI 2012)



Figure 2.13 Egg carton (or mushroom) effect on rigid inclusions (ASIRI 2012)

Numerical simulation is used for the deformation analysis. It considers the “punching” effect of the CICs into the granular layer at the top and the socketing into the competent soil layer. It also considers the stress-strain behaviour of the CIC concrete and the surrounding soil as well as the load transfer between CICs and the surrounding soil.

The numerical analysis is usually carried out in two stages. First, using an axisymmetric model, a single CIC inclusion is simulated considering a certain spacing and diameter, mechanical properties of the CIC concrete, and the LTP with or without geosynthetic reinforcement. Stresses and deformations are then evaluated and simulation is continued into the second stage where two-dimensional or three-dimensional models of the embankment are analysed for a more detailed design to assess the lateral deformation close to the embankment batters.

2.3 Experimental Background on Column Supported Embankments

A summary of the experimental works performed on the column supported embankments is presented in this section.

The performed tests could be classified into three groups:

1. Tests investigating the stress concentration ratio
2. Tests investigating the failure modes of the columns
3. Tests investigating the impact of different parameters on the overall performance

2.3.1 Tests Investigating the Stress Concentration Ratio

CIC is a relatively new method for ground improvement and unlike other columnar ground improvement techniques such as deep cement mixing (DCM) or stone columns, there is not much reliable experimental work in the literature. Similar tests to those done on DCM and stone columns could result in a better understanding of the mechanism of CIC performance, and could provide verification for the numerical works.

Das & Deb (2018) conducted small scale 1g physical modelling on clay improved with stone columns to investigate the variations of stress concentration ratio for different spacing to diameter ratios. They conducted tests with S/d ratios of 2, 3, and 4 where (S) is the spacing and (d) is the stone column diameter. They simulated a group of 9 end-bearing stone columns 75mm in diameter and 600mm in height using tanks of 3S×3S in cross-section and 1200mm in height with two detachable halves. They concluded that the SCR increased with the height of the embankment, modular ratio, and S/d ratio. SCR also increased with time and reached a constant value. In the case of higher embankment height, S/d ratio, and modular ratio, the SCR reached a peak and then decreased. This pattern was explained by the reduction in the initial arching effect and the increase in the soft soil stress level.

Fattah et al. (2010) conducted 30 laboratory tests on stone columns to investigate the SCR values for stone columns with the length to diameter ratios (l/d) of 6 and 8 in soft soil with shear strengths of 6, 9, and 12 kPa. They performed the experiments on single, and groups of two, three, and four stone columns made of crushed stone. Using steel plates, they applied the load on the reconstituted natural soil and stone columns in a tank of 1100×1100×800mm. They concluded that the values of SCR increases with the shear strength of the treated soil. Ambily & Gandhi (2007) found contradicting results.

Chen et al. (2008) reported a total of 15 two dimensional experiments to investigate the effects of pile-soil relative displacement, embankment height, cap beam width, clear spacing, and geosynthetic strength on the SCR. They used a tank made of toughened glass with dimensions of 1500×1000mm in cross-section, and 1440mm in height for the experiments. Two water bags were placed under the sand embankment to simulate the consolidation of the soft soil by allowing the gradual flow of the water. They also used geosynthetics with three tensile strengths of 0.35, 1.40 and 22.5 kN/m at 8% axial strain in both directions. They concluded that as the ratio of the embankment height to the clear spacing increases, the SCR also increases. The SCR also increases when a geosynthetic layer is included. However, they revealed through their experiments that SCR has upper and lower bounds. They also reached a critical embankment height to clear spacing ratio of 1.4 under which differential settlements occurred on the embankment surface, whereas for ratios over 1.6 no differential settlements were observed on the surface.

Fang & Yin (2007) investigated the responses of excess pore water pressure in soft marine clay around a soil–cement column. Again, the stress concentration ratio was one of the main concerns in this research. The stress concentration ratio and pore water pressure were measured and presented in graphs in the course of the tests as the soil consolidated under the applied pressure.

A cylindrical stainless steel mould of 300mm in diameter and 450mm in height was used for this experiment. A rigid platen was placed on the top of the model

ground to apply the same displacement on the DCM column and untreated soft clay. This physical model test aimed to simulate a ground reinforced by vertical DCM columns in a triangular/square pattern at the same spacing under vertical large-surface fill loading. A unit cell was assumed to be able to model the consolidation behaviour of the whole treated ground by DCM columns. They used Hong Kong marine clay slurry, preconsolidated uniaxially at a stress of 20 kPa to simulate the soft soil behaviour. They used two-surface drainage from the top and bottom surfaces during preconsolidation; however, they allowed drainage only from the model top during the test. Measured data of pore water pressure, and vertical pressures shared by the DCM column, and the untreated soft clay were presented, interpreted, and discussed. It was argued that faster dissipation of excess pore water pressure was caused due to the presence of the DCM column in the model ground. The DCM column reduced the vertical stress increment in the soil, resulting in a lower value of excess pore pressure. During the unloading stages, at the instant of unloading, it is found that the stress on the DCM column decreased in approximately the same magnitude as the total vertical pressure on the model ground. Local crushability and cracks of DCM column in the model ground seemed to have influence on the responses of negative pore water pressures in the unloading stages. They reported a residual pore pressure of about 2–3 kPa in the soil at the end of each unloading stage; the likely reason of which they explained to be the stagnated water in the cracks of the DCM column.

Porbaha et al. (2001) performed laboratory tests to study the static response of ground improved by fly ash columns. Their work presented undrained triaxial compression tests on clay specimens improved by columnar reinforcement. The process of loading and stress redistribution of a fly ash–clay specimen (FCS), in comparison with a sand–clay specimen (SCS), is examined in terms of stress–strain characteristics, generation of excess pore-water pressure, effective and total earth pressures, development of stress concentration, and the normalized undrained shear strength of the improved soil. They found, predictably, that the deviator stress of the composite specimens was influenced by the consolidation stress, replacement area ratio, and properties of the column material. The stress concentration at the top of the

composite ground which depends on the loading stage reached a peak after the consolidation state and reduced due to stress redistribution between the column and the soft ground.

2.3.2 Tests Investigating the Failure Modes of the Columns

Rashid et al. (2018) conducted ten 1g laboratory tests to investigate the failure mechanisms and bearing capacity of floating soil cement columns using particle image velocimetry (PIV) and close range photogrammetry. They used a replacement method to construct groups of 6, 9, and 12 floating soil-cement columns 24mm in diameter and 100mm in length in a soft clay bed inside a rigid chamber 400mm×150mm in cross-section and 430mm in depth. The chamber had a Perspex plate on the front wall allowing for PIV measurements. They used artificial texture on the kaolin clay to enhance the white clay surface for the displacements to be detected by the PIV method. The improved soft clay bed had an area replacement ratio of 17, 26, and 35%. They used a rigid plate to load the treated ground to failure. They also included two benchmark tests with no reinforcements to compare with the reinforced cases. They found a 60%-85% improvement in the bearing capacity compared to the untreated cases. They used the Limit State, GEO software to compare their PIV results on the failure patterns, and found significant differences.

Rashid et al. (2015) investigated the behaviour of end-bearing soil-cement columns using PIV method. They used similar area ratios of 17, 26, and 35% using longer columns of 24mm in diameter and 200mm in length loaded with a rigid plate. They achieved improvement ratios of up to 200%. They again reported differences between the failure patterns from the PIV method and the Limit State, Geo software.

Yin & Fang (2010) performed physical modelling of a footing on soft soil ground with deep cement mixed soil columns under vertical loading. In this study, an instrumented plane-strain physical model was created and used to investigate the bearing capacity and failure modes of a soft soil improved by an end-bearing DCM column group. A steel tank with dimensions of 900mm by 300mm in cross-section and 900mm in depth was used for performing the plane-strain physical model test. The

columns had a diameter of 40mm and a height of 450mm. A square rigid plate of 300mm by 300mm and 30mm in thickness was mounted on the treated area of soil ground. Vertical loading was applied manually through a hydraulic jack with a vertical penetration rate of 1mm/min that resulted in an approximate undrained condition of the model ground.

That study focused on the observed wedge-shaped shear failure of the model ground and attempted to give an account of the failure. Two different methods were used to calculate the bearing capacity of the model ground, and the computed values were compared with the measured ones. They found that the simple Brom's method gave a better estimate of the bearing capacity of the model ground. They also found that the measured data of pore water pressures at different locations in the soft soil indicated coupling between failure of columns and consolidation of the soft soil. This study presented the first time a wedge-shaped block failure pattern for DCM treated soil ground.

Kitazume & Maruyama (2006; 2005) performed centrifuge model tests on improved ground using deep mixing method (DMM) columns to study the external stability. They used a strong box of 700mm×200mm in cross-section, and 600mm in depth to conduct their plane-strain tests. They used acrylic pipe columns to prevent the columns from rupturing and allowing the study of external stability. They sand blasted all the acrylic pipes to create a rough surface. They used 5 sets of two strain gauges on the outside surface of some of the columns to measure the bending moments while passing the strain-gauge wires through the inside of the pipe. They performed tests using different number of column rows, and also a test on the unimproved ground as a baseline. Their small scale centrifuge models failed with collapse failure pattern and not sliding failure pattern. Using FEM simulation, they confirmed their results, and concluded that sliding failure could happen under certain circumstances such as the ground improved using floating DM columns. They emphasized the importance of failure pattern and argued that the failing to consider it might overestimate the external stability.

Kitazume et al. (2000) also performed centrifuge model tests to investigate the effect of DMM strength and loading condition on the failure pattern. They used DMM columns with different strengths under a combination of vertical and horizontal loads to study the failure envelopes. Their study revealed that the DMM columns collapsed or were ruptured depending on the column strength and the loading condition. As for the ruptured columns, depending on their location and loading condition, they either failed under shear or bending. They also compared their results with FEM analyses.

Kitazume & Maruyama (2007) investigated the internal failure modes through centrifuge tests, conducted at 50g. They used a strong box of 700×200mm and 600mm in depth to preconsolidate Kaolin clay slurry for the DM columns to be installed. They reported an area replacement ratio of 28%. They installed Acrylic pipes and cement treated columns by inserting a thin walled tube with a diameter of 20mm into the clay bed and emptying the soil inside. They used carbon rods with low electrical resistance to detect column failure as the resistance changes to infinity when the rupture breaking occurs. Their study revealed that shear, tensile, and bending failure modes occur depending on the loading, ground conditions, and the location of the columns. They highlighted the importance of area replacement ratio in the internal stability of the embankments on column-improved grounds. They concluded that in the case of small improvement width, the columns failed in the order of the farthest to the embankment centreline to the closest. In the case of the wider improvement width, the three columns closest to the toe of the embankment failed, and then the column closest to the centreline failed due to the excessive embankment settlement. They also suggested a simple method for stability check for the bending failure.

Broms (2004), based on the past experiments performed by several researchers detailed the failure modes as illustrated in Figure 2.14. In the case of the column (a), the moment capacity of the column is enough to resist the lateral soil pressure; however, for column (b), the lateral pressure has exceeded the moment capacity of the column and a plastic hinge is formed. Two plastic hinges have formed in the locations of the maximum and minimum bending moments in columns (c), (d),

and (e). Failure mode (f) is for the case when the column is extended to the firm layer and the slip surface is deep, while in case (g), the slip surface is deep and the column moves with the soft soil. For column (h), the shear resistance of the column governs the failure mode, whereas for column (i), the compression failure is the governing failure mode, and for the case (j) it is the tensile failure mode.

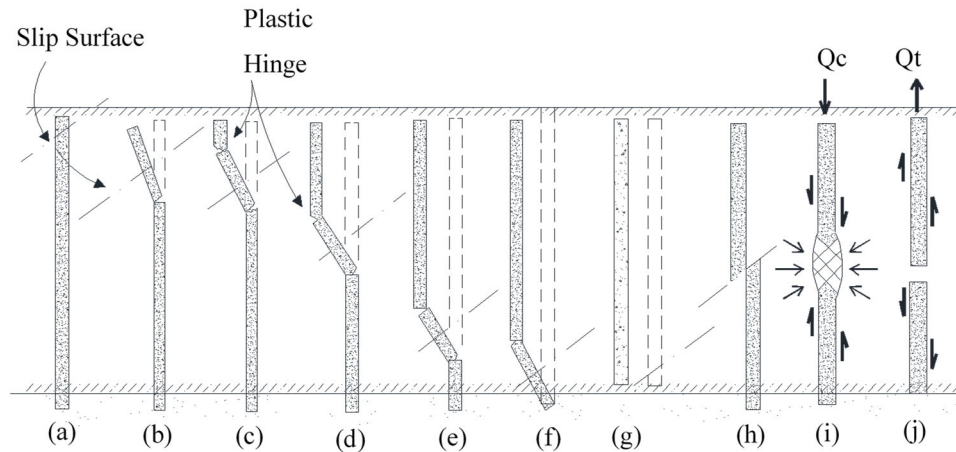


Figure 2.14 Failure modes for single columns (Modified after Broms 2004)

McKelvey et al. (2004) performed tests on vibrated stone columns in soft clay. Different failure mechanisms of bulging, bending, punching, or shearing were examined in this paper. The study involved a series of laboratory model tests on a consolidated clay bed. The tests were carried out using two different materials: (a) transparent material with 'clay like' properties, and (b) speswhite kaolin. Three sand columns, 25 mm in diameter, were installed in a triangular arrangement beneath the circular footing (100mm in diameter), and in a row beneath the strip footing (100×50mm) to depths of 150 mm and 250 mm. This corresponded to L/d ratios of 6 and 10, where L is the column length and d is the column diameter. Displacement controlled loading was applied to the model footing at a rate of 0.0064 mm/min until the footing penetrated approximately 35mm into the clay. The tests on the transparent material permitted visual examination of the deforming granular columns during loading. They showed the bulging was significant in long columns, whereas punching was prominent in shorter columns. The presence of the columns also greatly improved

the load-carrying capacity of the soft clay bed. However, columns longer than about six times their diameter did not lead to further increase in the load-carrying capacity. This suggested that there was an optimum column length for a given arrangement of stone columns beneath a rigid footing.

Wood et al. (2000) investigated the group effect in stone column foundations using laboratory modelling. Model tests were performed to determine the mechanisms of response for beds of clay reinforced with stone columns under surface footing loads. An exhumation technique was used to discover the deformed shapes of the model stone columns, and to understand the way columns transferred the load to the surrounding clay. Tests explored the effect of varying the diameter, length and spacing of the model stone columns. As they pointed out, these parameters control whether the columns act as somewhat rigid inclusions transferring load to their tips and eventually deforming either by bulging or by the formation of a failure plane, or whether they are able to compress axially or even, if sufficiently slender, to 'bend' and undergo significant lateral deformation. Miniature pressure transducers were used to reveal the distribution of contact pressure between columns and clay at various stages during the loading of the footings.

They concluded that the columns at mid-radius of the footing are typically the most heavily loaded. Results from numerical analysis were also used to provide qualitative support for some of the findings from the physical model tests. Photographs of deformed sand columns have been provided in Figure 2.15 and different deformation modes are illustrated in Figure 2.16.

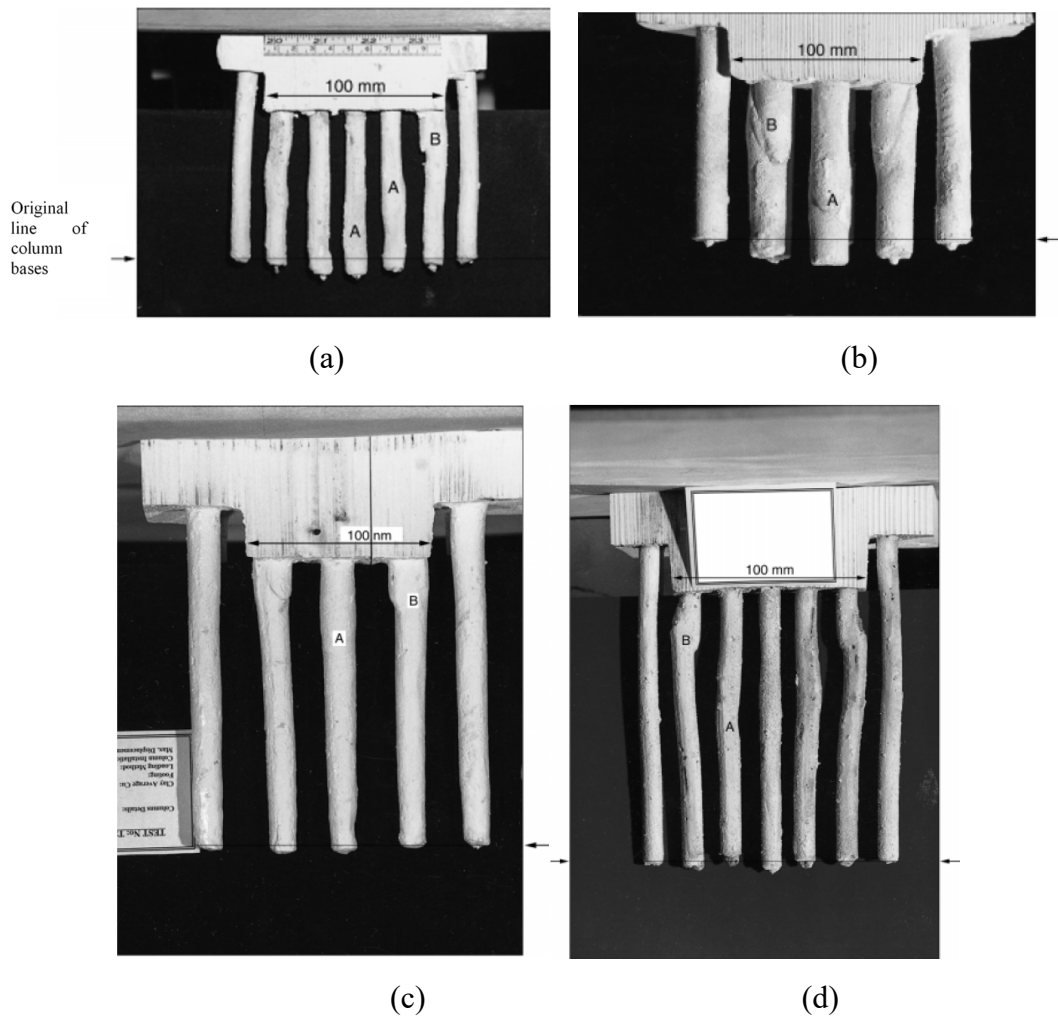
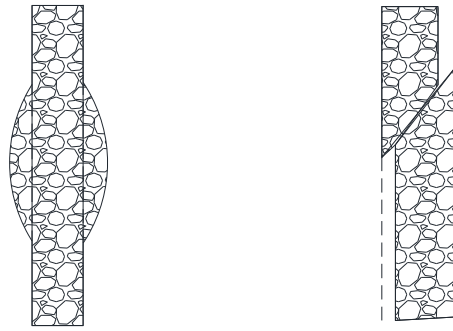
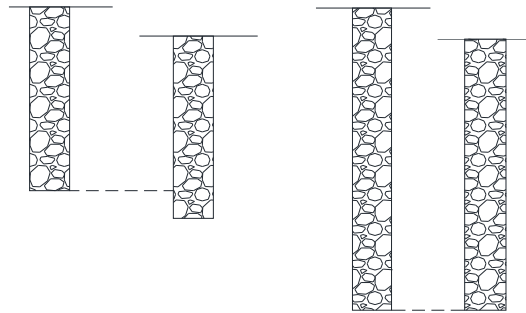


Figure 2.15 Photographs of deformed sand columns exhumed at the end of footing penetration (arrows indicate original level of column bases): (a) $L/r_o=2$, $A_s=24\%$, $r_c=5:5$ mm, (b) $L/r_o=2$, $A_s=30\%$, $r_c=8:75$ mm, (c) $L/r_o=3:4$, $A_s=24\%$, $r_c=8:75$ mm and (d) $L/r_o=3:2$, $A_s=24\%$, $r_c=5:5$ mm (Wood et al. 2000)



(a) Mode 1: bulging

Mode 2: shear failure plane



(b) Mode 3: Short column penetrates clay; long column absorbs deformation along its length



(c) Mode 4: slender column acts as laterally loaded pile

Figure 2.16 Sketches of deformation modes: (a) bulging and shear failure plane mode, (b) Short column versus long column, and (c) slender column (Modified after Wood et al. 2000)

2.3.3 Tests Investigating the Influence of Different Parameters on the Overall Performance

Several researchers (Girout et al. 2018; Fagundes et al. 2017; Okyay et al. 2014; Blanc et al. 2014) have used a device called the mobile tray (MT) to investigate the behaviour of the load transfer platform (LTP) in piled embankments. The MT simulates the compressibility of the soft soil through the downward displacement of a tray.

Nineteen 1g scaled tests with scales of 1:3 to 1:5 were reported by van Eekelen & Bezuijen (2014) and van Eekelen et al. (2012a, 2012b). They used a foam cushion to model the soft soil around 4 piles and placed a 15 to 20mm layer of sand on top with one or two GR layers. They used traditional strain gauges in three tests and bicycle gear cable to which they referred to “strain cables” in others to measure the strains in GR. They found no difference between using two uniaxial geosynthetic layers on top of each other, and a biaxial geogrid layer. However, they experienced a limited difference when a granular layer was used between the two uniaxial geosynthetics. They revealed that the load on the geosynthetic is concentrated on the bands between the two adjacent piles, and referred to it as “GR strips”. They proposed an inverse triangle load distribution pattern on the GR strips based on the deformed shape of the geosynthetic layer as opposed to the triangular distribution proposed by Zaeske (2001). They measured the loads transferred to the subsoil, the geosynthetic layer, and the piles independently, so that the comparison could be made between the measurements and the analytical methods. They reported the measurements from their experiments, and compared their results with EBGEO (2010), and proposed improvements to this method.

Shahu & Reddy (2011) conducted 15 small scale 1g laboratory tests on floating stone columns in kaolinite clay consolidated in a Perspex cylindrical tank of 300mm in diameter and 600mm in depth. They evaluated the effect of different parameters such as area replacement ratio, column length, moisture content and relative density of the column material. The tests were conducted on 13-25mm

diameter stone columns with the lengths of 100-150mm, and area replacement ratios of 10, 20, and 30%. The load was applied using a loading plate on a granular mat of 20mm thick. They divided the investigated parameters into two groups with major or minor effect on the behaviour of floating stone columns. They concluded that area replacement ratio, column length to diameter ratio, Young's modulus of elasticity of the column, overconsolidation ratio, and clay parameters were of major importance.

Deb et al. (2011) conducted studies on unreinforced and geogrid-reinforced sand bed over stone column-improved soft clay using laboratory models. To prepare the soft soil bed, a square tank of 525mm×525mm in cross-section, and 400mm in height was used in all the tests. The diameter of stone columns was 50mm in all the tests and the depth of clay bed was maintained at 300mm. Steel circular plate of diameter 100mm and thickness 12.5mm was used as footing to apply the load. In case of geogrid-reinforced sand bed, initially a sand layer of 5mm thickness was placed in between the geogrid layer and the clay bed. Thereafter, the circular geogrid layer was placed in such a way that the centre of geogrid was on the same line as the centre of stone column. Short-term loading test was conducted in all the cases. Loading was applied until the total settlement of the footing attained was at least 20% of the footing diameter.

The results showed that the presence of the stone column in soft clay improves the load carrying capacity and decreases the settlement of the soft soil. The placement of sand bed further increased the load-carrying capacity and decreased the settlement of the stone column improved soil. The inclusion of the geogrid layer as a reinforcing element in the sand bed significantly improved the load-carrying capacity and reduced the settlement of the soil. They observed 69%, 141% and 233% improvement in load carrying capacity compared to the unimproved soft clay (at settlement equal to 20% of the footing diameter), when soft clay was improved by stone column alone, and by placing of unreinforced and geogrid-reinforced sand bed of optimum thickness over stone column, respectively. They also concluded that the optimum thickness of unreinforced sand bed placed over the stone column-improved soft clay is 1.7 times the optimum thickness of the geogrid-reinforced sand bed. They

concluded that the optimum thickness of the unreinforced and geogrid-reinforced sand bed is 0.5 and 0.3 times the diameter of the footing, respectively. Under optimum thickness of geogrid-reinforced sand bed, the optimum diameter of the reinforcement is 3 times the diameter of the footing.

Ambily & Gandhi (2007) investigated the behaviour of stone columns based on experimental modelling and FEM analysis. They performed experimental studies on behaviour of single column and group of seven columns varying parameters like the spacing between the columns, shear strength of the soft clay, and loading conditions. Laboratory tests were carried out on a column of 100mm diameter surrounded by soft clay of different consistencies. The tests were carried out either with an entire equivalent area loaded to estimate the stiffness of improved ground or only a column loaded to estimate the limiting axial capacity. During the group experiments, the actual stress on column and clay were measured by fixing pressure cells in the loading plate. Ambily & Gandhi (2007) found that when the column area alone was loaded, failure was by bulging with maximum bulging at a depth of about 0.5 times the diameter of stone column. As spacing increased, the axial capacity of the column decreased and settlement increased up to s/d of 3, beyond which the change was negligible. The ratio of limiting axial stress on column to corresponding shear strength of surrounding clay was found to be constant for any given s/d and angle of internal friction of stones, and it was independent of the shear strength of the surrounding clay. Single column tests with an entire unit cell area loaded compared well with the group test results. Hence, they concluded that the single column behaviour with unit the cell concept can simulate the field behaviour for an interior column when a large number of columns are simultaneously loaded. The stiffness improvement factor was found to be independent of the shear strength of the surrounding clay, and depended mainly on the column spacing and the angle of internal friction of the stones.

Zaeske (2001) and Kempfert et al. (2004) reported a series of three-dimensional scaled (1:3 to 1:6) laboratory tests with four piles placed in weak peat, and different height of reinforced and unreinforced sand fills. Strain gauges were also

used to measure the GR strains. Based on the experiments, they developed theoretical models to capture the stress distribution and the membrane effect in the geosynthetic layer. Their research is the basis for the German guideline, EBGEO (2010).

Jenck et al. (2005) as part of the French national project ASIRI (2012), conducted two-dimensional physical simulation of the load transfer platform using the Taylor-Schneebeli analogical soil for the platform material, metal elements as piles, and foam to simulate the soft soil behaviour. They indicated that since the scaling laws were not strictly observed, their study was more of a qualitative work than a quantitative one, and the results should not be extrapolated to a real case. They also compared their laboratory results with analytical methods of BS 8006 (1995), EBGEO (2004), Russell & Pierpoint (1997), and Low et al. (1994), and Combarieu (1988). They found a good agreement between the Low et al. (1994) analytical method and their experimental results.

Although filed case studies on CICs (King et al. 2017; Briançon & Simon 2012; Fok et al. 2012; Wong & Muttuvel 2012a) have provided valuable information on the design and the behaviour of the CIC-improved ground, they lack the flexibility and the control of the small scale physical models.

A comparison between different studies has been provided in Table 2.1. The scaling and the instrumentations have been highlighted.

Table 2.1 Experimental studies on columnar ground improvement methods

GI Technique	Reference	Inclusion of GR	Experimental method	Column type
Stone columns	Das & Deb (2018)	No	1g	End-bearing
	Shahu & Reddy (2011)	No	1g	Floating
	Deb et al. (2011)	Yes	1g	End-bearing
	Ambily & Gandhi (2007)	No	1g	End-bearing
	McKelvey et al. (2004)	No	1g	Floating
	Wood et al. (2000)	No	1g	Floating
Soil-cement columns	Rashid et al. (2018)	No	1g	Floating
	Rashid et al. (2015)	No	1g	End-bearing
	Yin & Fang (2010)	No	1g	End-bearing

GI Technique	Reference	Inclusion of GR	Experimental method	Column type
Soil-cement columns	Kitazume & Maruyama (2007; 2006; 2005)	No	50g	End-bearing
	Kitazume et al. (2000)	No	30g	End-bearing
Piled-embankments	van Eekelen & Bezuijen (2014) and van Eekelen et al. (2012a, 2012b)	Yes	1g	End-bearing
	Jenck et al. (2005)	No	1g	End-bearing
	Zaeske (2001) and Kempfert et al. (2004)	Yes	1g	End-bearing

2.4 Raft Foundations

In most conventional designs for piled foundations, the required number of piles is decided assuming that all loads must be carried by the piles, ignoring any contribution from the raft or the pile cap, even though competent soil conditions may exist beneath the raft. This conservative approach appears to be due to limited understanding of the interactions of the pile group and raft with the soil, and the scarcity of validated methods of analysis for this complex three-dimensional problem. Consequently, conventional approaches generally result in the installation of more piles than are necessary, which automatically leads to much lower levels of overall settlement than could be tolerated by the structure.

Consider the simple case of a foundation loaded by only a vertical total structural load V_{PR} . In order to describe the portion of the total load taken by the piles (Figure 2.17), it is possible to introduce the load sharing ratio α_{pr} defined as:

$$\alpha_{pr} = \sum_{i=1}^n V_{Pile,i}/V_{PR} \quad (2.26)$$

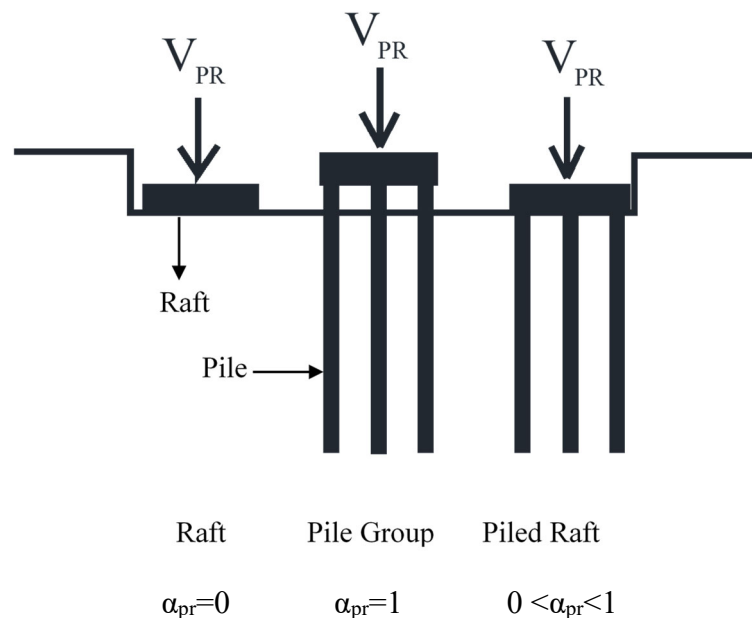


Figure 2.17 Foundation systems (Modified after Mandolini et al. 2013)

A load sharing ratio $\alpha_{pr}=0$ represents a shallow foundation with no piles, while $\alpha_{pr}=1$ represents a pile group with a raft not in contact with ground; piled raft foundations cover the range $0 < \alpha_{pr} < 1$.

There is a similarity between the CIC method and piled raft as such, in that, both systems transfer a portion of the applied load to the subsoil. However, there is a very significant difference in the load transfer mechanism of these two systems. Fioravante (2011) performed extensive experimental tests on piled rafts in dry sands using two different systems to apply the load; the first system which they called the contact piled raft included a raft in contact with the test piles, and the second system which they called the noncontact piled raft consisted of an additional interposed layer between the raft and the piles.

They concluded that the load transfer mechanism is completely altered when there is an interposed layer between the raft and the subsoil. The positive skin friction on the upper part of the pile shaft changes to negative skin friction in the noncontact case. As explained by the authors and the results from the experimental tests on single and group piles, the load sharing mechanism between the piles and the raft is also totally different in the two cases.

The tests were performed on single piles and pile groups in dry sand. Similar tests on piles in clay and pore water pressure measurements would shed more light on the behaviour of the piled rafts with an interposed layer.

2.5 Physical Modelling of Axially Loaded Piles

Concentric cylinders of soil could be assumed around a pile, with shear stresses on each cylinder. The magnitude of the shear stress on each cylinder must decrease inversely with the surface area of the cylinder to satisfy the vertical equilibrium ((Cooke 1974; Frank 1974) cited in Fleming et al. (2008)).

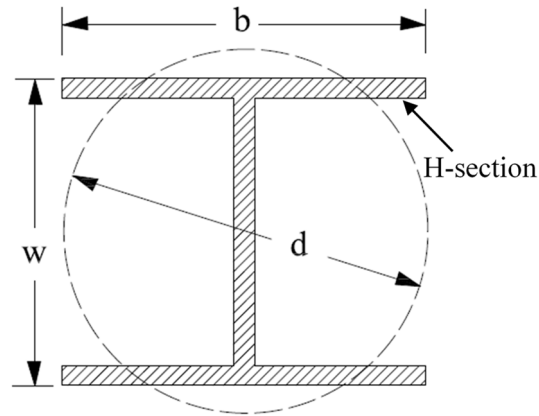


Figure 2.18 Idealization of H-section pile (Modified after Fleming et al. 2008)

Considering the shear stress on the pile shaft is τ_0 , the shear stress at radius r (for a pile of radius, r_0) is given by:

$$\tau = \frac{\tau_0 r_0}{r} \quad (2.27)$$

It is more appropriate to develop the solution in terms of the shear modulus G and Poisson's ratio, ν , rather than Young's modulus, E ($G=E/2(1+\nu)$) since shear deformation is the main mode of deformation around a pile. The shear strain in the soil, γ , will then be calculated by $\gamma = \tau/G$. Since the main deformation in the soil will be vertical, the shear strain may be written approximately as:

$$\gamma \sim \frac{dw}{dr} \quad (2.28)$$

where w is the vertical deflection.

Integrating these relationships will give:

$$w = \int_r^{r_m} \frac{\tau_0 r_0}{Gr} dr = \frac{\tau_0 r_0}{G} \ln\left(\frac{r_m}{r}\right) \quad (2.29)$$

where r_m is the radius at which the deflections in the soil are assumed to become very small. This radius has been empirically found to be of the order of the length of the

pile ((Randolph & Wroth 1979), cited in Fleming et al. (2008)). The deflection of the pile shaft, w_s , can be estimated as follows:

$$w_s = \zeta \frac{\tau_0 r_0}{G} = \zeta \frac{\tau_0 d}{2G} \quad \text{where } \zeta = \ln\left(\frac{r_m}{r_0}\right) = \ln\left(\frac{2r_m}{d}\right) \quad (2.30)$$

A few conclusions could be inferred from the Eq. (2.27):

- Stress changes in the soil are primarily of the shear type, inversely decreasing with distance from the pile axis; therefore, only soil very close to the pile is ever highly stressed.
- Significant deflections extend some distance away from the pile, up to about one pile length, since the resulting deflections decrease with the logarithm of distance from the pile axis.
- The deflection of the pile shaft, w_s , normalized by the pile radius r_0 , is ζ times the local shear strain, $\gamma_0 = \tau_0/G$, in the soil. The parameter ζ is found to vary between 3 and 5, with an average value of about 4 (Baguelin & Frank 1980).

A discussion on modelling the piles under axial load has been presented by Wood (2004). Piles are usually regarded as axially rigid inclusions so that axial deformation of the pile is not a constraint on physical modelling. However, the compression of a long friction pile may be comparable with the relative movements between the pile and the ground (see Figure 2.19).

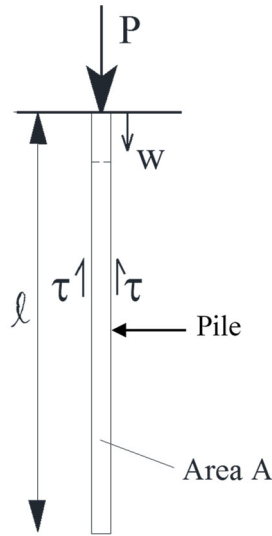


Figure 2.19 Pile under axial loading (Modified after Wood 2004)

The need to model axial stiffness of the pile should be considered. A dimensionless group can be formed by two characteristic forces ((Nunez & Randolph 1984), cited in Wood (2004)). Considering a pile sufficiently long and compressible that all the load is transferred to the soil by shaft resistance, and virtually no force reaches the toe of the pile when it is loaded at its top. For a pile with a Young's modulus E , cross-sectional area A , and length L , the force due to a settlement ws at the top will be related to $E Aws/L$ since ws/L provides some indication of the level of axial strain in the pile. The shear stress at the interface between a pile with a radius r_0 and in elastic soil is related to the relative movement as shown in Eq. (2.30) and rearranged in Eq. (2.31):

$$\frac{\tau_0}{ws/r_0} \approx \frac{G}{\zeta} \quad (2.31)$$

where $\zeta \approx 4$. Therefore, a characteristic shaft friction force is $2\pi r_0 L(G/4)(ws/r_0)$, and the dimensionless ratio of forces is:

$$\frac{1}{2} \left(\frac{L}{r_0} \right)^2 \left(\frac{G}{E_*} \right) \quad (2.32)$$

where E^* denotes the Young modulus for an equivalent solid pile so that $E^* \pi r_0^2 = EA$. Therefore, keeping the $\left(\frac{L}{r_0}\right) \sqrt{\frac{G}{E^*}}$ the same in the model and prototype will satisfy the similitude condition. Based on Eq. (2.31), w^S/r_0 ratio should also be the same if the development of limiting shear strength, c_u is a concern. Modelling on a centrifuge with the same G , and probably c_u , as the prototype, the similarity should be maintained so that L and r_0 (and w) scale directly with n_l . The selection of the material and cross-section of the model pile is the only choice left, and should be done in a way so that EA scales with n_l^2 . Interface behaviour and surface roughness effects are also of importance, and the nonlinearities of the pile-ground interaction as the relative movements develop may be of concern. The constraints imposed to maintain complete similarity may be quite tight.

2.6 Numerical Background on Column Supported Embankments

For the simulation of column-supported embankments, usually two-dimensional plane strain or axisymmetric numerical models are adopted since three-dimensional simulations are computationally demanding, especially when the coupled flow-deformation analysis should be undertaken to obtain time-dependent consolidation deformations. However, inaccuracies are introduced into models as three-dimensional problems are converted into plane strain two-dimensional equivalents. In many cases, the flow-deformation interaction is also disregarded and the short term or long term behaviour of the models are investigated by simply assigning the undrained or drained parameters to the material which could lead to an aggressive or underestimated deformations; and therefore, an unsafe design.

Yapage et al. (2013) suggested a constitutive model to simulate the strain softening in deep cement mix (DCM) columns beyond yield. This model was an extension of the Mohr-Coulomb criterion and was validated against triaxial test data from literature. They incorporated this model in a two-dimensional flow-deformation coupled finite element model in ABAQUS software to simulate a geotextile-reinforced DCM-supported embankment over soft soil in Finland. They observed a good

agreement between the measured and the predicted results although the DCM columns did not yield significantly in this case. They further investigated the progressive softening and failure of DCM columns arranged in a square pattern for a hypothetical case, and observed the development of plastic hinges and bending failure in the columns. They identified the bending failure of the columns as the most critical internal failure mode in GRCS embankments in ultimate limit state conditions. They argued that once the bending capacity of the column is exceeded, a slip surface will be formed due to the progressive failure of the columns, and this will lead to the embankment failure.

Yapage et al. (2014) implemented the aforementioned proposed constitutive model for strain softening in DCM columns in a two-dimensional flow-deformation coupled finite element model in ABAQUS software to simulate the Ballina Bypass part of the Pacific Highway project in Australia where apparently the measurements exceeded the predictions for the settlement. They argued that this discrepancy was due to the yielding of the DCM columns. They observed a better agreement between the predictions and the measurements when strain softening of the DCM columns was incorporated in the models. Based on the stress reduction on the columns and stress increase on the soft soil, they concluded that the stress was transferred from the soft soil to the DCM columns due to strain softening in the columns. They argued that the exclusion of strain softening behaviour in the columns from the numerical simulations will lead to an overestimation of the bearing capacity of the DCM-improved ground, and an underestimation of settlements, lateral displacements, and excess pore water pressures.

Yapage & Liyanapathirana (2014) used flow-deformation coupled two-dimensional plain strain models in ABAQUS software to perform a thorough parametric study on the effect of different parameters on the performance of the geosynthetic-reinforced column supported (GRCS) embankments. They investigated the effects of parameters such as the elastic modulus of the DCM columns, area replacement ratio, elastic modulus and permeability of the soft soil, geosynthetic stiffness, platform thickness, and the friction angle of the fill material. They evaluated

the performance of the system based on the total and differential settlements, mobilised tension in the geosynthetic layer, lateral displacement of the DCM columns, arching ratio, and the efficiency coefficient of the columns. They evaluated the degree of influence of each parameter in percentages as presented in Table 2.2, and they assigned three degrees of “low”, “medium”, and “high” significance to the influencing parameters based on the percentages.

Table 2.2 The degree of influence of different parameters in percentages(after Yapage & Liyanapathirana 2014)

Parameter	T _{Max}	S _{Max}	S _{Crest}	DL	ρ	S _{Dif}	f
DCM Column							
Young modulus, E_C	24	68	51	28	27	37	29
Column spacing, S	115	113	101	87	98	149	120
Column diameter, d	95	84	92	73	45	52	59
Soft soil							
Young modulus, E_s	158	107	139	173	74	171	45
Soil Permeability, k_s	41	18	30	100	12	10	24
Geosynthetic							
Tensile stiffness, J	106	16	58	69	22	37	10
Embankment							
Friction angle, ϕ'	61	17	71	62	14	39	13

T_{Max}: maximum tension in the geosynthetic, S_{Max}: maximum settlement at the base of the embankment at the clay surface, S_{Crest}: maximum settlement at the embankment crest, DL: lateral deformation, ρ : arching ratio, S_{Dif}: differential settlement, f: efficiency coefficient

The “low” influence was used for significance degree of less than 30%, “medium” for 30%-60%, and “high” for above 60%. They concluded that area replacement ratio and

the soft soil elastic modulus had a high impact on the overall performance of the embankment.

Huang et al. (2009) conducted a two-dimensional flow-deformation coupled finite difference model in FLAC to simulate a GRCS embankment in Finland. They used linearly elastic-perfectly plastic Mohr-Coulomb constitutive model to simulate the soft soil, deep-mixed columns, and the embankment material in their simulations. They performed a parametric study on the verified model and concluded that the post construction settlement reduced as the column modulus and the geosynthetic stiffness increased, and settlements increased as the rate of the construction increased. They also compared their simulation to a previous research by Han et al. (2005), and argued that the maximum settlements are always greater for drained analyses.

Huang & Han (2010) continued on their previous two-dimensional model (Huang et al. 2009) and conducted additional parametric studies to investigate the effects of factors such as soil modulus and permeability, and column spacing on the embankment performance. They determined the column spacing and the elastic modulus of the soft soil were the two most influential factors in the performance of GRCS embankments.

Hosseinpour et al. (2015) conducted two-dimensional axisymmetric finite element analyses using PLAXIS software to simulate a full-scale test embankment on soft ground. They simulated the soft soil using the Soft Soil model, and Mohr-Coulomb failure criterion to simulate the geotextile encased granular columns and the embankment material. They observed a satisfactory agreement between the predictions and the measured data for settlements and the total vertical stresses.

Han & Gabr (2002) used two-dimensional axisymmetric drained finite difference models using FLAC to investigate the effects of different parameters on the mobilised tensile forces in the geosynthetic reinforcement in GRCS embankments. They used a nonlinear hyperbolic elastic model to simulate the embankment fill and the foundation soil, and used a linear elastic model to simulate the geosynthetic layer and the pile material. They considered fully bonded interface elements between the

soil and the pile, and also between the geosynthetic and the soil. Their research revealed that the inclusion of a geosynthetic layer reduces the total and differential settlements and helps a better stress transfer to the columns. They also showed that the maximum tension in the geosynthetic reinforcement occurred at the edge of the pile, and increased with the height of the embankment, geosynthetic stiffness, and elastic modulus of the pile. They highlighted the shortcomings of the analytical methods such as Hewlett & Randolph (1988) and BS 8006 (1995) in not considering the effect of geosynthetic and pile stiffness in their predictions.

Zhuang et al. (2010) reported plane strain finite element analyses in ABAQUS using elastic-perfectly plastic Mohr-Coulomb model for the embankment, and vertical stress to represent the subsoil. They investigated arching in piled embankments and concluded that arching occurred at a small settlement in the soft soil, while for the geosynthetic reinforcement to reduce the stress on the soft soil, a higher settlement was required. They highlighted the importance of the embankment height to column spacing ratio in the behaviour of the piled embankments.

Zhang et al. (2013) through two-dimensional flow-deformation coupled analyses using PLAXIS software investigated a new ground improvement method referred to as fixed geosynthetic-reinforced and piled embankments (FGT) where the geosynthetic layer is fixed onto the pile heads. They compared different parameters such as vertical settlement, differential settlement, lateral displacement, and excess pore water pressure for the fixed geosynthetic case with the conventional GRCS embankments. They also performed a sensitivity analysis to evaluate the influencing factors. They concluded that the FGT embankments can reduce the total and differential settlements, lateral displacements, and excess pore water pressure efficiently.

Jenck et al. (2009) used discrete element method in two-dimensional particle flow code (PFC2D) to validate their two-dimensional physical model using Taylor-Schneebeli soil analogue. They also performed parametric studies using FLAC. Based on their observed divergence in the results of their discrete element analyses and the

continuum numerical model, they advised to take into consideration the limitation of the different numerical modelling approaches.

Jenck et al. (2007) conducted two-dimensional plane strain finite difference analysis using FLAC to numerically analyse their laboratory simulation of a piled embankment using Schneebeli's analogical soil. They used an elastic-perfectly plastic constitutive model with nonlinear elasticity and another elastoplastic model with isotropic hardening to simulate the platform material. They compared the results from both constitutive models and did not observe a marked difference. They further used their verified model to conduct parametric studies. However, they indicated the use of two-dimensional simulation, analogical soil, and the scale of the experiment prevents the extrapolation of the results to a real three-dimensional case.

Ariyaratne et al. (2013) investigated different two-dimensional idealisations for geosynthetic reinforced pile-supported (GRPS) embankments using ABAQUS software, and concluded that the three-dimensional simulations give the closest results to the actual field measurements. They simulated the soft soil using Cam-clay constitutive model, and the embankment, coarse grained layer, and the gravel bed using the Mohr-Coulomb model. They made the comparison between the different methods based on the stress on the foundation soil and the piles, tension in the geosynthetic, vertical and lateral settlements, and the excess pore water pressure. Comparing different two-dimensional idealisations, they concluded that equivalent area method yielded the next best predictions. They also revealed that using truss elements to simulate the geosynthetic layer in two-dimensional modelling gives the closest prediction to the three-dimensional simulation in terms of the mobilised tensile forces in the geosynthetic layer. However, they did not observe any significant difference in the vertical stresses, settlements, or excess pore water pressure in simulations using truss elements and plane strain elements. They did not consider the soil-pile interactions in this study.

Smith & Filz (2007) through their finite difference analyses in FLAC showed that although axisymmetric models give a reasonable estimate of the average vertical

load acting on the geosynthetic, these models are unable to predict the tension in the geosynthetic reinforcement accurately. They evaluated the drained axisymmetric numerical simulation against the field data, analytical solution, laboratory measurements, and three-dimensional numerical analyses using FLAC3D. They emphasised the use of three-dimensional simulation in order to evaluate the realistic stress and strain distribution in the geosynthetic layer. Their proposal of an alternative way to estimate the tensile forces in the geosynthetic was to estimate the vertical stresses on the geosynthetic layer and then estimate the tensile forces using guidelines such as BS 8006 (2010).

However, Yu et al. (2016) suggested a modified unit cell approach to take into account the lateral spreading of the embankment and foundation soil using lateral springs on one or both lateral boundaries. This is specifically important since the tension in the geosynthetic reinforcement is much lower from the unit cell analysis compared to the full-width simulation since the unit cell model does not simulate the lateral displacements or the batter slope effect of the embankment. They used FLAC finite difference software to compare the proposed approach with the normal unit cell analysis in small- and large-strain analysis modes. They concluded that the value of the tension in the geosynthetic reinforcement increased due to the lateral displacements of the embankment and the foundation soil using the proposed modified unit cell model.

Yu & Bathurst (2017) compared their modified unit cell approach (Yu et al. 2016) with a normal unit cell model, a full-width numerical model, and also an analytical model. Based on the analytical results, they concluded that the proposed modified unit cell, and also the full-width model produced better results compared to the normal unit cell model in predicting the tensile forces in the geosynthetic. They acknowledged that the proposed model had practical limitations as the calibration process can be very time consuming. Furthermore, Yu & Bathurst (2017) acknowledged that the advantages of their suggested modified unit cell model is limited to an embankment with a fixed geometry, and the calibration process is time consuming.

Yu & Bathurst (2017) and Yu et al. (2016) both investigated the effect of using large- or small-strain analysis modes in the numerical simulations. They found out that the settlements and the tensile stresses in the geosynthetic reinforcement are very sensitive to this choice. They emphasized the use of large-strain analysis mode in FLAC in order to capture the membrane effect of the geosynthetic. Yu et al. (2016) also revealed that unlike the tensile loads in the geosynthetic, the settlements and the maximum vertical stresses were not highly sensitive to the small- or large-strain mode analyses in the normal unit cell model.

Huang & Han (2009) presented a three-dimensional flow-deformation coupled finite difference model in FLAC^{3D} to simulate a GRCS embankment on deep mix (DM) columns in Finland. They used elastic-perfectly plastic Mohr-Coulomb failure criterion to simulate the different layers of the foundation soil and also the DM columns. Furthermore, they simulated a simplified model in FLAC to compare a case with a column and without a column to verify the load transfer mechanism. They concluded that the fast dissipation of the excess pore water pressure was due to the stress concentration on the column. They observed a good agreement between their predictions and the measured data from the field and concluded that the three-dimensional simulation is capable of accurately predicting the total and differential settlements of a GRCS embankments.

Khabbazian et al. (2015) compared a full three-dimensional, a three-dimensional unit cell, and an axisymmetric unit cell model to investigate the validity of the unit cell concept using finite element models in ABAQUS software. They concluded that in order to predict the mobilised tensile forces in the geosynthetic layer, a full three-dimensional simulation is essential since neither the axisymmetric unit cell nor the three-dimensional unit cell models are able to capture the slope batter effect of the embankment. They found the tension in the geosynthetic reinforcement from the full three-dimensional simulation was three times higher than the value they determined in the unit cell models due to the lateral displacement of the embankment in the full three-dimensional model. They also revealed that the axisymmetric unit cell analysis produced the same results as the three-dimensional unit cell analysis.

Zhuang et al. (2012) further developed their preceding plane strain study (Zhuang et al. 2010) into three-dimensional unit cell simulations. They found the vertical height of the arching as 2 or 2.5 times the clear spacing between the columns. Zhuang & Ellis (2014) added a single layer of biaxial geosynthetic to their model (Zhuang et al. 2012), and compared the finite element results with BS 8006 (2010) and its corrigendum BS 8006 (2012). In a later study, Zhuang & Ellis (2016), building on their previous studies, considered the contribution of the subsoil under the embankment as a modification to BS 8006 (2010), and compared the proposed modified method with their numerical simulations and found a good agreement. They determined that the subsoil contribution reduces the tension in the geosynthetic layer.

Girout et al. (2014) used two-dimensional axisymmetric and three-dimensional finite element models in PLAXIS to validate their experimental results from three-dimensional centrifuge models using the Mobile Tray. They used hypoplastic model considering the effect of density to simulate the granular layer. The results from their study showed a difference in vertical load distribution to the triangular distribution proposed by EBGeo (2010) and inverse triangle proposed by van Eekelen et al. (2013). However, they found that the shape of the deformed geosynthetic layer is in a closer agreement with the one proposed by van Eekelen et al. (2013) than the predictions of EBGeo (2010). They also concluded that the thicker granular mattress and the closer spacing of the piles increased the load transfer.

Rowe & Liu (2015) used three-dimensional coupled finite element analyses in ABAQUS to simulate four sections of a full scale project. The four selected sections were different as the first section had no piles, the second one had piles, the third section had a single layer of geosynthetic reinforcement on piles, and the fourth section had two layers of geosynthetic on piles. They concluded that the subsoil surface settlement in the piled embankment already reduced to 52% of the untreated section. They experienced a further reduction to 31% of the untreated soil using only a single layer of geosynthetic reinforcement. They also revealed that the inclusion of a single layer of geosynthetic reduced the total and differential settlements compared to the section with only piles, while the inclusion of a second layer had only minimal impact.

However, their research revealed that the inclusion of two layers was the most effective in reducing the lateral deformations.

Le Hello & Villard (2009) used coupled discrete and finite elements simulations (Le Hello et al. 2006) to investigate the behaviour of piled embankments including geosynthetic reinforcements. Discrete elements method was utilised to simulate the behaviour of granular soil and finite elements method was used to simulate the geosynthetic reinforcement layer and its interactions with the soil. Comparing their numerical results with a full-scale experiment, they concluded that the developed model was suitable for the simulation. They also performed parametric studies using their calibrated model.

Jenck & Dias (2009) used FLAC^{3D} to numerically simulate a three-dimensional unit cell, and a fully three-dimensional piled embankment with lateral slopes in drained conditions. They simulated the soft soil using Cam-clay soft soil model, and the embankment using elastic-perfectly plastic Mohr-Coulomb failure criterion and also an isotropic hardening elastoplastic model. They did not, however, include a geosynthetic reinforcement in their analyses, or consider the effect of consolidation of the soft soil. They assumed a full bond between the piles and the soil with no interface elements which prevented the accurate simulation of positive and negative skin friction along the pile shaft. They argued that the behaviour of the piles close to the centre of the embankment are quite close to a unit cell. Their study was not verified against experimental data as it was part of the French research project, ASIRI (2012), and the experimental data was not yet available.

Bhasi & Rajagopal (2015) used coupled three-dimensional single-column finite element analyses using ABAQUS software to study the impact of the length of the floating piles and compared the skin friction, axial force in the piles, and the arching to the corresponding values in end-bearing piles. They also compared the maximum force generated in the geosynthetic for the different lengths of the piles. They used full three-dimensional simulations to study the overall behaviour of the system. They concluded that the vertical and lateral settlements of the embankment

are significantly affected by the length of the floating piles. Their study revealed that the neutral plane where the negative skin friction turns to positive skin friction moves deeper as the consolidation happens. Furthermore, the maximum axial force at the end of the consolidation in the floating piles increased with the increase in the length of the piles. They also compared their numerical results with predictions of BS 8006 (2010), and found higher loads on piles than the loads calculated using BS 8006 (2010) equations. They proposed changes to the arching coefficient (C_c) recommended by BS 8006 (2010) incorporating the floating pile length and the depth of the neutral plane in the equations.

Jamsawang et al. (2016) used coupled flow-deformation three-dimensional finite element analysis using PLAXIS to simulate a well-instrumented embankment on DCM columns. They compared their numerical results with the field measurements and found a good agreement between the two. They further continued to use their verified numerical model to perform parametric studies. They investigated the efficiency of floating Deep Cement Mixing (DCM) columns, and suggested an improvement depth ratio of 0.7 as a critical value for economical design with floating DCM columns. Their comparison between floating columns, fixed columns where the column tip rests on the stronger layer, and embedded columns where the columns are embedded in the stiff layer revealed that the embedded columns, while achieving the same reduction ratios, had a higher bending capacity, and therefore, more economical.

In addition, in a parametric study, Zhuang & Wang (2015) concluded that the pile spacing has the biggest effect on the maximum geogrid tension compared to other parameters such as embankment height, geogrid stiffness, and compression index of the soft soil. They also compared their results with BS 8006 (2010), EBGEO (2011) and concluded that they both overestimate the tension in the geosynthetic. However, their results were in good agreement with the method proposed by Zhuang et al. (2014). Zhuang & Wang (2015) adopted three methods to simulate the behaviour of biaxial geogrids including the isotropic membrane model, orthotropic membrane model, and the truss element model. They concluded that the same results were achieved using the orthotropic membrane model and the truss element model;

however, the isotropic membrane results were 33% higher compared to the other two methods.

In another study, Zhuang & Wang (2016), using a unit cell finite element analysis in ABAQUS investigated the effect of sub-soil in the GRPS embankments. They also compared their numerical results with the analytical solution proposed by Zhuang et al. (2014) and found a good agreement. They indicated that the carrying of the embankment loads by the geosynthetic layer could result in excessive strains in the geosynthetic and intolerable settlements, and highlighted the importance of considering the sub-soil effect in the design. They concluded that the maximum settlement of the soft soil is more sensitive to pile spacing than the geogrid stiffness.

In this study, full three-dimensional models have been simulated to properly capture the CIC-soil and geosynthetic-soil interactions, while the slope batter effect was also captured. The adopted mechanical analysis is fully coupled with the ground water flow to simulate the pore water pressure dissipation with time during the ground deformation.

A list of the numerical simulations by different researchers along with a brief explanation on their models is provided in Table 2.3.

Table 2.3 Numerical background on columnar ground improvement methods

GI Technique	Reference	Numerical Program	Modelling Approach	Inclusion of GR
Soil-cement columns	Jamsawang et al. (2016)	PLAXIS	3D	No
	Yapage et al. (2014)	ABAQUS	2D	No
	Yapage & Liyanapathirana (2014)	ABAQUS	2D	Yes
	Yapage et al. (2013)	ABAQUS	2D	Yes
	Huang & Han (2010)	FLAC	2D	Yes
	Huang et al. (2009)	FLAC	2D	Yes
	Huang & Han (2009)	FLAC ^{3D}	3D	Yes
Geosynthetic-reinforced column-supported embankments	Yu & Bathurst (2017)	FLAC	2D	Yes
	Yu et al. (2016)	FLAC	2D	Yes

GI Technique	Reference	Numerical Program	Modelling Approach	Inclusion of GR
Geosynthetic-reinforced column-supported embankments	Zhuang & Ellis (2016)	ABAQUS	3D	Yes
	Zhuang & Wang (2016)	ABAQUS	3D	Yes
	Rowe & Liu (2015)	ABAQUS	3D	Yes
	Bhasi & Rajagopal (2015)	ABAQUS	3D	Yes
	Zhuang & Wang (2015)	ABAQUS	3D	Yes
	Ariyaratne et al. (2013)	ABAQUS	2D/3D	Yes
	Zhuang et al. (2012)	ABAQUS	3D	No
	Zhuang et al. (2010)	ABAQUS	2D	Yes
	Le Hello & Villard (2009)	SDEC	3D	Yes
	Jenck & Dias (2009)	FLAC ^{3D}	3D	No

GI Technique	Reference	Numerical Program	Modelling Approach	Inclusion of GR
Geosynthetic-reinforced column-supported embankments	Smith & Filz (2007)	FLAC ^{3D} / FLAC	2D/3D	Yes
	Han & Gabr (2002)	FLAC	2D	Yes
Geosynthetic-encased columns	Khabbazian et al. (2015)	ABAQUS	2D/3D	Yes
	Hosseinpour et al. (2015)	PLAXIS	2D	Yes
Only LTP	Girout et al. (2014)	PLAXIS	2D/3D	Yes
	Jenck et al. (2007)	FLAC	2D	Yes

2.7 Material Models for Plain Concrete Simulation

In order to capture the behaviour of plain concrete under complex multi-axial loading, the use of a sophisticated constitutive model is essential. The first group of the constitutive models for plain concrete consider unequal principal stresses (Willam & Warnke 1974; Ottosen 1977; Kotsovos 1979; Elwi & Murray 1979; Pramono & Willam 1989; Bigoni & Piccolroaz 2004), and could be utilised in true three-dimensional problems in compression and tension. The disadvantage of the first group, however, is the difficulty in calibrating multiple parameters using scarce fully three-dimensional experimental data, and also the complexity of these methods limit their applicability. The second group, on the other hand, consider equal middle and minor principal stresses (Etse & Willam 1994; Xie et al. 1995; Richart et al. 1928; Considère 1902; Ansari & Li 1998). Hoek-Brown model as one of the models in the second group was proposed by Karam & Tabbara (2009) to be used to simulate the behaviour of the actively confined plain concrete. Hoek-Brown model is defined using two parameters, which are easily determined and calibrated using the available experimental data.

Researchers have used linear-elastic models (Rowe & Liu 2015; Nunez et al. 2013), or recommended elastic-perfectly plastic Mohr-Coulomb model (Gniel & Haberfield 2015; Wong & Muttuvel 2012a) to simulate CICs constructed of plain concrete. The advantage of the Hoek-Brown model though is that it is applicable to the columns with the existing damage (Wu & Zhou 2010).

2.8 Summary

The first section presented an introduction on CICs, including the construction process, highlighting the advantages and the drawbacks of the CIC system in comparison with similar ground improvement methods. The potential benefits or disadvantages of the displacement technique used for CIC installation was discussed. This section also provided a summary of load transfer mechanism, and design processes and guidelines for CIC-improved ground. A method was presented to estimate the negative skin friction on the inclusion shaft. Two methods recommended by ASIRI (2012) were also discussed to design a load transfer platform.

The next section gave an account of the experimental works on column-supported embankments. This section consisted of three groups of experiments each studying a different aspect including the following:

i) The stress concentration ratio: the main concern of the available experiments was the stress concentration ratio which is the ratio of the stress on the columns to the stress on the soft soil. It was concluded that SCR is a key factor in the design of column-supported embankments, and the number of studies performed on this parameter indicated the significance of the SCR in design.

ii) The failure modes of the columns: a wide range of studies investigating the failure patterns of the column-supported embankments were presented. Different failure patterns showed the different failure mechanisms forming in the system. Understanding the different failing mechanisms contributes to make a safe and economical design.

iii) Influence of different parameters: the corresponding tests available in the literature focused on parametric studies. These studies also shed more light on the degree of influence of each parameter, and the sensitivity of the design to them which could be very useful for designers

In addition, a brief summary of the load transfer mechanism in raft foundations was given, and the similarities and differences between CIC and raft foundations mechanism were illustrated. An experimental work conducted by Fioravante (2011), highlighted the differences between the inclusions with a granular layer as a load transfer platform, and raft foundations. An interposed layer between the load plate and the piles, which was referred to as non-contact piled rafts, caused a negative skin friction on the upper part of the pile shafts, and therefore, changed the load sharing between the piles and the soil compared to the contact piles.

Furthermore, modelling criteria for a scaled axially loaded pile was explained. It was concluded that similitude in modelling requires selection of model dimensions and stiffness so that $\left(\frac{L}{r_0}\right)\sqrt{\frac{G}{E^*}}$ is identical in model and prototype where E^* is the

Young's modulus for an equivalent solid pile so that $E_*\pi r_0^2 = EA$, in order for the model to present the behaviour of the prototype.

A general background on the numerical simulation of column-supported embankments was presented in the next section, and the popularity of unit cell and two-dimensional simulations was highlighted. Inaccuracies introduced by the simplifications considered in unit cell and two-dimensional models were discussed based on several studies. In the following section, a brief overview of the constitutive models for plain concrete simulation was also presented.

The lack of comprehensive experimental studies on CICs in the literature shows the necessity of further laboratory and physical modelling experiments on this ground improvement method. This could yield a better understanding of load transfer mechanism of the CIC system, and could be used to verify the results from numerical modellings.

This literature review concludes that frictional CICs have not been thoroughly studied in the available literature. The two options of utilising closely-spaced frictional CICs versus widely-spaced socketed CICs for the transition zone design have not been investigated in detail. The basic understanding of stress transfer mechanism in frictional CICs compared to the socketed CICs could provide designers with a better understanding of the CIC behaviour, especially in the transition zone.

This literature review also illustrates the popularity of drained simulation due to the computationally demanding analyses of coupled flow-deformation models. However, a clear comparison between the two modelling approaches is not presented in the available literature.

CHAPTER 3

3 PHYSICAL AND NUMERICAL MODELLING OF GROUND IMPROVEMENT USING CONCRETE INJECTED COLUMNS

3.1 General

Soft clays such as estuarine soils due to low shear strength, low bearing capacity, and high shrinkage ability are prone to excessive settlement under heavy superstructures such as silos, buildings, and embankments. However, when cautious field observations and laboratory tests are combined, ground improvement techniques such as preloading, wick drains, and column inclusions are used to improve these weak soils. Concrete Injected Columns (CICs) are semi-rigid inclusions which try to increase the stiffness of the soil mass, but unlike piles, they are not specifically designed to take the entire load of the structures above. Although part of the load is transferred to the underlying competent layer, the soil-CIC mass behaves as a composite with improved stiffness. Moreover, CICs are constructed from unreinforced concrete and are not designed using the same design criteria as piles (King et al. 2017). The availability of modern equipment with a high torque capacity and static down thrust means that CICs can be installed using a special displacement auger which displaces the soil laterally which renders this technique virtually spoil-free. CICs can be constructed up to 30 m deep using standard piling equipment (Larisch et al. 2014). A granular layer, known as load transfer platform (LTP), consisting of one or more layers of geosynthetic is commonly placed on top of the columns to help transfer the load to columns. Fioravante (2011) showed through centrifuge physical model tests that the a granular layer beneath a raft changes the behaviour of the pile shaft significantly due to the generation of negative skin friction.

Several laboratory scale experimental studies have been carried out on columnar ground improvement methods such as stone columns (Das & Deb 2018; Shahu & Reddy 2011; Deb et al. 2011; Fattah et al. 2010; Ambily & Gandhi 2007; Wood et al. 2000), and deep cement mixing (DCM) (Rashid et al. 2018; Fang & Yin 2007; Kitazume & Maruyama 2007).

Piled embankments have also been studied extensively using laboratory scale models. For instance, Zaeske (2001) and Kempfert et al. (2004)) reported a series of three-dimensional scaled (scales of 1:3 to 1:6) laboratory tests with four piles placed in weak peat, and different thicknesses of reinforced and unreinforced sand fills; strain gauges were used to measure the geosynthetic strains. Chen et al. (2008) carried out two-dimensional experiments on piled embankments to investigate the effect of geosynthetic reinforcement on soil arching, while nineteen 1g scaled tests with scales of 1:3 to 1:5 were reported by van Eekelen et al. (2012a, 2012b) and van Eekelen & Bezuijen (2014). They used a foam cushion to model the soft soil around 4 piles, and placed a 15 to 20 mm layer of sand on top with one or two geosynthetic layers; they also used traditional strain gauges and bicycle gear cable referred to as “strain cables” to measure the strains in the geosynthetic.

Several researchers (Girout et al. 2018; Fagundes et al. 2017; Okyay et al. 2014; Blanc et al. 2014)) used a device called the mobile tray (MT) to investigate the behaviour of the load transfer platform (LTP) in piled embankments; the MT device simulates the compressibility of soft soil through the downward displacement of a tray.

Numerical modelling is also a popular way to study the behaviour of geosynthetic-reinforced column-supported (GRCS) embankments (Zhuang & Wang 2015; 2016; Zhuang & Ellis 2016; Han & Gabr 2002)), some of which have been validated against laboratory data (Girout et al. 2014; Jenck et al. 2009, 2007).

Although field case studies on Concrete Injected Columns (CICs) (King et al. 2017; Briançon & Simon 2012; Fok et al. 2012; Wong & Muttuvel 2012a) provide valuable information on the design and behaviour of CIC-improved ground, they lack the flexibility and control of small-scale physical models. In this study, CIC-improved

soft clay was physically simulated using a group of 7 CICs and a granular fill with a layer of geotextile to simulate the LTP. A distributed load was then applied in stages using a large loading frame and a plate on top of the LTP layer. The test was well instrumented and the pore water pressure, stress on the soil and CICs, as well as strains in the geotextile were measured with time. In addition, three-dimensional fully coupled flow-deformation numerical modelling was carried out using FLAC^{3D} and validated against the laboratory measurements.

3.2 Physical Modelling

3.2.1 Dimensional Analysis and Materials

Considering a CIC-improved ground such as the one illustrated in Figure 3.1, the applied load is transferred through the load transfer platform (LTP) to the CICs. The LTP consists of a granular layer reinforced by a geosynthetic layer to help transfer the load to the CICs and thus reduce the total and differential settlements. The settlements of ground such as this under a certain load will be influenced by the following independent parameters that correspond to the CIC, LTP, soft soil, and geosynthetic characteristics:

CIC parameters:

- CIC length, L (m)
- CIC diameter, D (m)
- CIC spacing, S (m)
- Unit weight of the CIC material, γ_c (kN/m³)
- Elastic modulus of the CIC material, E_c

LTP parameters:

- LTP height, H (m)
- Angle of internal friction for LTP material, ϕ'_{LTP} (°)
- Average size of the LTP granular material, d_{LTP} (m)

- Unit weight of the LTP soil, γ_{LTP} (kN/m³)
- Elastic modulus of the LTP material, E_{LTP} (kPa)

Soft soil parameters:

- Undrained shear strength of the soft soil, c_u (kPa)
- Unit weight of the soft soil, γ_s (kN/m³)
- Elastic modulus of soft soil, E_s (kPa)

Geosynthetic parameters:

- Geosynthetic thickness, t (m)
- Geosynthetic stiffness, J (N/m)
- Geosynthetic strength, T_{ult} (N/m)

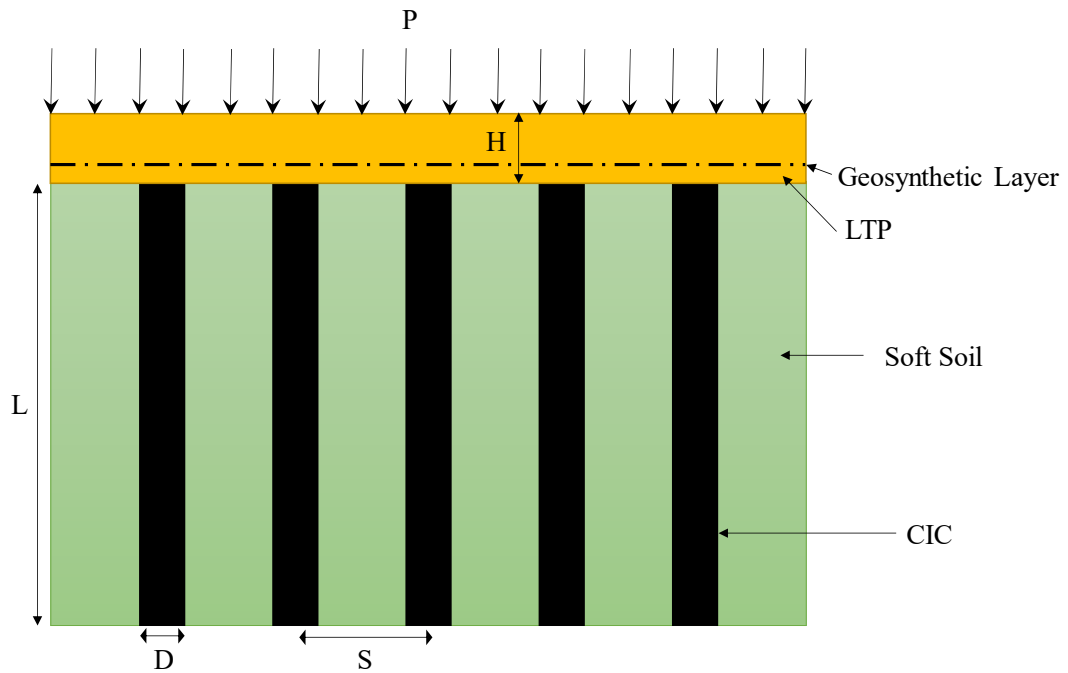


Figure 3.1 The set-up of CIC-improved ground

The ideal condition is where all the dimensions and material properties of the model is scaled by appropriate scaling factors, but it may not be possible to maintain similarity of all parameters in scaled physical models. In this study, however, a

reasonable effort was taken to keep the influencing normalised parameters in realistic ranges. Although every aspect of physical modelling may not be satisfied, considering the typical values for the parameters in the field, many required similarities between the prototype and the model were satisfied in this study; the details of which are discussed below.

A group of dimensionless parameters established using Buckingham's Pi theorem (Buckingham 1914; Butterfield 1999) is presented in Eq. (3.1); it consists of the most influential parameters on the load - settlement response of column-supported grounds:

$$Q_{ult}/c_u = f\left(L/D, Ar, H/S, E_c/E_s, \varphi'_{LTP}, d_{LTP}/S\right) \quad (3.1)$$

where Q_{ult} is the ultimate bearing capacity of the CIC-supported ground. The effect of the spacing of the columns is captured in the area replacement ratio; Ar , which is defined as follows:

$$Ar = \frac{D^2}{nS^2} \quad (3.2)$$

where n is different for different column arrangements, and Ar is calculated for different cases based on the values for S and D . In this study, $Ar = 7\%$ (which corresponds to the prototype CIC diameter of 0.5 m and spacing of 1.67 m) was adopted which is in line with what is used in practice and by other researchers (e.g. Plomteux & Porbaha 2004).

3.2.1.1 CIC

Considering the circular geometry of the cell used for this experiment, the CICs are arranged in a triangular pattern; Figure 3.2 shows the tributary area of every CIC in the triangular pattern using unit cell representation of the CICs by a hexagon surrounding it. Considering an area replacement ratio of 7% in the prototype, and keeping this ratio the same in the model, given that the diameter of the cell for this experiment is $D = 500 \text{ mm}$ (i.e. $A = \pi r^2 = 196349 \text{ mm}^2$); other design details such as the CIC spacing and diameter could be determined based on the circular distribution of the model.

Figure 3.2 also shows that the number of possible hexagonal cells is 7, where their size is determined such that their total area is equal to the circular cross-section of the cell; the spacing (S) of the columns is then specified accordingly. The diameter of the column (D) is calculated based on assuming that the area replacement ratio in the model and the prototype are the same. The diameter of the CIC was determined to be 50 mm for an $Ar = 7\%$. The soft clay in the cell was 480 mm in the cell after the consolidation of the clay slurry was completed, yielding a length to diameter (L/D) ratio of 9.6 ($L = 480\text{mm}$ and $D = 50\text{mm}$) for the CICs.

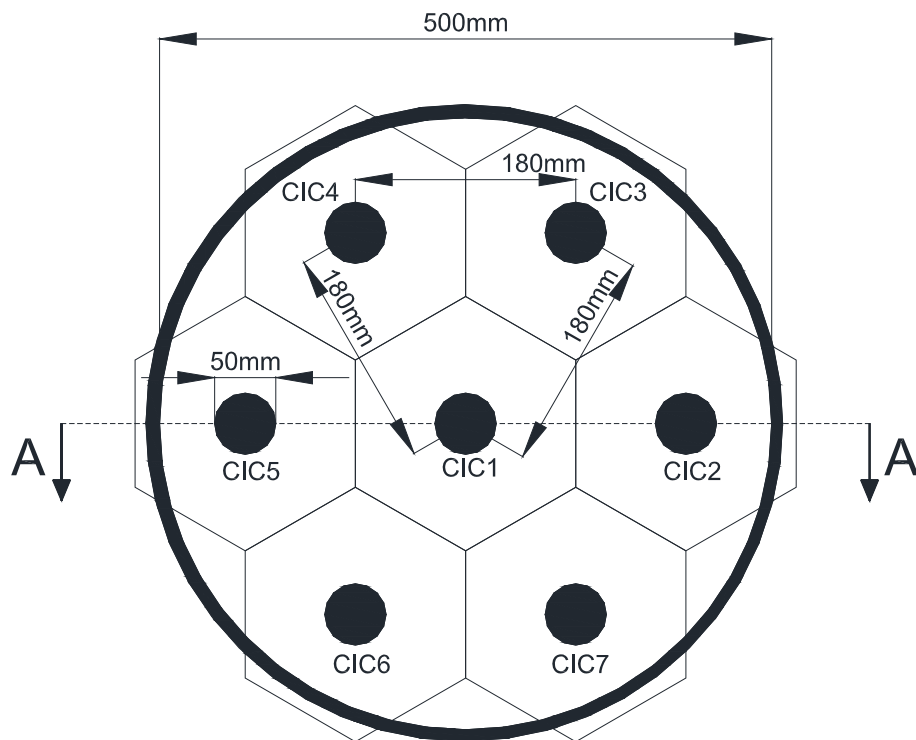


Figure 3.2 CIC arrangement in the consolidation cell showing hexagonal unit cell tributary area

CICs are semi-rigid inclusions constructed using grout, concrete, or a combination of cementitious materials, including waste products such as fly ash and slag (Fok et al. 2012; Wong & Muttuvel 2012c). This cement grout is a lean cementitious mixture (Buschmeier et al. 2012) with a compressive strength of 10–20 MPa (Yee et al. 2012). To enable the model to represent the fundamental behaviour of the prototype, the E_c/E_s

ratio for the model must be kept in the typical range for prototypes. As Yee et al. (2012) reported, in field conditions (i.e. prototype), the ratio of stiffness of soil to CIC material is typically 1:1,000 to 1:10,000.

A concrete mix for the CIC was designed by following the usual mixes for their construction; however, the maximum size of the aggregates used in the prototype were scaled down to enable failure mechanisms to form in the scaled laboratory model. The specifications of this mix were similar to the concrete used for CIC construction, in that its strength was based on the strength of 20 MPa and a slump of 200 mm, and contained 50% fly ash, following the usual specifications of the concrete used for CIC construction and a superplasticizer similar to that used on site was used to increase the workability of the mix. The maximum aggregate size of 6.7 mm was used considering the size of the CIC in the experiment. Table 3.1 presents the detailed concrete mix design used in this study.

Table 3.1 Concrete mix design for CIC construction for one cubic meter

Material	Content
GP Cement (kg)	174
Fly Ash (kg)	174
6.7mm Aggregate (SSD) (kg)	989
Coarse Sand (SSD) (kg) (0.075mm - 4.75mm)	566
Fine Sand (SSD) (kg) (0.075mm - 0.6mm)	243
Water (kg)	163
High Range Water Reducing Admixture (Grace) (ml)	1630
Water to Binder Ratio (kg)	0.468
Slump (mm)	210

Three cylindrical samples were cured for 28 days and then tested to measure the compressive strength according to Australian Standard AS 1012.9 (2014); the average unconfined compressive strength of 21 MPa was measured for the adopted concrete.

3.2.1.2 LTP

Considering the LTP height to be 0.75 m to 1 m in the prototype scale, and with a scale factor of $N=10$ for this test, the granular layer LTP layer was 80 mm thick. Since the behaviour of the models would involve the formation of bands of localised deformation in granular material, they would be strongly influenced by the ratio of particle size to the typical dimension of the problem (Stone & Wood 1992; Bolton & Lau 1988), so the size of the aggregates to be used for LTP had to be scaled down. Assuming a maximum particle size for the LTP material to be 50 mm in the prototype, a granular layer with a maximum size of 4.75 mm was used to model the LTP layer. Granular material that passed through a 4.75 mm sieve and was retained on the 2.36 mm sieve was used to prepare the LTP material. The minimum and maximum dry densities for this aggregate were 12.8 kN/m^3 and 13.8 kN/m^3 , respectively, according to ASTM D4253-16 (2016). The surface of soft clay was levelled and then a layer of filter paper was used to separate it from the granular material. The granular material was weighed and placed manually in layers in the cell. The granular layer was then vibrated using a small-scale handheld vibrator to achieve a relative density of 98%. To avoid damaging the geotextile layer due to the concentration of stresses at the corners of the CICs, the geotextile layer was not placed directly above the CICs as recommended by EBGeo (2010), and was positioned in the middle of the LTP layer (i.e. 40 mm below the LTP surface; note that the entire LTP was 80 mm thick). The angle of internal friction and the angle of dilation for the material used in the LTP were determined by direct shear test according to Australian Standard AS 1289.6.2.2. (1998), and are reported in Table 3.4.

3.2.1.3 Geosynthetic

Unlike soils, in studies of reinforced soils, identical products in a scaled model and a prototype cannot be used, so geosynthetic materials must be scaled in 1g

and Ng small-scale physical modelling to simulate a correct response of the soil - structure system. In this study, a geotextile layer was used to simulate the geosynthetic behaviour, and tensile strength and the thickness of the geotextile material had to be simulated (Viswanadham & König 2004). The scaling laws for modelling geosynthetics have been discussed in detail by several other researchers (Kuwano & Izawa 2010; Viswanadham & König 2004; Mahajan & Viswanadham 2007; Zornberg et al. 1997). The load applied onto the deposit of CIC-improved clay was simulated in this experiment by using surface loading. By assuming the same stress level in the model and prototype, the scaling law could be derived using a scaling factor of one for stress and strain in the reinforcement ($\alpha_\sigma = 1$ for stress and $\alpha_\epsilon = 1$ for strain). The tensile strength in the geosynthetic reinforcement, however, is defined in unit tension, T_{Ult} , and not force per unit area, σ_{Ult} , as in Eq. (3.3):

$$T_{Ult} = \sigma_{Ult} \cdot t \quad (3.3)$$

where t denotes the thickness of the planar reinforcement and is related to the confining pressure. By considering the scaling factors for σ_{Ult} and t , the scaling factor for the tensile strength is as obtained below:

$$\alpha_T = \alpha_\sigma \cdot \alpha_L = 1 \cdot \frac{1}{N} = \frac{1}{N} \quad (3.4)$$

The stiffness of the planar reinforcement is also presented by a stiffness parameter J [F/L] instead of considering conventional Young's Modulus E [F/L^2], and is defined as:

$$J = E \cdot t \quad (3.5)$$

this implies the following scaling relationship:

$$\alpha_J = \alpha_\sigma \cdot \alpha_L = 1 \cdot \frac{1}{N} = \frac{1}{N} \quad (3.6)$$

If the mechanical properties of the geotextile are proportional to its mass, the tensile strength and stiffness requirements of a geotextile model could be satisfied using the same prototype geotextile material with a thickness N times smaller, or by using the same prototype geotextile material with a mass per unit area N times smaller (Zornberg et al. 1997).

By adopting a scale factor of $\frac{1}{N}$ for the stiffness and strength of the geotextile, and by considering the dimensional analysis provided, a woven geotextile with the properties provided in Table 3.6 was used. A woven biaxial Polypropylene geotextile with the same strength in both directions was chosen considering the symmetry of the test.

In practice, the friction mobilised along the layer of geotextile reinforcement prevents pull-out; however, it can happen easily in laboratory models since the scaled model is not long enough, so there is not enough friction generated along the geotextile layer to prevent slippage. To simulate boundary conditions, a timber ring was designed to restrain the geotextile radially and prevent pull-out. Two timber washers were placed and screwed on top of each other with a layer of geotextile between them; these washers were 498mm in diameter (2 mm smaller than the diameter of the cell) and could move easily up and down, but not side-ways. Special 3M structural epoxy adhesive was applied between the top and bottom timber washers and the geotextile, and then the screws were tightened to hold the layer of geotextile in place. The outside diameter of the top timber washer was 2 mm smaller than the bottom timber washer so that the geotextile could be wrapped around and glued onto it using the epoxy adhesive to strengthen the bond. Simulating the boundary condition was an extremely important step since any slippage of the geotextile layer would result in erroneous tensile stresses. The timber washers were then coated with marine varnish to protect them from the wet conditions inside the cell. The timber washers also enabled the wires from the sensors positioned under the geotextile to exit through the holes created in them without perforating the geotextile layer.

3.2.1.4 Soil mix

The soft soil was simulated using a UTS recipe that contains Q38 kaolinite, Active Bond 23 bentonite, and uniformly graded fine sand (KBS) (Le et al. 2015; Le 2015). Table 3.2 presents the composition of the KBS mix, while Table 3.3 summarises the Atterberg limits for the mix.

Table 3.2 Composition of the soil mix used in this study

Material	Q38 Kaolinite (%)	ActiveBond 23 Bentonite (%)	Fine sand (%)
Percentage	70	15	15

After dry mixing the kaolinite (70%), bentonite (15%), and fine sand (15%), water was added to the mix at a water content of 1.2 times the liquid limit (i.e. water content of 96%) to ensure complete saturation. The mix was then stored in an airtight container for a week to ensure complete saturation and uniformity. The slurry was then placed in layers in the large consolidometer and preconsolidated under a 20 kPa surcharge for 200 days to consolidate and prepare the deposit of soft clay. Using a hand held shear vane, the average shear strength of the clay deposit after preconsolidation was determined to be 4 kPa.

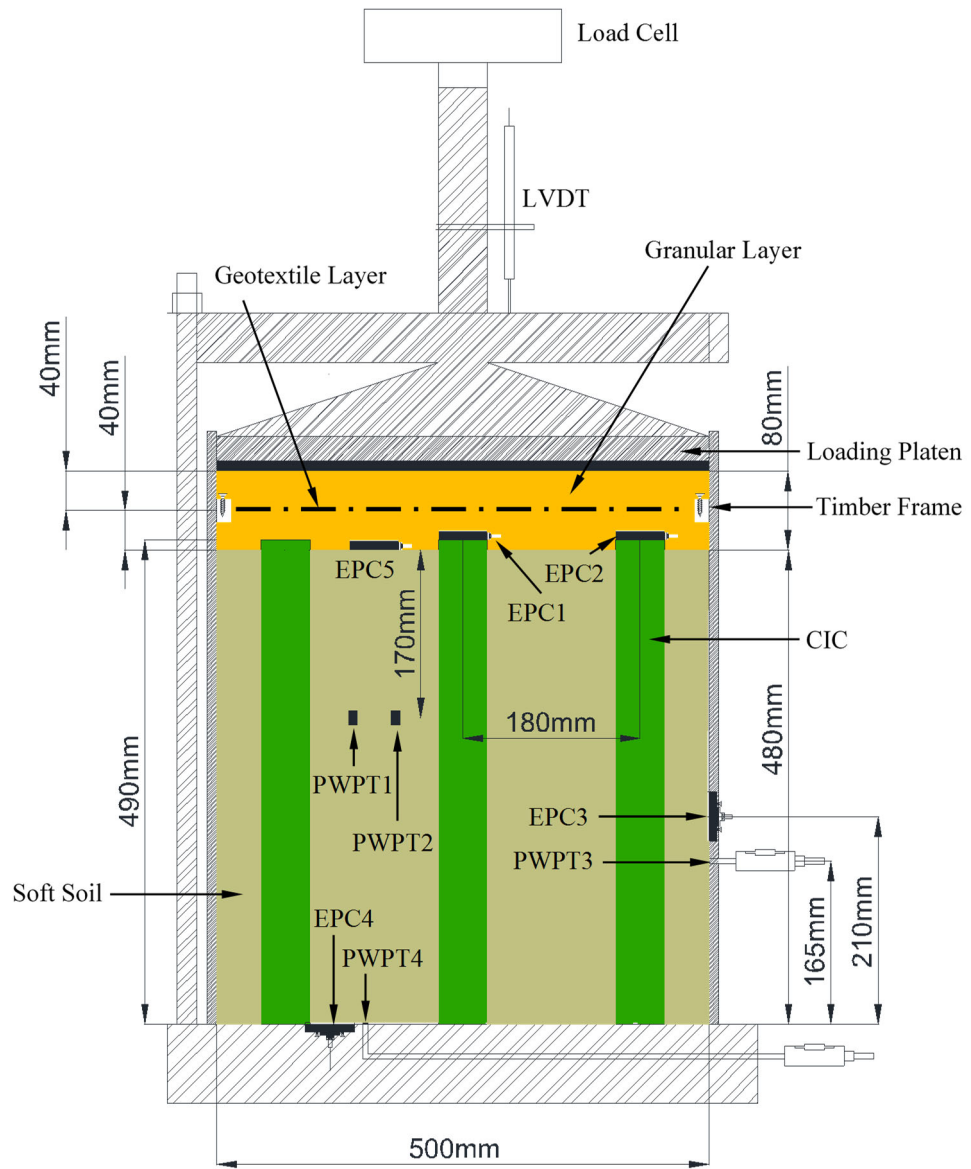
Table 3.3 Properties of the soil mix used in this study

Parameter	Value
Water Content, w (%)	96
Liquid Limit, LL (%)	80
Plastic Limit, PL (%)	22
Plasticity Index, PI (%)	58

3.2.2 Test set-up

3.2.2.1 Instrumentation

Figure 3.3 is a schematic diagram of the experiment that shows the positions of the instruments used.



(a)

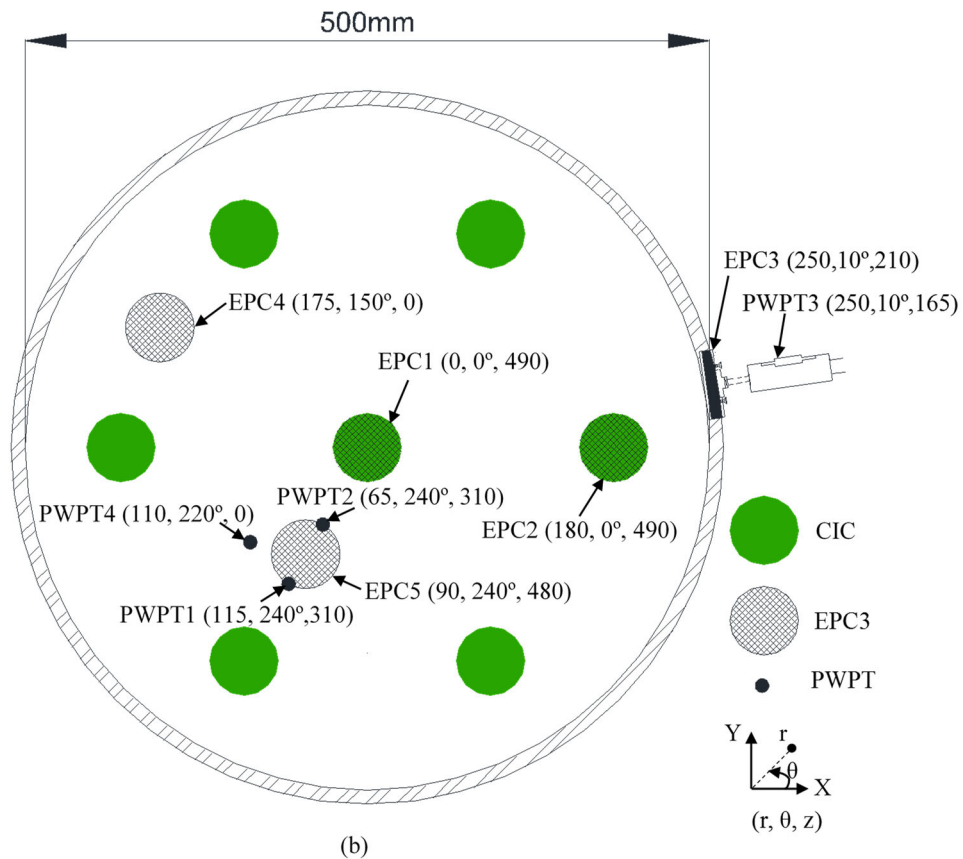
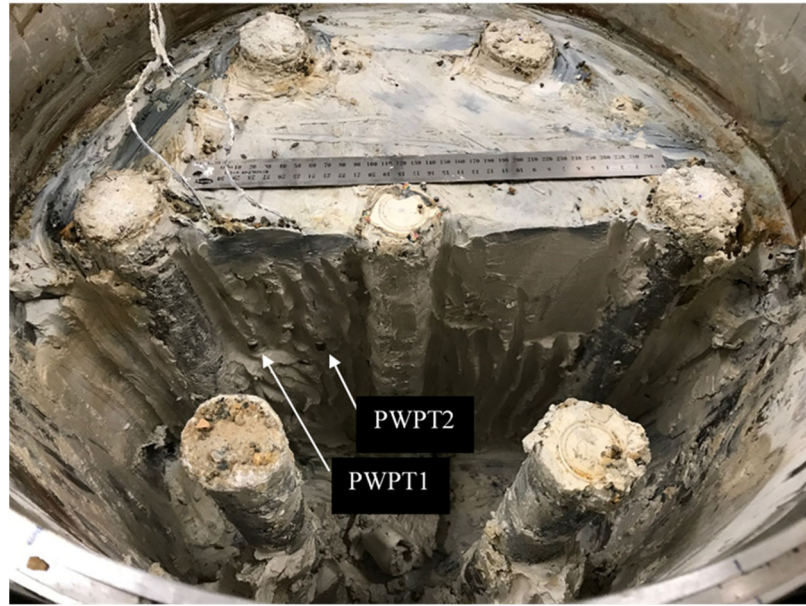


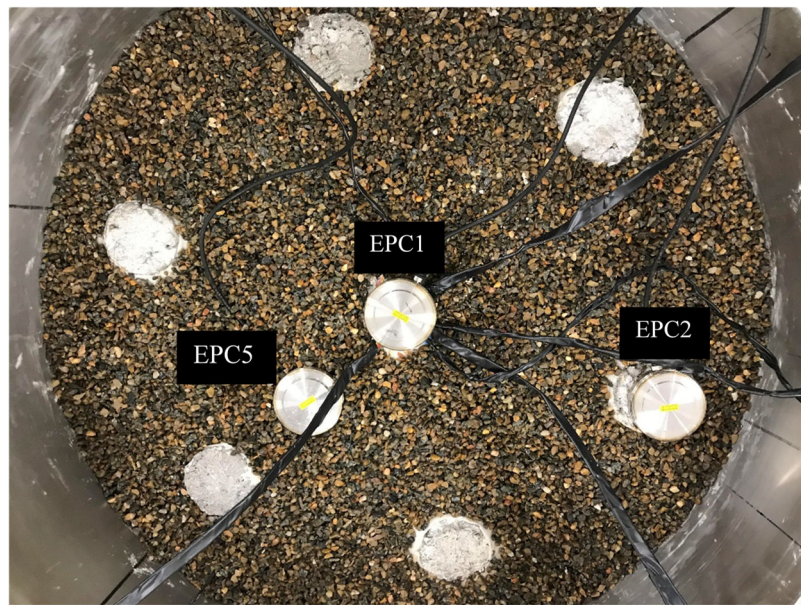
Figure 3.3 Schematic diagram of the physical model and instrument locations (in mm) (a) cross-section view and (b) plan view (Note: cylindrical coordinates in brackets; first number shows the radial distance (mm), second number is the azimuth or angular coordinate, and the third number is the distance from the bottom of the cell (mm))

The test was carried out in a large, 500mm diameter by 600mm high consolidometer equipped with 2 PWPTs, at the bottom of the cell and another fixed externally on the wall (Figure 3.3). In addition, two in-soil PWPTs were used to monitor the pore water pressure away from the model boundaries and between the installed columns. The two in-soil PWPTs were inserted into the soft clay after the preconsolidation process was completed. These PWPTs were also exhumed after the test was completed with only vertical displacement consistent with the soil settlements. This consolidometer is also equipped with 50mm diameter Earth Pressure Cells (EPCs) or soil pressure gauges to measure the total stress at different locations in the cell. One KDF-PA 200 kPa pressure sensor was installed on the wall, adjacent to the PWPT to measure horizontal

stress, and also determine the effective stress. In addition, a KDF-PA 500 kPa pressure sensor was positioned at the base of the model and 175 mm from the centre of the cell to measure the vertical stress in the soft soil. Considerable effort was taken to waterproof the cell with the sensors in place and to exit the sensor wires using O-rings to seal the sensors and to prevent any leakage. All the sensors were connected to data loggers and computers to log the data using the data acquisition software. Figure 3.5 is a schematic diagram of the test setup for this experiment. Referring to Figure 3.3, two other KDE-PA 2 MPa pressure sensors were placed on top of the CICs, and one KDE-PA 200 kPa sensor was placed on the surface of the soft soil at the mid-span between the two CICs, to measure any variations of stress on the soil and CICs, and to determine the stress concentration ratio during consolidation. Figure 3.4 shows the installed CICs with sensors positioned on top of the columns and the soft soil while the LTP was being constructed. An in-built load cell on the loading frame controlled the load applied to the sample. As Figure 3.3 (a) shows, an LVDT, in addition to the in-built frame positioning system was used to measure the settlement of the CIC composite ground.

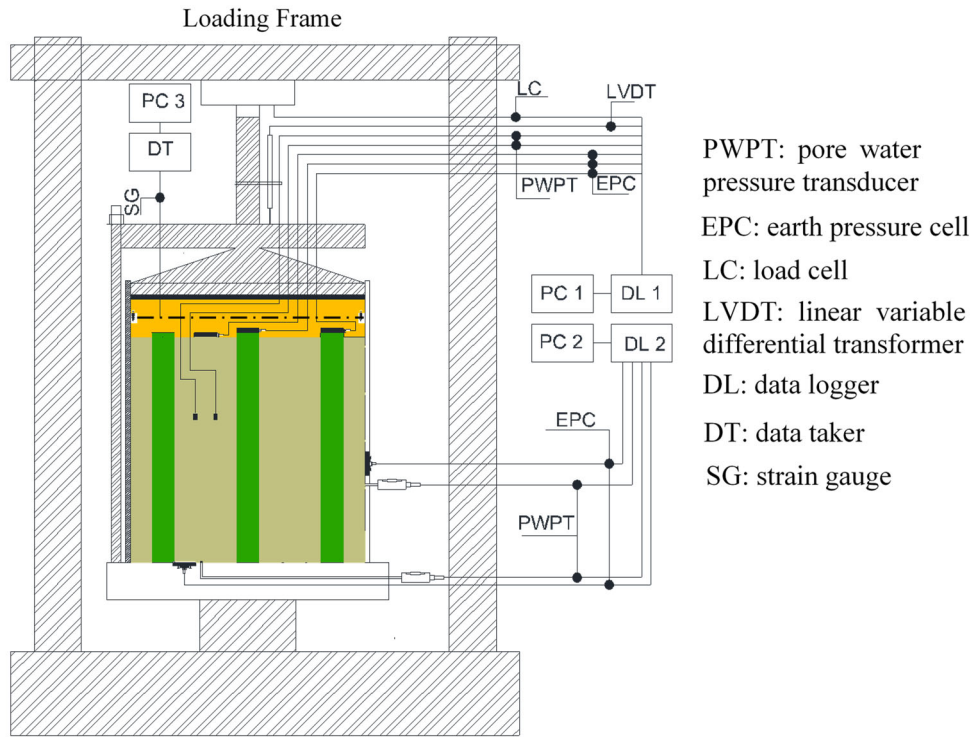


(a)

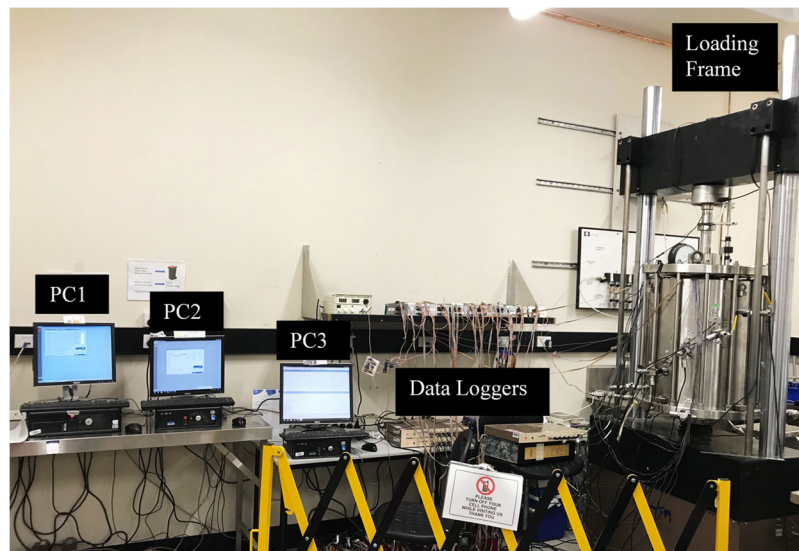


(b)

Figure 3.4 (a) Three-dimensional view of the CICs with the clay excavated after the test completion and (b) Plan view of the position of EPCs on the CICs and soft soil



(a)



(b)

Figure 3.5 Schematic diagram of the large consolidometer set-up

Strain gauges are usually used to measure strains on stiff materials such as metals, whereas strain gauges used on flexible materials such as geotextiles and geogrids pose several challenges. Springman et al. (1992) and Sharma & Bolton (1996) introduced a method of instrumenting woven geotextiles with strain gauges, and also carried out a centrifuge test on an instrumented model geogrid using a similar technique. In this study, the geosynthetic layer was instrumented using strain gauges similar to Viswanadham & König (2004). Special TML Cu-Ni alloy foil strain gauges with a nominal resistance of 120 Ω and a gauge factor of 2.1 designed for use on materials with low elastic modulus were used to measure the strains of the geotextile layer in a quarter bridge configuration. A layer of epoxy was applied onto the geotextile to provide an even base to attach the strain gauges, as shown in Figure 3.6. A small, 25 mm by 25 mm square base was formed in order to minimise the effect of this layer on the material properties. The intended area was framed and separated using masking tape. A very small amount of epoxy was spread evenly across the square, a thin polyethylene sheet was placed over it and the excess epoxy was squeezed out applying even pressure to form a layer as thin as possible. The thin epoxy layer was then left for a day to cure at room temperature. This method created a very smooth surface for the gauges which were then attached using Cyanoacrylate adhesive on the epoxy base on two opposite sides.

Figure 3.6 shows the locations and orientations of the strain gauges on the instrumented geotextile. Several trials were carried out to evaluate their performance, during which the strains due to bending were significant and had to be eliminated. The strain gauges were wired up in series to give an average of the two values; this effectively eliminated the bending effects. These measurements were only due to tensile stress in the fabric, and were not sensitive to bending. However, using single gauges in a quarter bridge configuration allows the condition of each gauge to be known separately, particularly if there is any damage under the soil. This is why individual strain gauges were used in quarter bridge configuration and the values from

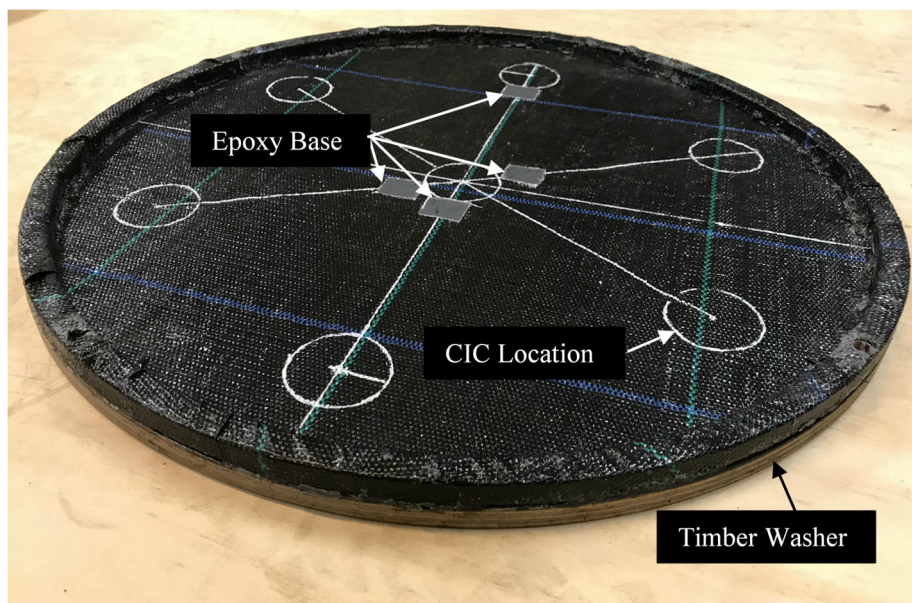
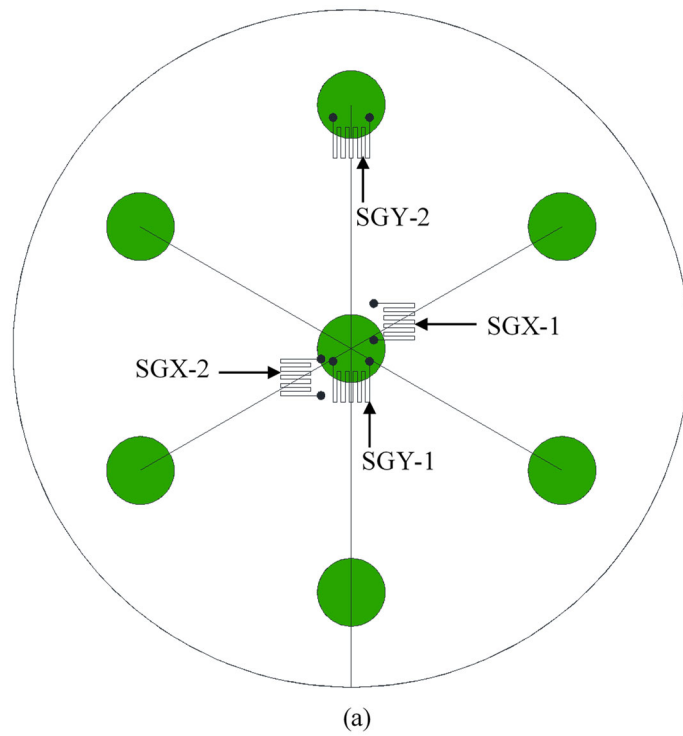


Figure 3.6 (a) Locations and orientations of strain gauges on the geotextile layer (Note: SGX: strain gauge in X direction; SGY: strain gauge in Y direction) and (b) Geotextile harnessed using two timber washers and epoxy glue

both sides of the fabric were averaged to ascertain tensile stress in the fabric by cancelling the strains from bending. Butyl rubber (SB) tape was used to water proof the gauges and then further tests were carried out to determine whether the water-

proofing material would affect specimen performance; it was concluded that water proofing had no effect on the tensile or flexural behaviour of the material. SB tape also provided a degree of physical protection for the gauges buried under the granular material. This water proofing procedure was also tested to check for any electrical leakage.

3.2.2.2 Test procedures

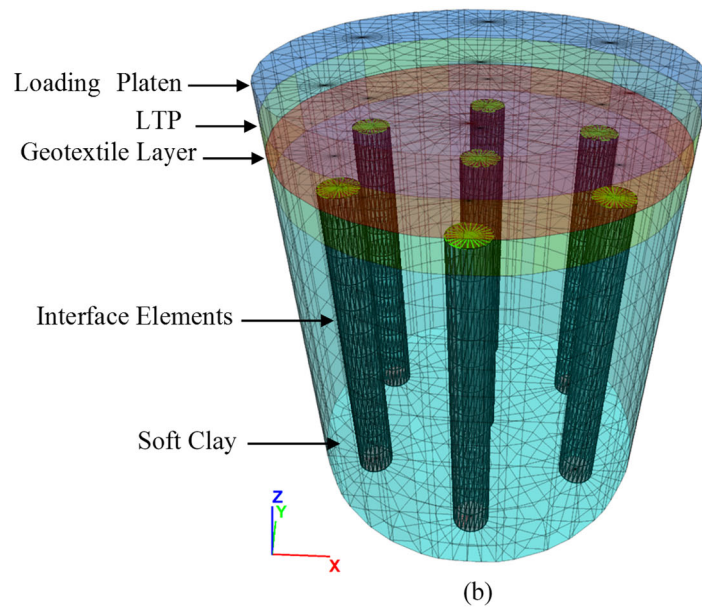
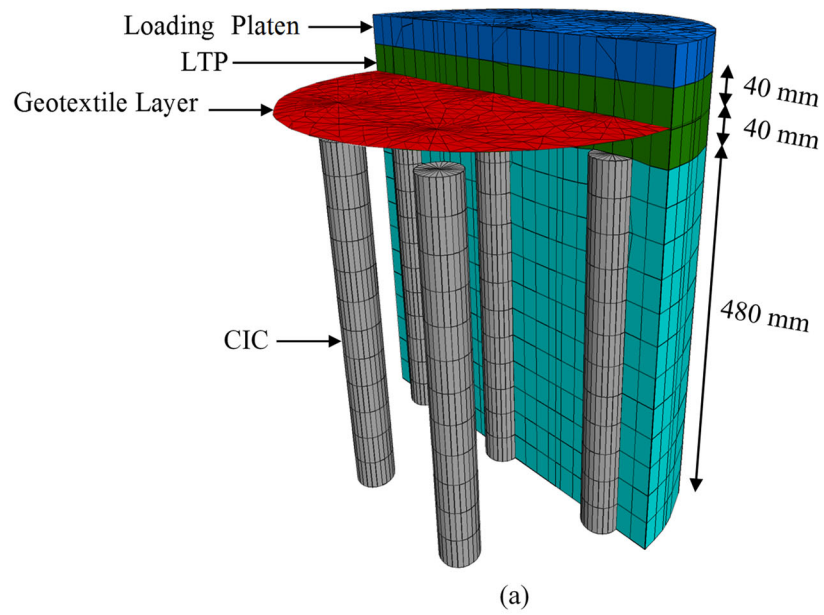
Fresh concrete was poured in stages into the hollow pipe pushed by an actuator with a constant penetration rate into the soft soil preconsolidated in the large consolidometer. A small-scale vibrator was then used to compact the concrete and help to release any entrapped air. The actuator was also used to retract the pipe after each concrete pour. The casting procedure commenced with the middle CIC and continued with the side CICs until all the CICs were cast. The system was then loaded after the CICs had gained their full strength at 28 days.

A load was applied onto this improved ground in stages using a rigid plate on the LTP layer. The frame could sustain a constant load on the large consolidometer using the internal load cell and testing software. A porous disk was placed on the granular layer to allow the model to drain from the top, and a loading platen was used to apply the load onto the brass porous disk. A 10 kPa load was applied onto the CIC-improved sample and was sustained for two days before proceeding to the next stage. The applied stress was increased to 20 kPa for another two weeks. The stress was then doubled to 40 kPa and held for three weeks, and increased again to 80 kPa for another 19 days, when the stress on the soil and CICs had stabilised. Further photographs from the experiment are provided in Appendix A.

3.3 Three-Dimensional Numerical Simulation

FLAC^{3D} finite difference software was used for the numerical simulation in this study since it has proven to be successful in many other studies (Das & Deb 2018; Jenck & Dias 2009; Smith & Filz 2007)) that investigated columnar ground improvement methods.

Zone generation in this numerical model involved connecting basic mesh shapes to form a complete model with the desired geometry. The model geometry was constructed using a radially graded mesh of 'radcylinder' to create the meshes for the hexagonal tributary area around the CICs, and then a subroutine code was developed to create cell geometry that would suit the CIC arrangement. Figure 3.7 shows the model geometry and the zoning in three dimensions and in cross-section.



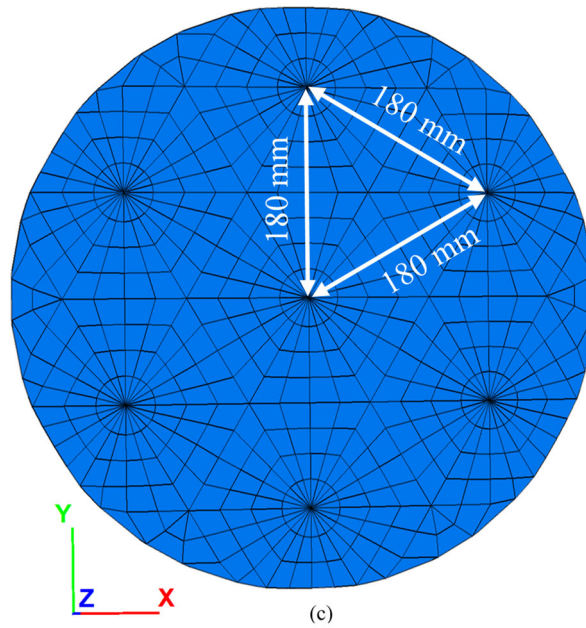


Figure 3.7 Model geometry and zoning (a) elevation view, (b) 3D view and (c) cross section view

The boundary conditions stopped the soil from moving perpendicular to the cylindrical surface, thus simulating the real boundary of the steel cell wall, while the soil could move freely up and down. The model base, however, was restrained in the vertical direction since it is a rigid surface, as shown in Figure 3.8. The numerical modelling captured the fully coupled flow-deformation and predictions of the pore pressure changes were monitored during each loading stage at specific locations. The ground water level was considered to be at the clay surface, while the soft soil would remain fully saturated during the analysis. The cylindrical and bottom boundaries of the model were simulated as impervious and the model was allowed to drain from the top in accordance with the laboratory experiment arranged and shown in Figure 3.8.

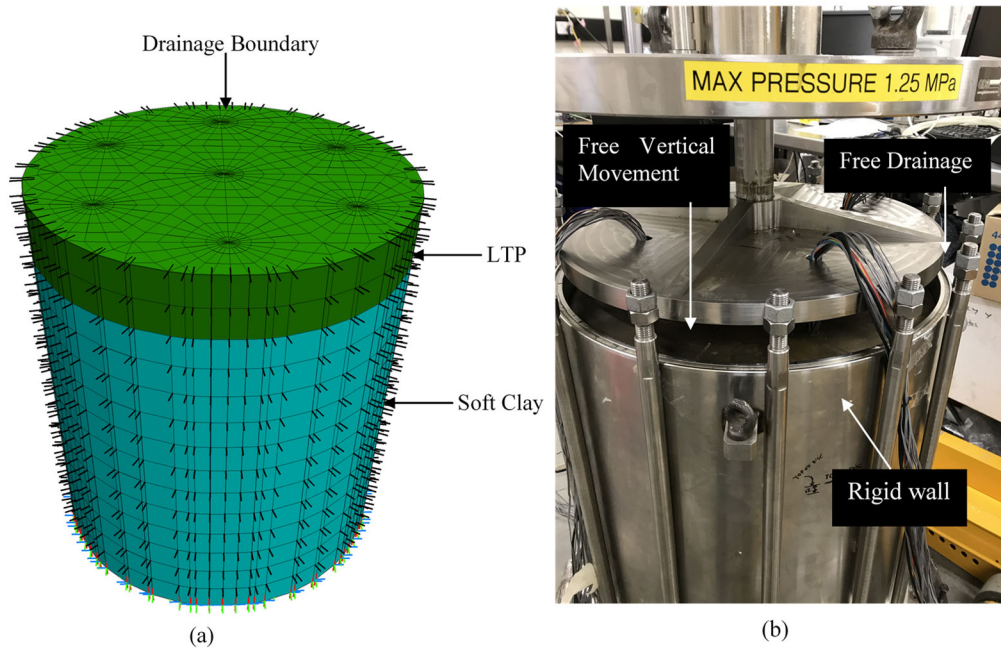


Figure 3.8 Boundary conditions in (a) the numerical simulation and (b) the experiment

3.3.1 Clay Deposit Properties

Soft clay was simulated by the Modified Cam-clay (MCC) (Roscoe & Burland 1968) constitutive model. The properties of the KBS (Kaolinite-Bentonite-Sand; UTS recipe) soil were calculated based on the results of Rowe cell consolidation tests reported by Le et al. (2015) and Le (2015). The granular layer used for the LTP was simulated using linear elastic-perfectly plastic Mohr-Coulomb model; the properties of the KBS soft soil and the LTP material in the numerical model are presented in Table 3.4.

Variations in the permeability of the clay deposit were changed during consolidation process according to Eq. (4.1) (Taylor 1948) using a subroutine developed in FLAC^{3D}:

$$\log k = \log k_i - \frac{e_0 - e}{C_k} \quad (3.7)$$

where k_i is the reference permeability at the reference void ratio, e_0 , and C_k is the slope of the $\log k$ - e graph. C_k was 1.03 for KBS in this study, by referring to Le et al. (2015).

Table 3.4 Properties adopted in the numerical simulation

Parameters	Soft Soil*	LTP
Material model	MCC	MC
Depth (mm)	480	80
Dry unit weight, γ_{dry} (kN/m ³)	10.4	13.5
Critical state stress ratio, M	1.1	-
Normalised compression index, λ/v	0.1237	-
Normalised swelling index, κ/v	0.0184	-
Initial void ratio, e_0	2.8	0.5
Preconsolidation pressure, p'_c (kPa)	20	-
Permeability, k (m/sec)	8×10^{-9}	-
Young's Modulus, E (MPa)	-	10
Poisson's Ratio, ν	0.3	0.3
Effective cohesion, c' (kPa)	0	0
Dilation angle, Ψ (degrees)	0	4°
Effective friction angle, ϕ' (degrees)	27°	35°

* Parameter values for the soft soil were calculated based on the test results reported by Le et al. (2015)

Figure 3.9 shows the linear variation of permeability in log scale with the void ratio, adopted in this study.

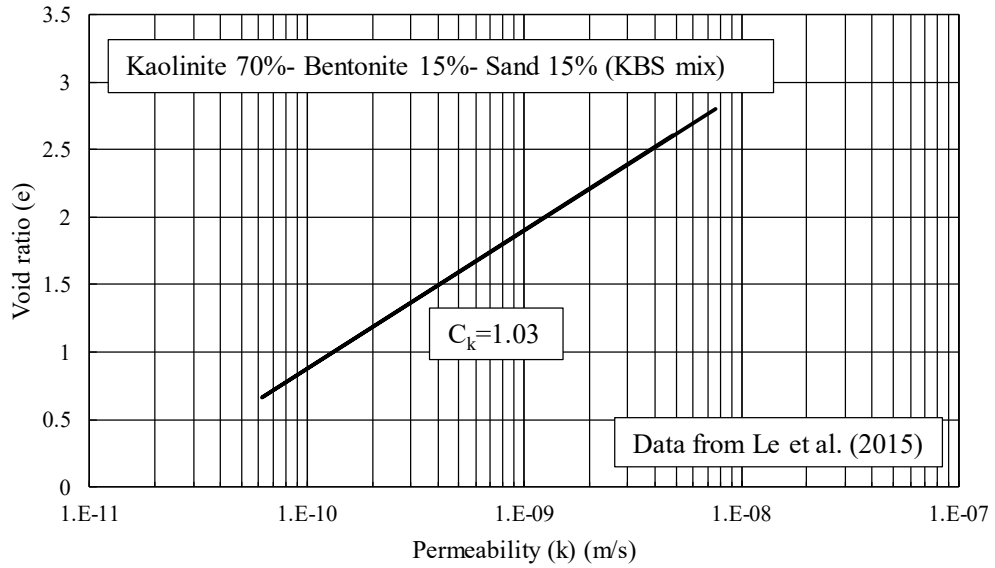


Figure 3.9 Permeability variation versus void ratio

3.3.2 CIC Simulation

CICs are constructed from plain concrete with no reinforcement. The triaxial strength of concrete can be described by the Hoek-Brown (Hoek & Brown 1980) model, which is an extension of the model proposed by Leon (1935); it is an accepted and widely used model in rock mechanics (Pramono & Willam 1989). The Hoek-Brown failure criterion is a combined two-parameter Mohr-coulomb law with a one-parameter Rankine tension cut-off (Etse & Willam 1994) that can be presented in the form of Eq. (4.5) (Hoek et al. 2002; Hoek & Brown 1980):

$$\frac{\sigma_1}{\sigma_c} = \frac{\sigma_3}{\sigma_c} + \sqrt{m \frac{\sigma_3}{\sigma_c} + s} \quad (3.8)$$

where σ_1 is the major principal effective stress at failure, σ_3 is the minor principal effective stresses at failure, σ_c is the uniaxial compressive strength for the intact rock material, and m and s are constants which are determined experimentally. It should be noted that $s=1$ for the intact rock, and when $\sigma_1 = 0$, σ_3 equals the tensile strength of the rock mass, and Eq. (4.5) can be rewritten as:

$$\sigma_t = \sigma_3 = \frac{\sigma_c}{2}(m - \sqrt{m^2 + 4s}) \quad (3.9)$$

Different values of m for different types of concrete can be determined using Eq. (3.10) when the tensile and compressive strengths are known (Wu & Zhou 2010):

$$\frac{\sigma_t}{\sigma_c} = \frac{1}{2}(m - \sqrt{m^2 + 4s}) \quad (3.10)$$

When $\sigma_3 = 0$ in Eq. (4.5), the uniaxial strength of the rock mass can be calculated as follows:

$$\sigma_{CS} = \sigma_1 = \sigma_c \sqrt{s} \quad (3.11)$$

In this study, uniaxial strength of 21 MPa corresponding to $f'_c = 20$ MPa, $m=12$ and $s=1$ were adopted following the values proposed by Karam & Tabbara (2009) for actively confined concrete. Their proposal is based on an exhaustive study of the collection of published data from 1928 to 2009.

The CIC concrete had an average cylinder compressive strength of 21 MPa, while the elastic modulus was determined to be 22 GPa at 28 days using Eq. (3.12), and in accordance with Australian Standard AS 3600 (2009):

$$E_c = (\rho)^{1.5} \times (0.043\sqrt{f_{cmi}}) \quad (3.12)$$

where ρ is the density of the concrete, and f_{cmi} is the mean value of the in situ compressive strength and was taken as 90% of the mean value of the cylinder strength, as recommended by Australian Standard AS 3600 (2009).

Australian Standard AS 3600 (2009) was also used to determine the tensile strength of the concrete at 28 days:

$$f'_{ct} = 0.36\sqrt{f'_c} \quad (3.13)$$

where f'_{ct} is the characteristic uniaxial tensile strength of concrete, and f'_c is the characteristic compressive (cylinder) strength of concrete at 28 days and standard curing. The concrete used in this study had a $f'_c = 20$ MPa, so its tensile strength was determined as $f'_{ct} = 1.6$ MPa, by following Eq. (3.13). Table 3.5 summarises the properties of the CIC adopted in the numerical simulation.

Table 3.5 Proprieties adopted for CIC simulation

Parameter	CIC
Material model	Hoek-Brown
Unit weight, γ_c (kN/m ³)	24
Young's Modulus, E_c (MPa)	22,000
Poisson's ratio, ν_c	0.2
Uniaxial strength of the concrete, σ_{cS} (MPa)	20
Uniaxial tensile strength of concrete, f'_{ct} (kPa)	1600
Hoek-Brown constant, m	12
Hoek-Brown constant, s	1
Interface normal stiffness, k_n (N/m ³)	2.38×10^8
Interface shear stiffness, k_s (N/m ³)	2.38×10^8
Interface interaction coefficient, R_c	0.8

3.3.3 Interface Elements

Interface elements capable of modelling slipping and separation were implemented in this model. The normal and shear stiffness values (k_n and k_s , respectively) were calculated as recommended by Itasca (2012) and are based on Eq. (3.14):

$$k_n = k_s = 10 * \text{Max} \left[\frac{\left(K + \frac{4}{3} G \right)}{\Delta z_{min}} \right] \quad (3.14)$$

where K and G are the bulk and shear moduli, respectively; and Δz_{min} is the smallest width of an adjoining zone in the normal direction. Since the CIC material on one side

of the interface is much stiffer than the soft soil on the other side, the properties of the soft soil were used in Eq. (3.14) to obtain the interface parameters whose adopted values are $k_n = k_s = 238 \frac{MPa}{m}$. A reduction factor of $R_c=0.8$ was considered for the interface strength properties (see Table 3.5).

3.3.4 Geotextile Layer

The geogridSEL element available in FLAC^{3D} was utilised to simulate the geotextile layer. Table 3.6 summarises the properties of the geotextile adopted in this study which are reported by the manufacturer according to Australian Standard AS 3706.2 (2012). A single layer of biaxial geotextile with an ultimate strength of $T_{ult} = 16 \text{ kN/m}$ and a stiffness of $J = 200 \text{ kN/m}$ for 2% strain in both directions was modelled in the middle of the granular layer to simulate the behaviour of LTP.

*Table 3.6 Adopted geotextile properties in the numerical simulation**

Parameter	Tensile stiffness, J (kN/m) for 2% strain	Tensile strength T_{Ult} (kN/m)	Poisson's Ratio, ν	Coefficient for interface strength reduction, R_G
Geotextile	200	16	0.3	0.8

* Parameters reported by the manufacturer based on Australian Standard AS 3706.2 (2012)

The geogridSEL elements only resist membrane loads and have no bending resistance; they are rigidly attached to the model grid in the normal direction and to a spring slider in the tangent plane to the geogrid surface in order to simulate frictional interaction with the model grid. The frictional geogridSEL-soil interface is defined by cohesion, the friction angle, and the stiffness per unit area for the coupling springs. The shear stress and maximum shear strength are defined by Eqs. (3.16) and (3.15), respectively:

$$|\tau| = k|u_s| \quad (3.15)$$

$$\tau_{max} = c + \sigma_m \tan \varphi \quad (3.16)$$

where c is the cohesive strength, φ is the friction angle, σ_m is the effective confining stress acting perpendicular to the geogrid surface, k is the stiffness per unit area for coupling springs, and u_s is the relative shear displacement between the geogrid element and the model zones.

A reduction factor of $R_G=0.8$ was assumed for the strength properties of the interface between the geotextile and granular layer (Huang & Han 2009).

The membrane effect of the geotextile was captured by the large strain analysis mode. In large strain mode, the geogridSEL elements are updated (Smith & Filz 2007) and the membrane effect of the geotextile helps transfer the loads to the CICs. The large strain mode has a significant impact on the tensile forces generated due to differential settlements in the three-dimensional model. Yu et al. (2016) and Yu & Bathurst (2017) also highlighted the importance of using large strain analysis mode when simulating geosynthetics in two dimensions.

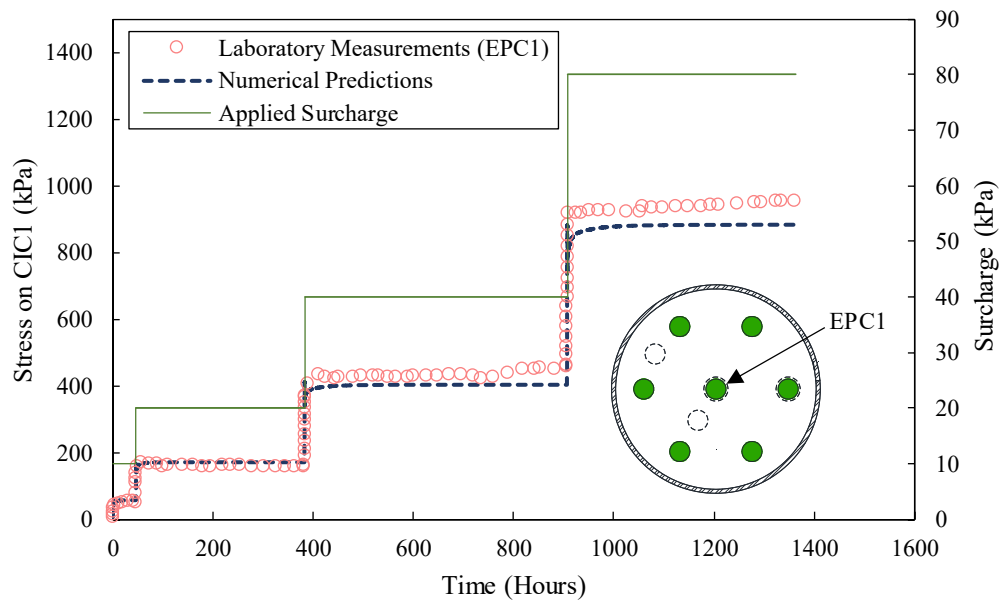
3.4 Results and Discussion

The results of this experiment are reported in the following sections, and the numerical results are compared against the experimental results to verify the numerical model and help interpret the laboratory observations.

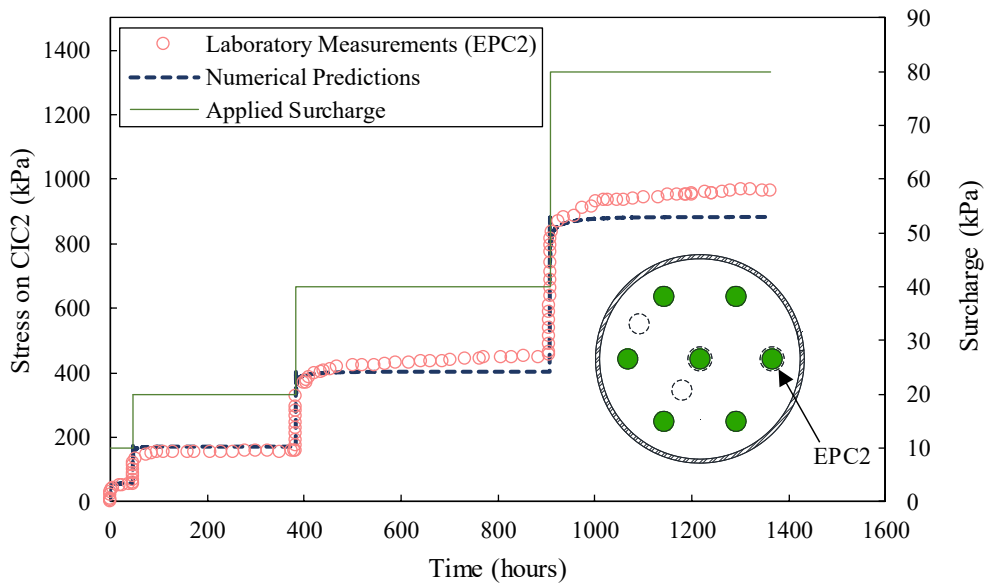
3.4.1 Stress Concentration Ratio (SCR)

Figure 3.10 (a) and (b) show the total stresses on CIC1 and CIC2, as measured by EPCs 1 and 2, respectively, as well as numerical predictions from the three-dimensional simulation. Figure 3.10 shows that the stress in CICs are much higher than the applied surcharge since the CICs are much stiffer than the soft clay and thus sustain a significant portion of the applied load. As Figure 3.10 (b) illustrates, when a 10 kPa load was applied onto the surface, the stress in CIC2 measured by EPC2 had already reached 56 kPa in the experiment. If the stress intensity factor (SIF) is defined as the ratio of the stress in the column to the applied load (Murugesan & Rajagopal 2006), then SIF was 5.6 (i.e. 56/10) for the first loading stage in the laboratory, but when the applied surcharge increased to 20 and 40 kPa, the stress on

CIC2 plateaued at 158 and 449 kPa (i.e. corresponding to $SIF=8$ and 11.2), respectively. As both Figure 3.10 (a) and (b) demonstrate, stresses on the CICs increased quite fast as the load was applied at the beginning of each loading stage, but the stress increased at a slower rate with time as the soft clay consolidated, and more stress was then transferred from the soft clay to the CICs until they finally reached a steady value. Despite the numerical predictions and experimental measurements at the 40 kPa and 80 kPa loading stages deviating, the numerical model could still capture the trend of stress transfer to the CICs. These deviations could be as a result of the possible development of microcracks in one or more of the other CICs under the increased applied loads which could have led to a stress transfer and an increase in the measurements of the stresses in CICs 1 and 2. Another contributing factor could be the adopted parameters as small element tests were tested in the laboratory to derive the material parameters.



(a)



(b)

Figure 3.10 Stress on (a) CIC1 measured by EPC1 and (b) CIC2 measured by EPC2 versus time

Figure 3.11 shows the load on the soft clay surface measured by EPC5, along with the numerical predictions. As Figure 3.11 suggests there was a sharp increase in stress on soft clay after the load was applied to the surface, while stress on the soft soil decreased quickly over time since it transferred onto the CICs. Initially, due to the undrained condition and therefore high stiffness, the soft clay attracted a considerable portion of the applied load, as seen at the beginning of each loading stage in Figure 3.11. As the soft soil settled due to the dissipation of excess pore water pressure and consolidation, the differential settlement between the soft clay and CICs due to differences in the stiffness generated shear stresses in the LTP and induced the arching effect in the granular material.

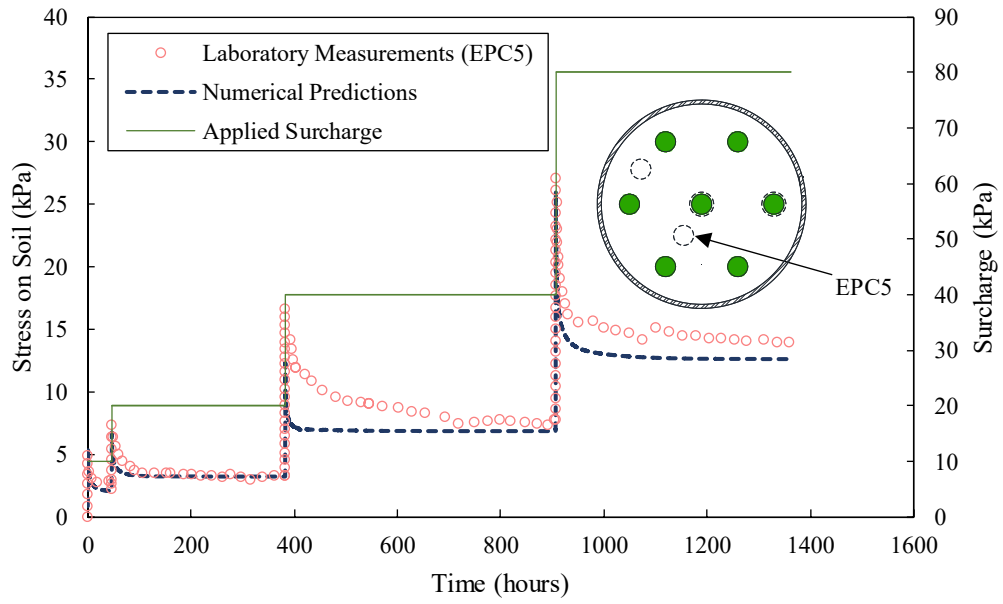


Figure 3.11 Stress on soil measured by EPC5 versus time

The combined effect of arching and the membrane effect of the geotextile layer redistributed more loads from the soft clay onto the CICs over time, as Figure 3.11 suggests. Referring to Figure 3.10 (a) and (b), the initial high rate of increasing stress on the CICs was due to the high rate of stress reduction on the soft clay, although both these rates decreased over time.

The stress concentration ratio (n_s) is defined as the ratio of the stress on column (σ_c) to the stress on soil (σ_s) (Han & Gabr 2002), and is defined by Eq. (3.17):

$$n_s = \frac{\sigma_c}{\sigma_s} \quad (3.17)$$

Since the stress on soil varies with depth and radially, n_s also varies with depth and radial distance (Alamgir et al. 1996). Indeed, n_s depends on factors such as the dimensions and stiffness of the CICs, the properties of soft soil, and the applied load. Figure 3.12 presents the changes in the stress concentration ratio over time, showing the stress concentration ratio did not remain constant, and in fact varied over time and at different loading stages.

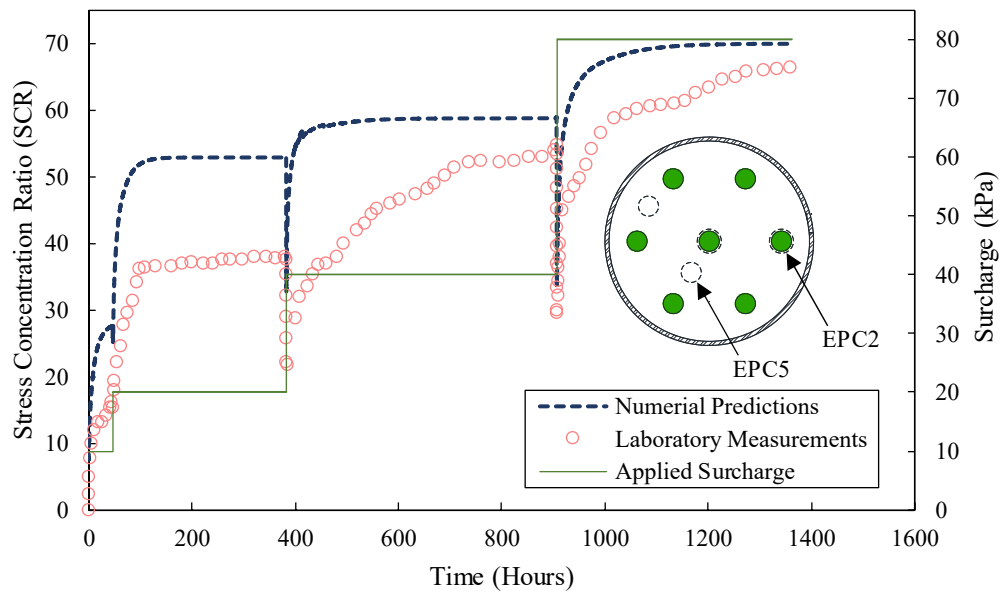


Figure 3.12 Stress concentration ratio (SCR) versus time based on stresses measured by EPC2 and EPC5

A minimum SCR was observed at the beginning of each loading stage when the soft soil attracted the highest load, after which the SCR increased as the soft soil consolidated and the load on the soil was transferred onto the CICs; this is shown in Figure 3.10 and Figure 3.11. Han & Ye (2001) also discussed how the SCR increased over time and then reached a steady value. Das & Deb (2018) also reached similar conclusions when investigating how the SCR for stone columns varied over time. Figure 3.12 also suggests that the SCR increased with the applied loads; for example, the maximum SCR for the 80 kPa loading stage reached 66, while the corresponding value for the 40 kPa loading stage was 54. This result agrees with the findings of Han & Gabr (2002), Chen et al. (2008), and Murugesan & Rajagopal (2006) on piled embankments as they concluded that the SCR increased with the height of the embankment.

Figure 3.13 and Figure 3.14 show that the stresses measured by EPC3 and EPC4 on the side wall and the bottom of the cell have a similar pattern to measurements made by EPC5 on the surface of the soil. Figure 3.14 and Figure 3.11 show that the values of the stress on the surface of the clay, as measured by EPC5, was

higher than the corresponding values at the bottom of the cell, as measured by EPC4. This can be explained by the negative skin friction on the CICs where the stress in the soft clay was shed onto the CIC shaft moving down the cell. Deformation in the CICs was negligible compared to the soft clay since the concrete was much stiffer than the soft soil and the CICs were extended to the rigid base of the cell to simulate a very stiff stratum. Therefore, since the soft soil between columns settled more than the CICs (shown in Figure 3.20), a negative skin friction was generated on the columns which reduced stress in the soil moving down to the bottom of the cell as is evident comparing Figure 3.14 and Figure 3.11.

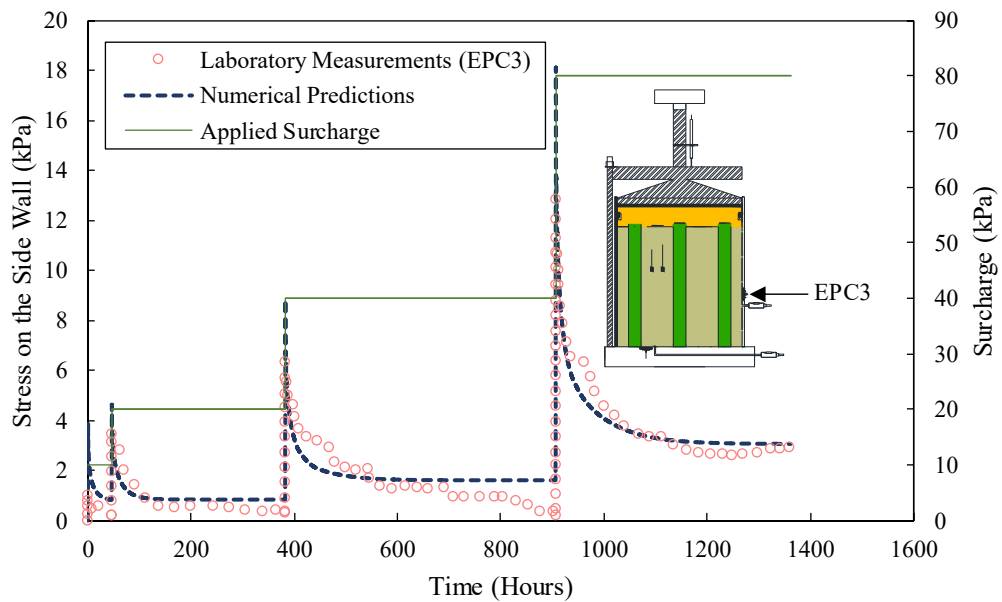


Figure 3.13 Stress on the side wall measured by EPC3

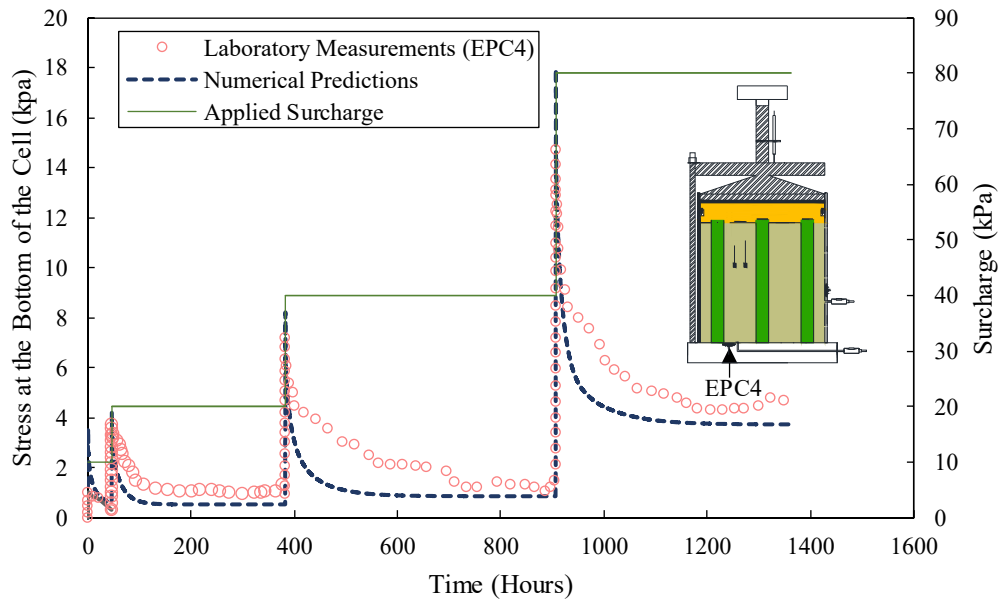


Figure 3.14 Stress at the bottom of the cell measured by EPC4

Figure 3.15 shows the predicted variations of stress with depth in CIC1 and the soft soil, midway between CIC1 and CIC6. As Figure 3.15 demonstrates, stress in the soft soil decreased due to the negative skin friction, and then it stabilised due to the weight of the soft soil and a reduction in negative skin friction. However, stress in CIC1 increased along its entire length due to the combined effect of negative skin friction and self-weight of the concrete. Since the unit weight $\gamma_c = 24 \text{ kN/m}^3$ was used for concrete, an increase of only 12 kPa (i.e. $24 \times 0.49 = 11.8$) could be attributed to the self-weight, so the remaining increase was due to negative skin friction induced by the soft soil settlement.

Figure 3.16 shows the variations of SCR with depth, where the SCR increased with depth as stress in the CIC increased and stress in soft clay decreased. As shown in Figure 3.15, the SCR then plateaued as stress in the soft soil stabilised closer to the base of the cell. This trend of variations of SCR with depth agrees with the findings of Alamgir et al. (1996).

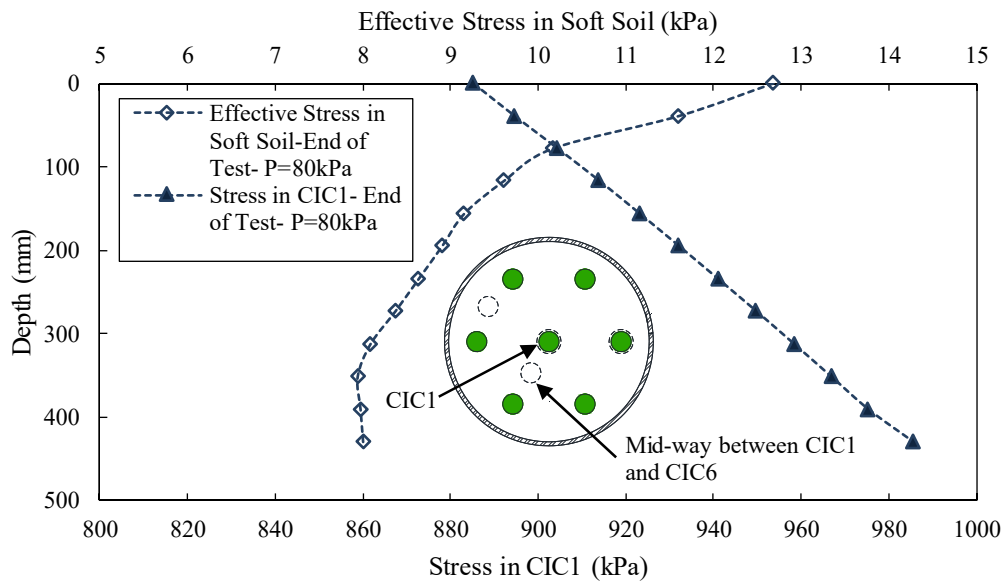


Figure 3.15 Stress variation with depth in CIC1 and the soft soil midway between CIC1 and CIC6 at the end of the test under 80 kPa surcharge

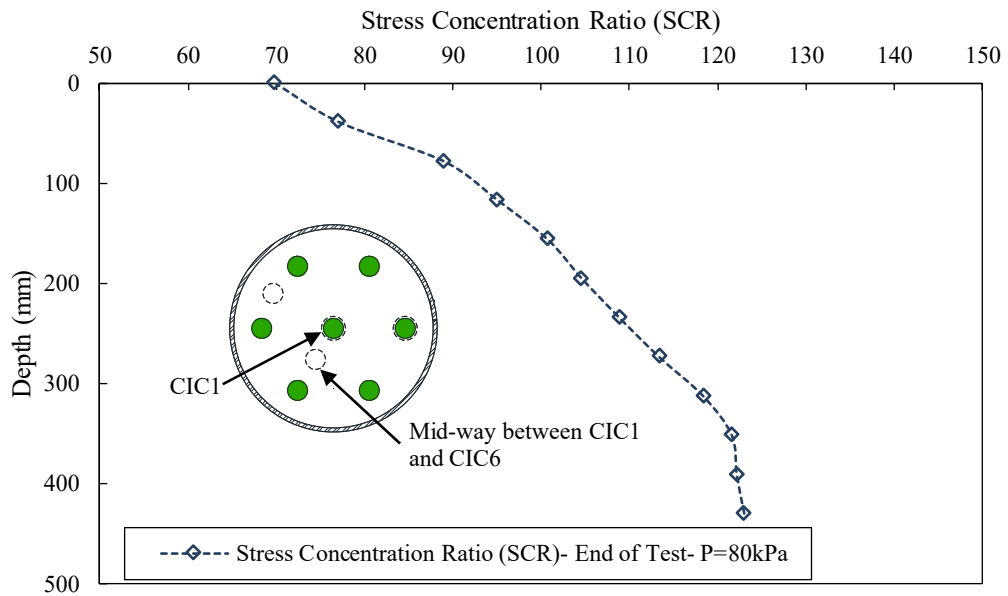


Figure 3.16 Variations of stress concentration ratio (SCR) with depth at the end of the test under 80 kPa surcharge

Figure 3.17 demonstrates the contours of stress on the soil surface where the stress mid-span between the two CICs was at its maximum and then decreased closer to the CICs. By considering concentric cylinders of soil around the CICs with shear stress on each cylinder, the magnitude of the shear stress on each cylinder must decrease inversely with the surface area of the cylinder to satisfy the vertical equilibrium (Cooke 1974; Frank 1974); therefore, the negative skin friction decreased as the radial distance from the CICs increased.

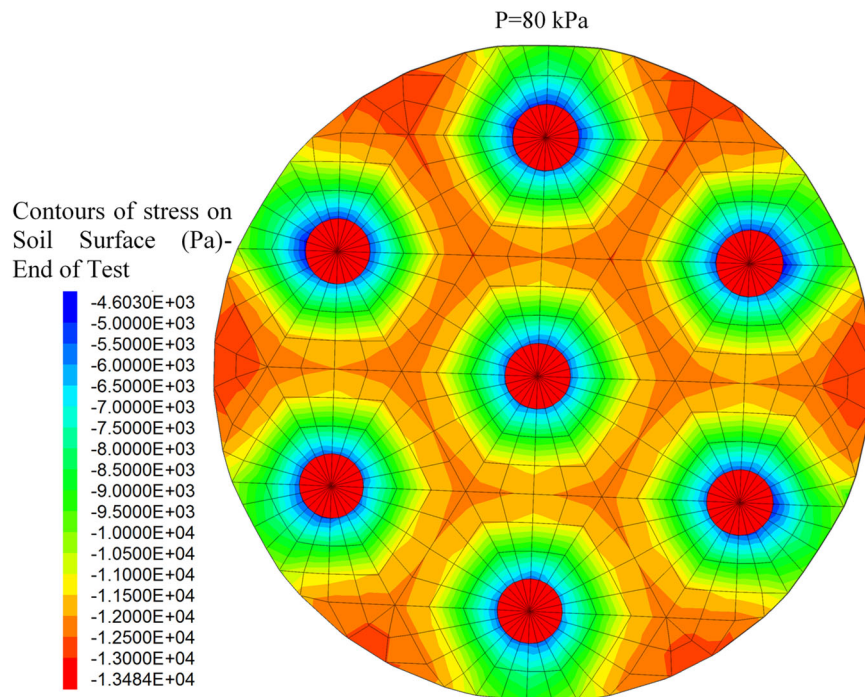


Figure 3.17 Contours of vertical stress on the soil surface at the end of the test

3.4.2 Settlement

Figure 3.18 shows settlement of the soil surface over time, as measured by the LVDT, as well as the numerical prediction for every stage of loading. As Figure 3.18 depicts, the system settled immediately once the load was applied instantaneously at the beginning of each loading stage, after which settlement increased at a slower rate over time. This rather fast reduction in settlement rate can be attributed to the quick reduction in stress in the soft clay, as shown in Figure 3.11. A reasonably good agreement was observed between the experimental measurements and numerical predictions. The deviations towards the end of the 40 kPa and 80 kPa loading stages could be a result of secondary compression in the soft clay which was not taken into account in the numerical model. Creep deformation of the soil could also be a contributing factor to the observed increase in the CIC stresses shown in Figure 3.10.

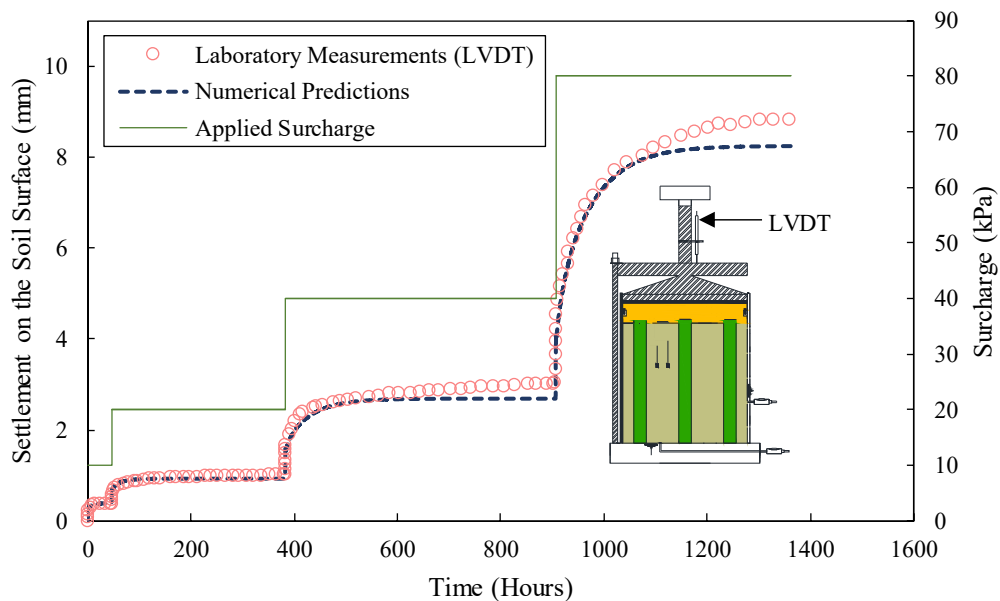


Figure 3.18 Settlement of the soil surface measured by the LVDT on the loading platen

Figure 3.19 depicts the predicted deformed shape of the soft soil and LTP, and the membrane effect of the GR at the end of the test under 80 kPa surcharge

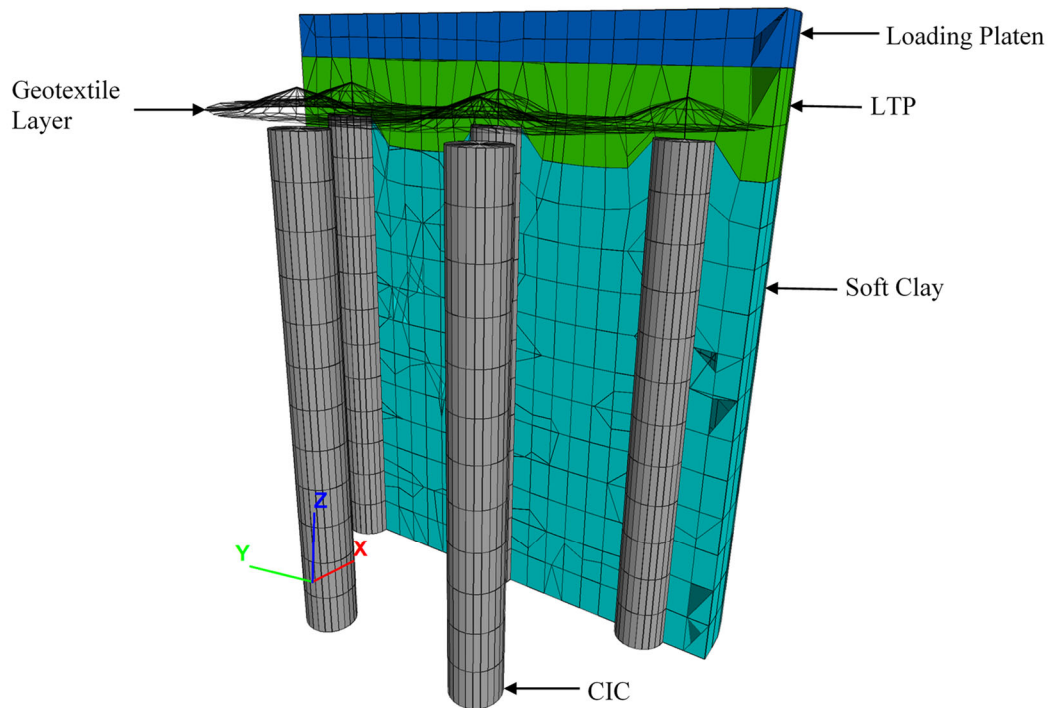


Figure 3.19 Deformed shape of the system at the end of the test under 80 kPa surcharge

Figure 3.20 presents the predicted settlement profile along Section A-A (refer to Figure 3.2) at the CIC-head level; here the settlement of CICs was negligible compared to the settlement of soft soil since the CICs were stiffer. Maximum settlement of soft soil occurred mid-span between the two CICs, it then gradually reduced at points closer to the CICs due to the reduced stress shown in Figure 3.17. As Figure 3.21 demonstrates, maximum differential settlement at the CIC-head level occurred near the edges of the CIC, whereas minimum settlement was predicted at mid-span between the CICs. It should be noted that differential settlement here is defined as the difference in settlement between the two adjacent zones.

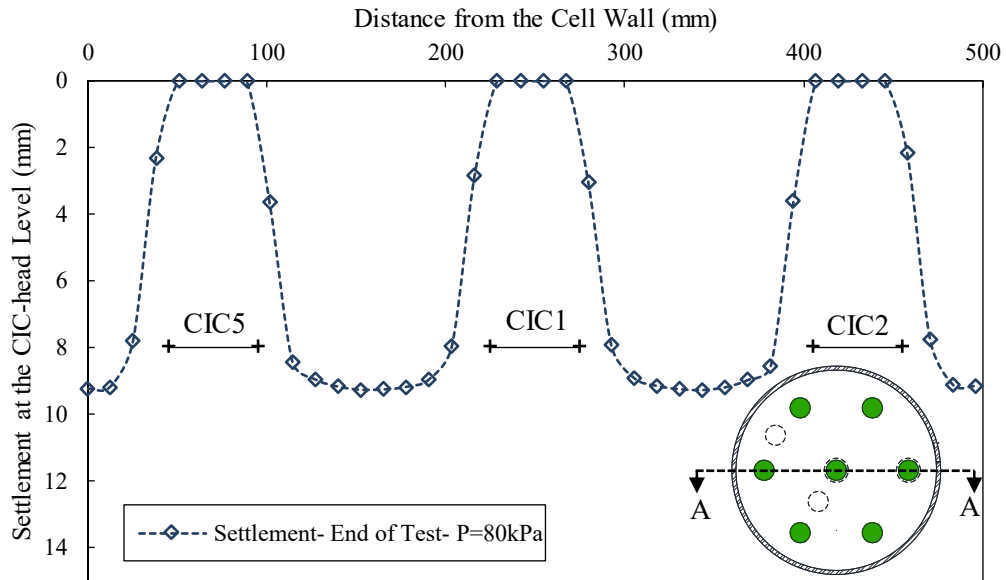


Figure 3.20 Settlement profile at the CIC-head level along Section A-A at the end of the test under 80 kPa surcharge

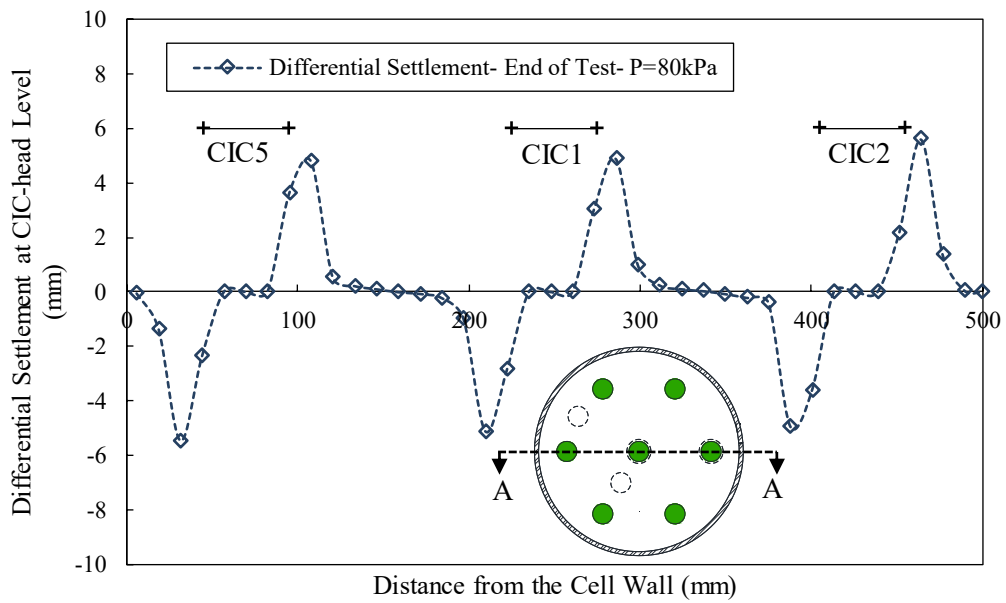


Figure 3.21 Differential settlement at the CIC-head level along Section A-A at the end of the test under 80 kPa surcharge

3.4.3 Pore Pressure

Figure 3.22 and Figure 3.23 show the variations of excess pore water pressure (EPWP) over time for PWPTs 1 and 2, respectively, as well as the numerical predictions. Here the EPWP increased to a peak immediately after the surcharge was applied and then quickly decreased over time. The excess pore water pressure induced in soft clays is a function of the applied load (i.e. a change in total stress) and the rate of dissipation through the drainage boundaries. Although the combined effect of consolidation and variations in the total stress is responsible for variations of EPWP, the rather quick reduction of EPWP (Δu) observed in Figure 3.22 and Figure 3.23 can be mainly attributed to the total stress reduction ($\Delta\sigma$) (see Figure 3.11) in the soil and a very similar trend in the reduction is noted. Dissipation due to consolidation process requires a longer time considering the low permeability of the adopted soft clay.

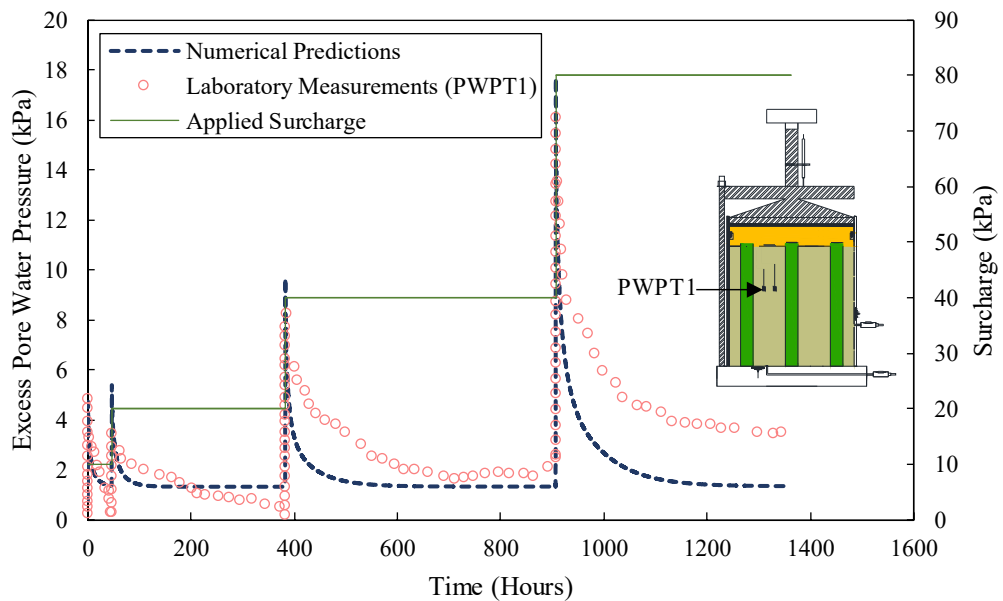


Figure 3.22 Variations of EPWP with time measured by PWPT1 between the two CICs

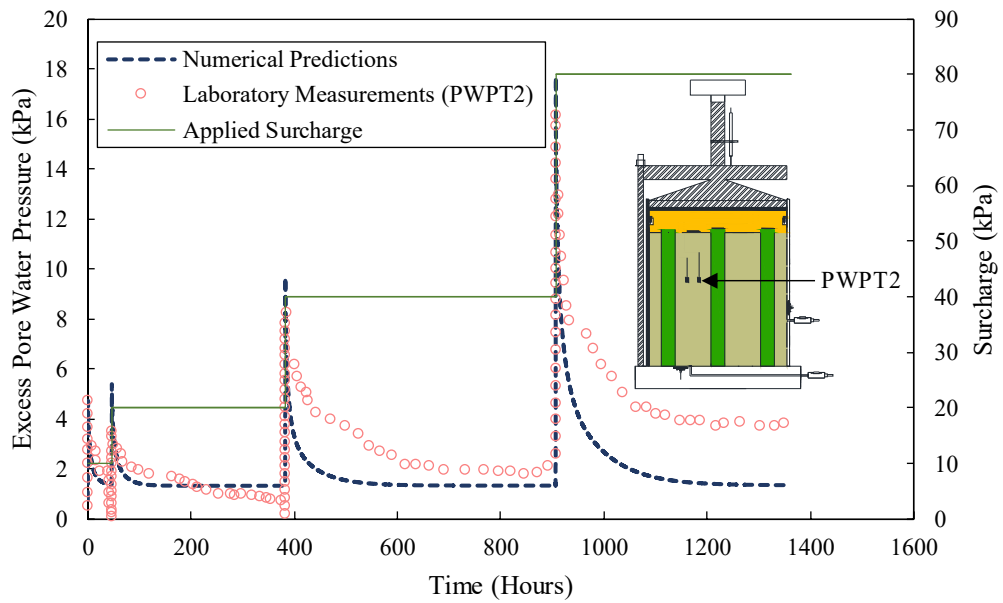


Figure 3.23 Variations of EPWP with time measured by PWPT2 between the two CIC

Figure 3.24 and Figure 3.25 present the changes in EPWP for PWPTs 3 and 4 that are located on the wall and the base of the cell marked in Figure 3.3. As discussed previously, comparing Figure 3.24 and Figure 3.25 with Figure 3.13 and Figure 3.14, it is also noted that the changes in the pore water pressures at PWPTs 3 and 4 are primarily due to changes in the total stresses as recorded by EPC3 and EPC4. There is a similar pattern in Figure 3.22 and Figure 3.23; however, the corresponding values for PWPTs 3 and 4 are less than the peak values for PWPTs 1 and 2 since the increase in the stress level was less for these points, as shown in Figure 3.13 and Figure 3.14. The deviations of the initial increase in the measured EPWP by the PWPTs on the boundary (Figure 3.24 and Figure 3.25) from the numerical predictions could be explained by the boundary effect on these sensors. The observed discrepancies in the EPWP dissipation, however, could be attributed to the creep deformation of the soft clay. Secondary compression has been explained as the possible cause of the delayed dissipation of the EPWP by other researchers (Li & Rowe 2002; Yin & Zhu 1999; Yin et al. 1994; Holzer et al. 1973). Furthermore, altered permeability of the soft clay due to the inclusion of the CICs could also be a contributing factor to the observed disparities.

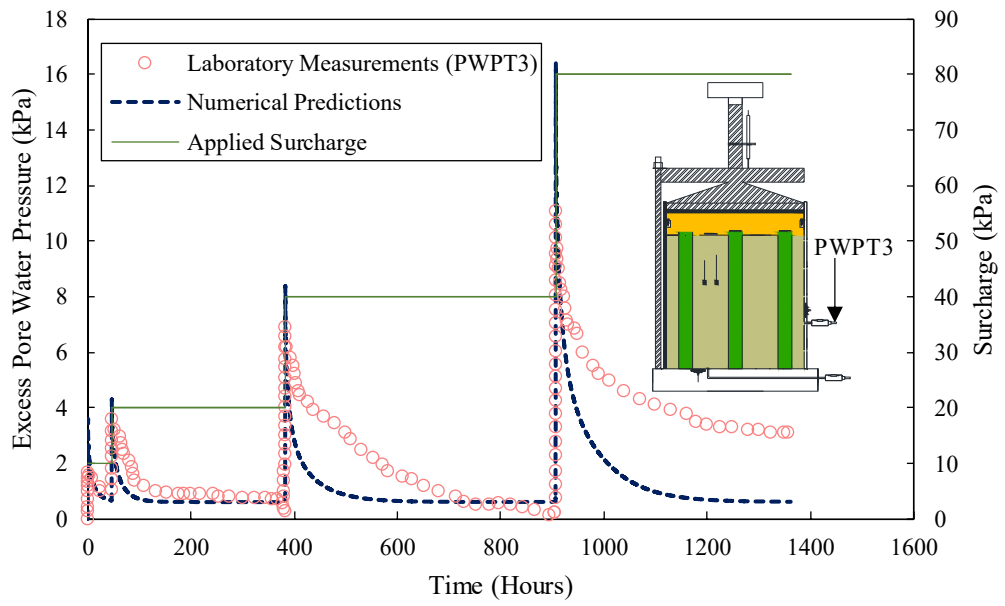


Figure 3.24 Variations of EPWP with time for PWPT3 on the side wall

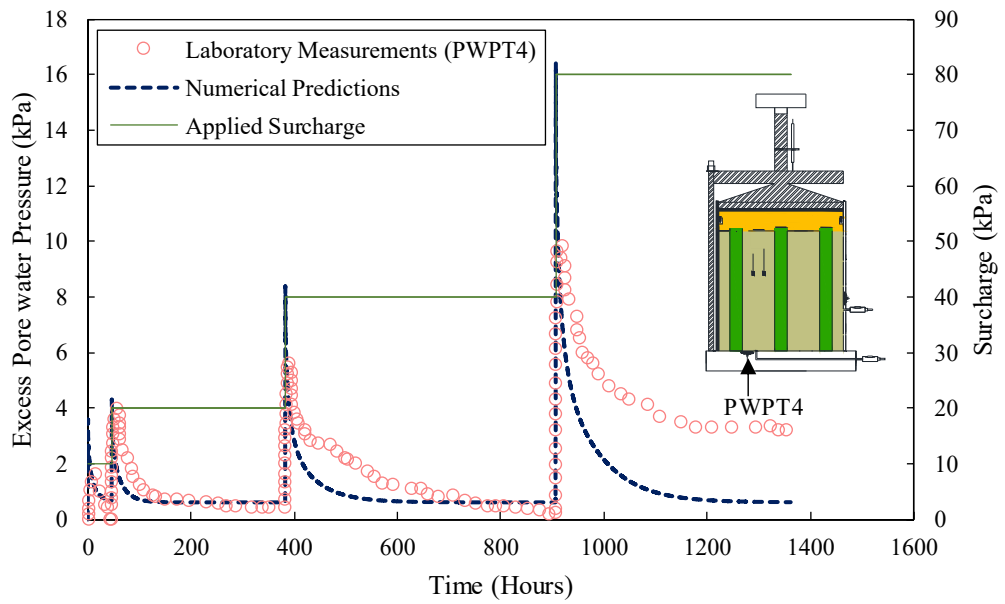


Figure 3.25 Variations of EPWP with time for PWPT4 at the bottom of the cell

3.4.4 Tension in the Geotextile Layer

Figure 3.26 and Figure 3.27 show the tensile forces mobilised in the geotextile layer that were measured by the strain gauges SGY-1 and SGY-2 in the Y direction, and SGX-1 and SGX-2 in the X direction, respectively (refer to Figure 3.6), as well as the numerical predictions. Following the application of 80 kPa on top, the strain gauges were damaged due to excessive deformation, so the results are reported up to the end of 40 kPa stage. As illustrated in Figure 3.6, points SGY-1 and SGY-2 are shown in symmetrical positions, so the tensile stresses that developed are comparable, as shown in Figure 3.26. Furthermore, although there is a generally reasonable agreement between the numerical predictions and the experimental measurements of the tensile forces mobilised in the geotextile, disparities were observed which could be as a result of the reduced sensitivity of the strain gauges under bending due to the differential settlement of the granular layer.

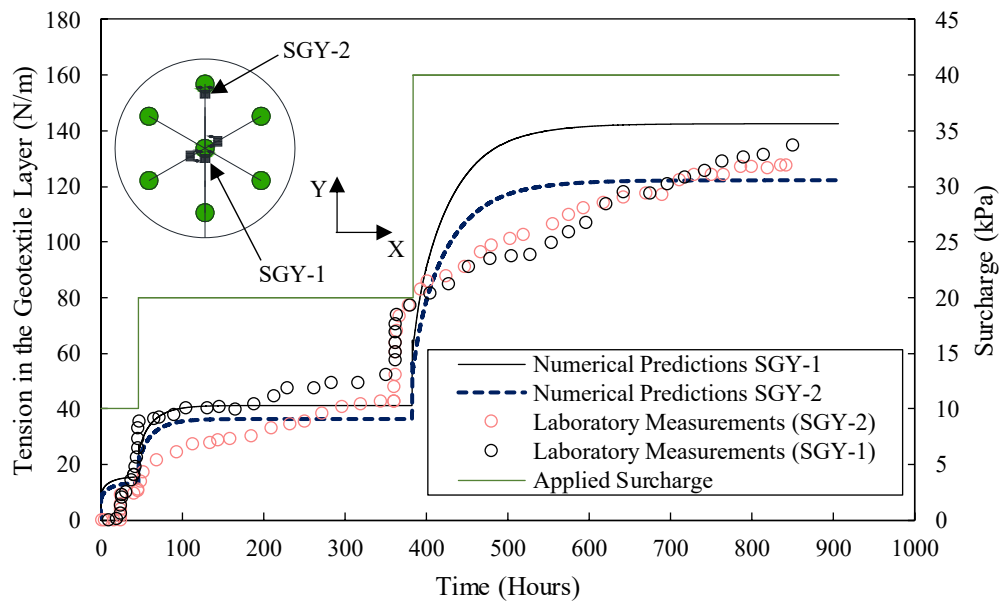


Figure 3.26 Tension in the geotextile layer in Y-direction

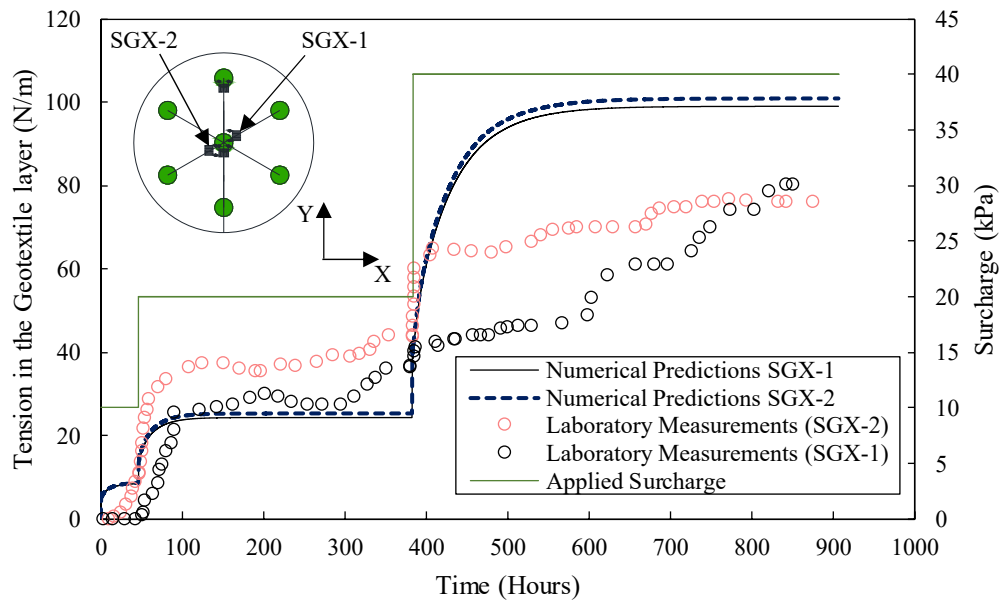


Figure 3.27 Tension in the geotextile layer in X-direction

As the soft soil consolidated and settled under the applied loads, tensile forces were generated due to deflections in the geotextile layer. An increase in the geotextile force at the beginning of loading stages with 20 kPa and 40 kPa indicates an increase in the settlement of soft soil, as presented in Figure 3.18. The increase in the mobilised tensile forces, however, continued at a reduced rate as the settlement of soft soil decreased over time (refer to Figure 3.18). The delayed increase in geotextile tension measured at 10 kPa stage could be explained by possible slack in the GR when the test first started.

Figure 3.28 depicts the profile of the mobilised tensile stresses predicted in the geotextile along Section A-A (refer to Figure 3.2). As observed in Figure 3.28, tension in the geotextile was at its maximum on the CICs, and then it decreased to a minimum above the soft soil mid-way between two CICs. Indeed, as Figure 3.28 indicates, maximum tension in the geotextile occurred where maximum differential settlement occurred (refer to Figure 3.21), while minimum tension in the geotextile occurred where differential

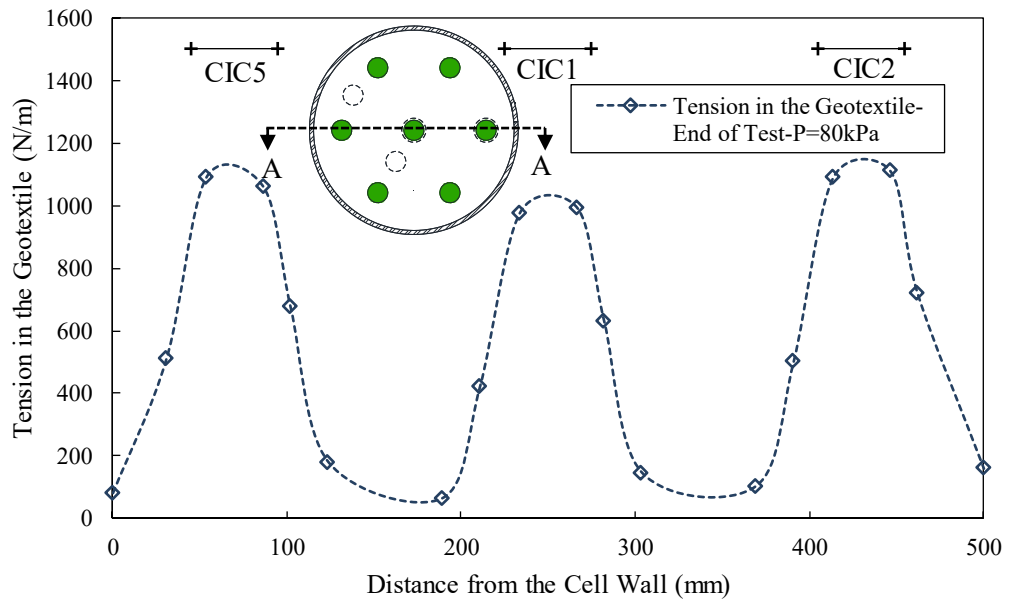


Figure 3.28 Profile of the tension in the geotextile along Section A-A at the end of the test under 80kPa surcharge

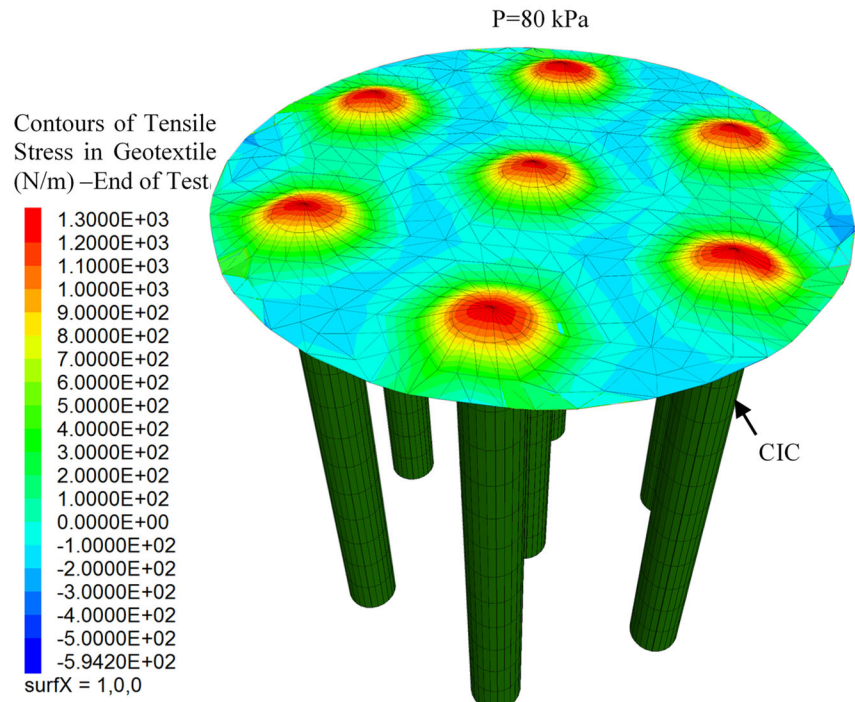


Figure 3.29 Contours of tensile stress in the geotextile at the end of the test under 80kPa surcharge

settlement was minimal. Figure 3.29 shows the three-dimensional contours of tension in the geotextile.

3.5 Summary

This study has attempted to physically model a composite ground with soft soil and concrete injected columns (CIC). In order to satisfy the scaling laws, considerable steps were taken in selecting design and material properties. CICs were cast in situ by the displacement method using an actuator to push a hollow pipe into preconsolidated soft clay. Concrete with a high fly ash content was designed, and a superplasticiser was used to achieve the high workability similar to site properties. Staged loading was simulated by the application of a surcharge through a large loading frame applied onto a 500mm diameter sample of soil. The geotextile layer was restrained at the boundaries with a purpose designed timber ring to prevent the reinforcement layer from being pulled out. Variations of the stress concentration ratio (SCR) were monitored over time using earth pressure sensors on CICs and in the soft clay. A minimum SCR occurred at the beginning of every loading stage and then gradually increased over time. The higher surcharge also resulted in a higher SCR value, in fact the load transferred to the CICs increased rapidly when the surcharge was applied, and kept on increasing over time as the load was being transferred from the soft clay to the CICs. Measurements indicated that the maximum load transferred to the soft soil occurred immediately after the surcharge load was applied, and then the load was gradually transferred from soft soil to the CICs as differential settlement occurred between the soft clay and CICs. The dissipation of excess pore water pressure was monitored and compared with the variations of stress on the soft soil. The quick dissipation of excess pore water pressure was mainly due to the stress transfer from the soil to the columns and thus reduction of the stress on the soft clay (and therefore not due to consolidation/drainage alone). Strains in the geotextile were measured by strain gauges and were observed to increase rapidly and reach a rather stable value at the end of the loading stage.

A three-dimensional fully coupled flow-deformation numerical analysis was carried out using the finite difference program FLAC^{3D}, while the Modified Cam-Clay (MCC) model and the Hoek-Brown model were used to simulate the soft clay and behaviour of CICs, respectively. The response of the load transfer platform (LTP) was captured by adopting the linear elastic- perfectly plastic Mohr-Coulomb model. Interface elements between the soft clay and CICs were used to capture any separation or slip between the two materials. The GeogridSEL element available in FLAC^{3D} was utilised to simulate the geotextile layer in large strain analysis mode. There was a good agreement between the predictions from the developed numerical code and the experimental results indicating the reliability of the numerical model. Moreover, the numerical results indicated a reduction of stress in the soft clay with depth, and therefore an increase in the SCR with depth. These numerical findings also revealed that the maximum tensile stress in the geotextile layer occurred close to the CIC heads where the differential settlement was at its maximum.

The results of these experimental and numerical studies can shed more light on the basic pattern of behaviour of CIC-improved ground and also help practicing engineers better understand and design this ground improvement technique.

CHAPTER 4

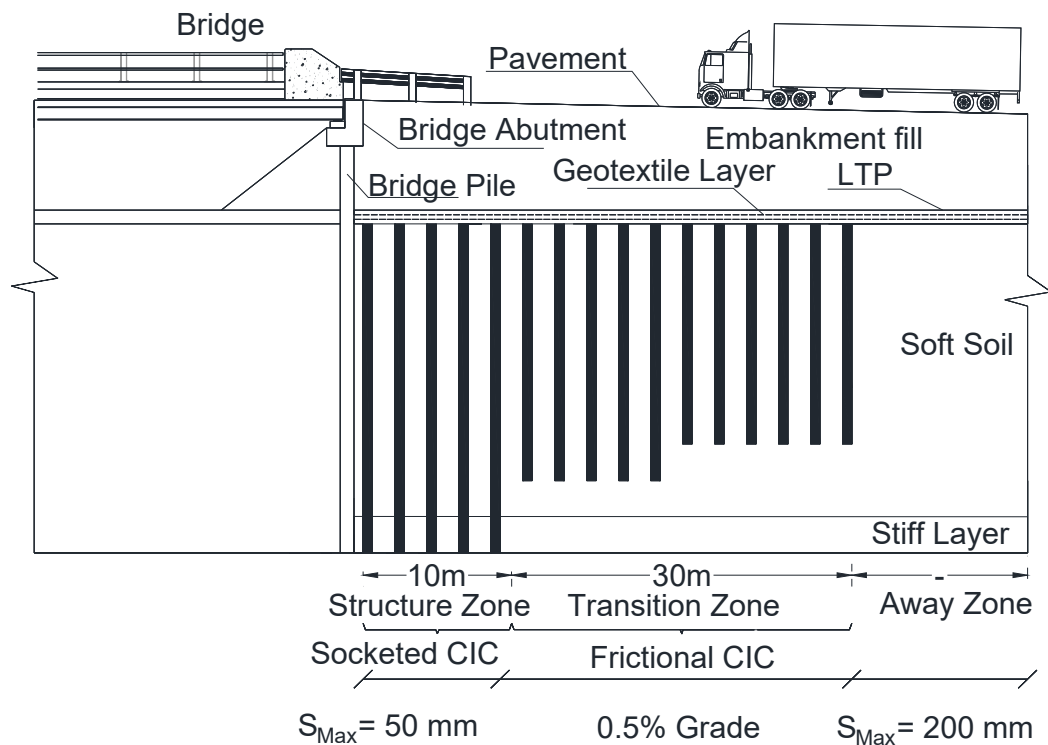
4 A COMPARISON BETWEEN FRICTIONAL AND SOCKETED CONCRETE INJECTED COLUMNS FOR DESIGNING GROUND IMPROVEMENT IN A TRANSITION ZONE

4.1 General

This chapter provides a comparison between two equivalent alternatives for the design of the transition zone. A transition zone is where ground improvement changes from a rigid or semi-rigid technique to a flexible or semi-flexible method. Two common options used by engineers for designing the transition zone near a bridge approach are discussed and investigated in this study. In the first method, CICs are socketed into a stiff layer where the spacing between columns gradually increases further away from the bridge abutment (Figure 4.1a), while in the second, the spacing between CICs is the same as the structural zone, but the columns are shorter further away from the bridge abutment (Figure 4.1b) (Wong & Muttuvel 2012b). In essence, the first approach reduces the area replacement ratio (a_r) ($a_r = A_c/A$, where A is the unit cell or tributary area depending on the CIC spacing, and A_c is the column area), while the second approach reduces the improvement depth ratio ($d_r = H_L/H$, where H_L is the CIC length and H is the soft soil depth).

Studies on evaluating the behaviour of frictional versus socketed inclusions, such as the ones mentioned above, are usually performed by varying the inclusion length without changing the spacing, while equivalent cases are rarely compared. As expected, for a given column spacing, the shorter length of the inclusions leads to higher settlements, and thus the frictional option would show a poor performance

compared to the socketed case. In this study, two equivalent cases (same volume of concrete used) with frictional and socketed CICs were compared, and full three-dimensional models were simulated to capture the interactions between CIC-soil and geosynthetic-soil, and the slope batter effect. This mechanical analysis was fully coupled with the groundwater flow to simulate the dissipation of pore water pressure with time during ground deformation. Predictions from numerical models of frictional and socketed CICs were compared in transverse cross-sections to evaluate their effectiveness in designing the bridge transition zone. It was concluded that frictional CICs can effectively reduce settlements and lateral displacements, and result in a lower tension in the geosynthetic than the socketed CICs. In the final section, a verification exercise was undertaken to compare the numerical results with the analytical method by Low et al. (1994), and a reasonable agreement was perceived.



(a)

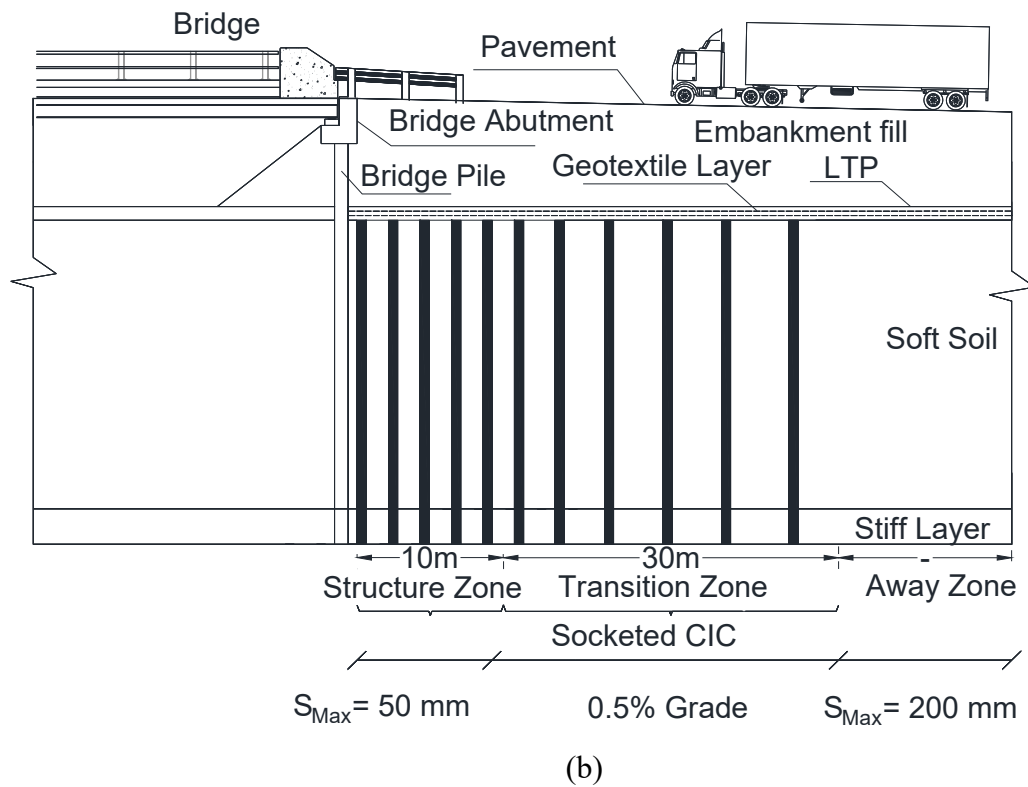


Figure 4.1 Longitudinal cross section of a typical transition zone design of a CIC project (a) Frictional CICs (b) Socketed CICs

4.2 Numerical Modelling

4.2.1 Model Geometry and Overview

FLAC^{3D} software was used for the numerical simulation in this study. The explicit numerical analysis scheme employed in FLAC^{3D} code, while solving governing equations at small time steps using constitutive equations in incremental form, makes this code suitable for modelling the nonlinear behaviour of composite ground, which has also been utilised in many other studies (Huang & Han 2009; Jenck & Dias 2009; Martin & Chen 2005; Karim 2013). Two models were created to compare the two alternatives available for the transition zone design; the CICs in both models have the same total length or volume of concrete. The geometry and

dimensions of the socketed and frictional models are shown in Figure 4.2 and Figure 4.3, respectively. The socketed CICs extend through the soft soil and are embedded into the stiff clay, as shown in Figure 4.2, while the frictional CICs end 17.5m into the soft soil (see Figure 4.3). The frictional CICs are spaced 1.75m apart (centre to centre), while socketed CICs are 2m apart. It should be noted that another added CIC in the frictional case makes up for the shortened length, hence the two cases have the same CIC total length. Figure 4.2 and Figure 4.3 show that the soft soil was 19m deep, underlain by a 5m thick layer of stiff clay.

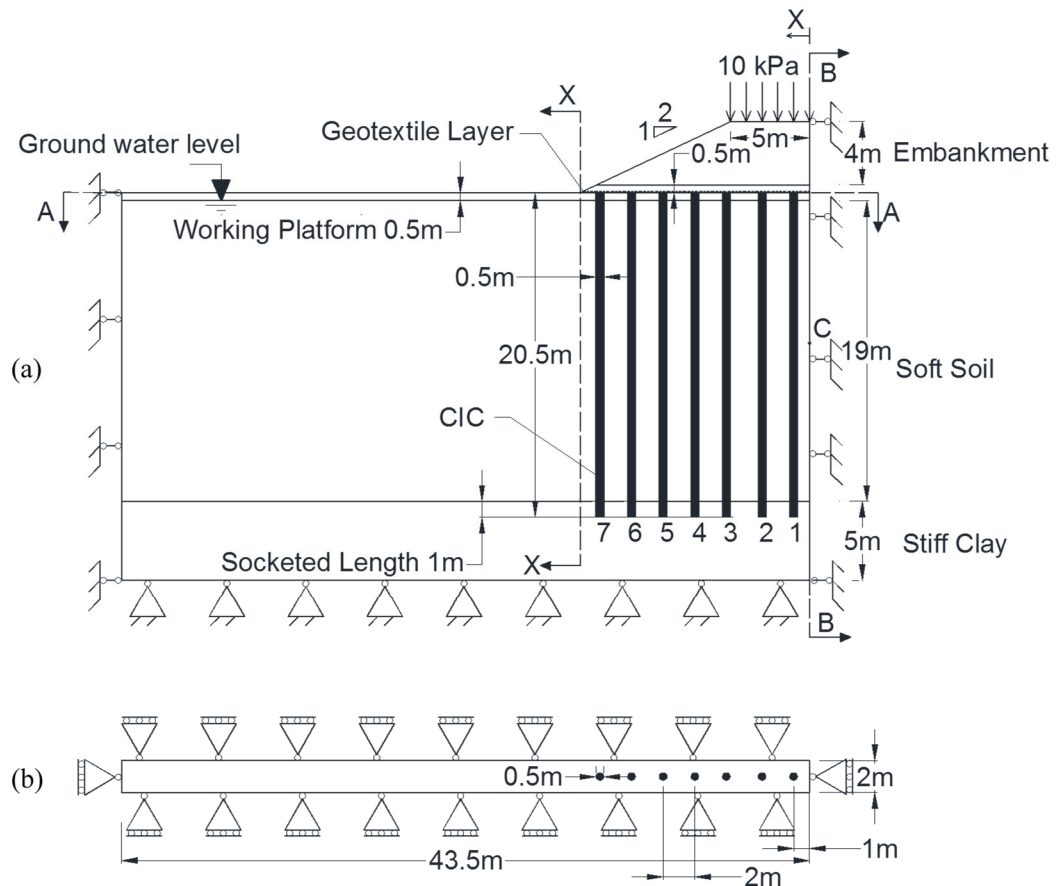


Figure 4.2 Model geometry for socketed CICs: (a) elevation view (b) cross section A-A

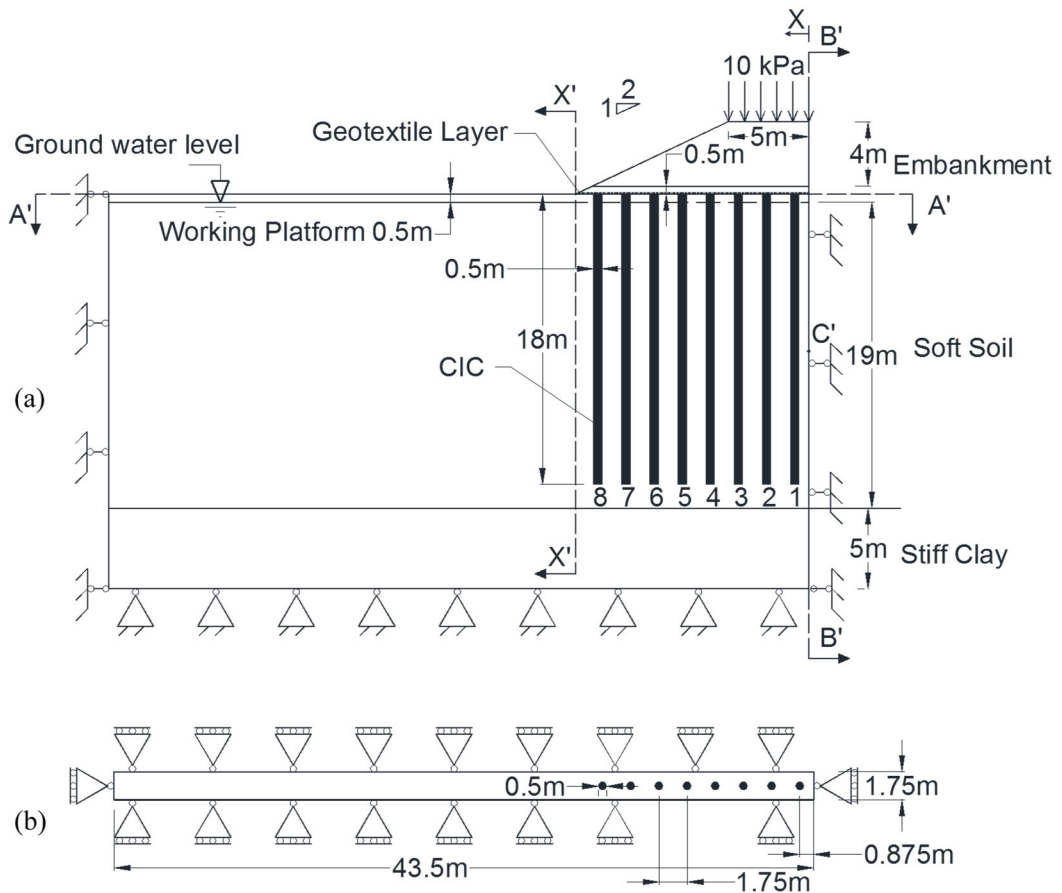


Figure 4.3 Model geometry for frictional CICs: (a) elevation view (b) cross section A'-A'

The CICs were installed through a 0.5m thick granular working platform which was built before installing the CICs. A 0.5m thick load transfer platform (LTP) that consists of a geosynthetic layer and granular material was built above the CICs to transfer loads more efficiently (see Figure 4.2). The embankment in this model was 4m above the LTP layer, and a 10 kPa uniformly distributed load was applied on the embankment to model the traffic load as commonly adopted in practice (Han & Gabr 2002). Only half the model was simulated due to a symmetrical cross-section. The model was very long in the direction of traffic, so only one row of columns in three-dimensional modelling was used to represent the system behaviour. These considerations saved considerable calculation time while simulating the problem in three dimensions. The boundary conditions are shown in Figure 4.2 and Figure 4.3. The end boundary was determined

by trial and error, but it was far enough not to impact on the model response. The total number of the zones (i.e. the mesh) used for the frictional and the socketed cases were 42652 and 38732, respectively. To determine the size of the zones, the models were run with the zones reduced by half. Observing no difference in prediction, this confirmed that the size of the proposed zone was suitable. A fully coupled flow-deformation analysis was carried out, during which the pore water pressures were also monitored at different locations in the soil. As shown in Figure 4.2 and Figure 4.3, the groundwater level was considered to be at the soft soil surface and soil below the groundwater level was considered to be fully saturated during the analysis.

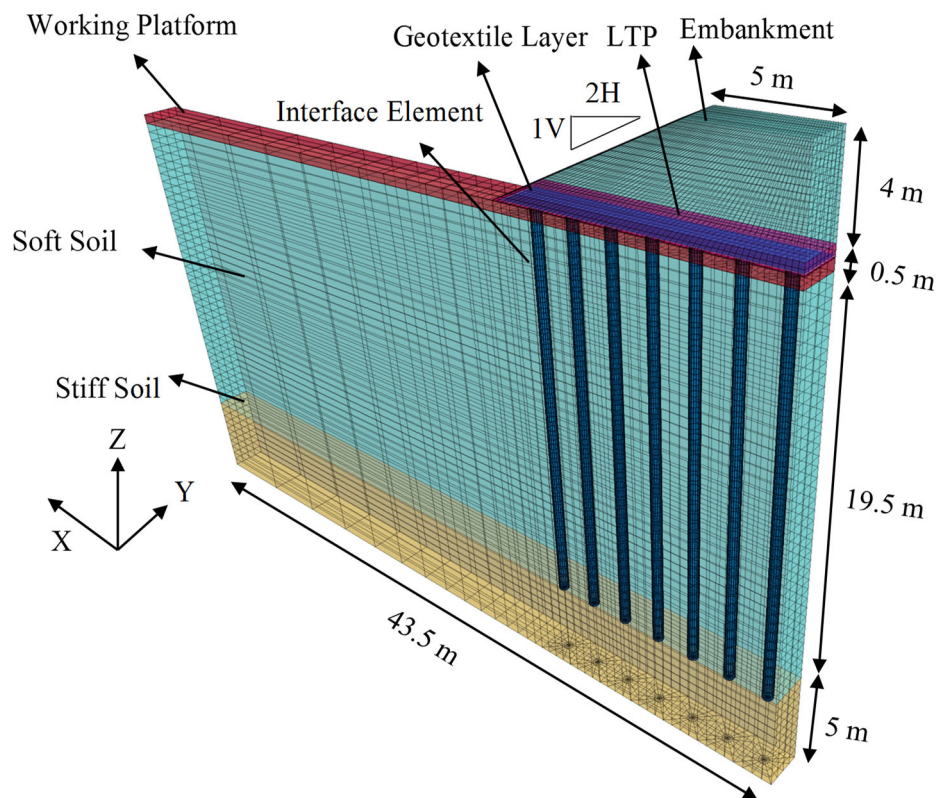


Figure 4.4 $FLAC^{3D}$ model for socketed CICs

The symmetric boundaries and the bottom boundary of the model were assumed impervious since flow cannot happen in any direction on the symmetry line, and the underlying layer had a very low permeability. Finally, since the far left side boundary was distant enough not to influence the behaviour of the model, it was also considered impervious.

4.2.2 Soft Soil Properties

The properties of the materials used in the numerical modelling were taken from a project conducted in southern New South Wales, Australia, and are summarised in Table 4.1. The upgrade of the Princes Highway consisted of 7.5 kilometres of upgraded highway and included two new interchanges. The geology along the proposed alignment was classified as the sandstone and the volcanic facies. The alignment was largely underlain by weathered rock and residual soils, and significant sections along the alignment were underlain by alluvial and estuarine deposits, typically highly compressible. A Modified Cam-Clay (MCC) (Roscoe & Burland 1968) soil model was used to simulate the behaviour of the soft soil, and elastic-perfectly plastic Mohr-Coulomb failure criterion was used to model the stiff clay.

Table 4.1 Material models and properties

Parameter	Soft Soil	Stiff Clay	Working Platform	LTP	Embankment
Material model	MCC	MC	MC	MC	MC
Depth (m)	19	5	0.5	0.5	4
Unit weight, γ (kN/m ³)	16	19	20	20	20
Coefficient of lateral earth pressure at rest, K_0	0.94	1.33	0.5	0.5	0.5
Overconsolidation ratio (OCR)	2	4	-	-	-
Critical state stress ratio, M	0.9	-	-	-	-
Slope of normal consolidation line, λ	0.31	-	-	-	-
Slope of elastic swelling line, κ	0.031	-	-	-	-
Initial void ratio, e_0	1.9	1	-	-	-
Initial permeability, k (m/sec)	1×10^{-9}	1×10^{-10}	-	-	-
Young's Modulus, E (MPa)	-	20	60	60	30
Poisson's Ratio, ν	0.3	0.3	0.3	0.3	0.3
Effective cohesion, c' (kPa)	-	5	1	1	5
Effective friction angle, ϕ' (degrees)	23°	30°	45°	45°	30°

A subroutine code was developed to allow the soil to vary its permeability with the void ratio during consolidation according to the relationship proposed by Taylor (1948):

$$\log k = \log k_i - \frac{e_0 - e}{C_k} \quad (4.1)$$

where the reference permeability k_i , is the permeability at the reference void ratio, e_0 . This relationship represents the $\log K$ - e graph where C_k is the slope of the graph. C_k was adopted as $0.5 e_0$ in this study by referring to Chai et al. (2015) and Tavenas et al. (1983). Figure 4.5 shows the linear variation of permeability in log scale with the void ratio.

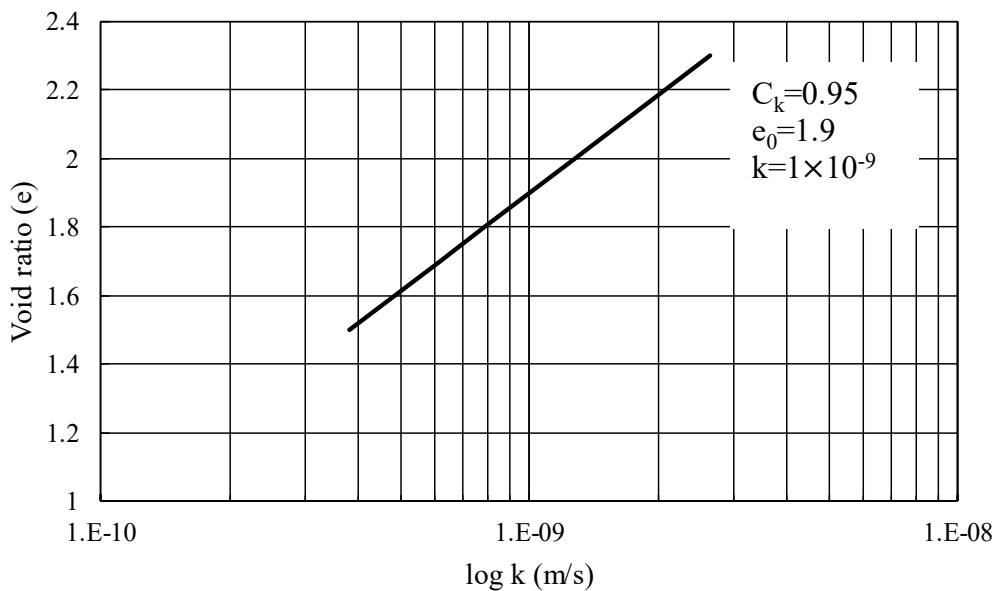


Figure 4.5 Variation of permeability versus void ratio in the soft soil

The variation of shear strength with depth can be estimated using the Stress History and Normalised Soil Engineering Properties (SHANSEP) equation (Ladd & Foott 1974) as follows:

$$\frac{S_u}{\sigma'_v} = S. (OCR)^m \quad (4.2)$$

where S is the value of $(\frac{S_u}{\sigma'_v})$ for normally consolidated soil, m is the exponent capturing the increase in strength due to the preconsolidation (0.9 in this study), and OCR is the over consolidation ratio. An OCR of 2 was used for the soft soil, and a 1m thick crust with a preconsolidation pressure of 100 kPa was simulated. The variation of vertical effective stress (σ'_v), the over consolidation ratio (OCR), and shear strength (S_u) of soil with depth is plotted in Figure 4.6 a, b, and c, respectively.

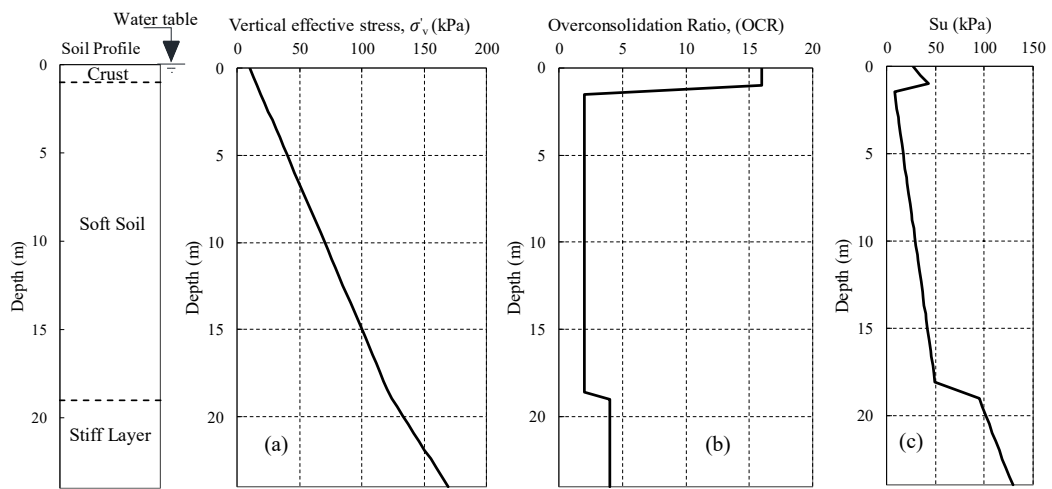


Figure 4.6 Variations of (a) vertical effective stress; (b) overconsolidation ratio; (c) shear strength of the soil with depth

K_0 was estimated using Eq. (4.3) for normally consolidated soft soil (Sherif & Koch 1970):

$$K_0 = 10^{0.00275(LL\% - 20\%) - 0.2676} \quad (4.3)$$

The Liquid Limit (LL) was considered to be 53%, and K_0 for the over consolidated soil was then estimated using Eq. (4.4) (Schmidt 1966):

$$\frac{K_{0(OC)}}{K_{0(NC)}} = OCR^\alpha \quad (4.4)$$

where $K_{0(OC)}$ and $K_{0(NC)}$ are lateral earth pressure coefficient at rest for over-consolidated and normally consolidated soils, respectively, and α is the soil constant

considered as 0.5 in this study (Mayerhof 1976). By substituting these values in Eqs. (4.3) and (4.4), the K_0 value was determined to be 0.94 for soft soil.

4.2.3 CIC Simulation

CICs are made of plain concrete with no reinforcement. The failure criterion of concrete under combined tension-compression was first introduced by Leon (1935). The extended form of this criterion is known as Hoek & Brown (1980) and is a widely used model in rock mechanics (Pramono & Willam 1989). This model is a combination of Mohr-coulomb frictional law and the Rankine tension cut-off (Etse & Willam 1994). The Hoek-Brown failure criterion for rock mass can be written as shown below (Hoek & Brown 1980; Hoek et al. 2002):

$$\sigma_1 = \sigma_3 + \sigma_c \sqrt{m \frac{\sigma_3}{\sigma_c} + s} \quad (4.5)$$

where σ_1 and σ_3 are the major and minor principal effective stresses at failure, σ_c is the uniaxial compressive strength for the intact rock material, and m and s are constants which are determined experimentally. It should be noted that $s=1$ for the intact rock.

Substituting $\sigma_3 = 0$ into Eq. (4.5) gives the uniaxial strength of the rock mass:

$$\sigma_{CS} = \sigma_1 = \sigma_c \sqrt{s} \quad (4.6)$$

Indeed, when $s=1$ for the intact rock, the compressive strength equals σ_c , while $s=0$ for the highly jointed rock yields compressive strength equal to zero.

Karam & Tabbara (2009) investigated the application of the Hoek-Brown criterion for actively confined concrete. They used a very large database of experimental results from confined triaxial concrete strength tests to determine the s and m values for the Hoek-Brown model. They proposed to use the Hoek-Brown model for actively confined concrete with $m=12$ and $s=1$. Their proposal was used in this study to simulate the plain concrete used in CICs.

The uniaxial compressive strength of the concrete was 10 MPa, and the elastic modulus was 10 GPa at the usual 28 days for CIC construction (Wong & Muttuvel 2012a).

The tensile strength of the concrete was obtained using Eq. (4.7) from the Australian Standard AS 3600 (2009):

$$f'_{ct} = 0.36\sqrt{f'_c} \quad \text{at 28 days and standard curing} \quad (4.7)$$

(MPa)

where f'_{ct} is the characteristic uniaxial tensile strength of concrete, and f'_c is the characteristic compressive (cylinder) strength of concrete in MPa at 28 days. For concrete with $f'_c = 10 \text{ MPa}$, and a partial safety factor of 1.5 applied, the tensile strength was $f'_{ct} = 759 \text{ kPa}$. Table 4.2 presents the properties adopted for the CIC simulation.

Interface elements were used between the CICs and the soft soil, allowing possible gapping and slip. The values for the shear and normal stiffness of the interface were set to be ten times the equivalent stiffness of the stiffest neighbouring zone, as recommended by Itasca (2012), and also other researchers such as Kadhim et al. (2018) and Xu & Fatahi (2018). The apparent stiffness of the zone in a normal direction is determined using Eq. (4.8):

$$k_{Max} = \left[\frac{(K + \frac{4}{3}G)}{\Delta z_{min}} \right] \quad (4.8)$$

where K and G are the bulk and shear moduli, respectively, and Δz_{min} is the smallest width of the adjoining zone in a normal direction. This formulation, however, must be applied to the softer side of the interface (soil and not CIC) when the difference between the stiffness of the two sides of the interface is significant because the deformation of the system will be governed by the softer material (Itasca 2012). Interface shear stiffness k_s , and interface normal stiffness, k_n , were adopted as 1.6×10^9 , and an interface interaction coefficient, R_c equal to 0.8 was adopted for the interface

strength properties. The Coulomb strength properties of the interface between the CICs and the soft soil are summarised in Table 4.2.

Table 4.2 CIC material model and properties adopted in this study

Parameter	CIC
Material model	Hoek-Brown
Unit weight, γ (kN/m ³)	24
Elastic modulus, E_c (MPa)	10,000
Poisson's ratio, ν_c	0.2
Uniaxial strength of the concrete, σ_{CS} (MPa)	10
Uniaxial tensile strength of concrete, f'_{ct} (kPa)	759
Hoek-Brown constant, m	12
Hoek-Brown constant, s	1
Interface normal stiffness, k_n (N/m ³)	1.6×10^9
Interface shear stiffness, k_s (N/m ³)	1.6×10^9
Interface interaction coefficient, R_c	0.8
Interface friction angle, ϕ'_{int} (degrees)	18
Interface cohesion, c'_{int} (kPa)	0.001

4.2.4 Geosynthetic Layer

A geosynthetic layer was modelled using the in-built geogrid elements which can undergo in-plane forces. A single layer of geosynthetic with an ultimate strength of $T_{Ult} = 100$ kN/m and a stiffness of $J = 1000$ kN/m in both directions was placed 0.1m above the LTP base; this is a typical practice in construction (Han & Gabr 2002). A reduction factor of 0.8 was assumed for the geosynthetic-LTP interface strength properties (Huang & Han 2009). Table 4.3 shows the properties adopted for modelling the geosynthetic layer.

Table 4.3 Geosynthetic properties adopted in this study

Parameter	Tensile stiffness, J (kN/m)	Tensile strength T_{Ult} (kN/m)	Poisson's Ratio, ν	Coefficient for interface strength reduction, R_{int}
Geosynthetic	1000	100	0.3	0.8

A large strain analysis mode was used to capture the membrane or trampoline effect of the geosynthetic layer. By adopting a large strain analysis mode, the geosynthetic elements are updated and the out-of-plane response of the geosynthetic reinforcement layer contributes to the stress transfer onto the CICs, and reduces settlement of the embankment (Smith & Filz 2007). The tensile load generated due to differential settlement depends mainly on whether a small or large strain analysis mode is chosen. The sensitivity of the loads in the geosynthetic reinforcement to the choice of small or large strain mode was also discussed by Yu et al. (2016) and Yu & Bathurst (2017) for two-dimensional and unit cell models using FLAC.

4.2.5 Embankment Properties and Construction Sequence

Elastic-perfectly plastic Mohr-Coulomb model was used to simulate the LTP and the embankment. Figure 4.7 shows the construction sequence and material properties for the embankment. The 4m high embankment reached its full height in 8 weeks. One week after completing the final layer, a 10kPa load was applied onto the embankment to simulate possible pavement, machinery and traffic loads; the system was then allowed to consolidate for 20 years after construction. The developed FLAC^{3D} code for the socketed CICs is presented in Appendix B.

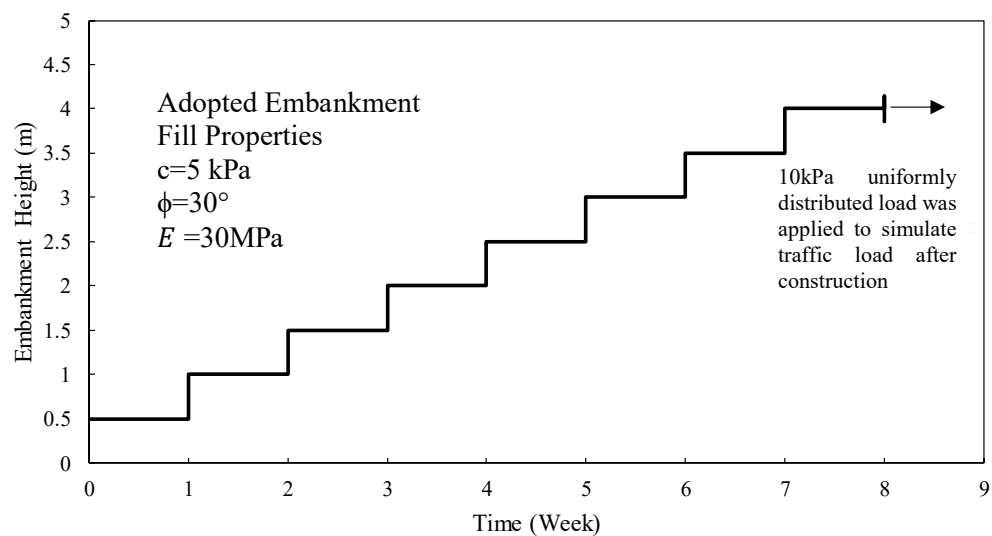


Figure 4.7 Construction sequence of the embankment

4.3 Results and Discussion

4.3.1 Settlement Predictions

Figure 4.8 and Figure 4.9 show the predicted settlement at the base and crest of the embankments, respectively, for different CIC arrangements; here, the maximum settlement occurred in the mid-span and settlements predicted for the embankment on the socketed CICs were much more than the corresponding values for the embankment on the frictional CICs.

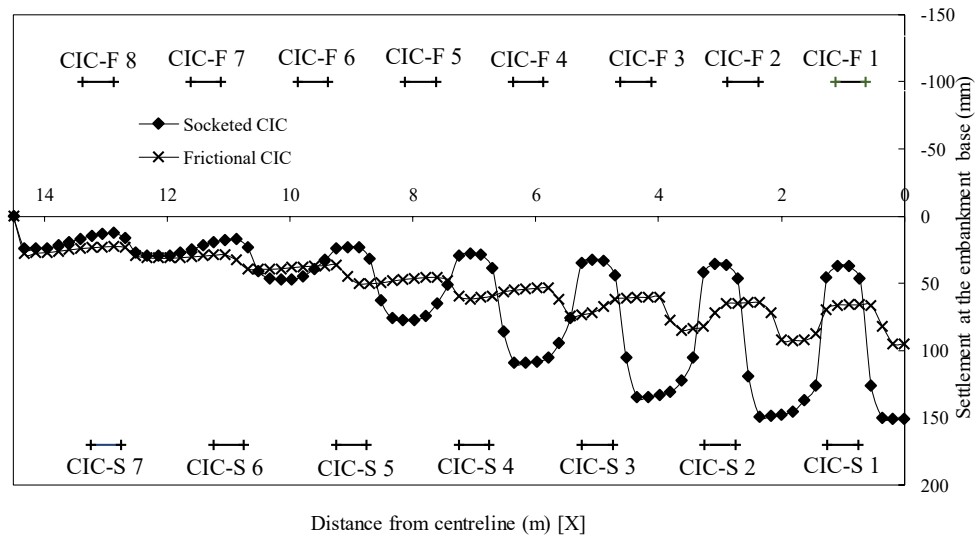


Figure 4.8 Settlement profile at the end of consolidation at the embankment base along Sections A-A and A'- A'

Figure 4.8 shows that although the settlement of socketed CICs was consistently lower than the frictional CICs due to tip resistance and a longer shaft, the settlement of soft soil between the CICs was much higher, which translated into larger surface settlements, as shown in Figure 4.9. As shown in Figure 4.9, the settlement of the embankment surface also decreased moving away from the embankment centre as the soft soil settlement decreased as shown in Figure 4.8. Figure 4.10 a and b show the deformed three-dimensional shape of the system that correspond to the socketed and frictional models, respectively. Figure 4.10 a highlights the larger differential settlement at the base of the embankment on socketed CICs, and the propagation of the soft soil settlement to the embankment surface despite the small settlement of the socketed CICs. In Figure 4.10 b, however, lower differential settlement between the frictional CICs and the soft soil in spite of the larger settlement of the frictional CICs is evident.

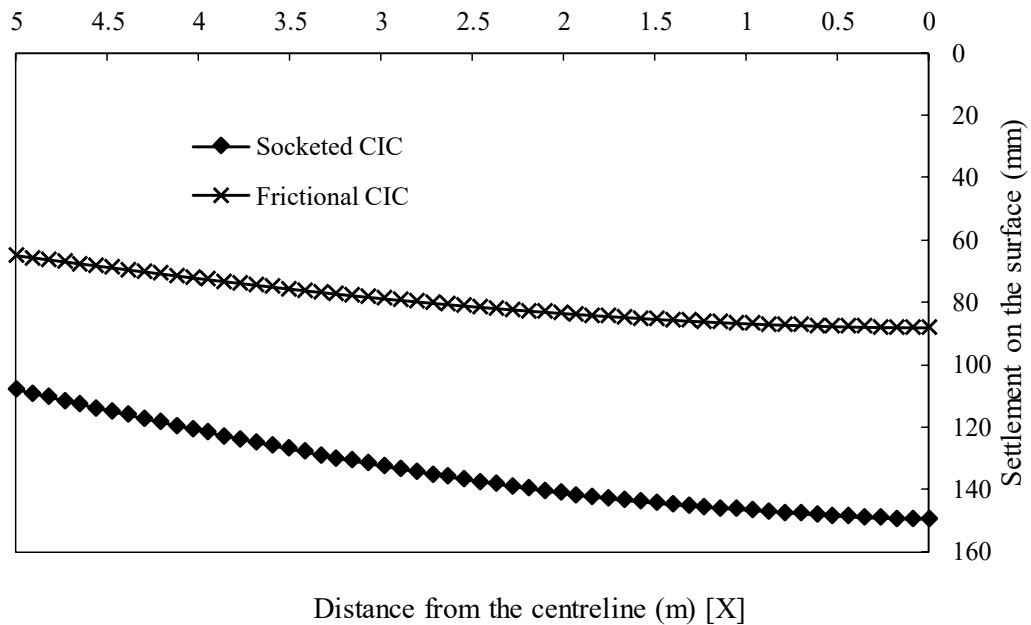


Figure 4.9 Settlement profile at the end of consolidation on the embankment surface

Figure 4.11 shows that due to the closer spacing and a higher area replacement ratio in the frictional CIC case, the soil closer to the surface sustained less load, while most of the load was transferred to the CICs, and therefore, to the deeper soil where the soil deposit is stronger. Consequently, the soft soil surface experienced less settlement when frictional CICs were used, whereas with the socketed CIC case, the columns were wider apart, thus most of the load was transferred to the soft soil surface where it induced settlement. Indeed, the socketed CICs transferred the load down to the stiff layer so there was less displacement in the actual columns compared to the frictional CIC case. However, the large displacements in the soft soil between the socketed CICs resulted in the larger differential settlement shown in Figure 4.12 and reflected as larger settlement on the surface of the embankment.

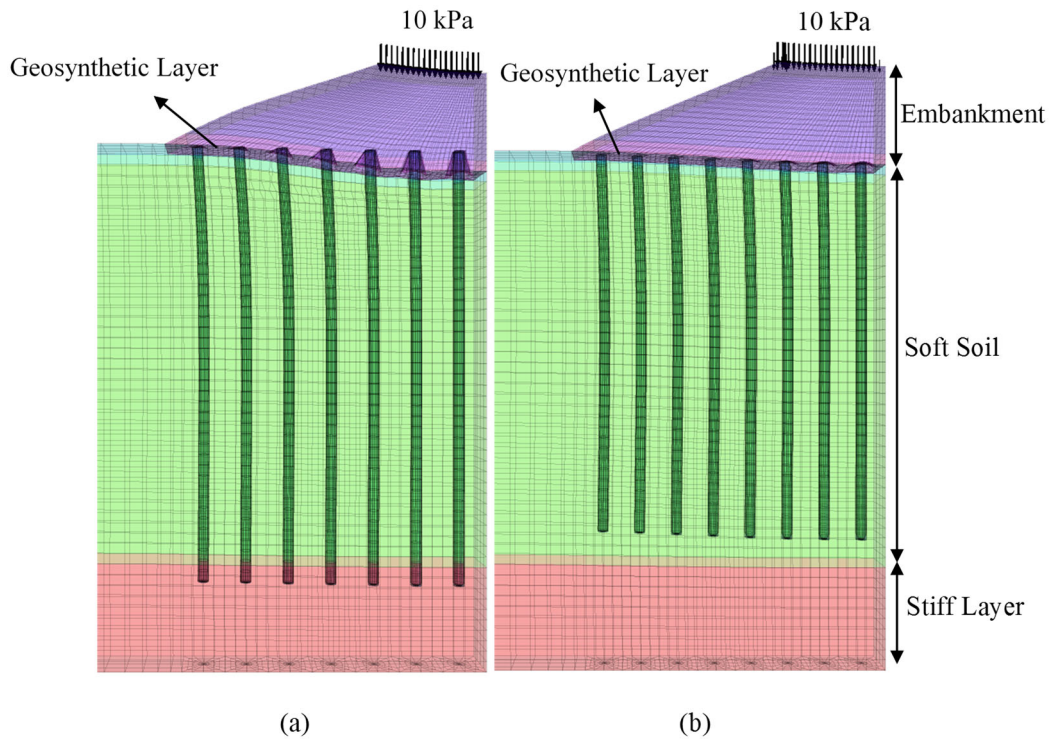


Figure 4.10 Deformed shape of the embankment at the end of consolidation for (a) socketed CICs (Magnification Factor: 10), and (b) frictional CICs (Magnification Factor: 10)

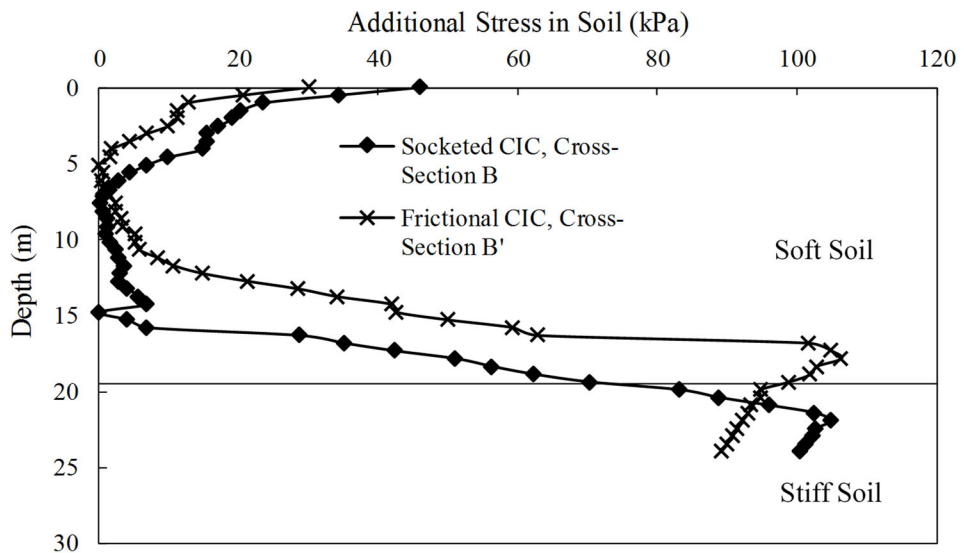


Figure 4.11 Additional stress in soil at the end of consolidation along Sections B-B and B'- B'

The differential settlements are compared in Figure 4.12 along sections A-A and A'- A' for socketed and frictional CICs, respectively. Differential settlement is defined here as the difference between the settlements of the two adjacent zones. Figure 4.12 shows that maximum differential settlement occurred at the edges of the CICs in both cases, and it reduced further away from the centre of the embankment with consistently higher values for the socketed case.

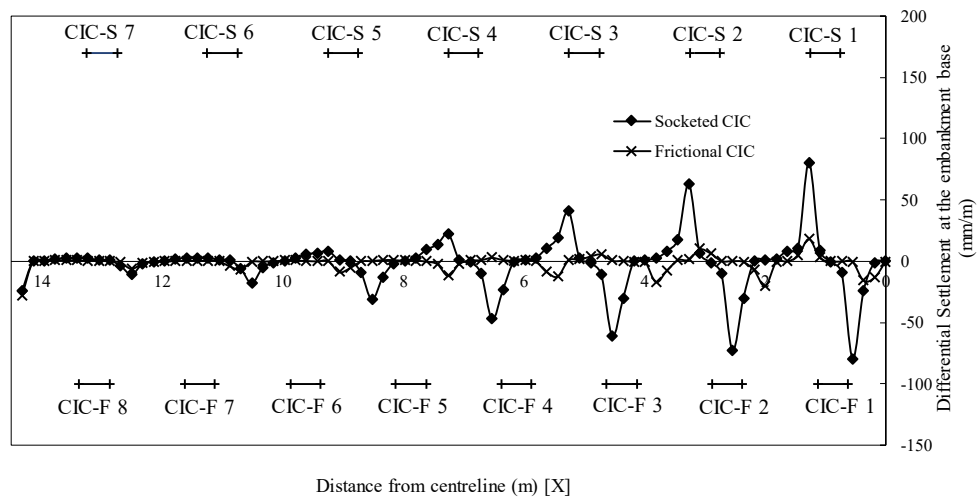


Figure 4.12 Differential settlement profile at the end of consolidation at the embankment base along Sections A-A and A'- A'

The criteria commonly used by road authorities and designers for measuring the maximum differential settlement as Change in Grade (CIG) over a 40-year period is 0.3% for rigid pavements and up to 0.5% for flexible pavements. CIG is defined as the difference between the slopes of the two chords shown in Figure 4.13, and it is calculated as presented below (Hsi 2016):

$$CIG = \frac{Y_1 - Y_2}{X_1 - X_2} - \frac{Y_2 - Y_3}{X_2 - X_3} \quad (4.9)$$

The half chord length required to calculate CIG (see Figure 4.13) is defined as:

$$T = |X_1 - X_2| - |X_2 - X_3| \quad (4.10)$$

The CIG calculated for the socketed CIC model in this study is 0.67%, which is well over the limit, even for a flexible pavement (i.e. CIG>0.5%), while CIG for frictional CICs is 0.26%, which satisfies the differential settlement criterion for 40-year post-construction settlement for rigid pavements (i.e. CIG<0.3%).

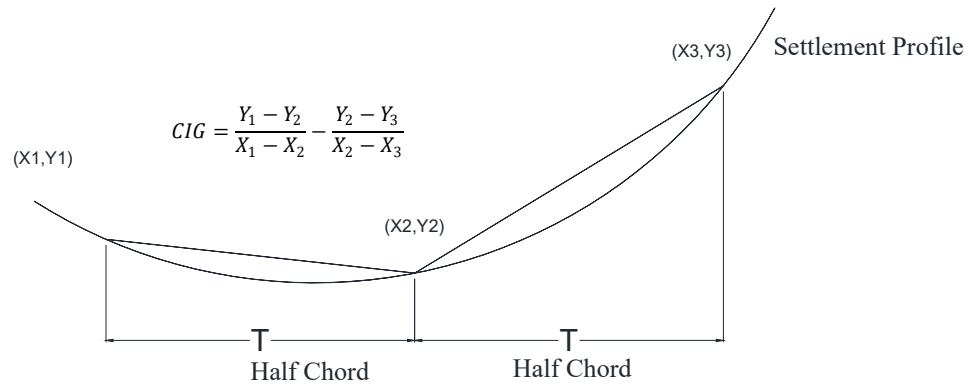


Figure 4.13 Illustration of method to determine Change in Grade (CIG) (modified after His 2016)

4.3.2 Excess Pore Water Pressure Predictions

Figure 4.14 shows the variations of excess pore water pressure (EPWP) with time at points C and C' located on the centreline of the model in the middle of the deposit of soft soil. As Figure 4.14 shows, the maximum EPWP is more in the frictional case (15 kPa) than the socketed case (12 kPa) since more embankment load was transferred to the soil (See Figure 4.11 for a corresponding depth of 9.75m).

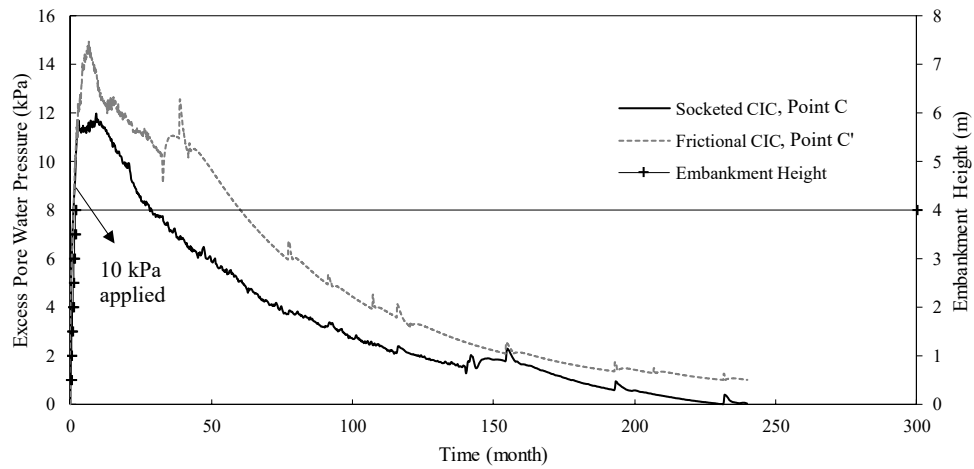


Figure 4.14 Pore pressure dissipation versus time at points C and C'

Figure 4.15 shows the EPWP with depth along Sections B-B and B'-B' for the socketed and frictional CICs, respectively. This Figure shows that the excess pore water pressure for the socketed CICs was more than the corresponding values for frictional CICs closer to the surface. However, the excess pore water pressure in the deeper layers was higher for frictional CICs. Figure 4.11 shows that since more stress was transferred to the soil closer to the surface in the socketed case, the excess pore water pressure was also higher, and since the stress was higher in the deeper layers for frictional CICs the EPWP was also higher than the socketed case.

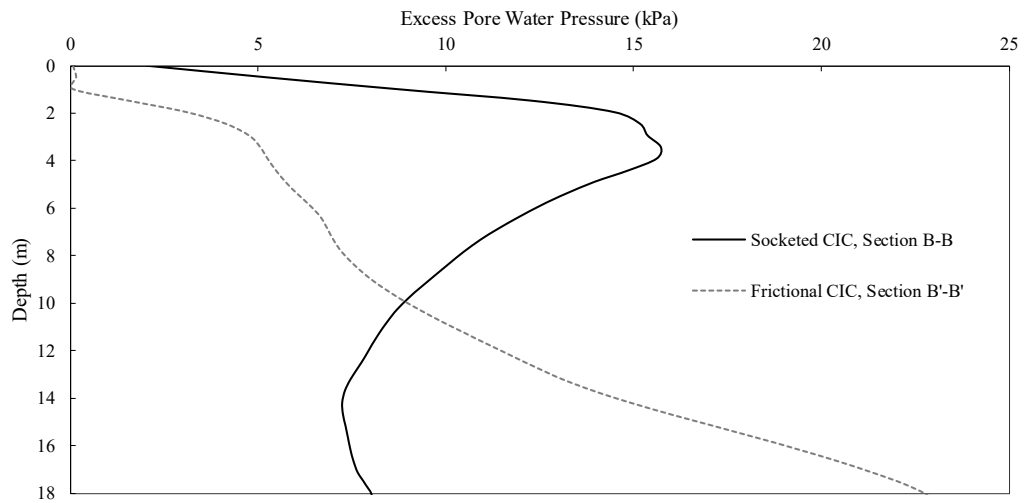


Figure 4.15 Excess pore water pressure profile with depth along Sections B-B and B'-B' one week after completion of embankment construction

4.3.3 Tension in the Geosynthetic Layer

Tension generated in the geosynthetic (GR) layer stemmed from a combination of lateral displacement of the embankment and differential settlement between the CICs and the soft soil. *Figure 4.16* shows the tension in the geosynthetic reinforcement layer in the LTP where a higher tensile force was generated when socketed CICs were used. In both cases maximum tensile forces occurred at the edges of the CICs where maximum differential settlement also occurred, as shown in *Figure 4.12*. These sharp changes in the tension in the socketed case correspond to a larger differential settlement between the soft soil and socketed CICs, as shown in *Figure 4.12*. Moreover, this larger lateral displacement of the embankment in the socketed case (to be discussed in *Figure 4.22*) also contributed to the increased tensile forces in the GR layer compared to the model with frictional CICs.

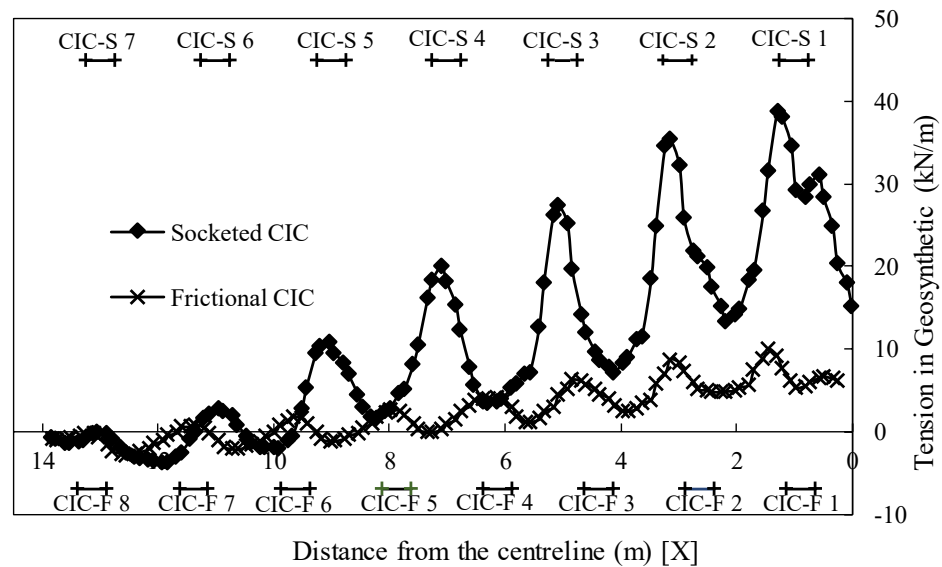


Figure 4.16 Tension in the geosynthetic layer at the end of consolidation along Sections A-A and A'-A'

Figure 4.17 a and b show the contours of the tensile forces in the geosynthetic layer (N/m) for socketed and frictional CICs, respectively. Here, deformation was magnified 2 times in both cases for better visualisation; the membrane or trampoline effect of the geosynthetic layer between CICs is clearly visible.

Figure 4.18 shows the variations of the maximum force in the geosynthetic over time. Here, the tension in GR in the socketed case (39 kN/m) was greater than the corresponding values for the frictional case (10 kN/m) since the surface of soft soil experienced larger differential settlement when socketed CICs were used compared to the frictional case, as shown in Figure 4.12. Since the socketed CICs settled less than the frictional CICs (see Figure 4.8), differential settlement in the socketed case kept on increasing as the soft soil consolidated, so the tension in GR also kept on increasing over time, as shown in Figure 4.18.

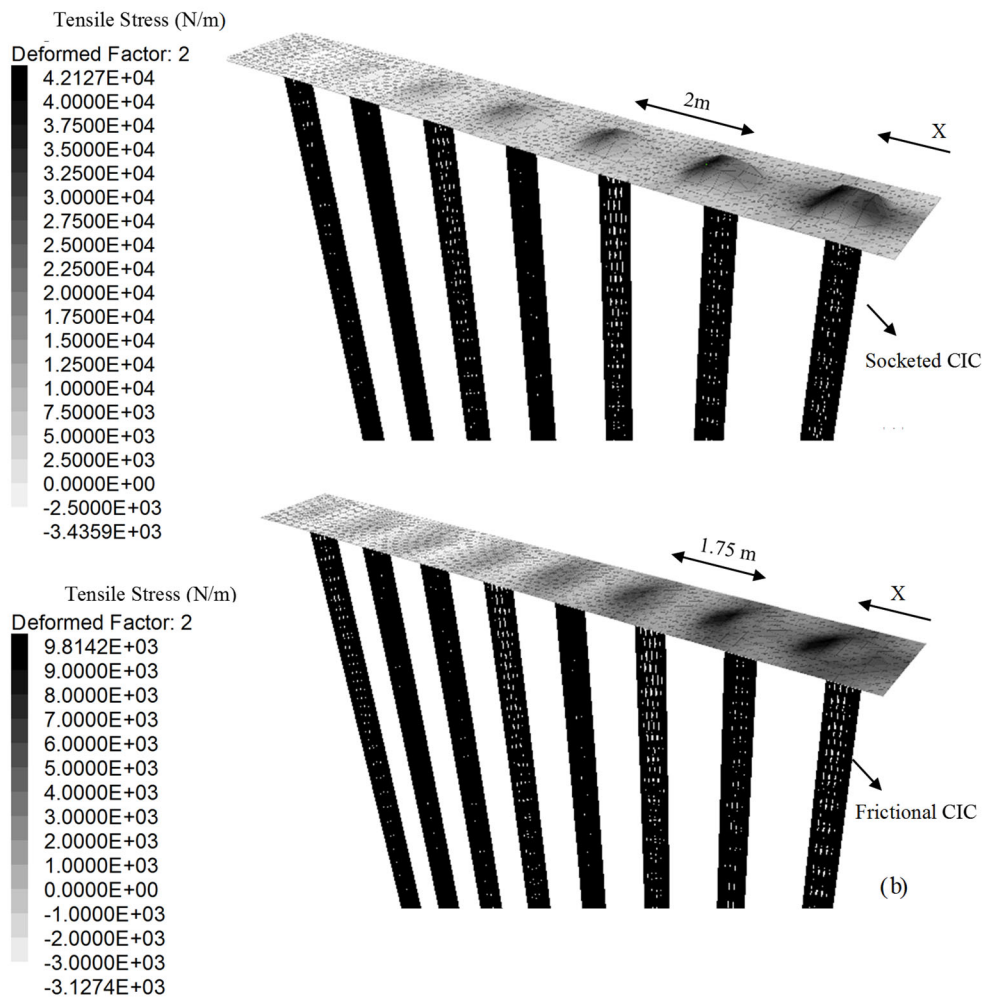


Figure 4.17 Contour of tensile forces in the geosynthetic layer at the end of consolidation for (a) socketed CICs (b) frictional CICs

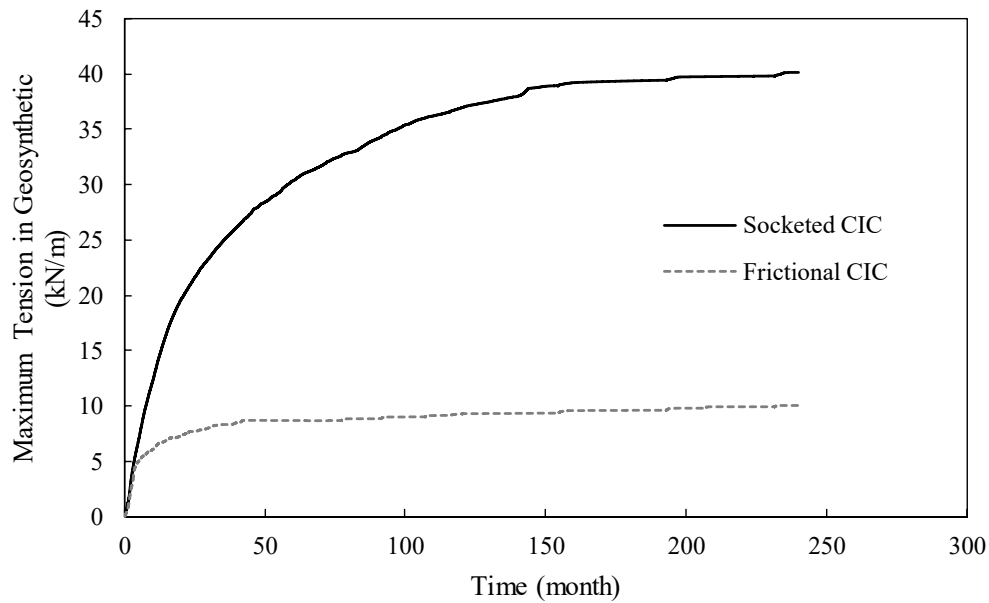


Figure 4.18 Change in the maximum tension in the geosynthetic layer vs. time at the edge of the socketed CIC1 and frictional CIC1

4.3.4 Axial Stresses in the CICs

Figure 4.19 compares the axial stresses in the socketed CIC 1 and frictional CIC 1, these CICs are the closest to the centreline of the two models (see Figure 4.2 and Figure 4.3), and therefore to the unit cell column model, which is why they were chosen. As Figure 4.19 suggests, the axial stresses transferred to the socketed CICs are consistently higher than the corresponding values for the frictional CICs. Socketed CICs are more rigid in their behaviour than the frictional CICs, so the differential settlement between the CICs and the surrounding soil (as shown in Figure 4.12) is higher, as is the membrane action of the geosynthetic layer, which then transfers more embankment load to the socketed CICs than the frictional CICs. Moreover, the lower

area replacement ratio leaves the socketed CICs with a larger tributary area, which means that each column carries an even larger load.

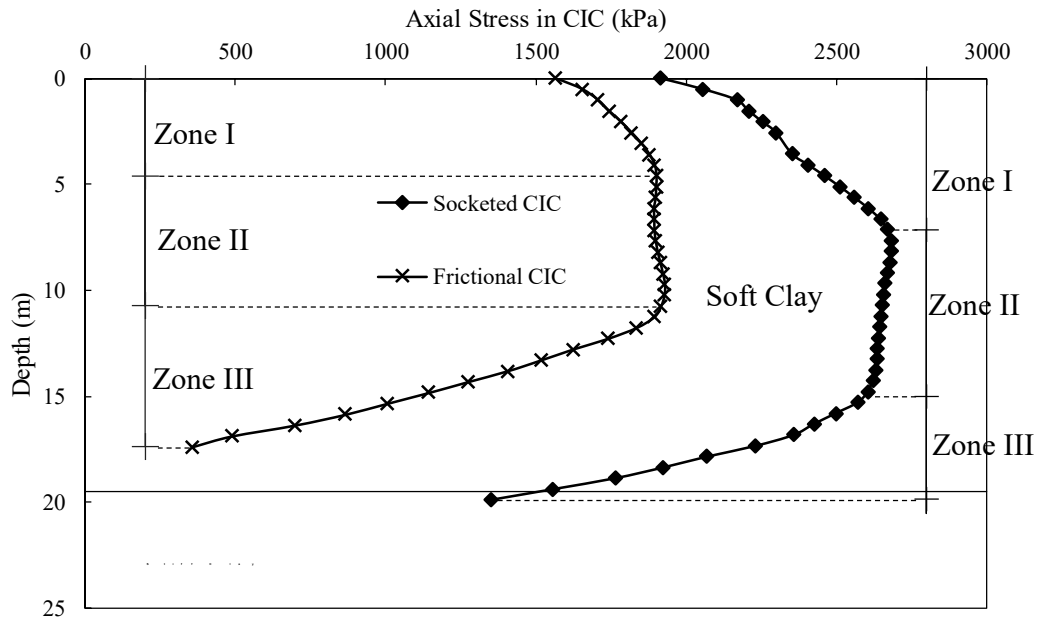


Figure 4.19 Axial stress at the end of consolidation in socketed CIC1 and frictional CIC1 versus depth

Figure 4.20 shows that in Zone I, the soft soil has settled more than the CIC, which generates a negative skin friction on the CIC and causes the level of axial stress to increase until it reaches a depth where the soil and CIC displacements are equal; this is interpreted as the neutral plane (refer to Figure 4.19, Zone II). Here the stress remains almost constant since the displacement of soft soil and the CIC are almost the same in Zone II. This positive skin friction reduces stress in the CIC as the column displacement becomes larger than the soil settlement (Figure 4.20, zone III), as shown in Zone III in Figure 4.19. It should be noted that distribution of shear stress along the column shaft depends on the degree of consolidation and as Chen et al. (2009) pointed out the shear stress on the column shaft may shift direction during consolidation.

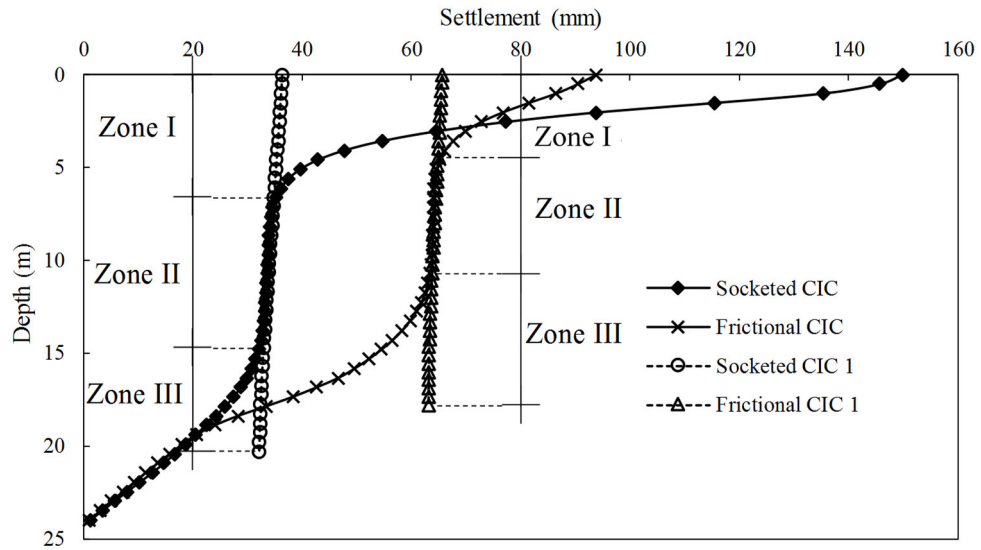
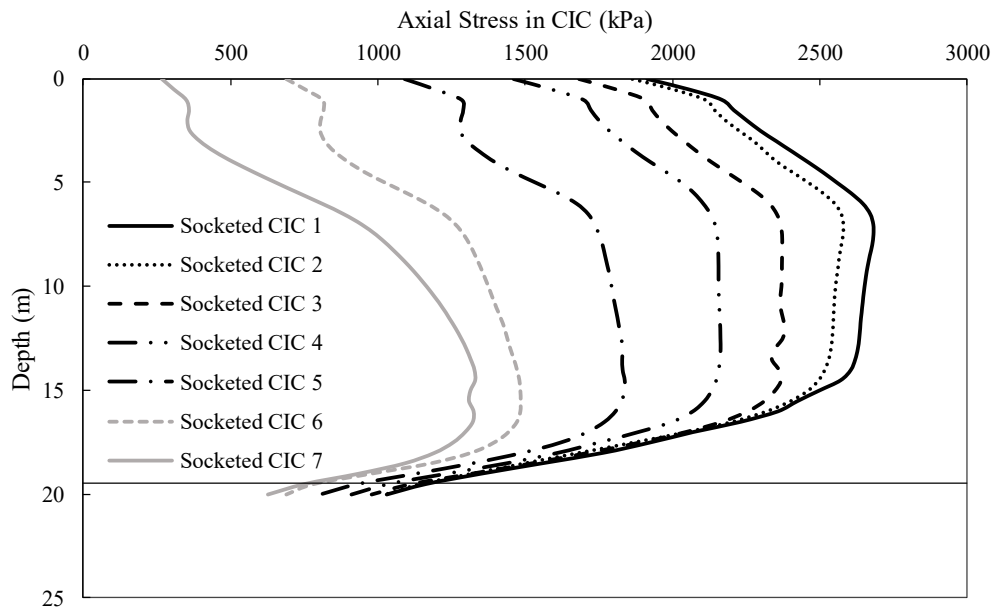


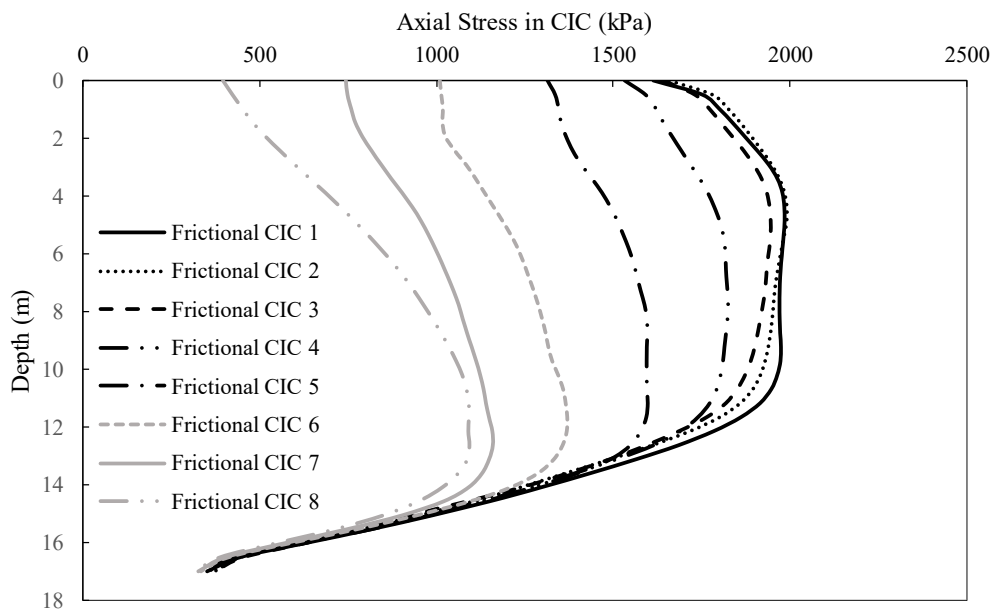
Figure 4.20 Settlement of the soil at the end of consolidation along Sections B-B and B'-B'

Figure 4.19 shows that the negative skin friction is higher for the socketed CIC and the negative friction zone (Zone I) is deeper than the frictional CIC because as Figure 4.20 shows, the difference in settlements in the socketed CIC and the soil in Zone I is much higher than the corresponding values for the frictional CIC case. Moreover, Figure 4.19 shows that the positive skin friction is lower for the socketed CIC and the length of the positive skin friction zone (Zone III) is shorter since in Zone III the difference in settlement between the columns and the soil is less for the socketed CIC.

Figure 4.21 a and b show the axial stresses for all the socketed and frictional CICs while Figure 4.8 shows the CIC settlement decreased moving away from the centreline of the embankment. Figure 4.21a and b also show that the depth of the neutral plane has increased, which means that for those CICs closer to the batter slope, the negative skin friction increased and the positive skin friction decreased.



(a)



(b)

Figure 4.21 Axial stress at the end of consolidation in (a) socketed CICs (b) frictional CICs

4.3.5 Predicted Lateral Displacement

Lateral displacement of soil near the toe of the embankment with depth along Section X-X for the socketed CICs (refer to Figure 4.2), and Section X'-X' for the frictional CICs (refer to Figure 4.3), are shown in Figure 4.22. Here, the lateral displacement of soil at the toe of the embankment on the soft soil surface for frictional CICs was less than the socketed case because more CICs were resisting lateral displacement induced by the embankment load. However, in the deeper layers closer to the CIC tip, lateral displacement of socketed CICs was less because as Figure 4.8 shows, the frictional CICs settled much more than the socketed CICs, and the soil near the tips of the frictional CICs displaced more laterally due to the soft soil below the tip. This means that more soil was displaced laterally in deeper layers in the frictional case than the CICs socketed in the stiff soil.

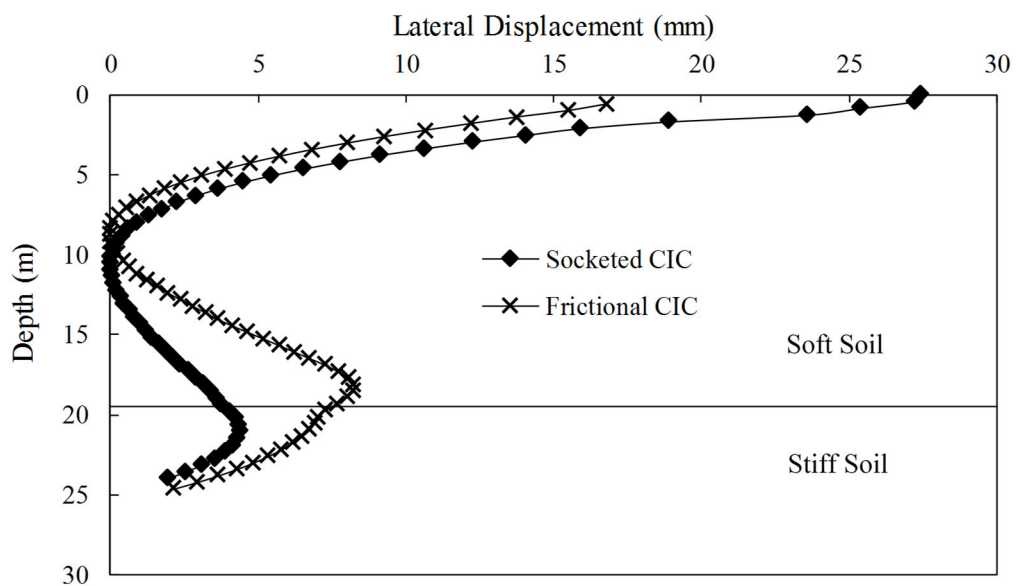
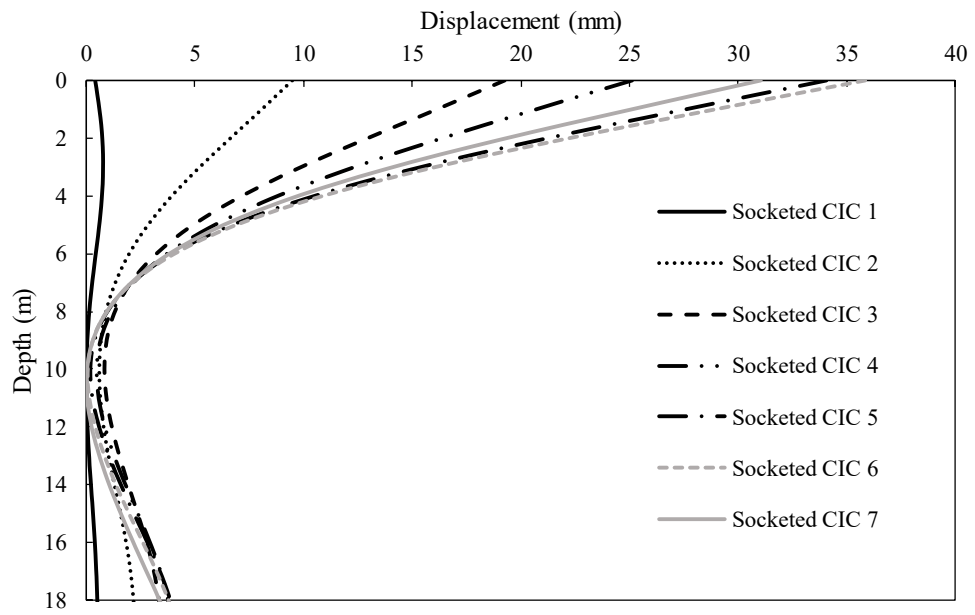
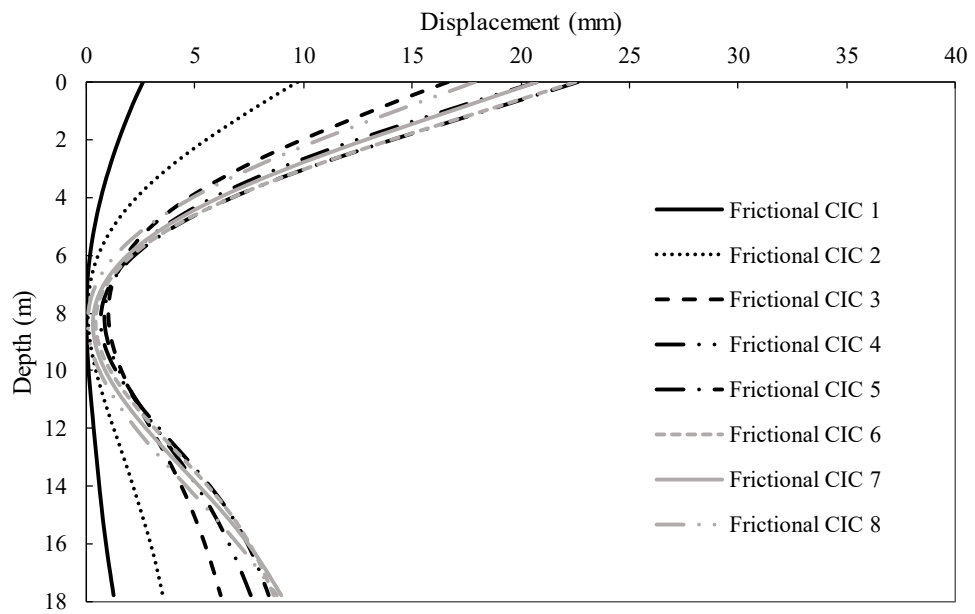


Figure 4.22 Lateral displacement at the end of consolidation in soil with depth along section X-X and X'-X'

Figure 4.23 a and b show the lateral displacement of all CICs with depth for socketed and frictional cases, respectively. Note there were more lateral deflection of the CICs closer to the toe of the embankment for both the frictional and socketed cases than the corresponding values for CICs closer to the centreline of the embankment. In both frictional and socketed cases, the tips of the columns moved vertically (see Figure 4.8) and displaced soil laterally (see Figure 4.22); as a consequence there was a large CIC deflection near the tip, as predicted in Figure 4.23. CICs socketed into stiff soil (Figure 4.23a) experienced smaller lateral displacement near the column tips than the frictional CICs (Figure 4.23b), but the CIC deflections near the ground surface were larger for the socketed CICs due to more soil movement, as shown in Figure 4.22. Figure 4.23 a and b also show that as the tip of the CIC closest to the middle of the embankment settled, it pushed the surrounding soil and the adjacent CIC away from the line of symmetry, while the adjacent CIC pushed the tip of the other CIC. This process created a ripple effect that caused lateral deformation to accumulate and lead to larger lateral displacement of CIC tips further away from the centreline of the embankment. Figure 4.24 a and b show the contours of lateral displacement predicted for embankments on socketed and frictional CICs. Figure 4.24 a shows that maximum lateral displacement predicted for socketed CICs was 48 mm, and 24mm for frictional CICs.

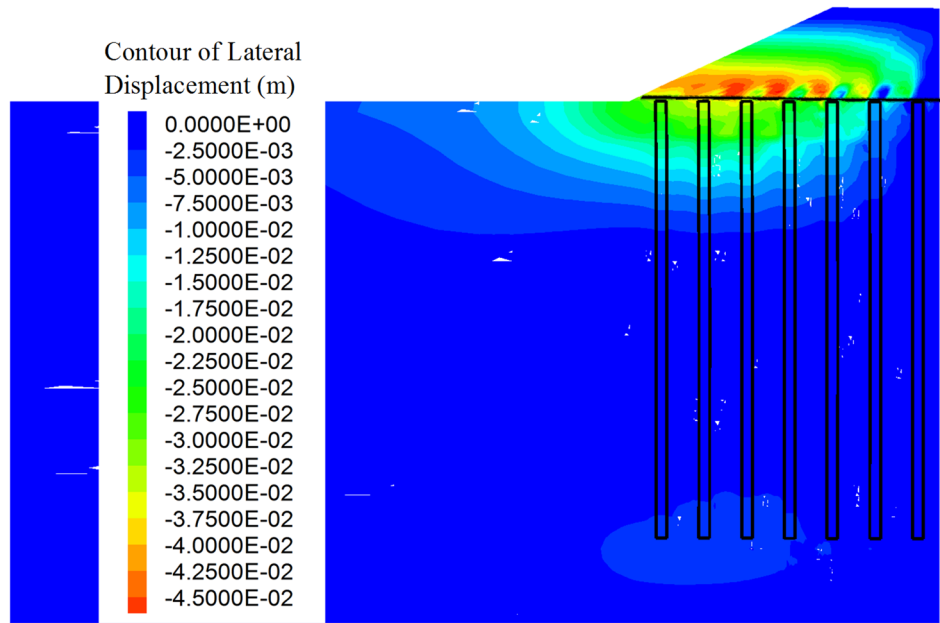


(a)

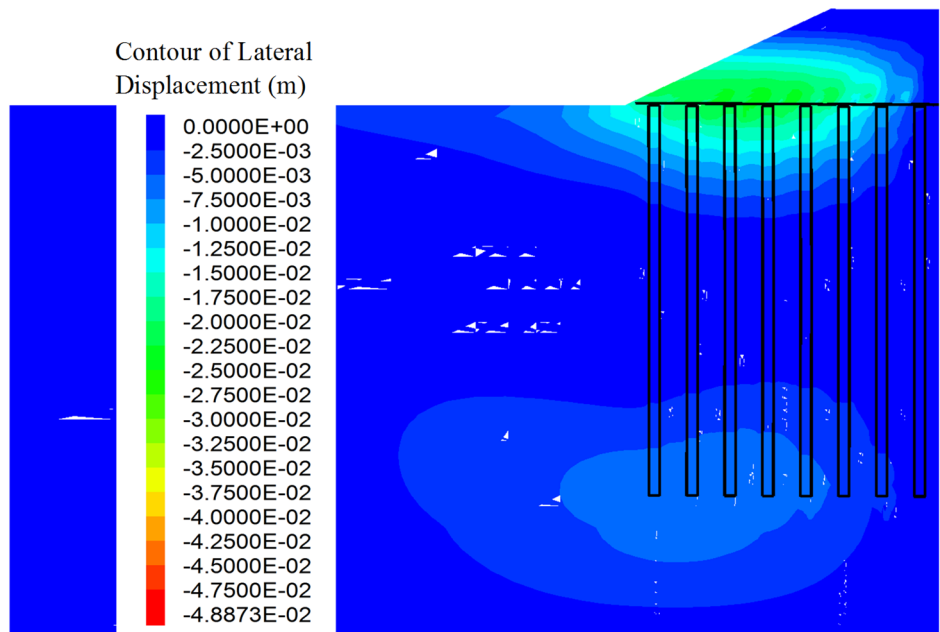


(b)

Figure 4.23 Lateral displacement at the end of consolidation of the (a) socketed CICs (b) frictional CICs with depth



(a)



(b)

Figure 4.24 Lateral displacement contours at the end of consolidation for (a) socketed CICs and (b) frictional CICs

Figure 4.26 a and b show the deformed shape of the socketed and frictional CICs, respectively. CICs deformed due to lateral displacement induced by the embankment load, vertical settlement, and tip displacement due to the vertical settlement of CICs relative to their original position.

4.3.6 Predicted Bending Moments and Shear Forces in CICs

Bending moments and shear forces were derived via Euler-Bernoulli's equation using the second and third derivatives of the lateral deflection of the piles, as follows:

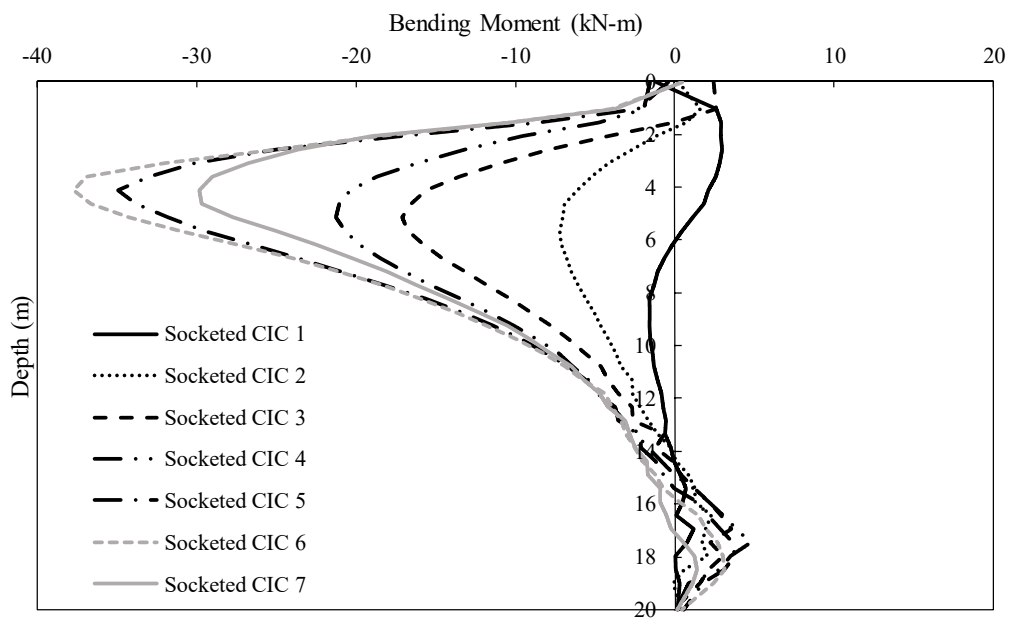
$$M(z) = EI \frac{d^2[d(z)]}{dz^2} \quad (4.11)$$

$$Q(z) = EI \frac{d^3[d(z)]}{dz^3} \quad (4.12)$$

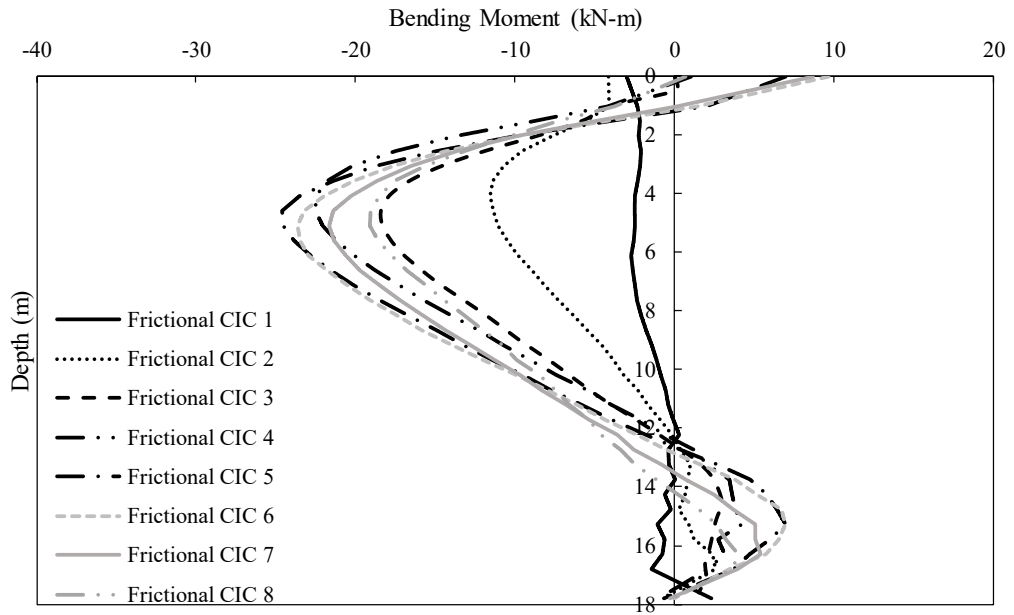
where E is the elastic modulus of the material of the pile ($E=10$ GPa for concrete), and I is the area moment of inertia of the pile cross-section ($I = 3.07 \times 10^{-3} \text{ m}^4$).

Figure 4.25 a shows the bending moments in CICs for the socketed case, and as seen in the predictions, the CICs closest to the toe of the embankment (e.g. CIC 6) experienced larger bending moments while the bending moments predicted in the CIC near the centreline were smaller and opposite in direction at a shallower depth. Moreover, Figure 4.22 shows that the predicted lateral soil displacements due to embankment load induces a counter clockwise rotation of the CICs close to the slope batter (see Figure 4.23 a), this is considered to be a negative direction bending moment in this study. The degree of settlement of ground near the centreline of the model (see Figure 4.8), also displaced the CIC head in a clockwise direction which in turn induced a positive bending moments in the CIC near the centreline. These findings are consistent with the results reported by Kitazume & Maruyama (2006) based on centrifuge tests for column improved soft soil.

As Figure 4.25 b shows, the bending moment in the frictional CICs was similar to the socketed CICs, while the maximum predicted bending moment for the frictional CIC was smaller than the corresponding value for socketed CIC. This occurred since the socketed CICs embedded in the firm layer resisted lateral deflection and rotation induced by the movement of soil; this then resulted in more bending moments. Figure 4.23 a and b show that the lateral displacements predicted for socketed CICs were more than the frictional ones, and therefore, there were larger negative bending moments in the socketed CICs. However, this pattern changed in deeper layers of soil since the lateral deflections predicted for the frictional CICs were greater near the tip of the CIC (as shown in Figure 4.23); this resulted in comparatively larger bending moments for the frictional CICs.



(a)



(b)

Figure 4.25 Bending moment at the end of consolidation in (a) socketed CICs (b) frictional CICs versus depth

Zones that exceeded the bending capacity of the CICs are highlighted in red in Figure 4.26; this Figure shows that the socketed CICs 5, 6, and 7 exceeded their bending capacity and had already cracked, whereas only CIC 7 for the frictional CICs exceeded this capacity. Yielding occurs when the sum of the axial stress on the CIC (σ_N) and the extreme stress due to bending moment (σ_M) exceeds the maximum tensile or compression strength of the concrete (Eqs. (4.13) and (4.14)):

$$\sigma_M = \frac{M}{\pi D^3/32} \quad (4.13)$$

$$f'_{ct} < \sigma_N + \sigma_M < f'_c \quad (4.14)$$

where σ_M is the extreme stress due to bending, M is the bending moment, D is the CIC diameter, σ_N is the axial stress in CIC, f'_{ct} is the characteristic uniaxial tensile strength of concrete, and f'_c is the characteristic compressive (cylinder) strength of concrete at

28 days. For example, the axial stress for socketed CIC 6 at a depth of 4m was 900 kPa, and the tensile stress in the extreme tensile fibre due to bending moment was $(\sigma_M = \frac{M}{\pi D^3/32} = \frac{35}{\pi(0.5)^3/32}) 2850 \text{ kPa}$. Therefore, $\sigma_N + \sigma_M = 900 - 2850 = -1950 \text{ kPa}$ exceeded the tensile strength of the concrete by a large amount, whereas the axial stress for frictional CIC 6 at a depth of 4m was 1150 kPa, and the tensile stress in the extreme tensile fibre due to bending moment was $(\sigma_M = \frac{M}{\pi D^3/32} = \frac{22}{\pi(0.5)^3/32}) 1790 \text{ kPa}$. Therefore, $\sigma_N + \sigma_M = 1150 - 1790 = -640$ did not exceed the tensile strength of the concrete, and as Figure 4.26 shows, it did not yield.

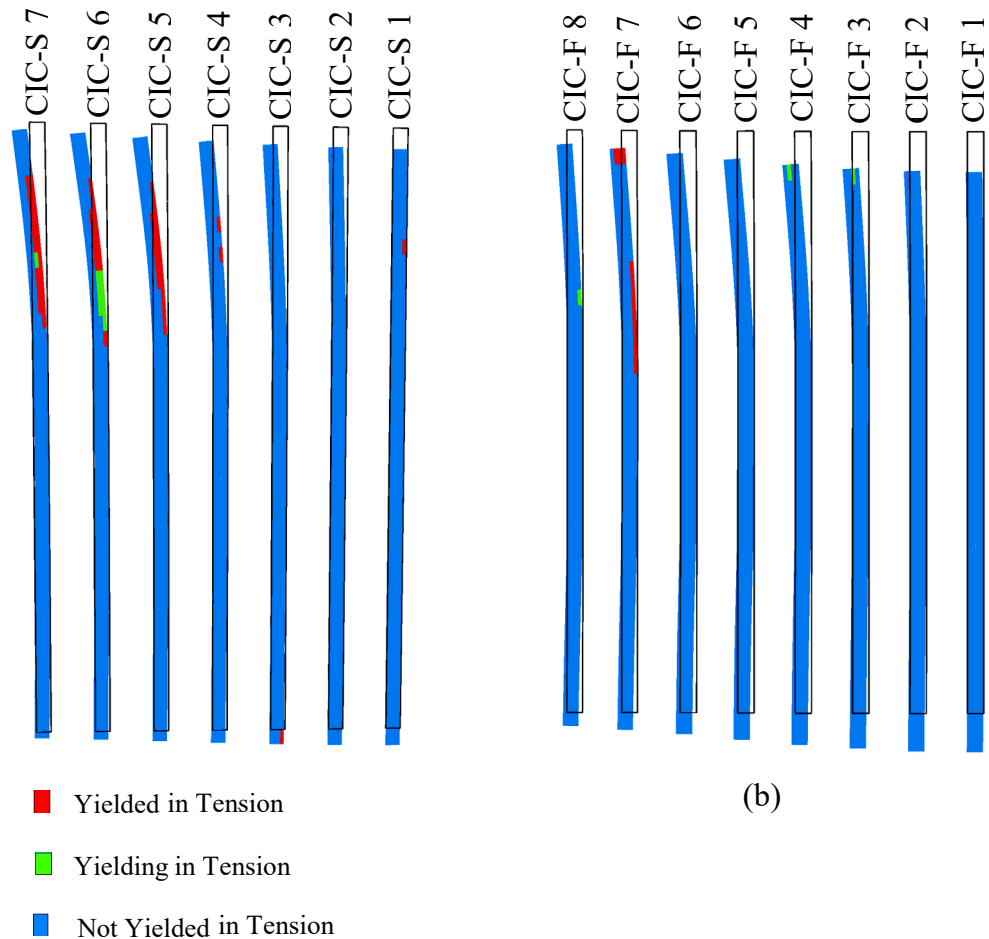
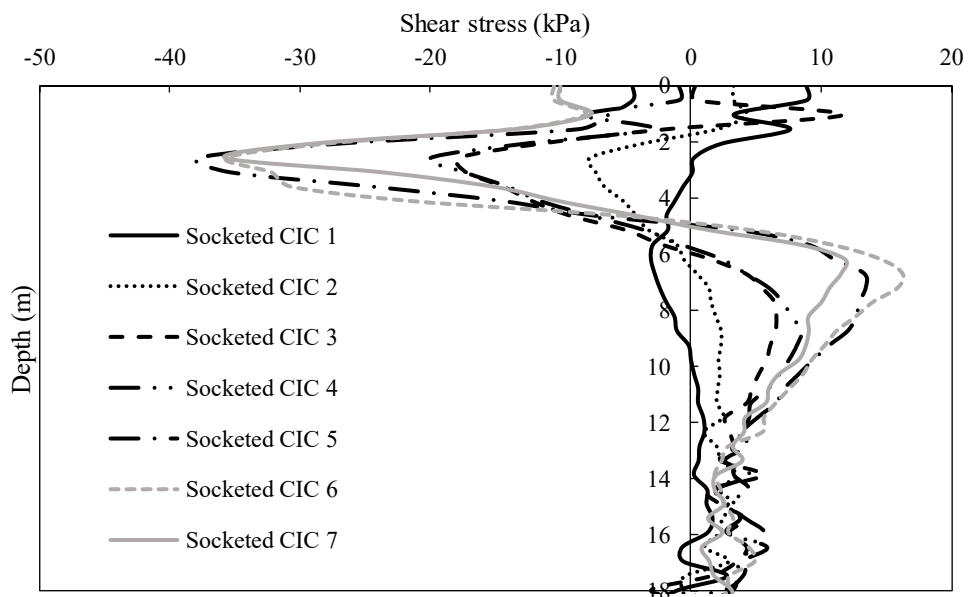


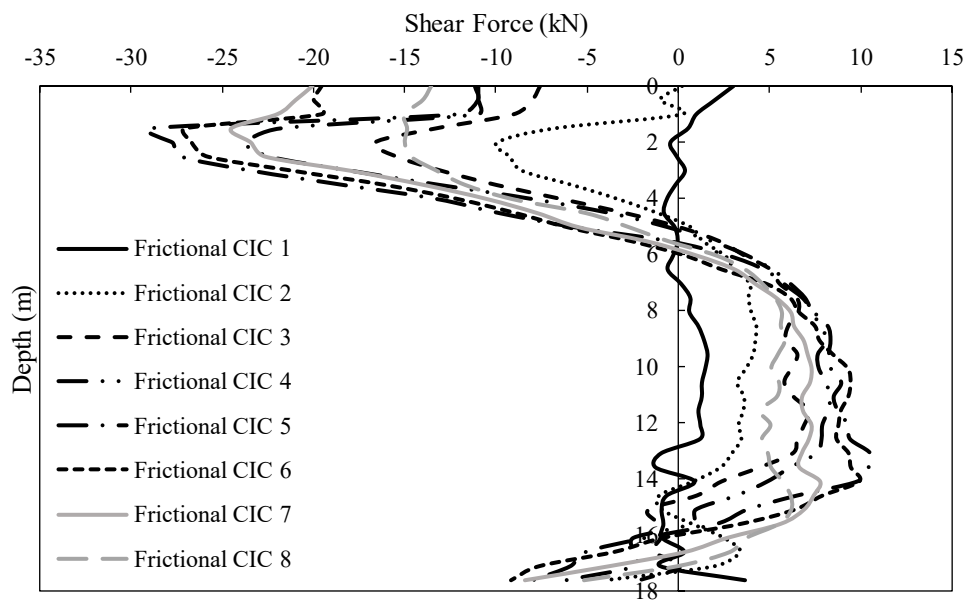
Figure 4.26 Yielded zones in tension at the end of consolidation on the (a) socketed CICs and (b) frictional CICs

It should be noted that there is a distinction between piled embankments and CIC-supported embankments. CICs, as a ground improvement technique, are designed as geotechnical elements with a higher level of redundancy (King et al. 2018) to improve the overall performance of the soft soil as a mass, whereas piles are considered as structural elements and are designed to take all the embankment loads and transfer the loads to a competent layer; and as such, are subject to rigorous tests and design criteria. CICs are semi-rigid inclusions constructed using unreinforced concrete where cracks could potentially develop as long as the deformations are within the limits (Wong & Muttuvel 2012a). Kitazume & Maruyama (2007) using centrifuge modelling of deep mixing method (DMM) columns, concluded that the columns provided support for the embankment even after cracking. They also concluded that all the columns did not fail simultaneously, but they failed one by one.

Figure 4.27 a and b show the shear forces in cross-section of the CICs with depth for the socketed and frictional CICs, respectively, where the maximum shear force for socketed CICs (i.e. 38 kN) was higher than the frictional CICs (i.e. 29 kN); this difference can be attributed to the larger lateral displacement for the socketed case as, shown previously in Figure 4.22 and Figure 4.24.



(a)



(b)

Figure 4.27 Shear forces at the end of consolidation in (a) socketed CICs and (b) frictional CICs

4.4 Verification Exercise Against Analytical Solution

In this section, a comparison is made between the numerical and analytical results for the central socketed CIC1 which is the closest to the model centreline, and therefore, closest to a unit cell idealisation. As the CICs are designed to share part of the load with the surrounding soil, the design methods (Hewlett & Randolph 1988; BS 8006 2010; Guido 1987; Terzaghi 1943; Carlsson 1987) which do not consider the sub-soil effect are not suitable for CIC design. Stewart & Filz (2005) also emphasised the great significance of the compressibility of the soil and the importance of considering it as a factor in the design. The limit equilibrium model by Hewlett & Randolph (1988) was adopted by the French ASIRI (2012), and also suggested in BS 8006 (2010) as an alternative to the empirical approach based on Jones et al. (1990). Low et al. (1994) improved the Hewlett & Randolph (1988) method by considering a geosynthetic layer, and the sub-soil effect. They also developed equations and charts to assess the geosynthetic effect in the load transfer.

Low et al. (1994) assumed the deformed shape of the geosynthetic as a circular arc with a radius R , subtended angle of 2θ , and the maximum settlement between the two piles as t . The tension in the geosynthetic is calculated using the following equations:

$$\sigma_s = \frac{\gamma(s-a)(k_p-1)}{2(k_p-2)} + \left(\frac{s-a}{s}\right)^{k_p-1} \left[\gamma H - \frac{\gamma s}{2} \left(1 + \frac{1}{k_p-2}\right) \right] \quad (4.15)$$

$$\theta = \text{Sin}^{-1} \left[\frac{\frac{4t}{(s-a)}}{1 + 4 \left(\frac{t}{s-a}\right)^2} \right] \quad (4.16)$$

$$R = \frac{s-a}{2 \text{Sin}\theta} \quad (4.17)$$

$$\frac{T}{R} = p_0 = \left(\sigma_s - \frac{tE_s}{D} \right) \quad (4.18)$$

$$k_p = \frac{1 + \text{Sin}\phi}{1 - \text{Sin}\phi} \quad (4.19)$$

where k_p is the passive lateral earth pressure calculated using ϕ , the friction angle of the embankment fill, σ_s is the vertical stress acting mid-way between the columns, γ is the soil unit weight, s is the pile spacing, a is the pile cap width, T is the tension in the geosynthetic, p_0 is the uniform pressure applied on the geosynthetic, E_s is the elastic modulus of the foundation soil, and D is the depth of the foundation soil. For trial values of t , the calculated T from Eq. (4.18) are compared with the values of T calculated from Eq. (4.20):

$$T = J\varepsilon \quad (4.20)$$

$$\varepsilon = \frac{\theta - \text{Sin}\theta}{\text{Sin}\theta} \quad (4.21)$$

where ε denotes the axial strain in the geosynthetic, and J is the geosynthetic tensile stiffness. The trial continues to reach the same values for T from Eqs. (4.18) and (4.20). The elastic modulus for the mid-depth of the soft soil was considered as the average elastic modulus for the sub-soil, and was derived using the MCC parameters. Table 4.4 compares the values of soft soil settlement, stress on the soft soil, stress on the CIC, and tension in the geosynthetic from the numerical analysis conducted in the current study with the analytical values obtained from Low et al. (1994) solution for the socketed CIC1, and a reasonably good agreement was observed between the two. The disparities in the tensile force in the geosynthetic layer could be attributed to the batter slope effect and the lateral displacement of the embankment as this is not accounted for in the analytical approach.

Table 4.4 Comparison of numerical predictions in this study and existing analytical solutions for the socketed CICs

Parameter	Soft soil settlement (mm)	Stress on the soft soil mid-span between CICs (kPa)	Stress on CIC head (kPa)	Tensile stress in the geosynthetic (kN/m)
Numerical Predictions (this study)	151	46	1913	38.8
Analytical Calculation (Low et al. 1994)	159	41.8	1727	30

4.5 Summary

This chapter has attempted to compare the frictional and socketed Concrete Injected Columns (CICs) for the transition zone of improved ground by considering two possible alternatives and keeping the same volume of concrete. The three-dimensional coupled flow-deformation numerical modelling carried out in FLAC^{3D} captured the variations of permeability and the void ratio during consolidation that were necessary to predict reliable excess pore water pressure and deformation. Cam-Clay and Hoek-Brown models were utilised to simulate the behaviours of soft soil and CICs, respectively; and the predictions of soil settlement and lateral displacements, and the stresses in CICs and tension in the geosynthetic layer were compared. A comparison was also made between the numerical results and Low et al. (1994) analytical solution, and a reasonable agreement was perceived. The numerical predictions showed the frictional CICs performed better than the socketed CICs for the soft soil improvement used in this study, and frictional CICs resulted in less settlements, less lateral displacements, and less forces in the geosynthetic. Indeed, the results clearly show that an increase in the area replacement ratio, and therefore, mass

improvement of composite ground rather than only relying on transferring the embankment loads to a deeper stiff layer in the transition zone, could reduce settlements better. However, the performance of frictional and socketed CICs may vary depending on parameters such as soft soil properties, or different CIC arrangements, and modelling in the longitudinal cross-section should also be undertaken in the future to investigate the CIC in the traffic direction. The CIC method can be economically competitive if designed as a ground improvement method used in conjunction with the surrounding soft soil. It was demonstrated that when a flexible granular LTP was used, the soft soil between columns would settle and induce a significant differential and total settlement on the embankment surface. Indeed, the efficiency of socketed CICs in reducing settlement depends on the LTP to transfer all embankment loads to the stiff layer in order to prevent large soil settlement between columns. CIC was developed to bridge the gap between piling and ground improvement, and as such, attempts to share part of the load with the surrounding soft soil where possible rather than completely bypassing it. Therefore, it is recommended that engineers consider using frictional CICs as an option to design the transition zone for CIC-improved ground.

CHAPTER 5

5 COMPARISON OF COUPLED FLOW-DEFORMATION AND DRAINED ANALYSES FOR ROAD EMBANKMENTS ON CIC-IMPROVED GROUND

5.1 General

Usually, to avoid the complications of the coupled modelling, long term or short term behaviour of the model is investigated only by assigning drained or undrained moduli to the material. In this research, coupled hydraulic and mechanical analysis was performed for a long period and was compared with the drained analysis results.

5.2 Numerical Modelling

Finite difference program FLAC^{3D} (version 5.01) was used in this study for numerical modelling. Two types of analyses were performed to compare the results for both approaches. The geometry and the mesh used for the models are presented in Figure 5.1 and Figure 5.2. Since the embankment is symmetrical in cross-section, half of the embankment has been modelled. The model is considered to be very long in the traffic direction; therefore, one row of columns was simulated to save the calculation time. The columns are circular in cross-section, and interface elements were considered between the columns and soil to allow slip and separation. Soft clay and the embankment soil were modelled as elastic perfectly plastic material using Mohr-Coulomb failure criterion, and the CICs were modelled as elastic elements. The geosynthetic layer was simulated using the in-built geogrid element in FLAC^{3D}. These

elastic geogrid elements are only able to sustain in-plane forces. Table 5.1 presents the properties considered for the soft clay, embankment, columns, and the geosynthetic layer. The initial in-situ stresses were established for the existing ground condition using the initial stresses and gravity in FLAC^{3D}. The initial static pore pressures were also generated in the model and the water level was specified. If FLAC^{3D} is configured for fluid flow, a transient fluid-flow analysis can be performed, and pore pressures, as well as the phreatic surface are able to change. Pore pressures are calculated at grid points, and zone values are derived using averaging. Both effective-stress (static pore-pressure distribution) and undrained calculations can be carried out in the fluid mode. In addition, a fully coupled analysis can be performed, in which changes in pore pressure generate deformation, and volumetric strain causes the pore pressure to evolve. The change in the pore water pressure was monitored as the stages of construction were carried out and the road was opened to traffic (application of surcharge on the embankment). The embankment height was considered 2 m, and its construction was assumed to take place in four stages of 0.5m thickness. A distributed load of 12 kPa, simulating the traffic load, was then applied on the embankment crest. For the drained simulation, drained parameters were assigned to the material to study the behaviour of the system in long term. The consolidation for the coupled analysis was performed for 1 week for every stage of the embankment construction and for 28 months after the road was opened to traffic (12kPa surcharge application). The shear behaviour of the geogrid-soil interface is cohesive and frictional in nature and a reduction factor of 0.8 was considered as a reduction coefficient of interaction for the interface strength (cohesive strength, c ; and friction angle, ϕ) between the geosynthetic and the embankment soil (Huang & Han 2009). As shown in Figure 5.1, soil can move freely in the vertical direction on the four boundaries, but has been fixed in the horizontal direction, and the base of the model has been fixed in all the directions. However, in reality CICs are usually founded in stiff clays; hence, providing a certain amount of deflection at the base of the inclusions, and reducing the stress differential between the soil and inclusions.

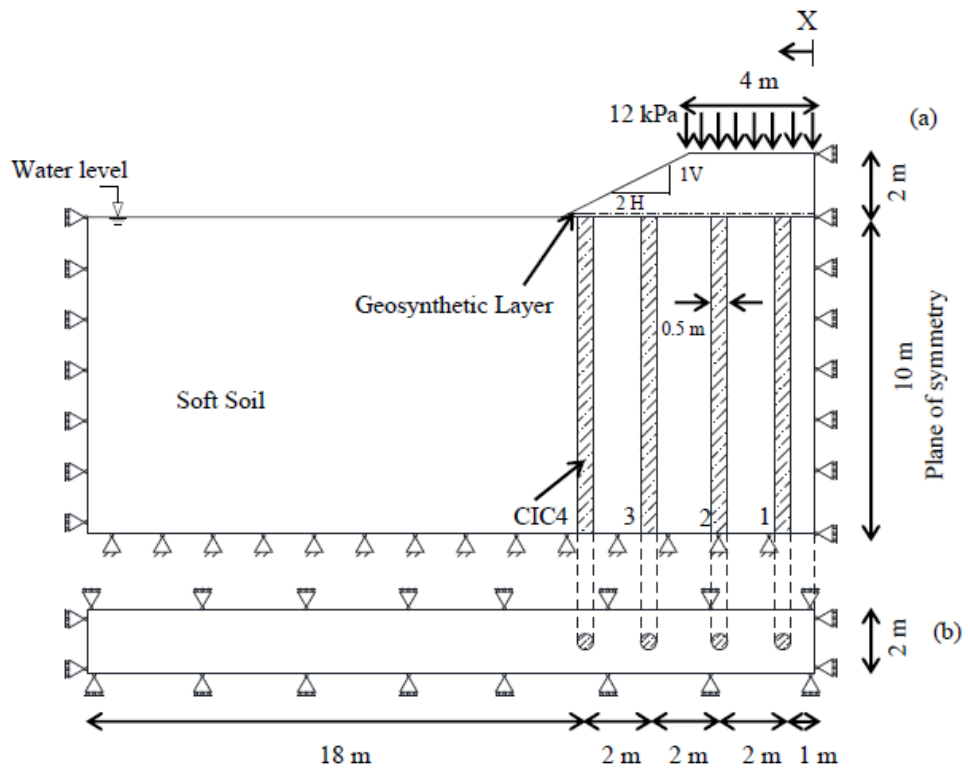


Figure 5.1 Model geometry for end-bearing CIC (a) cross-section view and (b) plan view

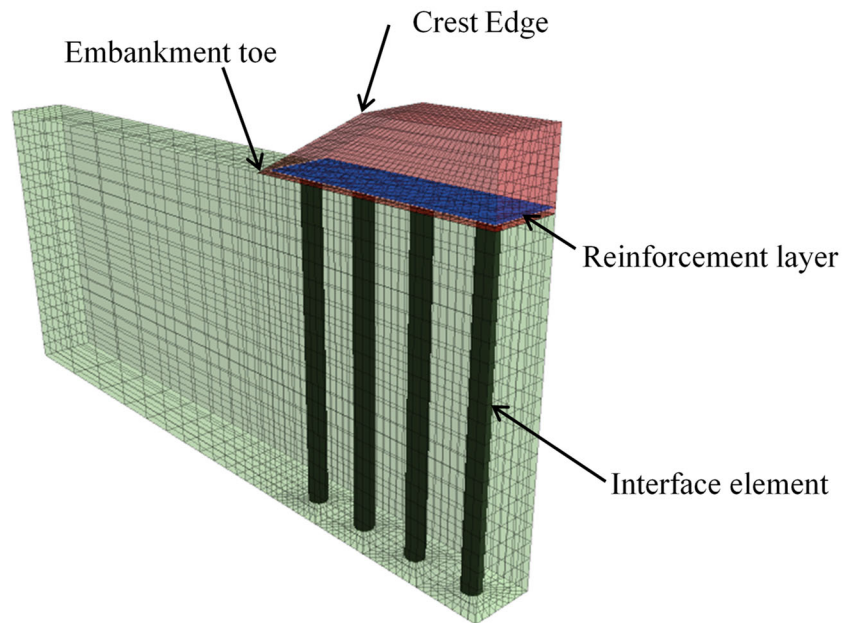


Figure 5.2 Model mesh with CIC-soil interfaces

Table 5.1 Material properties adopted in this study

Materials	c' (kPa)	ϕ'	E' (MPa)	ν	γ (kN/m ³)	k (m/s)
Embankment soil	5	32	30	0.3	20	-
Soft Clay	0	26	2	0.3	17	1×10^{-9}
CIC	-	-	10,000	0.15	24	-
Geosynthetic layer			$J = 1100$ kN/m	$k_s = 85000$ kN/m/m		

Note: c' = effective cohesion, ϕ' = effective friction angle, E = elastic modulus, ν = Poisson's ratio, γ = saturated unit weight, J = geosynthetic stiffness ($J=E.t$, t = geosynthetic thickness), k_s = interface stiffness between the geosynthetic reinforcement and the soil, k = soft soil permeability

5.3 Results and Discussion

5.3.1 Settlement

Figure 5.3 shows the profile of the settlement at the base of the embankment for the end-bearing CIC. The maximum settlement occurs in the middle of the embankment crest for both cases of coupled and drained analyses; however, it is 57mm for the coupled analysis while the drained analysis shows a maximum of 43mm settlement; showing 32% more settlement for the coupled analysis. The settlement on the crest level is also consistently higher for the coupled analysis. Figure 5.4 demonstrates the differential settlement happening at the base of the embankment. Differential settlement here is defined as the difference in the settlement of the two adjacent zones. It is also evident that the coupled analysis yields a higher differential settlement compared to the drained model. Excess pore water pressure generated in the coupled analysis causes the effective stress and shear strength to reduce; and therefore, more deformation is observed in the coupled analysis. Due to the soil plasticity, deformation of the soil is stress path dependent. Thus, the difference in the stress path for the two approaches results in a difference in predictions.

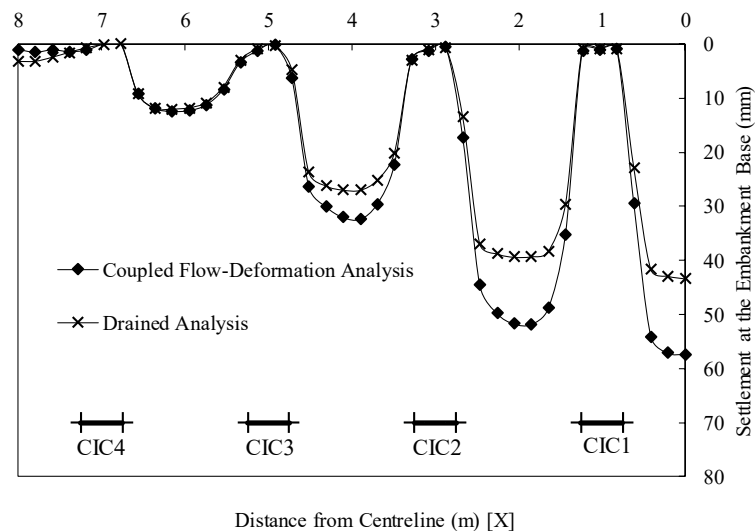


Figure 5.3 Settlement at the base of the embankment

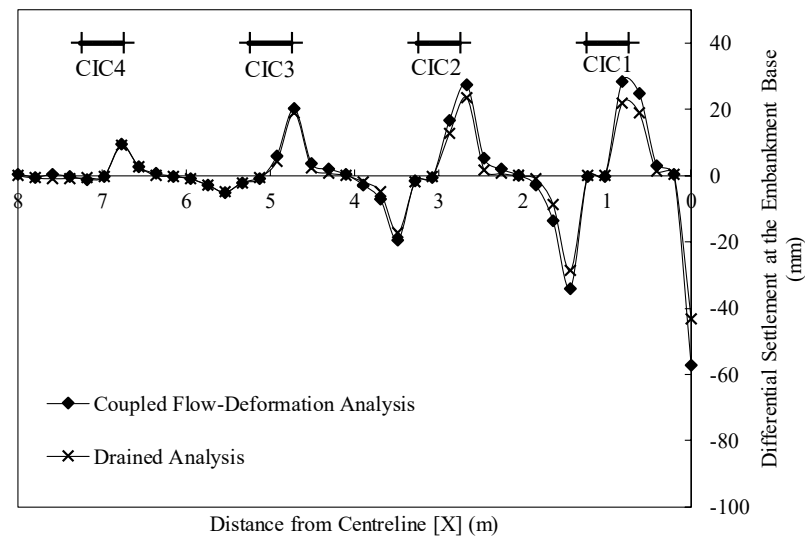


Figure 5.4 Differential settlement at the base of the embankment

5.3.2 Tension in the Geosynthetic Layer

Figure 5.5 shows the tension in the geosynthetic layer in the direction perpendicular to the traffic and through the columns centre. It can be noted that the maximum tension in the geosynthetic is underestimated in the drained analysis. The maximum tensile force in the drained analysis is 16 kN/m, while for the coupled analysis it is 26 kN/m, which shows an increase of 62%. This could be attributed to the underestimation of differential settlement and also the lateral displacement in the drained analysis. Differential settlement causes the membrane action in the geosynthetic, and the lateral spreading of the embankment generates a tensile force in the reinforcement layer. The graph also demonstrates that the maximum tension happens at the edge of the columns in either case, where the maximum differential settlement occurs as is evident in Figure 5.5. The minimum force in geosynthetic is generated in the mid-span of the columns for the same reason. More investigation is needed to see the differences in the results for different embankment heights.

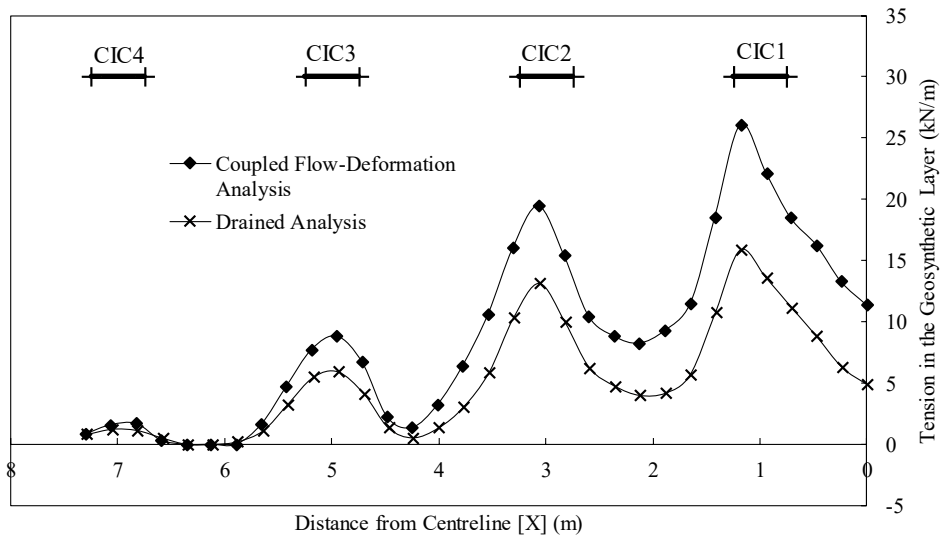


Figure 5.5 Tension in the geosynthetic layer

5.3.3 Lateral Displacement

Figure 5.6 compares the lateral displacement for drained and coupled analyses. It can be observed that the lateral displacement is significantly higher for the coupled analysis. The maximum lateral displacement for the drained analysis is 23mm while for the coupled analysis it increases to 38mm; a difference of 65%. This difference in the two modelling approaches is attributed to the different stress paths in modelling. The effect of reduced shear strength due to the increased pore water pressure is more pronounced in the lateral displacement as the generated shear is more due to the batter slope effect. The contours of lateral displacement have been presented in Figure 5.7 and Figure 5.8 to show the pattern of lateral displacement. The graphs show a similar pattern for both cases with the maximum displacement occurring close to the embankment toe; however, the values for the coupled case are significantly higher.

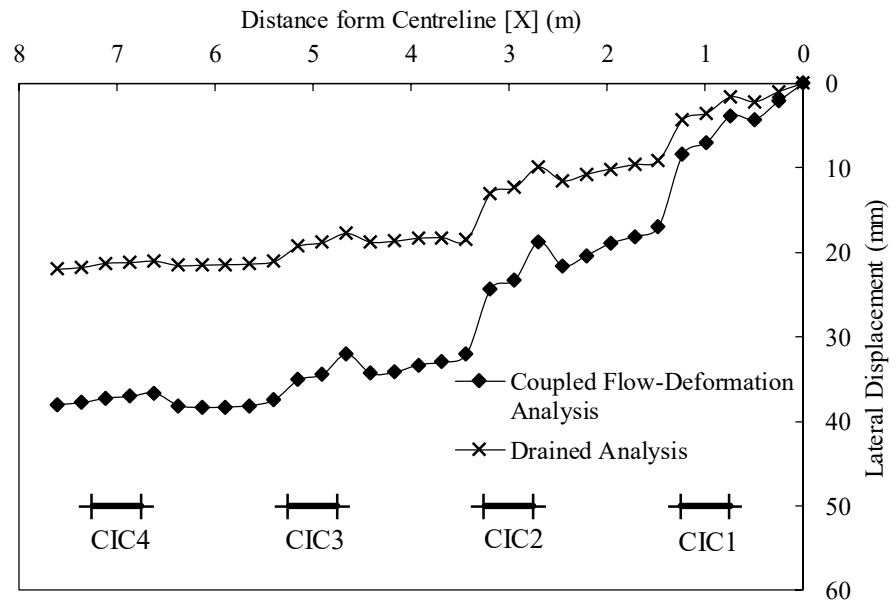


Figure 5.6 Lateral displacement at the geosynthetic level

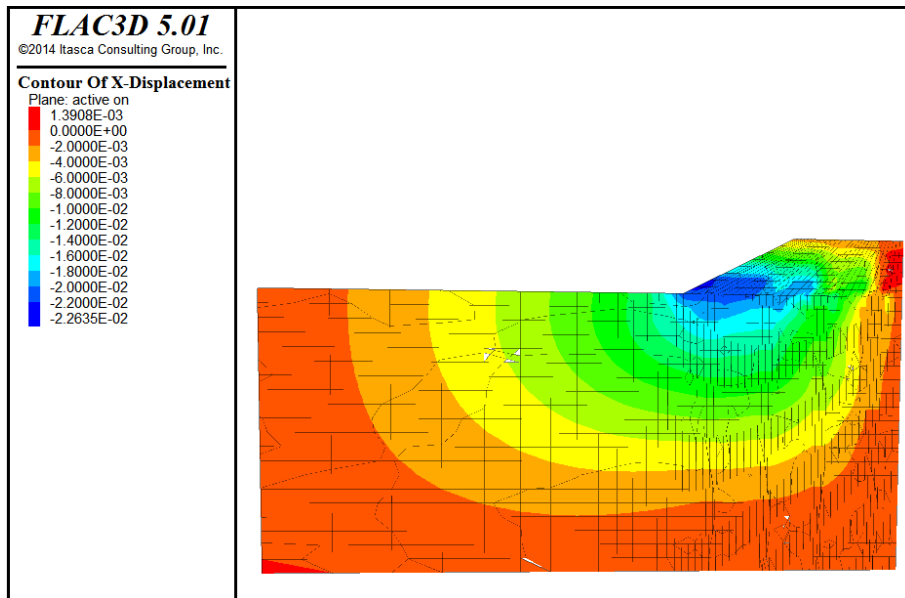


Figure 5.7 Lateral displacement contours for drained analysis (S_{max} : 23mm)

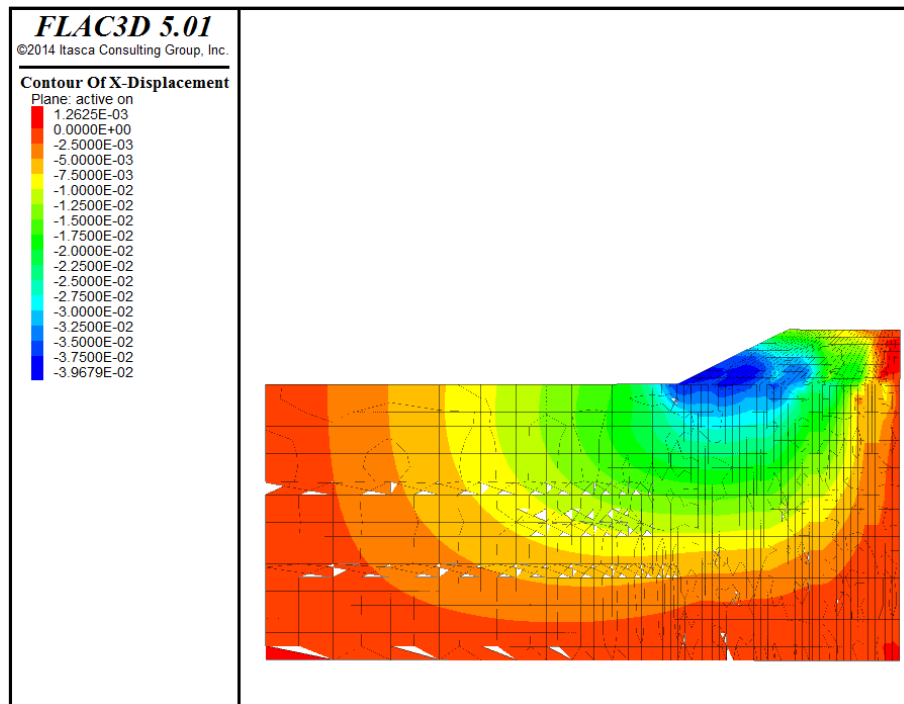


Figure 5.8 Lateral displacement contours for coupled flow-deformation analysis (S_{max} : 38mm)

5.3.4 Summary

Drained analysis is usually preferred to coupled flow-deformation simulation in the design process due to its convenience and short computation time. However, the simulations in this paper showed that drained analysis yields considerably lower estimates compared to the coupled analysis, especially lateral displacement; and therefore, the forces generated in the reinforcement layer. This requires more investigation and a comparison of the numerical results with the real field monitoring values.

Soil plasticity leads to the stress-path dependent behaviour of the soil. Although the final stress state is the same for the both approaches, the resulting deformation is not necessarily the same as they follow different stress paths to reach the final stress state. The generated excess pore water pressure causes a reduction in the soil strength and leads to a larger deformation in the coupled flow-deformation

analysis. More investigation is also required to evaluate the slope stability safety factors. Therefore, it is recommended to the practicing engineers to adopt the coupled analysis approach as the drained simulation may lead to an unsafe design.

CHAPTER 6

6 CONCLUSIONS AND RECOMMENDATIONS

6.1 Summary

This thesis provided an introduction and a review of the existing literature of the column-supported ground improvement methods in Chapters 1 and 2. Chapter 2 presented an introduction on CIC ground improvement method, construction process and the benefits and the draw backs of this system. A brief summary of the methods used for CIC design with an emphasis on ASIRI (2012) guideline were also presented. Furthermore, Chapter 2 summarised the scaled laboratory experiments on ground improvement techniques such as stone columns, deep cement mixing method, and piled-embankments. The studies were categorised into three groups based on the focus of their investigation. The three groups consisted of studies investigating the stress concentration ratio as one of the important parameters in design, failure pattern of the improved ground, and the parametric studies. The distinction between load transfer mechanism in raft foundations and the foundations on piles with an interposed granular layer was highlighted. Then, the modelling considerations in physical modelling of a pile was investigated.

The next section provided a background on numerical simulation of the columnar ground improvement methods. Drawing on several studies, it was explained that the simplicity and computation speed for unit cell numerical modelling comes at the cost of inaccuracy. The two-dimensional idealisations also did not capture the accurate three-dimensional behaviour of the columns and the embankment. It was shown that in order to capture the real behaviour of the column-supported

embankments, and especially to estimate the tensile forces mobilised in the geosynthetic, three-dimensional simulation is a necessity. A review of the constitutive models for plain concrete simulation was also presented.

Chapter 3 provided a dimensional analysis for the scaled physical modelling of the CIC-improved ground. The dimensional analysis and materials were explained in detail for the different components of the system such as the CICs, LTP, the geosynthetic layer, and the soil mix. Chapter 3 also provided the details of the numerical simulation in FLAC^{3D} and the comparison between the laboratory measurements and the numerical predictions. Further numerical results were also provided in Chapter 3 to better understand the load transfer mechanism in CIC-improved ground.

Chapter 4 compared the two options of closely spaced frictional CICs with larger spaced socketed CICs for the design of transition zone in CIC-improved ground. The two models were equivalent as they had the same length of CICs or the same volume of the concrete used in construction. The comparison was made in terms of vertical settlement, lateral displacement, mobilised tensile stresses in the geosynthetic, excess pore water pressure, stress in the soft soil, and axial stress, bending moment, and shear forces in the CICs.

Chapter 5 provided a numerical comparison between drained and coupled flow-deformation analyses. A CIC-supported embankment was simulated and the results were compared for vertical settlements, lateral displacements, axial stresses in the CICs, and the tension mobilised in the geosynthetic layer.

6.2 Key Conclusions

This study made an attempt to investigate the stress transfer mechanism in concrete injected column (CIC) -improved ground by means of physical modelling, and also compare two equivalent cases of frictional and socketed CICs for the transition zone design.

In the first section of this study, the physical modelling of the CIC-improved soft soil was conducted. Experiment design and material properties were determined based on scaling laws. CICs were installed by pushing a hollow specially designed closed-end pipe into the preconsolidated soft clay using an actuator, and CICs were constructed of plain concrete with a high slump and 50% fly ash content. A load transfer platform (LTP) was simulated using granular material and a geotextile layer. A timber washer was constructed to correctly simulate the boundary condition of the geotextile layer and to prevent pull-out due to the scaled length. The applied load on the improved ground was simulated using a rigid platen in stages, and earth pressure cells (EPCs) on CICs and the soft clay were utilised to monitor the variations of the stress concentration ratio (SCR). The findings of this study indicated that the SCR increased with time and the applied load, and was lowest at the beginning of each loading increment. There was an immediate increase at a high rate in the CIC axial stresses after the application of the load, and the increase continued as the load was transferred to the CICs from the soft clay. The soft soil absorbed a high load immediately after the application of the surcharge due to the undrained condition; however, differential settlement between the soft soil and the CICs caused a stress transfer from the soft soil to the stiffer CICs. The dissipation of excess pore water pressure was monitored and interpreted along with the variations of the stress on the soft soil. The fast dissipation of the excess pore water pressure was concluded not to be solely due to consolidation, and was attributed to the fast reduction of the stress on the soft clay. Strain gauges were utilised to measure the strain in the geotextile layer. The strains in GR layer experienced an immediate increase and reached a stable value as the consolidation of the soft soil stabilised.

FLAC^{3D} finite difference program was utilised to simulate a fully three-dimensional flow-deformation coupled numerical model. Soft clay and the CICs were simulated using Modified Cam-Clay (MCC) soft soil model and Hoek-Brown criterion, respectively. Linearly elastic- perfectly plastic Mohr-Coulomb strength criterion was used to simulate the behaviour of the load transfer platform (LTP).

Separation or slip was allowed to occur between the soft soil and the CICs considering interface elements between them. Elastic geogridSEL elements available in FLAC^{3D} were used in large strain analysis mode to model the geotextile layer. The results from the numerical simulation was verified against the experimental measurements and a reasonably good agreement was perceived. The findings of the numerical simulation indicated the reduction of the effective stress in the soft clay with depth due to the negative skin friction which lead to an increase of the SCR with depth. The results also indicated a radial increase of the stresses on the soft clay surface moving away from the CICs, and the maximum stress on the soft clay surface was perceived mid-span between two CICs.

This study also made an attempt in comparing two equivalent cases (same concrete volume) of frictional and socketed CICs for the transition zone of the improved ground. FLAC^{3D} was used for three-dimensional coupled flow-deformation simulation capturing the variations of permeability with void ratio during the consolidation process. Behaviour of the soft soil and the CICs was modelled using Cam-Clay and Hoek-Brown constitutive models, respectively. Soil settlements, lateral displacements, stresses in the CICs, and the mobilised tension in the geosynthetic layer were compared using the numerical predictions for the two cases. For the soft soil deposit used in this study, the results indicated a better performance of the frictional CICs compared to the socketed CICs. The findings of this study indicated that an increase in the area replacement ratio using frictional CICs and the mass improvement of the composite ground led to a more effective performance and reduction in the settlements than transferring the loads to a stiffer layer using socketed CICs and an overly-rigid LTP. Designing CICs as a ground improvement method and considering the contributions of the surrounding soft soil could make CICs an economically competitive method. This study demonstrated that the settlement of the soft soil between columns will induce significant differential and total settlements on the embankment surface when a flexible granular LTP is used. In order for the socketed CICs to perform efficiently in settlement reduction, a rigid LTP (similar to pile cap or

raft) is necessary to transfer all the embankment loads to the stiff layer to prevent the notable soil settlement between columns. CIC method makes an attempt to share a part of the load with the surrounding soft soil and not to completely bypass it; however, the stress-sensitivity of the soft soil may lead to large settlements if not designed properly. It is recommended to the practicing engineers to consider frictional CICs as an alternative to design the transition zone for CIC-improved ground.

Two modelling approaches of drained and flow-deformation coupled numerical simulations were compared in this study. Vertical total and differential settlements, lateral displacement, and tensile forces in the geosynthetic were compared for the both cases. The results revealed that even though the drained analysis may save computation time, it may lead to underestimation, in particular for the lateral displacement and the forces in the geosynthetic layer which was attributed to the different stress paths in the two modelling approaches.

The generated pore water pressure reduced the effective stress and therefore the soil strength which in turn led to larger deformations in the coupled analysis compared to the drained approach. Although the final state of the stress was the same for the both cases, the deformations were different as the behaviour of the soil is stress-path dependent.

It is expected that the results from this experimental and the numerical study will help the practicing engineers better understand the stress transfer mechanism in CIC-improved grounds, and have an optimised and safe design.

6.3 Recommendations for Future Research

This study could be extended in the following directions:

- Simulating the installation effect of the CICs. The displacement method used for CIC installation alters the properties of the surrounding soil by disturbing, the extent of which depends on factors such as soil type and penetration rate. Considering a smear zone around the CICs with different

properties such as shear strength and permeability could lead to more accurate predictions of the system behaviour

- Considering creep compression for the soft soil in the numerical simulations. The secondary compression or creep in soft soil occurring concurrently with the compression due to excess pore water pressure dissipation could have a significant impact on the predictions of long-term settlement and excess pore water pressure dissipation
- Assessing the transition zone performance using different options in the longitudinal cross-section. Evaluating the differential settlement in the longitudinal section considering the bridge piles is essential to keep the change in grade within the acceptable limits
- Assessing frictional CIC behaviour through field tests. Simulating frictional CICs in the laboratory is challenging mainly due to reduced scale effects on the skin friction generated on the CIC length which is the main stress transfer mechanism in frictional CICs. Field tests could be useful in realistic assessment of frictional CIC behaviour
- Investigating the effect of a CIC with pre-existing cracks on the performance of the system through laboratory simulation. This could be achieved by installing a precast CIC with pre-existing cracks and assessing the performance in terms of the settlement, forces in the geosynthetic, and the impact on the adjacent columns
- Evaluating the effect of using a large number of small-diameter CICs versus a smaller number of large-diameter CICs while keeping the area replacement ratio, and therefore concrete volume the same. This could be assessed in laboratory or through numerical simulation. Since the CIC-improved ground behaviour is highly influenced by the column spacing, the difference between these two options could be substantial

REFERENCES

- Alamgir, M., Miura, N., Poorooshasb, H.B. & Madhav, M.R. 1996, 'Deformation analysis of soft ground reinforced by columnar inclusions', *Computers and Geotechnics*, vol. 18, no. 4, pp. 267-90.
- Ambily, A.P. & Gandhi, S.R. 2007, 'Behavior of Stone Columns Based on Experimental and FEM Analysis', *Journal of Geotechnical and Geoenvironmental Engineering*, vol. 133, no. 4, pp. 405-15.
- Ansari, F. & Li, Q. 1998, 'High-strength concrete subjected to triaxial compression', *Materials Journal*, vol. 95, no. 6, pp. 747-55.
- Ariyaratne, P., Liyanapathirana, D. & Leo, C. 2013, 'Comparison of Different Two-Dimensional Idealizations for a Geosynthetic-Reinforced Pile-Supported Embankment', *International Journal of Geomechanics*, vol. 13, no. 6, pp. 754-68.
- Ariyaratne, P. & Liyanapathirana, D.S. 2015, 'Review of existing design methods for geosynthetic-reinforced pile-supported embankments', *Soils and Foundations*, vol. 55, no. 1, pp. 17-34.
- ASIRI 2012, 'Recommandations pour la conception, le dimensionnement, l'exécution et le contrôle de l'amélioration des sols de fondation par inclusions rigides'.
- ASTM D4253-16 2016, 'Test Methods for Maximum Index Density and Unit Weight of Soils Using a Vibratory Table', *ASTM International*.
- Australian Standard AS 1012.9 2014, 'A. S. 1012.9', *Methods for testing concrete*.
- Australian Standard AS 1289.6.2.2. 1998, 'Methods of testing soils for engineering purposes- Soil strength and consolidation tests- Determination of shear strength of a soil- Direct shear test using a shear box'.
- Australian Standard AS 3600 2009, 'Australian Standard: Concrete Structures.'
- Australian Standard AS 3706.2 2012, 'Geotextiles-Methods of Test-Determination of Tensile Properties Wide Strip and Grab Method'.
- Baguelin, F. & Frank, R. 1980, 'Theoretical studies of piles using the finite element method', *Numerical methods in offshore piling*, Thomas Telford Publishing, pp. 83-91.

- Basu, P., Prezzi, M. & Basu, D. 2010, 'Drilled displacement piles—current practice and design', *DFI Journal-The Journal of the Deep Foundations Institute*, vol. 4, no. 1, pp. 3-20.
- Basu, P., Prezzi, M. & Salgado, R. 2014, 'Modeling of Installation and Quantification of Shaft Resistance of Drilled-Displacement Piles in Sand', *International Journal of Geomechanics*, vol. 14, no. 2, pp. 214-29.
- Bhasi, A. & Rajagopal, K. 2015, 'Numerical study of basal reinforced embankments supported on floating/end bearing piles considering pile-soil interaction', *Geotextiles and Geomembranes*, vol. 43, no. 6, pp. 524-36.
- Bigoni, D. & Piccolroaz, A. 2004, 'Yield criteria for quasibrittle and frictional materials', *International Journal of Solids and Structures*, vol. 41, no. 11, pp. 2855-78.
- Blanc, M., Thorel, L., Girout, R. & Almeida, M. 2014, 'Geosynthetic reinforcement of a granular load transfer platform above rigid inclusions: comparison between centrifuge testing and analytical modelling', *Geosynthetics International*, vol. 21, no. 1, pp. 37-52.
- Bolton, M. & Lau, C. 1988, 'Scale effects arising from particle size', *Centrifuge 1988: Proceedings of the International Conference on Geotechnical Centrifuge Modeling*, vol. 1, pp. 127-31.
- Brettmann, T. & NeSmith, W. 2005, 'Advances in auger pressure grouted piles: design, construction and testing', paper presented to the *Advances in Deep Foundations*.
- Briaçon, L. & Simon, B. 2012, 'Performance of Pile-Supported Embankment over Soft Soil: Full-Scale Experiment', *Journal of Geotechnical and Geoenvironmental Engineering*, vol. 138, no. 4, pp. 551-61.
- Britton, E. & Naughton, P. 2008, 'An experimental investigation of arching in piled embankments', *Proceedings of the 4th European Geosynthetics Congress EuroGeo*, vol. 4, pp. 1-8.
- Broms, B.B. 2004, *Ground Improvement: Lime and lime/cement columns*, Spon Press.
- Brown, D.A. 2005, 'Practical considerations in the selection and use of continuous flight auger and drilled displacement piles', paper presented to the *Advances in Deep Foundations*.

- Brown, D.A., Dapp, S.D., Thompson, W.R. & Lazarte, C.A. 2007, 'Design and construction of continuous flight auger piles.', *FHWA Geotechnical Engineering Circular*, no. 8.
- BS 8006 1995, 'Code of practice for strengthened/reinforced soils and other fills', *British Standards Institution*.
- BS 8006 2010, 'Code of practice for strengthened/reinforced soils and other fills', *British Standards Institution*.
- BS 8006 2012, 'Code of practice for strengthened/reinforced soils and other fills', *British Standards Institution*.
- Buckingham, E. 1914, 'On physically similar systems; illustrations of the use of dimensional equations', *Physical Review*, vol. 4, no. 4, p. 345.
- Buschmeier, B., Masse, F., Swift, S. & Walker, M. 2012, 'Full Scale Instrumented Load Test for Support of Oil Tanks on Deep Soft Clay Deposits in Louisiana using Controlled Modulus Columns', paper presented to the *International Symposium on Ground Improvement (IS-GI) Brussels*.
- Butterfield, R. 1999, 'Dimensional analysis for geotechnical engineers', *Geotechnique* 49, vol. 3, no. 1, pp. 357-66.
- Carlsson, B. 1987, 'Armerad jord beräkningsprinciper för vertikala väggar, branta slänter, bankar på lös undergrund, bankra på pålar', *Terratema AB, Linköping (in Swedish)*.
- Chai, J.-C., Shrestha, S., Hino, T., Ding, W.-Q., Kamo, Y. & Carter, J. 2015, '2D and 3D analyses of an embankment on clay improved by soil-cement columns', *Computers and Geotechnics*, vol. 68, pp. 28-37.
- Chen, Y.-m., Wei-ping, C. & Ren-peng, C. 2008, 'An experimental investigation of soil arching within basal reinforced and unreinforced piled embankments', *Geotextiles and Geomembranes*, vol. 26, no. 2, pp. 164-74.
- Chevalier, B., Villard, P. & Combe, G. 2010, 'Investigation of load-transfer mechanisms in geotechnical earth structures with thin fill platforms reinforced by rigid inclusions', *International Journal of Geomechanics*, vol. 11, no. 3, pp. 239-50.
- Combarieu, O. 1974, 'Effet d'accrochage et methode d'evaluation du frottement negatif', *Bull Liaison Lab Ponts Chauss*, no. 71, pp. 93-107.
- Combarieu, O. 1985, *Frottement négatif sur les pieux*, Laboratoire Central des Ponts et Chausees (LCPC).

- Combarieu, O. 1988, 'Amélioration des sols par inclusions rigides verticales application à l'édification de remblais sur sols médiocres', *Revue française de géotechnique*, no. 44, pp. 57-79.
- Considère, A. 1902, 'Etude théorique de la résistance à la compression du Béton Fretté', *Comptes Rendus de l'Académie des Sciences*, vol. 25, pp. 365-8.
- Cooke, R. 1974, 'The settlement of friction pile foundations', *Proceedings, Confrence on Tall Buildings, Kuala Lumpur, Malaysia*, pp. 7-19.
- CUR226 2010, 'Ontwerprichtlijn paalmatrassystemen (Design Guideline Piled Embankments) ', (in Dutch).
- Das, A.K. & Deb, K. 2018, 'Experimental and 3D Numerical Study on Time-Dependent Behavior of Stone Column-Supported Embankments', *International Journal of Geomechanics*, vol. 18, no. 4, p. 04018011.
- Deb, K. 2010, 'A mathematical model to study the soil arching effect in stone column-supported embankment resting on soft foundation soil', *Applied Mathematical Modelling*, vol. 34, no. 12, pp. 3871-83.
- Deb, K. & Mohapatra, S.R. 2013, 'Analysis of stone column-supported geosynthetic-reinforced embankments', *Applied Mathematical Modelling*, vol. 37, no. 5, pp. 2943-60.
- Deb, K., Samadhiya, N.K. & Namdeo, J.B. 2011, 'Laboratory model studies on unreinforced and geogrid-reinforced sand bed over stone column-improved soft clay', *Geotextiles and Geomembranes*, vol. 29, no. 2, pp. 190-6.
- EBGEO 2004, 'Recommendations for Design and Analysis of Earth Structures using Geosynthetic Reinforcements - EBGEO'.
- EBGEO 2010, 'Recommendations for Design and Analysis of Earth Structures using Geosynthetic Reinforcements - EBGEO'.
- EBGEO 2011, 'Recommendations for Design and Analysis of Earth Structures using Geosynthetic Reinforcements - EBGEO'.
- Elwi, A.A. & Murray, D.W. 1979, 'A 3D hypoelastic concrete constitutive relationship', *Journal of the Engineering Mechanics Division*, vol. 105, no. 4, pp. 623-41.
- Etse, G. & Willam, K. 1994, 'Fracture energy formulation for inelastic behavior of plain concrete', *Journal of engineering mechanics*, vol. 120, no. 9, pp. 1983-2011.

- Fagundes, D.F., Almeida, M.S.S., Thorel, L. & Blanc, M. 2017, 'Load transfer mechanism and deformation of reinforced piled embankments', *Geotextiles and Geomembranes*, vol. 45, no. 2, pp. 1-10.
- Fang, Z. & Yin, J.-H. 2007, 'Responses of Excess Pore Water Pressure in Soft Marine Clay around a Soil–Cement Column', *International Journal of Geomechanics*, vol. 7, no. 3, pp. 167-75.
- Fattah, M.Y., Shlash, K.T. & Al-Waily, M.J.M. 2010, 'Stress concentration ratio of model stone columns in soft clays', *Geotechnical Testing Journal*, vol. 34, no. 1, pp. 50-60.
- Filz, G., Sloan, J., McGuire, M.P., Collin, J. & Smith, M. 2012, 'Column-supported embankments: settlement and load transfer', paper presented to the *Geotechnical Engineering State of the Art and Practice: Keynote Lectures from GeoCongress 2012*.
- Fioravante, V. 2011, 'Load transfer from a raft to a pile with an interposed layer', *Géotechnique*, vol. 61, no. 2, pp. 121-32.
- Fleming, K., Weltman, A., Randolph, M. & Elson, K. 2008, *Engineering, Piling*, CRC press.
- Fok, N., Qiu, T., Vincent, P. & Kreminsky, M. 2012, 'A Case Study of Ground Improvement using Semi-Rigid Inclusions for Breakwater Road Bridge', *Proceedings of the International Conference on Ground Improvement & Ground Control*, pp. 629-43.
- Frank, R. 1974, 'Etude theorique du comportement des pieux sous charge verticale: Introduction de la dilatance', *Laboratoire Central des Ponts et Chausees (LCPC)*, no. 46, p. 238P.
- Girout, R., Blanc, M., Dias, D. & Thorel, L. 2014, 'Numerical analysis of a geosynthetic-reinforced piled load transfer platform – Validation on centrifuge test', *Geotextiles and Geomembranes*, vol. 42, no. 5, pp. 525-39.
- Girout, R., Blanc, M., Thorel, L. & Dias, D. 2018, 'Geosynthetic reinforcement of pile-supported embankments', *Geosynthetics International*, vol. 25, no. 1, pp. 37-49.
- Gniel, J. & Haberfield, C. 2015, 'Design, construction and performance of a tied-wall embankment supported on concrete column ground improvement', *Proceedings of the International Conference on Geotechnical Engineering: Soil-Structure Interaction, Underground Structures and Retaining Walls St. Petersburg, Russia. IOS Press*, pp. 18-27.

- Guido, V. 1987, 'Plate loading tests on geogrid-reinforced earth slab', paper presented to the *Geosynthetic'87 Conf.*
- Han, J. & Gabr, M. 2002, 'Numerical Analysis of Geosynthetic-Reinforced and Pile-Supported Earth Platforms over Soft Soil', *Journal of Geotechnical and Geoenvironmental Engineering*, vol. 128, no. 1, pp. 44-53.
- Han, J., Huang, J. & Porbaha, A. 2005, '2D numerical modeling of a constructed geosynthetic-reinforced embankment over deep mixed columns', paper presented to the *Contemporary issues in foundation engineering*.
- Han, J. & Ye, S.-L. 2001, 'Simplified Method for Consolidation Rate of Stone Column Reinforced Foundations', *Journal of Geotechnical and Geoenvironmental Engineering*, vol. 127, no. 7, pp. 597-603.
- Hewlett, W. & Randolph, M. 1988, 'Analysis of piled embankments', *Ground Eng*, vol. 21, no. 3, pp. 12-8.
- Hoek, E. & Brown, E.T. 1980, 'Empirical strength criterion for rock masses', *Journal of Geotechnical and Geoenvironmental*, vol. 106, pp. 1013-35.
- Hoek, E., Carranza, C. & Corkum, B. 2002, 'Hoek-brown failure criterion – 2002 edition', *Narms-Tac*, pp. 267-73.
- Holzer, T.L., Höeg, K. & Arulanandan, K. 1973, 'Excess Pore Pressures During Undrained Clay Creep', *Canadian Geotechnical Journal*, vol. 10, no. 1, pp. 12-24.
- Hosseinpour, I., Almeida, M.S.S. & Riccio, M. 2015, 'Full-scale load test and finite-element analysis of soft ground improved by geotextile-encased granular columns', *Geosynthetics International*, vol. 22, no. 6, pp. 428-38.
- Hsi, J. 2016, 'Soft Soil Engineering in Practice', *Australian Geomechanics Society Sydney Chapter Symposium*, no. November, pp. 1-24.
- Huang, J. & Han, J. 2009, '3D coupled mechanical and hydraulic modeling of a geosynthetic-reinforced deep mixed column-supported embankment', *Geotextiles and Geomembranes*, vol. 27, no. 4, pp. 272-80.
- Huang, J. & Han, J. 2010, 'Two-dimensional parametric study of geosynthetic-reinforced column-supported embankments by coupled hydraulic and mechanical modeling', *Computers and Geotechnics*, vol. 37, no. 5, pp. 638-48.
- Huang, J., Han, J. & Oztoprak, S. 2009, 'Coupled mechanical and hydraulic modelling of geosynthetic-reinforced column-supported embankments', *Journal of*

Geotechnical and Geoenvironmental Engineering, vol. 135, no. 8, pp. 1011-21.

Itasca 2012, 'Online Manual ', *FLAC 3D Manual*.

Jamsawang, P., Yoobanpot, N., Thanasisathit, N., Voottipruex, P. & Jongpradist, P. 2016, 'Three-dimensional numerical analysis of a DCM column-supported highway embankment', *Computers and Geotechnics*, vol. 72, pp. 42-56.

Jenck, O. & Dias, D. 2009, 'Three-dimensional numerical modeling of a piled embankment', *International Journal of Geomechanics*, vol. 9, no. 3, pp. 102-12.

Jenck, O., Dias, D. & Kastner, R. 2005, 'Soft ground improvement by vertical rigid piles two-dimensional physical modelling and comparison with current design methods', *Soils and Foundations*, vol. 45, no. 6, pp. 15-30.

Jenck, O., Dias, D. & Kastner, R. 2007, 'Two-dimensional physical and numerical modeling of a pile-supported earth platform over soft soil', *Journal of Geotechnical and Geoenvironmental Engineering*, vol. 133, no. 3, pp. 295-305.

Jenck, O., Dias, D. & Kastner, R. 2009, 'Discrete element modelling of a granular platform supported by piles in soft soil – Validation on a small scale model test and comparison to a numerical analysis in a continuum', *Computers and Geotechnics*, vol. 36, no. 6, pp. 917-27.

Jones, C., Lawson, C. & Ayres, D. 1990, 'Geotextile reinforced piled embankments', *Geotextiles, Geomembranes and Related Products, Den Hoedt (ed.)*, pp. 155-60.

Karam, G. & Tabbara, M. 2009, 'Hoek – Brown Strength Criterion for Actively', *Journal of Materials*, vol. 21, no. 3, pp. 110-8.

Karim, M.R. 2013, 'Behaviour of piles subjected to passive subsoil movement due to embankment construction - A simplified 3D analysis', *Computers and Geotechnics*, vol. 53, pp. 1-8.

Kempfert, H., Göbel, C., Alexiew, D. & Heitz, C. 2004, 'German recommendations for reinforced embankments on pile-similar elements', *EuroGeo3-third European geosynthetics conference, geotechnical engineering with geosynthetics*, Deutsche Gesellschaft für Geotechnik Munich, Germany, pp. 279-84.

- Khabbazian, M., Kaliakin, V.N. & Meehan, C.L. 2015, 'Column Supported Embankments with Geosynthetic Encased Columns: Validity of the Unit Cell Concept', *Geotechnical and Geological Engineering*, vol. 33, no. 3, pp. 425-42.
- King, D.J., Bouazza, A., Gniel, J., Rowe, K. & Bui, H. 2018, 'Geosynthetic reinforced column supported embankments and the role of ground improvement installation effects', *Canadian Geotechnical Journal*, vol. 55, no. 6, pp. 792-809.
- King, D.J., Bouazza, A., Gniel, J.R., Rowe, R.K. & Bui, H.H. 2017, 'Load-transfer platform behaviour in embankments supported on semi-rigid columns: implications of the ground reaction curve', *Canadian Geotechnical Journal*, vol. 54, no. 8, pp. 1158-75.
- Kitazume, M. & Maruyama, K. 2005, 'Collapse failure of group column type deep mixing improved ground under embankment', *Proceedings of International Conference on Deep Mixing: Best Practice and Recent Advances. Kyoto*, pp. 245-54.
- Kitazume, M. & Maruyama, K. 2006, 'External stability of group column type deep mixing improved ground under embankment loading', *Soils and Foundations*, vol. 46, no. 3, pp. 323-40.
- Kitazume, M. & Maruyama, K. 2007, 'Internal stability of group column type deep mixing improved ground under embankment loading', *Soils and Foundations*, vol. 47, no. 3, pp. 437-55.
- Kitazume, M., Okano, K. & Miyajima, S. 2000, 'Centrifuge Model Tests on Failure Envelope of Column Tupe Deep Mixing Method Improved Ground', *Soils and Foundations*, vol. 40, no. 4, pp. 43-55.
- Kotsovos, M.D. 1979, 'A mathematical description of the strength properties of concrete under generalized stress', *Magazine of Concrete Research*, vol. 31, no. 108, pp. 151-8.
- Kuwano, J. & Izawa, J. 2010, 'Centrifuge modelling of geogrid reinforced soil walls subjected to pseudo-static loading', *International Journal of Physical Modelling in Geotechnics*, vol. 10, no. 1, pp. 1-18.
- Ladd, C.C. & Foott, R. 1974, 'New design procedure for stability of soft clays', *J. Geotech. Engrg.*, vol. 100, no. 7, pp. 763-86.
- Larisch, M., Williams, D. & Scheuermann, A. 2015, 'Effects of installation parameters of drilled displacement piles on in situ stress conditions in stiff clays', paper

presented to the *Geotechnical Engineering for Infrastructure and Development*.

- Larisch, M.D., Nacke, E., Arnold, M., Williams, D. & Scheuermann, A. 2014, 'Simulation of auger displacement pile installation', *International Journal of Geotechnical Engineering*, vol. 8, no. 4, pp. 458-62.
- Larisch, M.D. & Scheuermann, D.W.a.A. 2015, 'Influence of pile installation techniques on ground heave in clays', paper presented to the *12th Australia New Zeland Conference on Geomechanics*.
- Lawson, C. 2012, 'Role of modelling in the development of design methods for basal reinforced piled embankments', paper presented to the *Eurofuge 2012*.
- Le Hello, B. & Villard, P. 2009, 'Embankments reinforced by piles and geosynthetics- Numerical and experimental studies dealing with the transfer of load on the soil embankment', *Engineering Geology*, vol. 106, no. 1-2, pp. 78-91.
- Le Hello, B., Villard, P., Nancey, A. & Delmas, P. 2006, 'Coupling finite elements and discrete elements methods, application to reinforced embankment by piles and geosynthetics', paper presented to the *Numerical Methods in Geotechnical Engineering, 6th European Conference, Graz, Austria*.
- Le, T.M. 2015, 'Analysing consolidation data to optimise elastic visco-plastic model parameters for soft clay', PhD thesis, University of Technology, Sydney.
- Le, T.M., Fatahi, B. & Khabbaz, H. 2015, 'Numerical optimisation to obtain elastic viscoplastic model parameters for soft clay', *International Journal of Plasticity*, vol. 65, pp. 1-21.
- Leon, A. 1935, 'Ueber die scherfestigkeit des betons', *Beton und Eisen*, vol. 34, no. 8, pp. 130-5.
- Li, A.L. & Rowe, R.K. 2002, 'Some design considerations for embankments on rate sensitive soils', *Journal of Geotechnical and Geoenvironmental Engineering*, vol. 128, no. 11, pp. 885-97.
- Low, B., Tang, S. & Choa, V. 1994, 'Arching in piled embankments', *Journal of Geotechnical Engineering*, vol. 120, no. 11, pp. 1917-38.
- Mahajan, R.R. & Viswanadham, B.V.S. 2007, 'Centrifuge model tests on geotextile-reinforced slopes', *Geosynthetics International*, vol. 14, no. 6, pp. 365-79.
- Mandolini, A., Di Laora, R. & Mascarucci, Y. 2013, 'Rational Design of Piled Raft', *Procedia Engineering*, vol. 57, pp. 45-52.

- Martin, G.R. & Chen, C.Y. 2005, 'Response of piles due to lateral slope movement', *Computers & structures* vol. 83, no. 8-9, pp. 588-98.
- Mayerhof, G. 1976, 'Bearing capacity and settlement of pile foundations', *Journal of Geotechnical and Geoenvironmental Engineering*, vol. 102, no. GT3, pp. 197-228.
- McGuire, M., Sloan, J., Collin, J. & Filz, G. 2012, 'Critical height of column-supported embankments from bench-scale and field-scale tests', *ISSMGE-TC 211 International Symposium on Ground Improvement IS-GI Brussels*.
- McKelvey, D., Sivakumar, V., Bell, A. & Graham, J. 2004, 'Modelling vibrated stone columns in soft clay', *Proceedings of the Institution of Civil Engineers-Geotechnical Engineering*, vol. 157, no. 3, pp. 137-49.
- McKelvey, J.A. 1994, 'The anatomy of soil arching', *Geotextiles and Geomembranes*, vol. 13, no. 5, pp. 317-29.
- Menard 2016, *CMC Rigid Inclusions*, <<https://menardoceania.com.au/technique/cmc-rigid-inclusions/>>.
- Menard 2018, *Controlled Modulus Columns*, <<https://www.vibromenard.co.uk/techniques/controlled-modulus-columns/>>.
- Moshfeghi, S. & Eslami, A. 2018, 'Reliability-based assessment of drilled displacement piles bearing capacity using CPT records', *Marine Georesources & Geotechnology*, pp. 1-14.
- Murugesan, S. & Rajagopal, K. 2006, 'Geosynthetic-encased stone columns: Numerical evaluation', *Geotextiles and Geomembranes*, vol. 24, no. 6, pp. 349-58.
- Naughton, P. 2007, 'The significance of critical height in the design of piled embankments', *Proceedings of the 9th GeoDenver*, pp. 18-21.
- NeSmith, W.M. 2002, 'Static capacity analysis of augered, pressure-injected displacement piles', *Deep Foundations 2002: An International Perspective on Theory, Design, Construction, and Performance*, pp. 1174-86.
- NeSmith, W.M. & NeSmith, W.M. 2006a, 'Anatomy of a data acquisition system for drilled displacement piles', paper presented to the *GeoCongress 2006: Geotechnical Engineering in the Information Technology Age*.
- NeSmith, W.M. & NeSmith, W.M. 2006b, 'Application of data acquired during drilled displacement pile installation', paper presented to the *GeoCongress 2006: Geotechnical Engineering in the Information Technology Age*.

- Ni, Q., Hird, C. & Guymer, I. 2010, 'Physical modelling of pile penetration in clay using transparent soil and particle image velocimetry', *Géotechnique*, vol. 60, no. 2, p. 121.
- Nordic Handbook 2005, *Guidelines for reinforced soils and fills* Nordic geosynthetic group.
- Nunez, I. & Randolph, M.F. 1984, *Tension Pile Behaviour in Clay: Centrifuge Modelling Techniques*, Cambridge Univ., Engineering Department.
- Nunez, M.A., Briançon, L. & Dias, D. 2013, 'Analyses of a pile-supported embankment over soft clay: Full-scale experiment, analytical and numerical approaches', *Engineering Geology*, vol. 153, pp. 53-67.
- Okay, U.S., Dias, D., Thorel, L. & Rault, G. 2014, 'Centrifuge Modeling of a Pile-Supported Granular Earth-Platform', *Journal of Geotechnical and Geoenvironmental Engineering*, vol. 140, no. 2, p. 04013015.
- Ottosen, N.S. 1977, 'A failure criterion for concrete', *American Society of Civil Engineers. Engineering Mechanics Division. Journal*, vol. 103, no. 4, pp. 527-35.
- Park, S., Roberts, L. & Misra, A. 2011, 'Static load test interpretation using the tz model and LRFD resistance factors for auger cast-in-place (AC IP) and drilled displacement (DD) piles', *International Journal of Geotechnical Engineering*, vol. 5, no. 3, pp. 283-95.
- Park, S., Roberts, L.A. & Misra, A. 2012, 'Design Methodology for Axially Loaded Auger Cast-in-Place and Drilled Displacement Piles', *Journal of Geotechnical and Geoenvironmental Engineering*, vol. 138, no. 12, pp. 1431-41.
- Plomteux, C. & Porbaha, A. 2004, 'CMC foundation system for embankment support—A case history', paper presented to the *GeoSupport 2004: Drilled Shafts, Micropiling, Deep Mixing, Remedial Methods, and Specialty Foundation Systems*.
- Porbaha, a., Pradhan, T.B. & Kishida, T. 2001, 'Static response of fly ash columnar improved ground', *Canadian Geotechnical Journal*, vol. 38, no. 2, pp. 276-86.
- Pramono, B.E. & Willam, K. 1989, 'Fracture energy-based plasticity formulation of plain concrete', *Journal of Engineering Mechanics*, vol. 115, no. 6, pp. 1183-204.
- Randolph, M. & Wroth, C. 1979, 'A simple approach to pile design and the evaluation of pile tests', *Behavior of Deep Foundations*, ASTM International.

- Rashid, A.S., Black, J.A., Mohamad, H. & Mohd Noor, N. 2015, 'Behavior of Weak Soils Reinforced with End-Bearing Soil-Cement Columns Formed by the Deep Mixing Method', *Marine Georesources & Geotechnology*, vol. 33, no. 6, pp. 473-86.
- Rashid, A.S.A., Kueh, A.B.H. & Mohamad, H. 2018, 'Behaviour of soft soil improved by floating soil–cement columns', *International Journal of Physical Modelling in Geotechnics*, vol. 18, no. 2, pp. 95-116.
- Richart, F.E., Brandtzaeg, A. & Brown, R.L. 1928, *A study of the failure of concrete under combined compressive stresses*, University of Illinois at Urbana Champaign, College of Engineering. Engineering Experiment Station.
- Rogbeck, Y., Gustavsson, S., Sodergren, I. & Lindquist, D. 1998, 'Reinforced piled embankments in Sweden-design aspects', *Proceedings, Sixth International Conference on Geosynthetics*, vol. 2, pp. 755-62.
- Roscoe, K.H. & Burland, J. 1968, 'On the generalized stress-strain behaviour of wet clay', *Engineering plasticity* pp. 535-609, .
- Rowe, R.K. & Liu, K.W. 2015, 'Three-dimensional finite element modelling of a full-scale geosynthetic-reinforced, pile-supported embankment', *Canadian Geotechnical Journal*, vol. 52, no. 12, pp. 2041-54.
- Russell, D. & Pierpoint, N. 1997, 'An assessment of design methods for piled embankments', *Ground Engineering*, vol. 30, no. 10.
- Sagaseta, C. 1987, 'Analysis of undraind soil deformation due to ground loss', *Géotechnique*, vol. 37, no. 3, pp. 301-20.
- Schmidt, B. 1966, 'Earth pressures at rest related to stress history', *Canadian Geotechnical Journal*, vol. 3, no. 4, pp. 239-42.
- Shahu, J.T. & Reddy, Y.R. 2011, 'Clayey Soil Reinforced with Stone Column Group: Model Tests and Analyses', *Journal of Geotechnical and Geoenvironmental Engineering*, vol. 137, no. 12, pp. 1265-74.
- Sharma, J.S. & Bolton, M.D. 1996, 'Centrifuge Modelling of an Embankment on Soft Clay Reinforced with a Geogrid', *Geotextiles and Geomembranes*, vol. 14, no. 1, pp. 1-17.
- Sherif, M.A. & Koch, D.E. 1970, 'Coefficient of earth pressure at rest as related to soil precompression ratio and liquid limit', *Highway Research Record*, no. 323, pp. 39-48.

- Simon, B. & Schlosser, F. 2006, 'Soil reinforcement by vertical stiff inclusions in France', *Symp. on Rigid Inclusions in difficult subsoils condtions. Mexican Society of Soil Mechanics. UNAM Mexico.*
- Skinner, H., Powell, J., Morris, J. & England, M. 2003, 'Results from a piling trial on bored, CFA and rotary displacement piles in stiff clay', *BGA International Conference on Foundations: Innovations, observations, design and practice: Proceedings of the international conference organised by British Geotechnical Association* Thomas Telford Publishing, pp. 825-34.
- Smith, M. & Filz, G. 2007, 'Axisymmetric numerical modeling of a unit cell in geosynthetic-reinforced, column-supported embankments', *Geosynthetics International*, vol. 14, no. 1, pp. 13-22.
- Springman, S.M., Bolton, M.D., Sharma, J. & Balachandran, S. 1992, 'Modelling and instrumentation of a geotextile in the geotechnical centrifuge', pp. Vol 167 p72-Vol p72.
- Stewart, M.E. & Filz, G.M. 2005, 'Influence of Clay Compressibility on Geosynthetic Loads in Bridging Layers for Column-Supported Embankments', *Geo-Frontiers Congress*, pp. 1-14.
- Stone, K.J. & Wood, D.M. 1992, 'Effects of dilatancy and particle size observed in model tests on sand', *Soils and Foundations*, vol. 32, no. 4, pp. 43-57.
- Suleiman, M.T., Ni, L., Davis, C., Lin, H. & Xiao, S. 2016, 'Installation Effects of Controlled Modulus Column Ground Improvement Piles on Surrounding Soil', *Journal of Geotechnical and Geoenvironmental Engineering*, vol. 142, no. 1, p. 04015059.
- Svanø, G., Ilstad, T., Eiksund, G. & Want, A. 2000, 'Alternative calculation principle for design of piled embankments with base reinforcement', *Proceedings of the 4th Conference of the GIGS.*
- Taylor, D.W. 1948, *Fundamentals of soil mechanics*, J. Wiley.
- Terzaghi, K. 1943, *Theoretical soil mechanics*, John Wiley & Sons, New York.
- van Eekelen, S. & Bezuijen, A. 2014, 'Is 1+ 1= 2? Results of 3D model experiments on piled embankments', paper presented to the *10th International conference on geosynthetics (IGS-2014).*
- Van Eekelen, S.J., Bezuijen, A. & Oung, O. 2003, 'Arching in piled embankments; experiments and design calculations', *Proceedings of Foundations: Innovations, observations, design and practice*, pp. 885-94.

- van Eekelen, S.J.M., Bezuijen, A., Lodder, H.J. & van Tol, A.F. 2012a, 'Model experiments on piled embankments. Part I', *Geotextiles and Geomembranes*, vol. 32, pp. 69-81.
- van Eekelen, S.J.M., Bezuijen, A., Lodder, H.J. & van Tol, A.F. 2012b, 'Model experiments on piled embankments. Part II', *Geotextiles and Geomembranes*, vol. 32, pp. 82-94.
- van Eekelen, S.J.M., Bezuijen, A. & van Tol, A.F. 2013, 'An analytical model for arching in piled embankments', *Geotextiles and Geomembranes*, vol. 39, pp. 78-102.
- Van Eekelen, S.J.M. & Brugman, M.H.A. 2016, *Basal Reinforced Piled Embankments*, CRC Press LLC.
- Viggiani, C. 1993, 'Further experiences with auger piles in Naples area', *Deep Foundations on Bored and Auger Piles*, pp. 445-55.
- Viswanadham, B.V.S. & König, D. 2004, 'Studies on scaling and instrumentation of a geogrid', *Geotextiles and Geomembranes*, vol. 22, no. 5, pp. 307-28.
- Willam, K. & Warnke, E. 1974, 'Constitutive Model for Triaxial Behaviour of Concrete', Seminar on Concrete Structures Subject to Triaxial Stresses', *International Association of Bridge and Structural Engineering Conference, Bergamo, Italy*, p. 174.
- Wong, P. & Muttuvel, T. 2012a, 'Design of embankments supported on controlled modulus columns', *International Journal of Geotechnical Engineering*, vol. 6, no. 2, pp. 207-13.
- Wong, P. & Muttuvel, T. 2012b, 'Lateral Deformation and Stability of Embankments Supported on Controlled Modulus Columns', *International Conference on Ground Improvement & Ground Control*, Research Publishing Services, Singapore, pp. 807-12.
- Wong, P.K. & Muttuvel, T. 2012c, 'Economic Design of Controlled Modulus Columns for Ground Improvement', paper presented to the *ANZ Conference*.
- Wood, D.M. 2004, *Geotechnical modelling*, CRC Press.
- Wood, D.M., Hu, W. & Nash, D.F.T. 2000, 'Group effects in stone column foundations: model tests', *Géotechnique*, vol. 50, no. 6, pp. 689-98.
- Wu, Y.-F. & Zhou, Y.-W. 2010, 'Unified strength model based on Hoek-Brown failure criterion for circular and square concrete columns confined by FRP', *Journal of Composites for Construction*, vol. 14, no. 2, pp. 175-84.

- Xie, J., Elwi, A. & MacGregor, J. 1995, 'Mechanical properties of three high-strength concretes containing silica fume', *Materials Journal*, vol. 92, no. 2, pp. 135-45.
- Yapage, N., Liyanapathirana, D., Kelly, R., Poulos, H. & Leo, C. 2014, 'Numerical Modeling of an Embankment over Soft Ground Improved with Deep Cement Mixed Columns: Case History', *Journal of Geotechnical and Geoenvironmental Engineering*, vol. 140, no. 11, pp. 4014062-.
- Yapage, N., Liyanapathirana, D., Poulos, H., Kelly, R. & Leo, C. 2013, 'Numerical Modeling of Geotextile-Reinforced Embankments over Deep Cement Mixed Columns Incorporating Strain-Softening Behavior of Columns', *International Journal of Geomechanics*, vol. 15, no. 2012, pp. 4014047-.
- Yapage, N.N.S. & Liyanapathirana, D.S. 2014, 'A parametric study of geosynthetic-reinforced column-supported embankments', *Geosynthetics International*, vol. 21, no. 3, pp. 213-32.
- Yee, K., Setiawan, R. & Bechet, O. 2012, 'Controlled Modulus Columns (CMC): A New Trend in Ground Improvement and Potential Applications to Indonesian Soils', *ISSMGE—TC211—International Symposium on Ground Improvement*.
- Yin, J.-H. & Fang, Z. 2010, 'Physical Modeling of a Footing on Soft Soil Ground with Deep Cement Mixed Soil Columns under Vertical Loading', *Marine Georesources & Geotechnology*, vol. 28, no. 2, pp. 173-88.
- Yin, J.-H. & Zhu, J.-G. 1999, 'Elastic viscoplastic consolidation modelling and interpretation of pore-water pressure responses in clay underneath Tarsiut Island', *Canadian Geotechnical Journal*, vol. 36, no. 4, pp. 708-17.
- Yin, J., Graham, J., Clark, J.I. & Gao, L. 1994, 'Modelling unanticipated pore-water pressures in soft clays', *Canadian Geotechnical Journal*, vol. 31, no. 5, pp. 773-8.
- Yu, Y. & Bathurst, R.J. 2017, 'Modelling of geosynthetic-reinforced column-supported embankments using 2D full-width model and modified unit cell approach', *Geotextiles and Geomembranes*, vol. 45, no. 2, pp. 103-20.
- Yu, Y., Bathurst, R.J. & Damians, I.P. 2016, 'Modified unit cell approach for modelling geosynthetic-reinforced column-supported embankments', *Geotextiles and Geomembranes*, vol. 44, no. 3, pp. 332-43.
- Zaeske, D. 2001, *Zur Wirkungsweise von unbewehrten und bewehrten mineralischen Tragschichten über pfahlartigen Gründungselementen*, Fachgebiet u. Versuchsanst. Geotechnik, Univ. Gh Kassel.

- Zhang, J., Zheng, J.-J., Chen, B.-G. & Yin, J.-H. 2013, 'Coupled mechanical and hydraulic modeling of a geosynthetic-reinforced and pile-supported embankment', *Computers and Geotechnics*, vol. 52, pp. 28-37.
- Zhang, L., Zhao, M., Hu, Y., Zhao, H. & Chen, B. 2012, 'Semi-analytical solutions for geosynthetic-reinforced and pile-supported embankment', *Computers and Geotechnics*, vol. 44, pp. 167-75.
- Zhuang, Y. & Ellis, E. 2014, 'Finite-element analysis of a piled embankment with reinforcement compared with BS 8006 predictions', *Géotechnique*, vol. 64, no. 11, pp. 910-7.
- Zhuang, Y., Ellis, E. & Yu, H. 2012, 'Three-dimensional finite-element analysis of arching in a piled embankment', *Géotechnique*, vol. 62, no. 12, p. 1127.
- Zhuang, Y. & Ellis, E.A. 2016, 'Finite-element analysis of a piled embankment with reinforcement and subsoil', *Géotechnique*, vol. 66, no. 7, pp. 596-601.
- Zhuang, Y., Ellis, E.A. & Yu, H.S. 2010, 'Plane strain FE analysis of arching in a piled embankment', *Proceedings of the Institution of Civil Engineers - Ground Improvement*, vol. 163, no. 4, pp. 207-15.
- Zhuang, Y. & Wang, K. 2015, 'Three-dimensional behavior of biaxial geogrid in a piled embankment: numerical investigation', *Canadian Geotechnical Journal*, vol. 52, no. 10, pp. 1629-35.
- Zhuang, Y. & Wang, K.Y. 2016, 'Finite-Element Analysis on the Effect of Subsoil in Reinforced Piled Embankments and Comparison with Theoretical Method Predictions', *International Journal of Geomechanics*, vol. 16, no. 5, p. 04016011.
- Zhuang, Y., Wang, K.Y. & Liu, H.L. 2014, 'A simplified model to analyze the reinforced piled embankments', *Geotextiles and Geomembranes*, vol. 42, no. 2, pp. 154-65.
- Zornberg, J.G., Mitchell, J.K. & Sitar, N. 1997, 'Testing of Reinforced Slopes in a Geotechnical Centrifuge', *Geotechnical Testing Journal*, vol. 20, no. 4, pp. 470-80.

APPENDIX A
FURTHER PHOTOGRAPHS FROM THE LABORATORY
EXPERIMENT

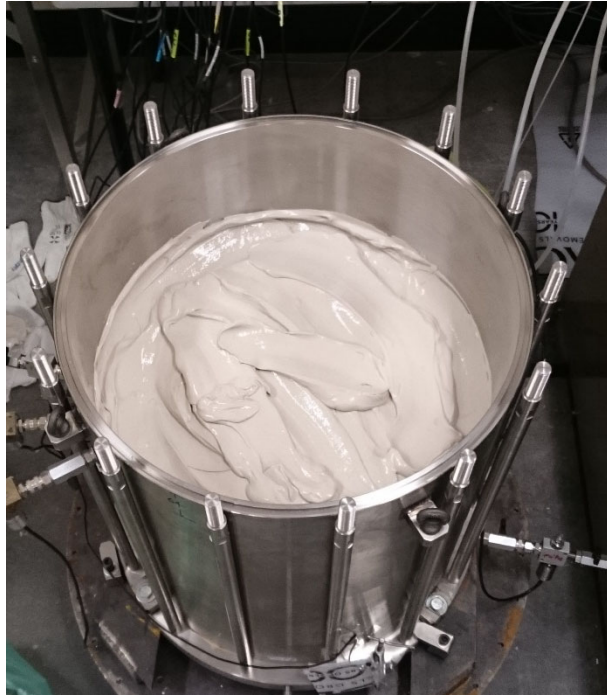


Figure A.1 Slurry placed in layers in the consolidation cell

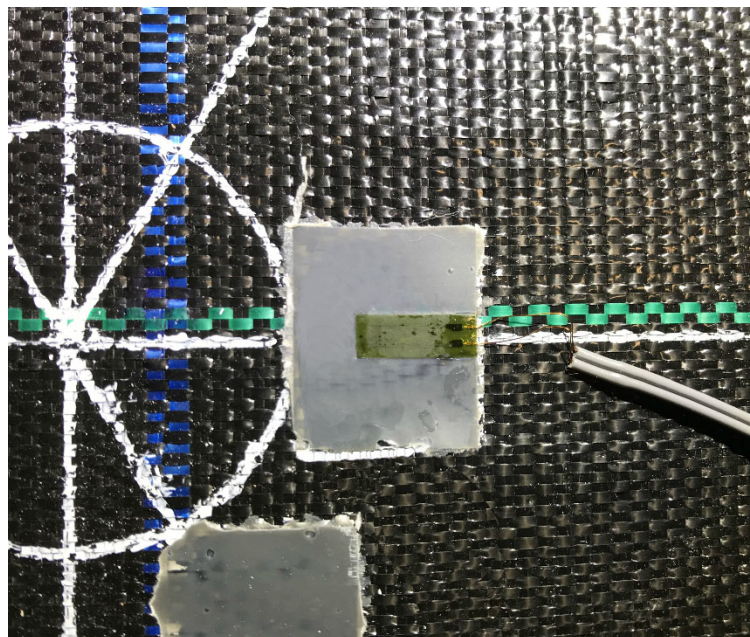


Figure A.2 A strain gauge attached on the epoxy base in the direction of the geotextile fibres



Figure A.3 Initial simplified tensile tests on a single strain gauge using weights



Figure A.4 Initial simplified tests on the effect of boundary condition on the geotextile layer



Figure A.5 Butyl rubber (SB) tape applied on the strain gauge to waterproof and protect the gauges



Figure A.6 Earth pressure cell (EPC) positioned and fixed on the CIC using plaster of Paris



Figure A.7 Top view of the test after half the soft soil was excavated



Figure A.8 CICs at the end of the test after the soft soil was excavated



Figure A.9 Vane shear test to determine the shear strength of the soft soil

APPENDIX B

DEVELOPED FLAC^{3D} CODE TO SIMULATE SOCKETED CICS

```

new
set fish safe on
config fluid
;-----
; Grid Generation Soil & CICs
;-----
gen zon radcyl p0 0 0 0 p1 1 0 0 p2 0 0 -24.5 p3 0 1 0 &
size 2 10 2 1 dim 0.25 0.25 0.25 0.25 rat 1 1 1 1 fill size 2 49 4 3
gen zon radcyl p0 0 0 0 p1 0 1 0 p2 0 0 -24.5 p3 -1 0 0 &
size 2 10 2 1 dim 0.25 0.25 0.25 0.25 rat 1 1 1 1 fill size 2 49 4 3
gen zone reflect dip 90 dd 0 ori 0 0 0
gen zone reflect dip 90 dd 90 ori 1 0 0
gen zone reflect dip 90 dd 90 ori 2 0 0 range x -1 1
gen zone reflect dip 90 dd 90 ori -1 0 0 range x -1 5
gen zone reflect dip 90 dd 90 ori -7 0 0 range x -7 -5
gen zone brick size 15 49 4 rat 0.85 1 1 p0 -38.5,-1,0 &
p1 -9,-1,0 p2 -38.5,-1,-24.5 p3 -38.5,1,0
;-----
; Grid Generation LTP
;-----
gen zone brick size 58,8,18 rat 1 1 1 p0 -9.5, -1, 0 ...
p1 5, -1, 0 p2 -9.5, 1, 0 p3 0, -1, 4.5 P4 5, 1, 0 &
P5 0, 1, 4.5 P6 5, -1, 4.5 P7 5, 1, 4.5 &
;-----
; Grouping
;-----
group zone WP range z 0 -0.5
group zone clay range z -0.5 -19.5
group zone stiffclay range z -19.5 -24.5
group zone Embankment range z 0.5 4.5
group zone LTP range z 0 0.5
group zone CIC range cy end1 0 0 0 end2 0 0 -20.5 r 0.25
group zone CIC range cy end1 2 0 0 end2 2 0 -20.5 r 0.25
group zone CIC range cy end1 4 0 0 end2 4 0 -20.5 r 0.25
group zone CIC range cy end1 -2 0 0 end2 -2 0 -20.5 r 0.25
group zone CIC range cy end1 -4 0 0 end2 -4 0 -20.5 r 0.25
group zone CIC range cy end1 -6 0 0 end2 -6 0 -20.5 r 0.25
group zone CIC range cy end1 -8 0 0 end2 -8 0 -20.5 r 0.25
save geometry
;-----
; Model Soil & CICs and Mechanical Parameters
;-----
gen separate range group CIC
model mech null range group LTP

```

```

model mech null range group Embankment
model mech cam-clay range z -0.5 -19.5
prop poisson 0.3
prop mm 0.898 lambda 0.31 kappa 0.031
prop mp1 5.9E+04 mv_1 3.0
ini density 945
model mech mohr range z 0.0 -0.5
prop bulk 5e7 she 2.3e7 fric 45 coh 1e3 density 2000 range z 0.0 -0.5
model mech mohr range z -19.5 -24.5
prop bulk 1.6e7 she 7.7e6 fric 30 coh 5e3 density 1400 tension 1e4 range z -19.5 -
24.5
;-----
; Boundary Conditions
;-----
fix x range x -38.4 -38.6
fix x range x 4.99 5.1
fix y range y -0.99 -1.1
fix y range y 0.99 1.1
fix x y z range z -24.6 -24.4
;-----
; Initial Conditions
;-----
set gravity 0 0 -10
ini syy 0.0 grad 0 0 13570 range z 0 -0.5
ini sxx 0.0 grad 0 0 13570 range z 0 -0.5
ini szz 0.0 grad 0 0 20000 range z 0 -0.5
ini syy 1038 grad 0 0 15646 range z -0.5 -20.5
ini sxx 1038 grad 0 0 15646 range z -0.5 -20.5
ini szz -2000 grad 0 0 16000 range z -0.5 -20.5
ini syy 130680 grad 0 0 21970 range z -20.5 -25.5
ini sxx 130680 grad 0 0 21970 range z -20.5 -25.5
ini szz 59500 grad 0 0 19000 range z -20.5 -25.5
;-----
; Flow Model and Hydraulic Parameters
;-----
model fluid fl_iso
set fluid biot off
prop perm 1e-13 por .655 range z -0.5 -20.5
prop perm 1e-14 por .5 range z -20.5 -25.5
ini fmod 5e7 ftens -1e20 fdens 1e3
;-----
; Initial Condition of Pore Pressure
;-----
ini pp 0 grad 0 0 -1e4 range z -0.5 -25.5

```

```

fix pp 0 range z -0.5 4.5
;-----
; Cam-clay
;-----
model fluid fl_null range group CIC
def camclay_ini_p
local nccz = 0
local mean_p = 0
local p_z = zone_head
loop while p_z # null
if z_model(p_z) = 'cam-clay' then
nccz = nccz + 1
mean_p = -(z_sxx(p_z) + z_syy(p_z) + z_szz(p_z))/3.0 - z_pp(p_z)
z_prop(p_z,'cam_p') = mean_p
end_if
p_z = z_next(p_z)
endloop
local oo=out(' '+string(nccz)+' zones with camclay')
end
@camclay_ini_p
;-----
; Bulk Bound
;-----
def set_prop
local pnt = zone_head
loop while pnt # null
if z_model(pnt) = 'cam-clay' then
local s1 = -z_sxx(pnt) - z_pp(pnt)
local s2 = -z_syy(pnt) - z_pp(pnt)
local s3 = -z_szz(pnt) - z_pp(pnt)
local p0 = (s1+s2+s3)/3
local q0 = sqrt(((s1-s2)*(s1-s2)+(s2-s3)*(s2-s3)+ (s3-s1)*(s3-s1))*0.5)
local e0 = q0/(z_prop(pnt, 'mm') * p0)
global pc = p0 * (1.+e0*e0)*2
z_prop(pnt,'mpc') = pc
local p1 = z_prop(pnt,'mp1')
local vc = z_prop(pnt,'mv_1') - z_prop(pnt,'lambda')*ln(pc/p1)
local v0 = vc - z_prop(pnt,'kappa') * ln(p0/pc)
local b0 = v0 * p0 / z_prop(pnt,'kappa')
local n0 = (v0 - 1.) / v0
global VR = v0
global bb = 120* b0
z_prop(pnt, 'bulk_bound') = bb
end_if

```

```

pnt=z_next(pnt)
endloop
end
@set_prop prop mpc 1e5 range z -0.5 -1.5
;-----
; Interface
;-----
interface 1 wrap CIC
interface 1 prop kn 1e10 ks 1e10 fric 18.4 coh 1e3
;-----
; Monitoring Points
;-----
History add id 11619 gp zdis id 9859
History add id 54 gp zdis id 18180
History add id 55 gp zdis id 18179
History add id 56 gp zdis id 18178
History add id 57 gp zdis id 18177
History add id 58 gp zdis id 18176
History add id 59 gp zdis id 18175
History add id 60 gp zdis id 18174
History add id 61 gp zdis id 18173
History add id 62 gp zdis id 18172
History add id 63 gp zdis id 18171
History add id 64 gp zdis id 18170
History add id 65 gp zdis id 18169
History add id 66 gp zdis id 18168
History add id 67 gp zdis id 18167
History add id 68 gp zdis id 18166
History add id 69 gp zdis id 18165
History add id 70 gp zdis id 18164
History add id 71 gp zdis id 18163
History add id 72 gp zdis id 18162
History add id 73 gp zdis id 18161
History add id 74 gp zdis id 18160
History add id 75 gp zdis id 18159
History add id 76 gp zdis id 18158
History add id 77 gp zdis id 18157
History add id 78 gp zdis id 18156
History add id 79 gp zdis id 18155
History add id 80 gp zdis id 18154
History add id 81 gp zdis id 18153
History add id 82 gp zdis id 18152
History add id 83 gp zdis id 18151
History add id 84 gp zdis id 18150

```

```

History add id 85 gp zdis id 18149
History add id 86 gp zdis id 18148
History add id 87 gp zdis id 18147
History add id 2221 gp zdis id 9910
History add id 6661 gp zdis id 9967
History add id 551 zone szz id 11619
History add id 661 zone szz id 11730
History add id 221 zone szz id 11673
Hist add id 51 zone pp id 11619
Hist add id 21 zone pp id 11673
Hist add id 61 zone pp id 11730
Hist add id 91 zone pp id 11760
set fluid off
History add id 1 unbal
set mech ratio 1e-5
solve
save soil
;-----
; Model CICs
;-----
model mhoekbrown range group CIC
prop bulk 5.56e9 shear 4.17e9 dens 2400 range group CIC
prop hbsig=10e6 hbmb=12 hbs=1 hba=0.5
prop hb_doption= 0 hbpsi=12 hbtension=759e3
solve
save CICs
;-----
; Model 0.5m Embankment, Consolidation for 1 Week
;-----
Def storeini_perm
local p_z = zone_head
loop while p_z # null
if z_group(p_z) = 'clay' then
z_extra(p_z,1) = z_prop(p_z,'permeability')
z_extra(p_z,2) = z_prop(p_z,'cv')
endif
p_z = z_next(p_z)
endloop
end
@storeini_perm
def set_perm
local p_z = zone_head
loop while p_z # null
if z_group(p_z) = 'clay' then

```

```

local vsinc = (1)* z_prop(p_z,'cam_ev') ;
local czv = (1)* z_prop(p_z,'cv')
local new_perm = z_extra(p_z,1) * 10^(vsinc * czv / 0.95)
z_prop(p_z,'permeability') = new_perm
endif
p_z = z_next(p_z)
endloop
end
@set_perm
set fishcall 13 set_perm
model mech mohr range z 0 0.2
prop bulk 5e7 she 2.3e7 fric 45 coh 1e3 density 2000 range z 0 0.2
fix x range x 4.99 5.1
fix y range y -0.99 -1.1
fix y range y 0.99 1.1
gen separate range group CIC
interface 2 face range z 0 group CIC
interface 2 prop kn 1e10 ks 1e10 c 1e3 fric 36
sel geogrid id=1 range z 0.2 0.3
sel node init zpos add -0.15
sel geogrid prop is=(20e7, 0.33) thick=5e-3 &
cs_sk=2e6 cs_scoh=1e3 cs_sfric=36.0
sel node fix x range x 4.99 5.1
sel node fix y range y -0.99 -1.1
sel node fix y range y 0.99 1.1
model mech mohr range z 0 0.5
prop bulk 5e7 she 2.3e7 fric 45 coh 1e3 density 2000 range z 0 0.5
fix x range x 4.99 5.1
fix y range y -0.99 -1.1
fix y range y 0.99 1.1
attach face range z -0.1 0.1
ini xdis 0 ydis 0 zdis 0
set large
hist fltime
set fluid on
set mech force 0 ratio 1e-4
set fluid substep 1
set mech substep 1 auto
solve age 604800
save LTPgeogrid0.5mEmbankment
;-----
; Model 1m Embankment, Consolidation for 1 Week
;-----
model mech mohr range z 0.51 1

```

```

prop bulk 2.5e7 she 1.15e7 fric 30 coh 5e3 density 2000 range z 0.51 1
fix x range x 4.99 5.1
fix y range y -0.99 -1.1
fix y range y 0.99 1.1
set fluid on
set mech force 0 ratio 1e-4
set fluid substep 1
set mech substep 1 auto ;slave
solve age 1209600
save LTPgeogrid1mEmbankment
;-----
; Model 1.5m Embankment, Consolidation for 1 Week
;-----
model mech mohr range z 0.51 1.5
prop bulk 2.5e7 she 1.15e7 fric 30 coh 5e3 density 2000 range z 0.51 1.5
fix x range x 4.99 5.1
fix y range y -0.99 -1.1
fix y range y 0.99 1.1
set fluid on
set mech force 0 ratio 1e-4
set fluid substep 1
set mech substep 1 auto
solve age 1814400
save LTPgeogrid1.5mEmbankment
;-----
; Model 2m Embankment, Consolidation for 1 Week
;-----
model mech mohr range z 0.51 2
prop bulk 2.5e7 she 1.15e7 fric 30 coh 5e3 density 2000 range z 0.51 2
fix x range x 4.99 5.1
fix y range y -0.99 -1.1
fix y range y 0.99 1.1
set fluid on
set mech force 0 ratio 1e-4
set fluid substep 1
set mech substep 1 auto ;slave
solve age 2419200
save LTPgeogrid2mEmbankment
;-----
; Model 2.5m Embankment, Consolidation for 1 Week
;-----
model mech mohr range z 0.51 2.5
prop bulk 2.5e7 she 1.15e7 fric 30 coh 5e3 density 2000 range z 0.51 2.5
fix x range x 4.99 5.1

```

```

fix y range y -0.99 -1.1
fix y range y 0.99 1.1
set fluid on
set mech force 0 ratio 1e-4
set fluid substep 1
set mech substep 1 auto
solve age 3024000
save LTPgeogrid2.5mEmbankment
;-----
; Model 3m Embankment, Consolidation for 1 Week
;-----
model mech mohr range z 0.51 3
prop bulk 2.5e7 she 1.15e7 fric 30 coh 5e3 density 2000 range z 0.51 3
fix x range x 4.99 5.1
fix y range y -0.99 -1.1
fix y range y 0.99 1.1
set fluid on
set mech force 0 ratio 1e-4
set fluid substep 1
set mech substep 1 auto ;slave
solve age 3628800
save LTPgeogrid3mEmbankment
;-----
; Model 3.5m Embankment, Consolidation for 1 Week
;-----
model mech mohr range z 0.51 3.5
prop bulk 2.5e7 she 1.15e7 fric 30 coh 5e3 density 2000 range z 0.51 3.5
fix x range x 4.99 5.1
fix y range y -0.99 -1.1
fix y range y 0.99 1.1
set fluid on
set mech force 0 ratio 1e-4
set fluid substep 1
set mech substep 1 auto ;slave
solve age 4233600
save LTPgeogrid3.5mEmbankment
;-----
; Model 4m Embankment, Consolidation for 1 Week
;-----
model mech mohr range z 0.51 4
prop bulk 2.5e7 she 1.15e7 fric 30 coh 5e3 density 2000 range z 0.51 4
fix x range x 4.99 5.1
fix y range y -0.99 -1.1
fix y range y 0.99 1.1

```

```

set fluid on
set mech force 0 ratio 1e-4
set fluid substep 1
set mech substep 1 auto
solve age 4838400
save LTPgeogrid4mEmbankment
;-----
; Model 4.5m Embankment, Consolidation for 1 Week
;-----
model mech mohr range z 0.51 4.5
prop bulk 2.5e7 she 1.15e7 fric 30 coh 5e3 density 2000 range z 0.51 4.5
fix x range x 4.99 5.1
fix y range y -0.99 -1.1
fix y range y 0.99 1.1
set fluid on
set mech force 0 ratio 1e-4
set fluid substep 1
set mech substep 1 auto
solve age 5443200
save LTPgeogrid4.5mEmbankment
;-----
; Applying 10kPa on the Embankment, Consolidation
;-----
def init
global _nsteps=10000
end
@init
def ramp
ramp = min(1.0,float(step)/_nsteps)
end
apply nstress=-1.0e4 his @ramp range z 4.45 4.65
set fluid on
set mech force 0 ratio 1e-4
set fluid substep 1
set mech substep 1 auto
solve age 236520000
save Load10kPa

```